Probing the processes driving distant and local star-formation in galaxies through dust and molecules

Luwenjia Zhou

▶ **To cite this version:**

Luwenjia Zhou. Probing the processes driving distant and local star-formation in galaxies through dust and molecules. Astrophysics [astro-ph]. Université Paris-Saclay; Nanjing University (Chine), 2020. English. NNT : 2020UPASP099 . tel-03187486

HAL Id: tel-03187486

https://theses.hal.science/tel-03187486

Submitted on 1 Apr 2021

HAL is a multi-disciplinary open access archive for the deposit and dissemination of scientific research documents, whether they are published or not. The documents may come from teaching and research institutions in France or abroad, or from public or private research centers.

L'archive ouverte pluridisciplinaire **HAL**, est destinée au dépôt et à la diffusion de documents scientifiques de niveau recherche, publiés ou non, émanant des établissements d'enseignement et de recherche français ou étrangers, des laboratoires publics ou privés.

université PARIS-SACLAY

NNT : 2020UPASP099

Thèse de doctorat

Probing the processes driving distant and local star-formation in galaxies through dust and molecules

Thèse de doctorat de l'Université Paris-Saclay et de Nanjing University

Ecole doctorale n°127 Astronomie et Astrophysique d'Ile de France (AAIF)
Spécialité de doctorat : Astronomie et Astrophysique

Unité de recherche : Université Paris-Saclay, CNRS, CEA, Astrophysique, Instrumentation et Modélisation de Paris-Saclay, 91191, Gif-sur-Yvette, France

Référent : Faculté des sciences d'Orsay

Thèse présentée et soutenue à Nanjing, Chine, le 13 novembre 2020, par

LUWENJIA ZHOU (周陆文嘉)

Composition du Jury :

Hervé Dole Professeur, Université Paris-Saclay	Président
Yiping Ao Directeur de Recherche, Purple Mountain Observatory	Rapporteur & examinateur
Bunyo Hatsukade Professeur assistant, University of Tokyo	Rapporteur & examinateur
Veronique Buat Professeure, Laboratoire d'Astrophysique de Marseille (LAM)	Examinatrice
Xu Kong Professeur, University of Science and Technology of China	Examinateur
Xianzhong Zheng Directeur de Recherche, Purple Mountain Observatory	Examinateur
David Elbaz Directeur de Recherche, Commissariat à l'énergie atomique (AIM)	Directeur de thèse
Yong Shi Professeur, Nanjing University	Directeur de thèse

Abstract

Les études sur l'évolution des galaxies ont été révolutionnées au cours des dernières décennies grce aux nouveau télescopes et aux instruments de pointe. Les interféromètres *Herschel*, ALMA et NOEMA permettent d'observer l'émission des poussières tracant la formation des étoiles, invisible dans les bandes infrarouges proche observées par les télescopes optiques. Leur grande sensibilité permet la détection des galaxies les plus lointaines, ainsi que des galaxies locales les plus faibles dont la formation et l'évolution remettent en question les théories et les modèles actuels. La technique de l'unité de champ intégrale permet de combiner l'information spatiale et les propriétés extraites des spectres, permettant une étude approfondie de la cinématique des galaxies.

Dans cette thèse, je me concentre sur la formation des étoiles aux grandes échelles des galaxies ($\sim$ kpc). En utilisant les données des téléscopes *Herschel*, ALMA, NOEMA, et SAMI IFU, ma thèse tente de mettre en lumière les questions suivantes : (1) Comment les premières galaxies ont-elles formé des étoiles à partir du gaz contenant peu de métaux ? (2) Comment les galaxies massives du début de l'Univers ont-elles rapidement constitué leur masse et finalement cessé de former des étoiles ? (3) Quel est le rle joué par les environnements dans lesquels elles résident ? (4) Comment la rétroaction de la formation des étoiles affecte-t-elle la cinématique des galaxies ?

Premièrement, je présente l'étude de six galaxies optiquement sombres extraites de l'étude GOODS-ALMA (la plus grande étude cosmologique à 1,1 m) dont le décalage vers le rouge est supérieur à $z = 3$. Je présente des preuves que quatre d'entre elles appartiennent à la même surdensité de galaxies, situé à $z \sim 3.5$. L'une d'entre elles, AGS24 ($M_\star = 10^{11.32^{+0.02}_{-0.19}}$ M$_\odot$), est la galaxie la plus massive, sans noyau galactique actif et situé à $z > 3$. Cette dernière se situe également au centre du pic de densité de surface des galaxies, suggèrant que la surdensité environnante est un proto-amas en cours de virialisation et qu'AGS24 est un candidat progéniteur d'un futur amas de galaxie plus brillant.

Deuxièmement, en me basant sur une observation NOEMA, j'ai étudié la teneur en gaz moléculaire dans IZw18, l'une des galaxies les plus pauvres en métal de l'Univers local. J'ai obtenu une limite supérieure d'émission de CO(J=2-1) qui est dix fois plus faible que précédemment déterminée, ceci malgré la forte activité de formation d'étoiles. Sa faible teneur en CO (par rapport à sa luminosité infrarouge), son taux de formation d'étoiles, et sa luminosité [C II] indiquent un changement drastique dans la structure du MIS (environ quelques pourcents de la métallicité solaire). En particulier, la luminosité élevée [C II] par rapport au CO implique un réservoir moléculaire plus important que l'émetteur de CO dans l'IZw18.

Troisièmement, mes travaux sur les sources d'énergie des mouvements turbulents montrent qu'à des échelles inférieures au kpc, les galaxies locales formant des étoiles du relevé SAMI présentent une

distribution plate de la dispersion de vitesse du gaz ionisé en fonction de la densité de surface du taux de formation d'étoiles. Cependant, le plancher de dispersion de vitesse est plus élevé que ce que prédisent les modèles "feedback-driven". Cela suggère que des sources supplémentaires à la rétroaction de formation d'étoiles entranent des mouvements aléatoires du MIS dans les galaxies formant des étoiles.

Enfin, je présente mes travaux sur l'émission de poussières spatiallement résolue des galaxies extrêmement pauvres en métaux observées par *Herschel*. Ces galaxies présentent des températures de poussière plus élevées et des indices d'émissivité plus faibles que ceux des galaxies spirales. Environ la moitié de l'émission à 100 μm provient de la poussière chaude (50 K), par opposition à la composante froide ($\sim$20 K) de la poussière. Les couleurs de l'infrarouge lointain sont toutes liées aux densités de surface des jeunes étoiles, mais pas aux densités de surface des masses stellaires. Cela suggère que leur poussière (70 $\sim$ 350 μm) est principalement chauffée par le rayonnement des jeunes étoiles.

Acknowledgement

It came as a surprise when I got to know that I could also do a joint-PhD at Université de Paris Saclay and it was already such a great pleasure to come to CEA as a visiting student for two years, thanks to everyone at CEA as a host and the financial support from China Scholar Council.

During the two years in France, I have gained a lot of knowledge not only from academia but also from everyone I met.

First of all, thank you, David. Thanks for hosting me at CEA and for mentoring me in this thesis. Your passion for science inspires me. It reminds me that being a researcher is not only a way to make a living, but more essentially a lifestyle. A lifestyle to stay curious about everything, to observe what is happening around us, to crack down what is behind what we see. It reminds me of how I was originally fascinated about science: to think, to ask questions originated from my daily life and finally to describe, to explain, and to predict these phenomena. I am grateful for your patience with me, for explaining to me the big pictures and for so much help with my life in France.

Thanks Emanuele for always taking so much time for the Journal Club and for the valuable discussions, your door is always open when I need help. Thanks also to many other people, Jérôme, Alain, Pascale, Laure, Tao, Corentin, Benjamin, Frederic, Emeric, Koryo for always being so warm-hearted, I have learnt a lot from you.

And all the friends at CEA, my two years at CEA would not have been so fruitful and unforgettable without you. Max, my office mate, you have been always helping me in the most critical time. You offered me valuable suggestions when I got stuck at work. And our tea/coffee breaks, bicycle trips, cheese and wine... Chiara, I feel so lucky to have had you by my side during all these adventures (the opening day, the D-day, the interviews with the committees... and our trip to Giverny, hanging out in Paris). Antonello, you are one of the old friends since I came to CEA for a short internship three years ago. You have been always sharing your good ideas with me. I am so grateful for your immediate help after my laptop was stolen. Anna, you always have the magic to make the atmosphere so lively and cheerful. Ivan, you are so organized and taking care of everyone of us. Baptise and Solène, you introduced to me the French culture and shared with me so many fun facts about life in France. Dangning, thanks to you, our "2019 Chinese New Year's Eve dinner" was such a success. You also offered me so many useful tips as an experienced "Chinese in France". And many other friends I met at CEA: Rose, Maud, Valeska, Benjamin, Antigone, Anita, Daizhong, Francesco, Jeremy.

And my life at the center of the world, Gif-sur-Yvette: Thank you, Judica, for hosting me at your place. You have been like a mother to teach me how to take care of myself in your own special way, and have shown me how to think critically, how to take actions actively to solve problems efficiently.

Thank you, Pascale. You have never regarded me as an outsider, and have always kindly invited me to all kinds of activities. This makes me feel integrated to the life in France and so much less lonely when I was in France.

And many thanks to all my friends, my teachers and my family back in China, what I want to say to you are included in the Chinese version of my thesis. Thanks Mum and Dad for your unconditional support of all time.

Merci Anoine. Mille mercis pour ton grand soutien lors de ma thèsis et l'écriture de ce manuscript. Merci d'être toujours là et de me motiver. Merci d'être venu dans ma vie.

To my grandfather, Baoshan Wang（王宝山）.

Contents

1 Introduction **1**
- 1.1 Star formation: the driver of galaxy evolution . . . 1
- 1.2 Star formation obscured by interstellar dust . . . 2
  - 1.2.1 Multi-wavelength study of galaxies . . . 3
  - 1.2.2 The main sequence of star-forming galaxies . . . 5
  - 1.2.3 Cosmic star formation history . . . 7
  - 1.2.4 Observing star-forming galaxies in the (sub)millimeter . . . 9
  - 1.2.5 Optically-dark galaxies . . . 13
- 1.3 Star formation fueled by gas . . . 15
  - 1.3.1 Gas tracers . . . 15
  - 1.3.2 Star formation law . . . 16
  - 1.3.3 Gas content . . . 18
- 1.4 Star formation as one of the energy sources of gas . . . 18
  - 1.4.1 Gas velocity dispersion and the energy sources . . . 18
  - 1.4.2 Integral field unit (IFU), datacube and beam smearing effect . . . 19

2 Summary of the work done in this thesis **21**
- 2.1 GOODS-ALMA . . . 21
  - 2.1.1 Optically dark galaxies and their association with a proto-cluster in formation at $z \sim 3.5$ . . . 21
  - 2.1.2 Data compilation . . . 22
  - 2.1.3 Nascent AGNs in GOODS-ALMA . . . 23
  - 2.1.4 Contribution as third author . . . 23
- 2.2 Extremely metal-poor galaxies . . . 24
  - 2.2.1 Spatially resolved dust emission . . . 24
  - 2.2.2 Gas content in IZw18 . . . 24
- 2.3 The SAMI Integral field Units (IFU) Survey . . . 25
  - 2.3.1 Energy source of turbulence in star-forming galaxies . . . 25
- 2.4 Observations . . . 25

3 GOODS-ALMA: optically-dark ALMA galaxies shed light on a cluster in formation at $z = 3.5$ **27**
- 3.1 Introduction . . . 27
- 3.2 Data and observations . . . 29
  - 3.2.1 ALMA data and observations . . . 30
  - 3.2.2 Ancillary data . . . 31
  - 3.2.3 Origin of the redshifts and stellar masses . . . 32

3.2.4 Derived parameters of the optically dark galaxies . . . 32
3.3 Results of the ALMA spectroscopic follow-up . . . 34
3.3.1 AGS4 . . . 35
3.3.2 AGS17 . . . 36
3.3.3 Upper limits of AGS11, AGS15 and AGS24 . . . 37
3.4 GOODS-ALMA optically-dark galaxies . . . 37
3.4.1 AGS4, an extremely massive galaxy at z=3.556 and a case of blending in the Hubble H-band image . . . 38
3.4.2 AGS25, the most distant optically-dark galaxy in GOODS-ALMA . . . 40
3.5 An over-density at $z\sim3.5$ in GOODS-ALMA . . . 41
3.5.1 Clustering properties of optically dark galaxies . . . 41
3.5.2 A clear peak at $z\sim3.5$ in the redshift distribution . . . 41
3.5.3 Optically-dark galaxies at $z\sim3.5$ . . . 42
3.5.4 Spatial distribution of galaxies at $z\sim3.5$ in the GOODS-ALMA field . . . 48
3.5.5 Dynamical state of the proto-cluster at $z\sim3.5$ . . . 53
3.6 Conclusions . . . 54

4 Extremely weak CO emission in IZw 18 57
4.1 Introduction . . . 57
4.2 Observations . . . 58
4.3 Results . . . 58
4.3.1 CO J=2-1 . . . 58
4.3.2 1.3 mm continuum . . . 59
4.4 Discussion . . . 59
4.4.1 SED and Submilimetre excess . . . 60
4.4.2 Infrared luminosity and SFR versus $L'_{\rm CO}$ . . . 61
4.4.3 The structure of the interstellar medium . . . 62
4.5 Conclusion . . . 63

5 The SAMI Galaxy Survey: energy sources of the turbulent velocity dispersion in spatially-resolved local star-forming galaxies 65
5.1 Introduction . . . 65
5.2 Sample and data analysis . . . 67
5.2.1 Sample selection . . . 67
5.2.2 Gas kinematic information . . . 70
5.2.3 Spatial resolution . . . 72
5.3 Results . . . 73
5.3.1 The spatial distribution of $\Sigma_{\rm SFR}$, $v_{\rm gas}$, and $\sigma_{\rm gas}$ . . . 73
5.3.2 The $\sigma_{\rm gas}-\Sigma_{\rm SFR}$ relation in local and high redshift star-forming galaxies . . . 73
5.4 Discussion . . . 78
5.4.1 Main driver(s) of velocity dispersion . . . 78
5.4.2 Caveats . . . 79
5.5 conclusion . . . 81

6 Spatially resolved dust emission of extremely metal poor galaxies[1] 83
6.1 Introduction . . . 83

6.2 Sample, observations and data analysis . . . 84
6.2.1 The sample . . . 84
6.2.2 Observations . . . 86
6.2.3 Photometric measurements . . . 86
6.3 The far-IR SEDs . . . 88
6.3.1 The color-color diagrams . . . 88
6.3.2 Modified black-body fitting . . . 89
6.3.3 Spatial variations of SEDs and dust heating Mechanism . . . 91
6.4 Dust-to-stellar mass ratio . . . 94
6.5 Conclusions . . . 96

7 Conclusion and perspectives **97**
7.1 Conclusion . . . 97
7.2 Perspective . . . 98
7.2.1 More on the optically dark galaxies . . . 98
7.2.2 AGN feedback on high-z star-forming galaxies . . . 99

Bibliography **103**

1 Introduction

> 小时不识月　*When a kid I didn't cognize the moon,*
> 呼作白玉盘　*Called it a jade dish just as soon.*
> 又疑瑶台镜　*Wondered if it a dresser mirror, too*
> 飞在青云端　*Flying over the cloud blue.*
>
> —《古朗月行》　**Ballad of Ancient Bright Moon**
> 李白　Bai Li

1.1 Star formation: the driver of galaxy evolution

Galaxies are made of stars, dust, gas and dark matters. They are gravitationally bound systems showing various properties in morphologies, luminosities, colors, sizes and masses, etc. Such diversities suggest complicated processes in galaxy evolution and formation (e.g., Mo et al., 2010). Nowadays, most studies converge to a scenario where galaxies grow mainly through a secular process (e.g., Schreiber et al., 2015): Gas accretes from the intergalactic medium (IGM), then it cools, condenses into molecular clouds and finally collapses into stars, hence, fuels star formation (White and Rees, 1978). At the late stage of their lives, stars release part of their masses back to the interstellar medium (ISM) through stellar winds, planetary nebulae and supernovae. The released gas and dust, as well as energy, are involved in the formation of the next generation of stars(e.g., Larson, 1974; Martin, 1999). Therefore, star formation is considered as the key process driving galaxy evolution.

However, the mechanisms that regulate each step mentioned above are complex: What controls the gas inflow from the surrounding environment of galaxies and stars? How efficient is the conversion of the available gas reservoir into stars? Whether the gas ejection and heating by star formation feedback accelerate or hinder further star formation?... In addition, supermassive black holes at the center of galaxies may undergo a temporarily active phase of active galactic nucleus (AGN). The efficient gas accretion triggers AGNs which then release a significant amount of energy into the host galaxies (Kormendy and Ho, 2013; Heckman and Best, 2014). This further complicates galaxy ecosystems.

Galaxies are not isolated systems. When we place them in a broader context, they pinpoint the most luminous and the most massive spots of matter distributions in the Universe. Such wide distributions are called large-scale structures, and are always in the form of web-like networks, hence also called cosmic web (Peacock et al., 2001). Large-scale structures provide passages for gas to accrete into galaxies and to replenish the fuel of star formation (Dekel et al., 2009). Some galaxies would gather in the knots of cosmic webs, therefore they are more likely to interact with each other. The interactions can be violent, such as mergers, or mild, such as fly-bys. In either case, the distribution and physical

states of the stars, ISM and halos in the galaxies can be dramatically altered after the interactions and the evolution paths of the galaxies will be significantly changed since then.

The extragalactic astronomy is a relatively young field of research. It was not until a century ago that, Hubble measured the distances of the Cepheid variable stars in Andromeda and confirmed that there are systems external to our Milky Way (Hubble, 1926). The study of galaxy formation and evolution relies heavily on observations. Compared to gravitational waves originating from extremely rare events of merging binary systems, electromagnetic emission from galaxies, mainly consist of direct or reprocessed starlight, are ubiquitous and relatively easier to obtain. Thanks to the rapid development of the modern technology, especially the tremendous progress in manufacturing powerful telescopes, exciting breakthroughs have been made through astrophysics observations, for example, last year, astrophysicists obtained the first direct confirmation of the existence of black holes in M83 (Event Horizon Telescope Collaboration et al., 2019), using the Event Horizon Telescope, a planet-scale array of ground-based radio telescopes. Yet, there is more to explore.

So far in extragalactic astronomy, despite the broad diversities of galaxies, extensive observations have revealed tight scaling relations between galaxy properties, such as the star formation law (star formation rate surface density *vs.* gas surface density), the galaxy main sequence (star formation rate *vs.* stellar mass), which will be introduced in detail below, as well as the stellar mass-metallicity relation, the Tully-Fisher relation (total mass *vs.* rotational velocity) *etc*. The comparison between these relations with models can better constrain the processes regulating the star formation activity in galaxies to further understand how galaxies in the early Universe evolved to the ones on the present day.

In this thesis I have worked on different topics on star formation in galaxies. In the following, I am going to specify the main topics I have been working on during my thesis on star formation in galaxies.

1.2 Star formation obscured by interstellar dust

UV emission of galaxies is dominated by the most massive stars (OB stars), which end their lives shortly after their birth (<100Myr), compared to the vast majority of other stars (e.g., it is estimated to be 10 Gyr for the Sun). Therefore, the existence of OB stars, as indicated by their UV emission, suggests a recent star formation within a time scale of $\sim$100 Myr. Then UV luminosity is an idea tracer of the star formation rate (SFR) of galaxies (Kennicutt, 1998a). However, as mentioned above, stars produce heavy elements, also known as metals, and release them into the ISM at the late stage of their evolution. A significant fraction of metals are locked into the interstellar dust. This suggests that star formation is always accompanied by dust formation. UV photons are energetic, with wavelengths between 150 and 300 nm, smaller than the typical size of dusts. As UV photons emitted by a massive galaxy travel through the galaxy, they can be easily absorbed or scattered by dust. Hence SFR estimated from UV can be heavily underestimated. Nevertheless, the absorbed energy will be re-emitted by dust in the far-infrared (FIR) through thermal radiation. An example is shown in Fig. 1.1-b. By observing in the FIR[1], astrophysicists can recover star formation hidden by the interstellar dust.

[1] It can be redshifted to longer wavelength as will be discussed later.

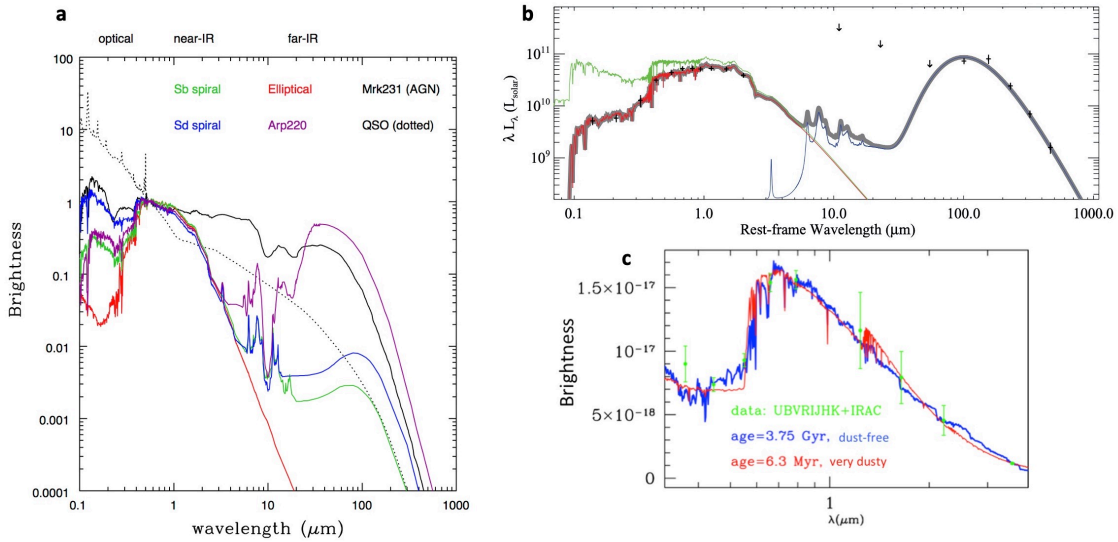

Fig. 1.1: **a**: Spectral energy distributions (SEDs) for typical galaxies - an old elliptical galaxy (red), two types of spiral galaxies (Sb in green and Sd in blue), an AGN (Markarian 231, solid black), a QSO (dotted black), and a merging and star-bursting galaxy Arp 220. Template spectra are taken from Polletta et al. (2007). Courtesy: CANDELS blog. **b** The spectral energy distributions (SEDs) of a typical star-forming galaxy (H-ATLAS J090713.1-000322). The total SED is in grey, with the stellar component in red and the corresponding dust emission in blue. The green curve denotes the unattenuated stellar light. Figure from Smith et al. (2012). **c**: Example of SED fitting - an old, dust free galaxy (blue) and a young, dusty galaxy (red) both fit the observed data points (green) in the UV to mid-infrared (MIR) regime. Courtesy: CANDELS blog.

1.2.1 Multi-wavelength study of galaxies

Based on morphologies, Edwin Hubble proposed a classification scheme dividing galaxies into spirals, lenticulars and ellipticals (Hubble, 1926). This is the so-called *Hubble tuning fork* or *Hubble sequence*. Later on, as more photometric filters are available to observe galaxies, a bimodal distribution of red and blue[2] galaxies was discovered by the Sloan Digital Sky Survey (SDSS), see Fig. 1.3-Left as an example (Strateva et al., 2001; Bell et al., 2004; Baldry et al., 2004). This bimodality in color was later found to be related to their morphologies, with galaxies falling in the red sequence mostly elliptical and galaxies falling in the blue cloud mostly spiral [3]. The colors of galaxies is a natural result of their spectral energy distributions (SEDs).

An SED shows the energy distribution of a galaxy across the electromagnetic spectrum, where physical processes occur to the stars, gas, dust and possibly AGNs in galaxies leave their imprints. In Fig. 1.1-a, we show the SEDs of typical galaxies: an old elliptical galaxy, two types of spiral galaxies, an AGN, a QSO, and a merging and star-bursting galaxy Arp220. They show distinct features in their SEDs. Ellipticals show fainter emission in the UV-optical and FIR compared to spirals, because they have few young stars and little dust to emit at these two regimes. In mergers, the intensive star formation produce an enormous amount of young stars and dust that contribute to the bright UV-optical emission

[2] "red" and "blue": In astronomy, we define "color" as the magnitude difference of a galaxy through two different photometric filters. Conventionally, it is the magnitude of the filter at the shorter wavelength minus the other one. Then the higher the value of the color, the redder we assume the galaxy is, otherwise, it is blue.

[3] This is not always true as red spiral galaxies and blue ellipticals do exist, rare though (e.g., van den Bergh, 1976; Moran et al., 2006; Rowlands et al., 2012).

and the huge FIR bump respectively. Meanwhile, a large amount of light from young stars is absorbed by the dust. Hence its SED at UV to mid-infrared (MIR) regime resembles the one of a galaxy with older stellar population but less dust. Fig. 1.1-c shows an extreme case. The SED templates of both an old, dust-free galaxy and a young, dusty galaxy give indistinguishable good fits to the data points. A full SED-fitting from UV to FIR is necessary to break the degeneracy in such cases.

For distant galaxies, which are much fainter, observationally, than local galaxies, the observed data points do not have very good coverage from rest-frame UV to FIR wavelengths. However, taking advantage of the prominent features in the UV to MIR spectrum, the colors can be good indicators to classify galaxies. On the other hand, according to Hubble-Lemaître law (Hubble and Humason, 1931; Lemaître, 1931), the Universe is expanding, and the more distant the galaxy is, the faster it is receding from us. As a result, the SEDs of distant galaxies are redshifted. Steidel et al. (1996) identified star forming galaxies at $z \sim 3$ with $U_{\rm n}GR_{\rm s}$ rest-frame UV colors. They used a "drop-out" technique: the Lyman break[4], at $\lambda \sim 912$ Å, is redshifted to ~ 3600 Å at $z \sim 3$. When a star-forming galaxy at $z \sim 3$ is imaged with a series of filters, e.g., as in Fig. 1.2, it is invisible in the image taken with the filter(s) covering $\lambda \leq 3600$ Å, or it is "dropped-out". In addition, the roughly flat spectrum ($F_\nu \propto \nu^0$) in the far-UV, where emission is dominated by massive stars, is the other feature they used. Star-forming galaxies selected with this technique are called Lyman break galaxies (LBG)[4]. They are biased to UV bright galaxies with low dust content, because dust would absorb the photons emitting at rest frame wavelengths longer than 912 Å, hence the Lyman break would be washed out. *BzK* colors (observed frame) proposed by Daddi et al. (2004), making use of the CIV absorption line at 1550 Å (rest-frame, same below), the breaks and absorption features at 2200 – 3000 Å, and the 4000 Å break[5], can effectively select both star-forming galaxies and passive galaxies at $1.4 \lesssim z \lesssim 2.5$. In order to include dusty galaxies, which tend to be massive so that dust content is bound in their potential well, into the selection, rest-frame infrared colors are needed. Williams et al. (2009) proposed a *UVJ* selection based on the strong bimodal behaviour found between quiescent galaxies and dusty star-forming galaxies in the rest-frame U - V versus V - J space. The introduced infrared band, J, in V - J, is used to break the age-attenuation degeneracy while the U - V mimics the traditional color-magnitude diagram (Strateva et al., 2001; Bell et al., 2004; Baldry et al., 2004). Pushing forward to higher redshifts, at $z > 3$, Wang et al. (2016b) introduced the observed MIR Infrared Array Camera(IRAC) band at 4.5 μm, in the H - [4.5] (observed frame) color to select massive galaxies which have been largely missed by previous methods. The H band traces the 4000 Å break at

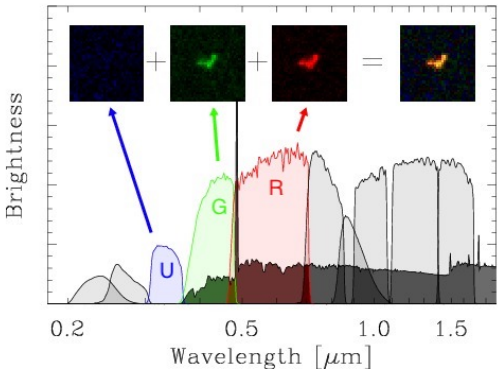

Fig. 1.2: The SED of a typical Lyman break galaxy at $z \sim 3$, and the images of this galaxy taken with photometric filters at $U_{\rm n}$, G, $R_{\rm s}$ bands. Courtesy: CANDELS blog.

[4] Lyman break is a sharp decrease in the SED at $\lambda \leq 912$ Å. Energetic photons with $E > 13.6$ keV, the ionization energy of a hydrogen atom, emit at $\lambda \leq 912$ Å. They can be are easily absorbed by the hydrogen gas from the ISM within the galaxy or from the IGM outside the galaxy, hence hardly observable in the SED.

[5] 4000 Å break is caused by the blanket absorption of high energy radiation from metals in stellar atmospheres and by a deficiency of hot, blue stars. It coincides with the Balmer break at 3646 Å which arises from a similar mechanism to the one of Lyman break, but the energetic photons at $\lambda > 3646$ Å ionize the first excitation state of hydrogen atom instead of ground state hydrogen atom. It is an indicator of stellar population age (Kauffmann et al., 2003)

$z > 3$ while [4.5] is the redshifted *J* as used in the *UVJ* (rest-frame) color selection by Williams et al. (2009). An additional *J*-*H* (observed frame) color is used to rule out the contamination from extremely dusty galaxies at $z < 3$.

With all these effective methods, a large amount of star-forming galaxies with great diversities (redshift, mass, dust content, *etc.*) have been accumulated to allow a systematic study of the star formation in galaxies over the cosmic history.

1.2.2 The main sequence of star-forming galaxies

The study of the present and past star formation in individual galaxies relies on detailed studies of the stellar populations within galaxies. Such studies are only feasible with galaxies in the Local Group (within 1.5 Mpc from us) due to observation limitations. However, we can study the dominant drivers of the changes in star formation of galaxies statistically.

Although galaxies show a broad diversity, many tight scaling relations have been found. Hubble tried to interpret the *Hubble sequence* as a galaxy evolution sequence where ellipticals formed first and spirals later[6] (Hubble, 1926). With the advent of large surveys like SDSS, as mentioned previously, the galaxy color-magnitude diagram shows a distinctive bimodal distribution (Fig. 1.3-Left). The *u*-*r* color is a proxy of specific star formation rates ($\mathrm{sSFRs} \equiv \mathrm{SFR}/\mathrm{M_{star}}$) and the magnitude can be converted into stellar masses. Therefore, the distribution of red and blue galaxies in the color-magnitude diagram indicates that stellar masses are regulating the star formation in galaxies. Indeed, star-forming galaxies show a tight correlation (with a dispersion less than 0.3 dex, Sargent et al. (2012); Schreiber et al. (2015)) between their SFR and stellar masses over a large redshift range, from $z \sim 0$ to $z \gtrsim 4$, and over a broad stellar mass range from down to $10^{9.0}\,\mathrm{M_\odot}$ to up to $10^{11.4}\,\mathrm{M_\odot}$ (Brinchmann et al., 2004; Elbaz et al., 2007; Daddi et al., 2007; Noeske et al., 2007; Rodighiero et al., 2011; Whitaker et al., 2012; Daddi et al., 2009; Pannella et al., 2009; Magdis et al., 2010; Heinis et al., 2013; Pannella et al., 2015; Steinhardt et al., 2014; Bouwens et al., 2012; Stark et al., 2009; Stark et al., 2013). This is the so-called "main sequence" correlation. A minority of galaxies ("starbursts", only a few percent of the total star-forming galaxies, Rodighiero et al. (2011); Sargent et al. (2012); Schreiber et al. (2015), see also Fig. 1.4-Right) have highly elevated SFRs above the main sequence (Elbaz et al., 2011) and there are also galaxies with deeply reduced SFRs below the main sequence. This is illustrated in Fig. 1.3-Right.

The main sequence evolves with redshift, as shown in Fig. 1.4-Left, which implies that at a specific stellar mass, a galaxy would form stars more rapidly at higher redshift, *i.e.,* the sSFR evolves continuously with redshift. In another word, the SFR of a main sequence galaxy at high redshift would be associated to a starburst galaxy with the same stellar mass but at lower redshift. On the other hand, the dispersion of the main sequence barely evolves with redshift, which means that at a specific stellar mass and a specific redshift, $\sim 68\%$ of star-forming galaxies form stars at a rate within a factor of ~ 2 (Schreiber et al., 2015). If we define the galaxies on the main sequence as "normal" star-forming galaxies, then the normal and starburst galaxies represent the two main modes that control the growth of galaxies,

[6] That's why conventionally elliptical galaxies are called "early-type" galaxies and spiral galaxies are called "late-type" galaxies.

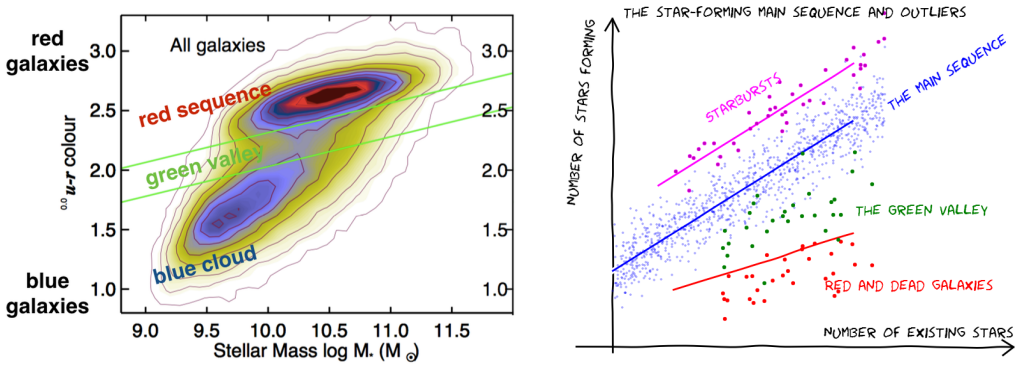

Fig. 1.3: **Left**: The galaxy absolute magnitude-color diagram in SDSS filter colors, where absolute magnitude has been converted to stellar mass. Figure adapted from Schawinski et al. (2014) by S. Majewski. **Right**: Schematic representation of the main sequence and other galaxies with different star formation modes. Courtesy: CANDELS blog.

because starbursts are not simply an extension of main-sequence galaxies, as shown by the double Gaussian decomposition of the starburstiness ($R_{SB} = SFR/SFR_{MS}$) distribution of star-forming galaxies in Fig. 1.3-Right. In fact, these two populations show different evolution paths. Starbursts are often interpreted as driven by mergers which can substantially boost SFR instantaneously, while normal galaxies form stars more steadily. The low percentage of starburst in star-forming galaxies indicates that galaxy mergers have very limited contribution to the global star formation history. Moreover, at $0 < z < 3$, the fraction of starbursts is not evolving with redshift, which means that the "normal" mode dominates the star formation in most galaxies (Rodighiero et al., 2011; Sargent et al., 2012; Schreiber et al., 2015). The steadily evolving main sequence has been used to constrain the cosmic star formation histories.

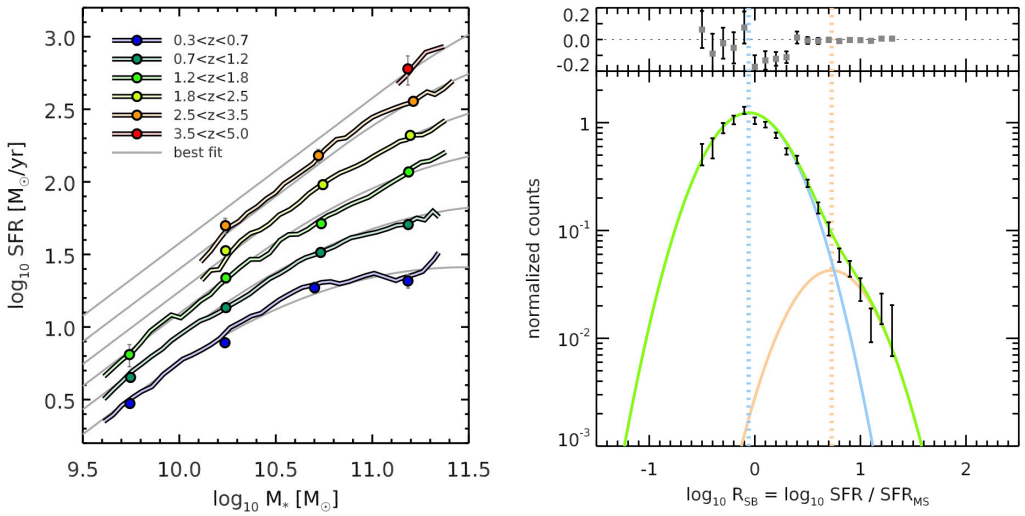

Fig. 1.4: **Left**: The evolution of star formation main sequence with redshift. The average SFR of star-forming galaxies as a function of redshift and stellar mass are parameterized as in Eq. 1.1, see also Schreiber et al. (2015). **Right**: Double Gaussian decomposition of the distribution of starburstiness ($R_{SB} = SFR/SFR_{MS}$). Figures from Schreiber et al. (2015).

The property of a galaxy is reflected on its position relative to the main sequence. For example, galaxies along the main sequence form stars at roughly constant efficiency (SFE $\equiv$ SFR/$M_{\rm gas}$) (Daddi et al., 2010a; Tacconi et al., 2013; Genzel et al., 2015), which means that SFE is not controlled by the stellar mass of a galaxy. However, SFE increases as galaxies move above the main sequence, and stars form more efficiently in galaxies at higher redshifts (see Tacconi et al., 2018, and references therein). Dust properties show similar behaviours. The dust temperature, $T_{\rm dust}$, of galaxies, is also roughly constant along the main sequence (Magdis et al., 2012; Béthermin et al., 2015; Schreiber et al., 2016), but it gets higher at higher redshifts (Magdis et al., 2012; Magnelli et al., 2014; Béthermin et al., 2015; Schreiber et al., 2018a) and at higher $R_{\rm SB}$ (Elbaz et al., 2011; Magdis et al., 2012; Magnelli et al., 2014; Béthermin et al., 2015; Schreiber et al., 2018a). In the aspect of morphologies, starbursts are likely to be more compact, as indicated by the emission from the polycyclic aromatic hydrocarbon (PAH) molecules in galaxies. PAH emits in photo-dissociation regions (PDRs), which is always on the surface of molecular clouds while the FIR luminosity depends on the volume of molecular clouds. Hence, the PAH deficit found in starbursts (Díaz-Santos et al., 2013) indicates a shrink in the surface of molecular clouds, where star formation takes place in galaxies. The IR8 $\equiv L_{\rm IR}/L_8$[7] proposed by Elbaz et al. (2011) quantify the compactness of the starburst galaxies. The high SFE and compact geometry are also a natural result of galaxy mergers where the ISM are dramatically compressed, leading to enhanced SFE and morphologies are largely disturbed, resulting in a compact core at the interfaces. This again supports the association of starbursts and mergers. Although minor, starbursts may play an important role in the transition from star-forming galaxies to quiescent galaxies.

In my thesis, I adopt the parameterized main sequence as quantified in Eq (9) in Schreiber et al. (2015):

$$\log_{10}(\mathrm{SFR_{MS}}[M_\odot/yr]) \;=\; m \;-\; m_0 \;+\; a_0 r \;-\; a_1[\max(0, m \;-\; m_1 \;-\; a_2 r]^2 \tag{1.1}$$

where $r \equiv \log_{10}(1+z)$, $m \equiv \log_{10}(M_* \,/\, 10^9\, M_\odot)$, $m_0 = 0.5 \pm 0.07$, $a_0 = 1.5 \pm 0.15$, $a_1 = 0.3 \pm 0.08$, $m_1 = 0.36 \pm 0.3$ and $a_2 = 2.5 \pm 0.6$.

1.2.3 Cosmic star formation history

As the lifetime of a human being is way shorter than the one of a galaxy, it is not possible to see how individual galaxies evolve directly with our own eyes. However, if we switch to a broader point of view, we can see the collective evolution of galaxies by looking deeper into the Universe, which is, observing the galaxies that are more distant. This is feasible because the speed of light is finite. When we look at galaxies from far away, we receive photons that were emitted from galaxies long time ago. Moreover, the universe is homogeneous and isotropic in space and time. It does not matter which direction we are looking from, or at which place we are observing. As long as we know the distance of the galaxies, we can identify we are observing galaxies from how long ago, this is the so-called lookback-time approach.

Owing to the large surveys with space telescopes like *Hubble* (HST), *Spitzer*, *etc.* and ground-based telescopes like the Visible and Infrared Survey Telescope for Astronomy (VISTA), the United Kingdom Infra-Red Telescope (UKIRT), *etc.*, as well as the follow-up observations with 8-m-class telescopes like

[7] L_8 is the luminosity at 8 μm dominated by the emission from PAH molecules.

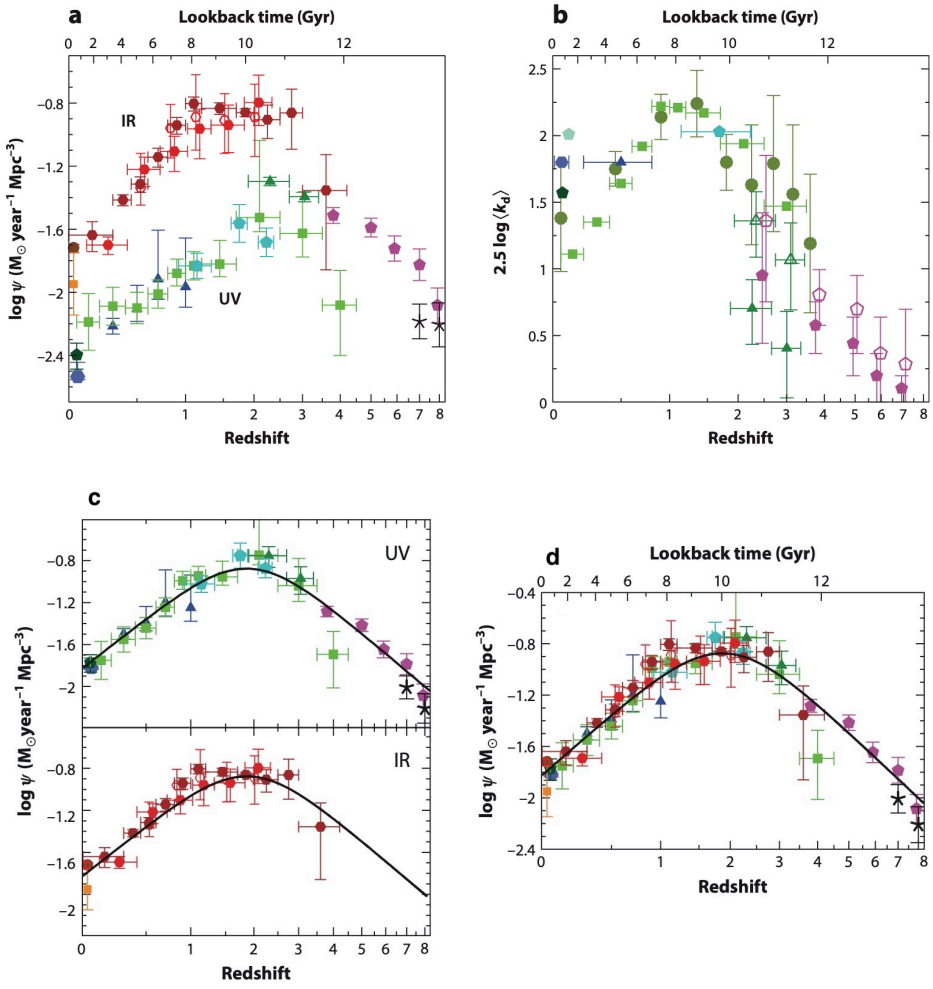

Fig. 1.5: Cosmic star formation rate density (SFRD). **a**: Cosmic SFRD before dust attenuation correction. **b**: Mean dust extinction in magnitude as a function of redshift. **c**: Cosmic SFRD derived from the UV data after dust attenuation correction and from IR, respectively. **d**: Cosmic SFRD derived from the combination of the UV data after dust attenuation correction and IR data. Figures from Madau and Dickinson (2014).

Very Large Telescope (VLT), Keck, Gemini, *etc.* to confirm the spectroscopic redshifts, galaxies with redshifts as large as $z = 11.1$, only around 400 Myr after the Big Bang (Oesch et al., 2016), have been identified. On the other hand, multi-wavelength observations from UV with, e.g., the *Galaxy Evolutionary Explorer* (GALEX) to FIR with, e.g., *Herschel* Space Observatory enable techniques like SED fitting to derive the properties of galaxies systematically. With abundant data in hand, astrophysicists are able to construct a picture of cosmic star formation history (Fig.1.5, see review by Madau and Dickinson, 2014).

In Fig.1.5-ab, it is clear that a large fraction of the emission from star formation is obscured by dust and re-emitted in the IR. The emission at UV only accounts for 10% to 40% of the total star formation rate density (SFRD). The overall dust extinction of galaxies varies with time, with the maximum occurring at around $z = 1$. Combining the observations at UV and IR, SFR can be calculated with high precision with dust attenuation taken into account properly. As shown by Madau and Dickinson (2014, Fig.1.5-d), the star formation rate density peaked at $z \sim 2$, around 3.5 Gyr after the Big Bang, the so-called cosmic noon, then dropped exponentially after $z < 1$. Cosmic star formation at $z \sim 2$ is nine times more intensive than it is today. From the profile of the cosmic SFRD, we can calculate that the majority of the stellar mass today was formed at cosmic noon, *i.e.,* $1 < z < 3$. However, we need to keep in mind that the cosmic SFRD by Madau and Dickinson (2014) at $z > 3$ is poorly constrained because IR data are missing and UV data are limited to the most luminous galaxies (e.g., LBGs) that are not representative (Fig.1.5-c).

1.2.4 Observing star-forming galaxies in the (sub)millimeter

1.2.4.1 Observational obstacles in the FIR

As mentioned previously, the FIR emission is important to fully understand the star formation activities of galaxies. However, there are two main obstacles to measure the FIR luminosity. One is the poor atmospheric transmission in the FIR. That's why the telescopes observing in the FIR are mostly space telescopes, *i.e., IRAS, ISO, Spitzer, Herschel*. And the other is that the angular resolution is worse in the FIR than at shorter wavelength as is defined by the diffraction limit of telescopes: $\theta = 1.22 \frac{\lambda}{D}$, where λ is the observing wavelength, D is the diameter of the telescope or the baseline of the interferometer. These two obstacles are resolved when we look further. The electromagnetic emission from distant galaxies is shifted to longer wavelengths, then the FIR emission is redshifted to submillimeter wavelength, hence observable on the ground by, for example, Submillimeter Common User Bolometric Array (SCUBA). Furthermore, interferometry technique has tremendously improved the angular resolution with the long baselines, which is the case for submillimeter Array (SMA), NOrthern Extended Millimeter Array (NOEMA) and Atacama Large Millimeter/submillimeter Array (ALMA), *etc.*.

1.2.4.2 K-correction

A K-correction is applied to convert the observed-frame flux to the rest-frame flux. It depends on the shape of SEDs. For star-forming galaxies, as already shown in Fig. 1.1, the dust emission approximates

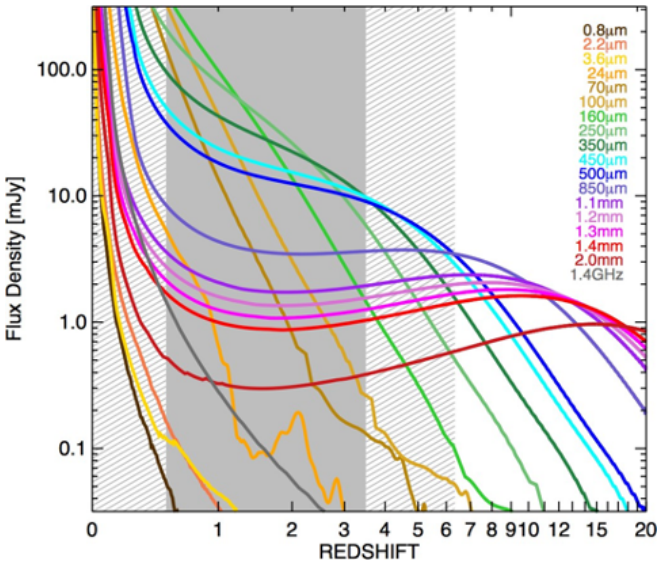

Fig. 1.6: Illustration of K-correction: The observed flux densities for a typical $10^{12.5}$ $L_\odot$ infrared-luminous galaxy as a function of redshift. The curves are color coded with the observed wavelength. Figure from Casey et al. (2014).

a modified blackbody which peaks at $\sim 100\,\mu$m[8]. For one such galaxy with luminosity L, its has a luminosity density $L_\nu \propto \nu^{\beta+2}$ at the Rayleigh-Jeans regime, where β is the dust emissivity, which has a typical value of $\beta = 1.5-2.0$. Simply put, if we observe at a specific observing wavelength λ_o, when the galaxy gets more distant, we are actually observing the emission at a shorter wavelength $\lambda_e = \lambda_o/(1+z)$, which gets brighter if it remains at the Rayleigh-Jeans regime. Then the diminishment from the increased luminosity distance[9] cancels out the elevation from the intrinsic flux density[10]. Therefore the observed flux density remains roughly constant as a galaxy gets farther away, as shown in Fig. 1.6.

1.2.4.3 Galaxies detected at submillimeter

The observations of the extragalactic background light (EBL) has revealed that that the cosmic infrared background (CIB) has the same brightness as the cosmic optical background (COB) (Fig. 1.7), implying that the amount of starlight absorbed and re-radiated by dust is comparable to the one directly from stars (see Cooray, 2016, for a review). The CIB can be resolved into bright sources by the submillimeter telescopes. It has been also found that star formation is more attenuated at high redshift (Hauser et al., 1998). Especially at the cosmic noon, dust reprocessed emission dominates the star formation emission, as much as one magnitude higher than direct starlight (Le Floc'h et al., 2005; Rodighiero et al., 2010; Gruppioni et al., 2013; Magnelli et al., 2013), as is also shown by Fig. 1.5-a. Therefore, the understanding of dust-obscured star formation at cosmic noon relies on the observation at submillimeter wavelength.

[8] This peak wavelength tends to shift a bit to shorter wavelength at higher redshift because of the higher $T_{\rm dust}$ as mentioned in Section 1.2.2.

[9] The luminosity distance D_L can be approximated as $D_L \propto (1+z)^2$ at $0.5 < z < 3$, and $D_L \propto (1+z)^{1.5}$ at $z > 3$. Given that dust emissivity has a typical value of $\beta = 1.5-2$, the observed flux density barely changes with redshift.

[10] The observed flux density $S_\nu = L_\nu/4\pi D^2 \propto (1+z)^{\beta+2}/(1+z)^4 \propto (1+z)^{\beta-2}$ at $0.5 < z < 3$ or $\propto (1+z)^{\beta-1.5}$ at $z > 3$.

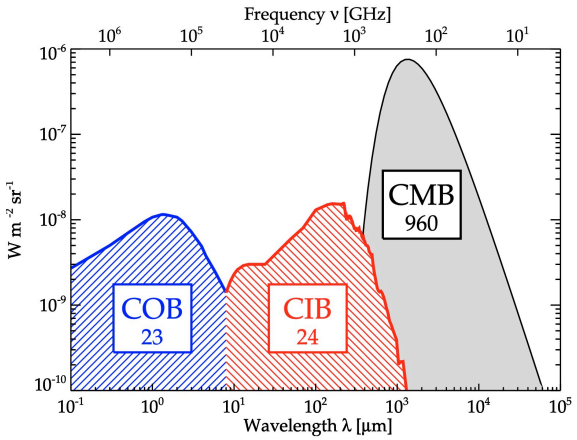

Fig. 1.7: Illustration of the SED the Cosmic Microwave Background (CMB), the Cosmic Infrared Background (CIB) and the Cosmic Optical Background (COB). Their approximate brightness in $\mathrm{nW\,m^{-2}\,sr^{-1}}$ is marked in the boxes. Figure from Dole et al. (2006).

Since their discovery, submillimeter-selected galaxies (SMGs, $S_{850\mu m} > 5$ mJy, see Blain et al., 2002, for a review) detected by single-dish submillimeter telescopes have unveiled a population of massive galaxies undergoing extremely intensive star formation accompanied with a huge amount of dust. This means that SMGs could accumulate a huge amount of stellar mass rapidly. Hence, they have been expected to be ideal progenitors of massive, passive and compact galaxies found at $z = 1 \sim 2$ and ultimately local elliptical galaxies (Cimatti et al., 2008; Whitaker et al., 2012; Toft et al., 2014; Simpson et al., 2014; Valentino et al., 2020b). Because of their high masses, SMGs have deep gravitational potential wells to sustain a huge amount of dust against outflows, and the heavy dust obscuration makes them extremely faint in the rest-frame UV-optical wavelength. That's why there were not discovered until the advent of submillimeter telescopes and that's why submillimeter telescopes are the most power tool to search for such massive objects in the early Universe. However, due to the poor angular resolution of single dishes, as mentioned previously, one detection at the resolution of more than 15″ may turn out to be multiple sources blended in the same beam. The ALMA interferometer array has brought unprecedented improvement to the sensitivity and spatial resolution of submillimeter observations and enables precise counterpart identifications of the SMGs and further study on their properties.

The definition of SMGs is based on the submillimeter flux, hence it is not physical. As a result, SMGs are not a homogeneous population. They show a wide variety of properties indicated by their multi-wavelength observations (see reviews by Casey et al., 2014; Hodge and da Cunha, 2020). Especially, when looking at the relation between their stellar masses and SFRs, some SMGs are on the main sequence, and some fall in the starburst regime, (Fig. 1.8-Left, e.g., da Cunha et al., 2015; Danielson et al., 2017; Lang et al., 2019; Franco et al., 2020a). In general, most SMGs show more compact dust distribution compared to their stellar component (Fig. 1.8-Right, e.g., Elbaz et al., 2018; Hodge et al., 2019; Puglisi et al., 2019; Lang et al., 2019), which supports the evolution path where SMGs are progenitors of the compact quiescent galaxies at $z = 1-2$, while some studies found extended (Rujopakarn et al., 2016; Cibinel et al., 2017). A statistic way to investigate the evolution of SMGs is to study their number counts (Blain et al., 2002; Stach et al., 2018; González-López et al., 2020; Popping et al., 2020). The significant normalization of the number counts challenges the current theoretical

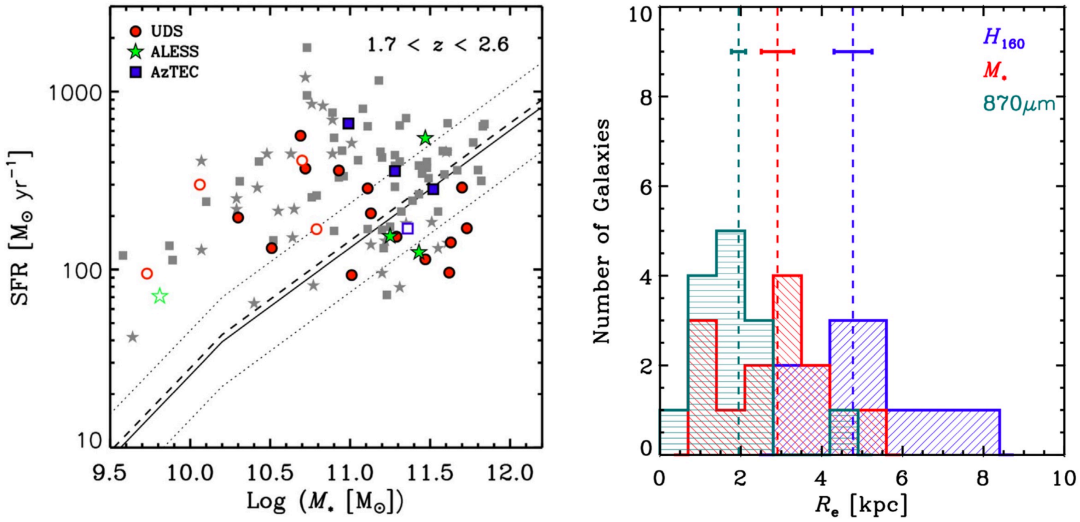

Fig. 1.8: **Left:** SFR as a function of stellar mass of the SMGs at $1.7 < z < 2.6$ studied by Lang et al. (2019). The solid and dotted lines indicate the main sequence and the 0.3 dex scatter from Whitaker et al. (2014). **Right:** Histograms of the effective radii for the ALMA 870μm continuum emission, stellar mass profiles, and *H*-band emission from the same work. Figures from Lang et al. (2019).

models to explain how these large number of massive galaxies formed in the early Universe (see Casey et al., 2014, for a review).

1.2.4.4 The GOODS-ALMA survey

The SMGs studied by ALMA have been the follow-ups of previously detected sources by single dish submillimeter telescopes and color- and mass-selected galaxies from deep surveys at optical/near-infrared wavelength. This will lead to a bias towards some specific population. In addition, the enormous dust content indicated by the bright submillimeter emission hinders some SMGs, perhaps the most massive ones, from emitting in the optical/NIR, hence missed from pre-selections. A homogeneous blind survey is needed to obtain a more general population.

The GOODS-ALMA survey (PI: D.Elbaz Franco et al., 2018; Franco et al., 2020b), covers the largest contiguous area of 69 arcmin^2 in the GOODS-South field by ALMA at 1.1 mm. The original image has a 0.24″ beam and mean depth of 110 μJy beam^{-1}. It was then tapered to 0.60″ to reduce the number of independent beams, hence the number of statistical spurious detections. The *rms* sensitivity is then 182 μJy beam^{-1}. A total of 35 galaxies have been detected above 3.5σ in GOODS-ALMA (Franco et al., 2020b). These include 19 galaxies detected above the 4.8σ limit from a blind detection approach (Franco et al., 2018) and 16 galaxies within 3.5 and 4.8σ detected using ancillary information, mainly *Spitzer*-IRAC prior positions (Franco et al., 2020b). The median redshift and stellar mass of the S/N $\geq$ 4.8 sources are $z = 2.73$ and $M_\star = 1.0 \times 10^{11}$ M$_\odot$, whereas the sources with a 4.8 > S/N $\geq$ 3.5, are both slightly closer ($z = 2.40$) and less massive ($M_\star = 7.2 \times 10^{10}$ M$_\odot$).

Compared with other blind surveys of dust continuum (Walter et al., 2016; Dunlop et al., 2017; Hatsukade et al., 2018; Decarli et al., 2019), GOODS-ALMA is the most efficient to probe distant galaxies, not only because it covers the largest area, but also because of the strategy to observe a

shallower but wider field within a limited amount of time. This is also confirmed by the flattening at ~ 0.1 mJy in the observed 1.1 mm number counts (Muñoz Arancibia et al., 2018; González-López et al., 2020; Popping et al., 2020). The significant decrease of galaxies fainter than 0.1 mJy suggests that deep pencil-beam surveys would be less efficient in searching for the sources contributing to the cosmic infrared background. Despite being counter-intuitive, this can be understood by the fact that submillimeter detected galaxies tend to be the most massive ones, which are rare and bright.

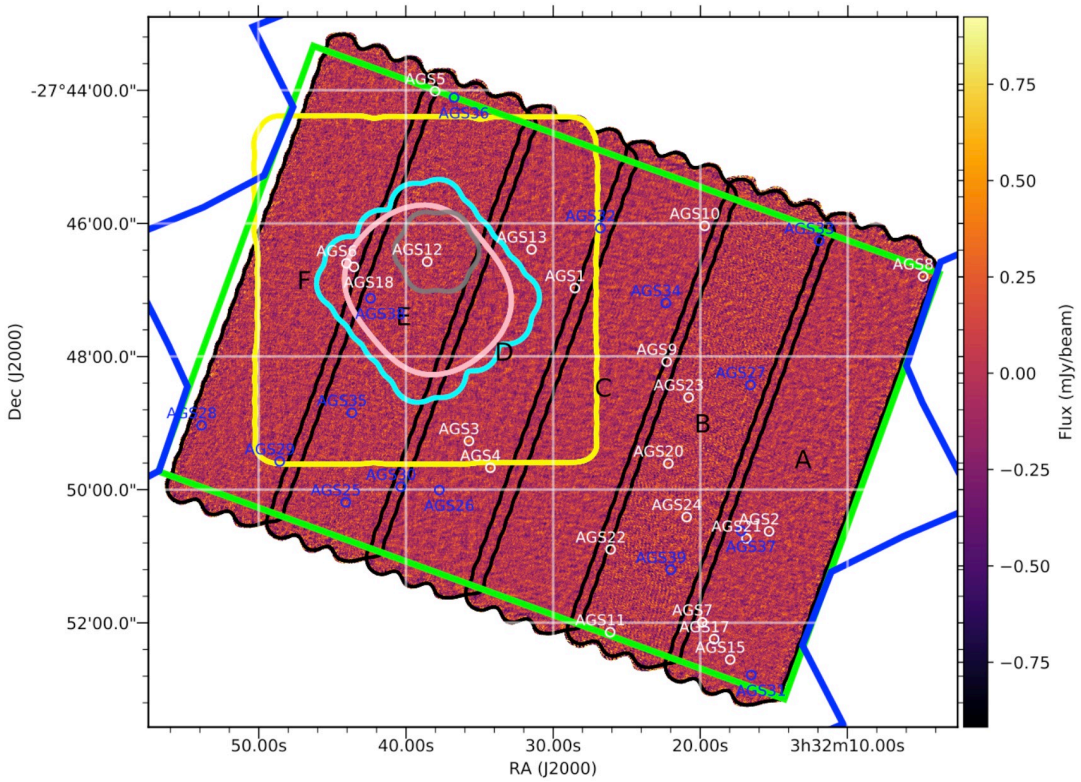

Fig. 1.9: GOODS-ALMA 1.1mm image tapered at 0″60, reaching an rms of 0.18 mJy beam^{-1} (Franco et al., 2020b). The white and blue circles with a diameter of 4″ indicate the blind detections with S/N above the 4.8σ and detections with priors at $3.5 \sim 4.8\sigma$, respectively. Black contours show the different slices (labeled A to F) used to construct the homogeneous 1.1 mm coverage. Blue lines indicate the HST/ACS field and the green lines indicate the HST-WFC3 deep field. The cyan contours represent the limit of the Dunlop et al. (2017) survey covering all of the Hubble Ultra Deep Field region, the yellow contours show the ASAGAO survey (Hatsukade et al., 2018), the gray contours show the ASPECS Pilot survey (Walter et al., 2016), the pink contours show the ASPECS Large Program (Decarli et al., 2019).

1.2.5 Optically-dark galaxies

As mentioned in Section 1.2.3, in pre-ALMA era, our understanding of the cosmic star formation history at $z > 3$ was limited to the rest-frame UV observed galaxies which are now known to under-represent the most massive and star-forming galaxies. For example, it was over a decade after the discovery of the brightest submillimeter source in the Hubble Deep Field (Hughes et al., 1998, HDF850.1, detected using SCUBA) that Walter et al. (2012b) finally identified with the molecular emission lines from ALMA observations that it is a starburst galaxy at $z = 5.183$, and invisible in shorter wavelength. In order to better constrain the cosmic star formation in the first two billion years ($z > 3$) with a statistically large

sample of optically-dark galaxies, Wang et al. (2019) pre-selected 63 optically-dark galaxies based on their NIR-MIR colors (see also in Section 1.2.1) and followed them up with ALMA. They found that these galaxies contribute ten times more to the cosmic SFRD at $z > 3$ compared with equivalently massive UV- bright galaxies (Fig. 1.10-Left). Different from the classic SMGs, these galaxies show an average SFR of 200 $M_\odot$ yr^{-1}, typical of main sequence galaxies at these redshifts although with a large scatter.

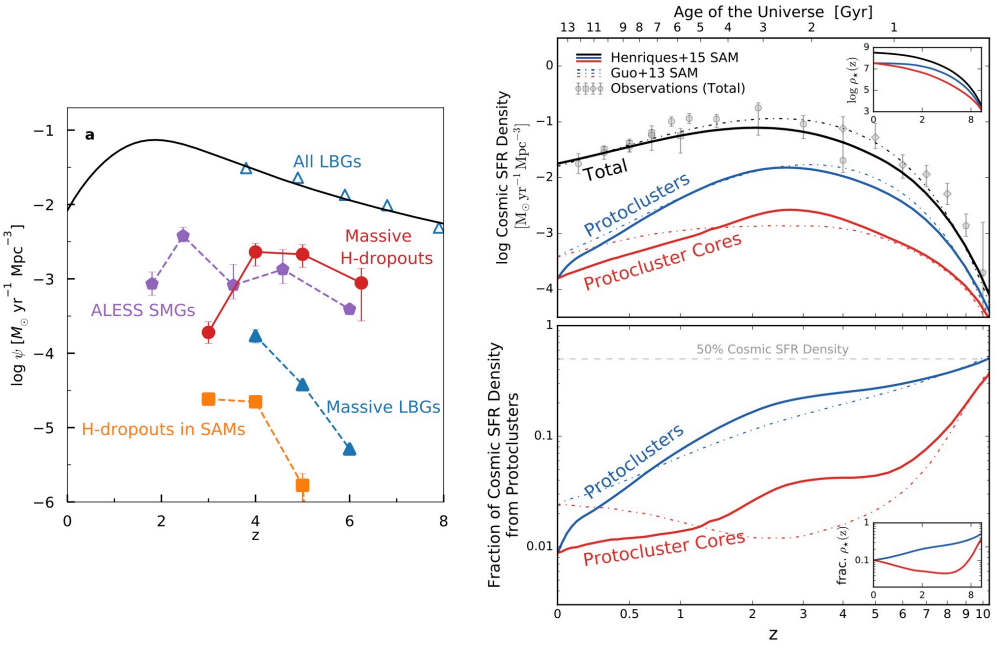

Fig. 1.10: **Left:** Contribution of optically dark galaxies to the cosmic SFRD. Figure from Wang et al. (2019). **Right:** Upper panel: SFR density for all galaxies (black), protoclusters (blue), and cores (red). Lower panel: Fractional contributions to the total cosmic SFRD. Figure from Chiang et al. (2017).

On the other hand, Wang et al. (2019) derived the clustering properties of these optically-dark galaxies from their cross-correlation with optically-detected galaxies with similar redshifts and masses. They found that these galaxies constitute excellent candidate progenitors of the most massive galaxies presently located in the center of massive groups and galaxy clusters. Comparing the contribution of these galaxies to the cosmic SFRD (Fig. 1.10-Left) with the one of the galaxies from protocluster cores predicted by simulations (Chiang et al., 2017) (Fig. 1.10-Right), both populations show a similar contribution of $\sim 10^{-3}$ at $3 < z < 6$, enhancing their association with large scale structures. This has been also indicated by the multiplicity of submillimeter galaxies. The observed high number density of submillimeter galaxies relative to that derived from blank-field counts suggests that at least 30% of the multiplicity are physically associated galaxies rather than due to pure projection effect (Simpson et al., 2015; Stach et al., 2018).

As the largest blind survey with ALMA, the GOODS-ALMA survey also overlaps the region with the deepest HST-WFC3 *H*-band imaging, down to a 5σ depth of $H = 28.2$ AB (Guo et al., 2013). Out of the 35 GOODS-ALMA detections, an ensemble of six galaxies are optically-dark since they are not detected in the optical to near-infrared HST images including the deep *H*-band image. In Chapter 3, I will show my work on the detailed study of these galaxies, especially a large-scale structure they are tracing.

1.3 Star formation fueled by gas

As the key ingredient of star formation, the gas component is vital to our understanding of galaxy evolution. The physical processes involving gas span a vast range of physical scales: from the accretion of intergalactic gas ($\sim$ Mpc), to the settling down and the cooling in galaxies ($\sim$ kpc), to the collapse into molecular clouds ($\sim$ 10-100 pc), then to the fragmentation into denser cores ($\sim$ 0.1-1 pc), finally to the formation of stars (see review by Kennicutt and Evans, 2012).

In extragalactic astrophysics, we are limited by observations to the processes down to sub-kpc scale, which leads to mostly statistical studies on the gas fraction, star formation efficiency/gas depletion time, etc.

1.3.1 Gas tracers

Atomic gas, HI, is traced by the hyperfine transition of hydrogen, at 21 cm (rest-frame). Molecular gas, H_2, is more complex because the H_2 molecule is symmetric and has no dipolar transition. The quadrupolar transitions can only be excited in gas with T $\gtrsim$ 100 K, which is not possible for gas in the cold molecular clouds where star formation takes place. The second most abundant molecule, CO, can be easily excited in cold molecular clouds. It is then used to trace the bulk distribution of molecular gas using a conversion factor from CO luminosity to H_2 mass, $M_{\rm mol} = \alpha_{\rm CO}\, L'_{\rm CO}$, or from CO line intensity to H_2 column density, $N_{\rm H_2} = X_{\rm CO}\, W({\rm CO})$ (Bolatto et al., 2013). On the other hand, dust is also a good tracer of molecular gas (e.g., Magdis et al., 2012; Magnelli et al., 2013; Genzel et al., 2015). The gas mass (H_2 and HI) can be derived by fitting the far-IR to submillimeter SEDs (e.g. Draine et al., 2007) with dust models and adopting a dust-to-gas mass ratio (e.g. Leroy et al., 2011). Scoville et al. (2014), Scoville et al. (2016), and Scoville et al. (2017) recently proposed to convert a single photometric measurement in the Rayleigh-Jeans tail ($\lambda > 100\,\mu$m) to gas mass with a conversion factor $\alpha_{850\mu{\rm m}}$ assuming the dominant dust temperature is 25 K and dust emission is optically thin. Moreover, molecules like HCN, HCO^+, CS are tracers of denser molecular gas in the cores of star-forming clouds.

Molecular gas is extremely challenging to detect in metal poor galaxies even if some of them do show ongoing star formation. Their low metallicity indicates low dust content, which allows far-UV photons to penetrate deeper in the molecular clouds, as illustrated in Figure 1.11. Compared to H_2 molecules which can effectively self-shield from the photodissociating far-UV photons, CO molecules are more fragile and can be easily dissociated into C atoms and C^+ ions. Therefore, there would be a large fraction of the so-called "CO-dark" molecular gas outside the CO-emitting core. [CII] is much brighter than CO in such metal poor galaxies (Cormier et al., 2015), the "CO-dark" H_2 gas could then be traced by [CII] (Madden et al., 2020). However, knowing that [CII] emission originates not only from neutral photodissociation regions (PDRs), but also from ionised gas, the calibration from [CII] to H_2 gas mass requires a precise estimation of the contribution from both origins, which is still unclear (Cormier et al., 2019; Accurso et al., 2017a). I will present my work on the search for molecular gas in one of the most metal poor galaxies, IZw18, in Chapter 4.

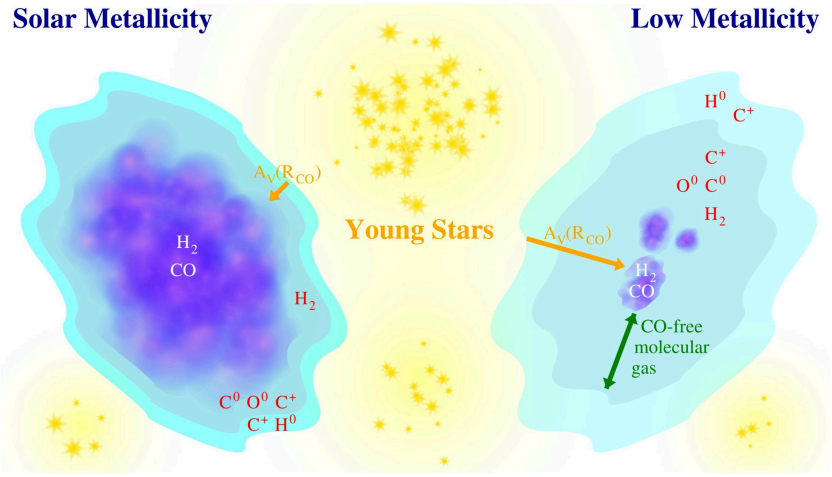

Fig. 1.11: Illustration of "CO dark" gas in molecular clouds. Figure from Madden et al. (2020).

1.3.2 Star formation law

The well-known scaling relation between gas column density and star formation rate surface density, $\Sigma_{\rm SFR} \propto \Sigma_{\rm gas}^N$, was established based on the observation of the Milky Way and nearby galaxies (see e.g., Figure 1.12, Kennicutt, 1998b; Bigiel et al., 2008) and it stands also for more distant galaxies (Daddi et al., 2010b; Tacconi et al., 2013). This relation shows how efficiently galaxies turn their gas into stars and constrains theoretical models.

The disk averaged star formation law has been studied extensively, from local galaxies to high-z galaxies, from normal star-forming galaxies to starbursts (see reviews by Kennicutt, 1998b; Kennicutt and Evans, 2012). A non-linear slope (N in $\Sigma_{\rm SFR} \propto \Sigma_{\rm gas}^N$, where $\Sigma_{\rm gas}$ is the total gas (H_2 and HI) column density) of ~ 1.4 is found in the tight scaling relation, with $\Sigma_{\rm SFR}$ spanning almost five orders of magnitude (Figure 1.12). Different normalizations of the scaling relation are also found in high-z starbursts (Daddi et al., 2010b) and metal-poor galaxies, but these results suffer from the infamous uncertainty of the CO-to-H_2 conversion factor which is related to the metallicity in galaxies and this relation is still unclear (Bolatto et al., 2013). However, Tacconi et al. (2020) found that the normalization is indeed related to the starburstiness ($\delta\,MS \equiv$ SFR/SFR$_{\rm MS}$) of a galaxy, as $\propto\ (\delta\,MS)^{0.44}$, based on their study on the large sample of 14444 star-forming galaxies at $0 < z < 4$. The low gas masses in the galaxies above the main sequence are explained by their dependence on $(\delta\,MS)^{0.44}$, instead the difference in $\alpha_{\rm CO}$.

Bigiel et al. (2008) spatially resolved seven nearby spiral galaxies down to 750 pc[11] and studied the atomic, molecular and total gas – star formation law in Figure 1.12. While there is little correlation between atomic gas and star formation, HI shows a clear saturation effect at $\sim 9\,M_\odot\,pc^{-2}$ (Figure 1.12-a, vertical dashed line). The gas with high surface density tends to be in the molecular phase. This saturation is not seen in molecular gas, and $\Sigma_{\rm H_2}$ shows a good linear relation with $\Sigma_{\rm SFR}$, i.e., $\Sigma_{\rm SFR} \propto \Sigma_{\rm H_2}^N$ with $N \sim 1$ and with $\Sigma_{\rm H_2}$ spanning two orders of magnitude from 1 $M_\odot\,pc^{-2}$ to 100 $M_\odot\,pc^{-2}$ and $\Sigma_{\rm SFR}$ scattering within a factor of ~ 2 (Figure 1.12-b). This indicates a constant star formation

[11] They also found that the results barely change with lower resolutions until 1 kpc.

efficiency (SFE $\equiv$ SFR/M_{H_2}), and equivalently, a constant gas depletion time ($\tau_{dep} \equiv M_{H_2}$/SFR) of $\sim$2 Gyr. This is interpreted as evidence that star formation proceeds in a uniform way in giant molecular clouds in spiral galaxies (Bigiel et al., 2008; Bigiel et al., 2011). They also found that the SFE declines with radius and dwarf galaxies have similar SFEs to the outskirts of spirals as they both have low gas density and are HI dominated.

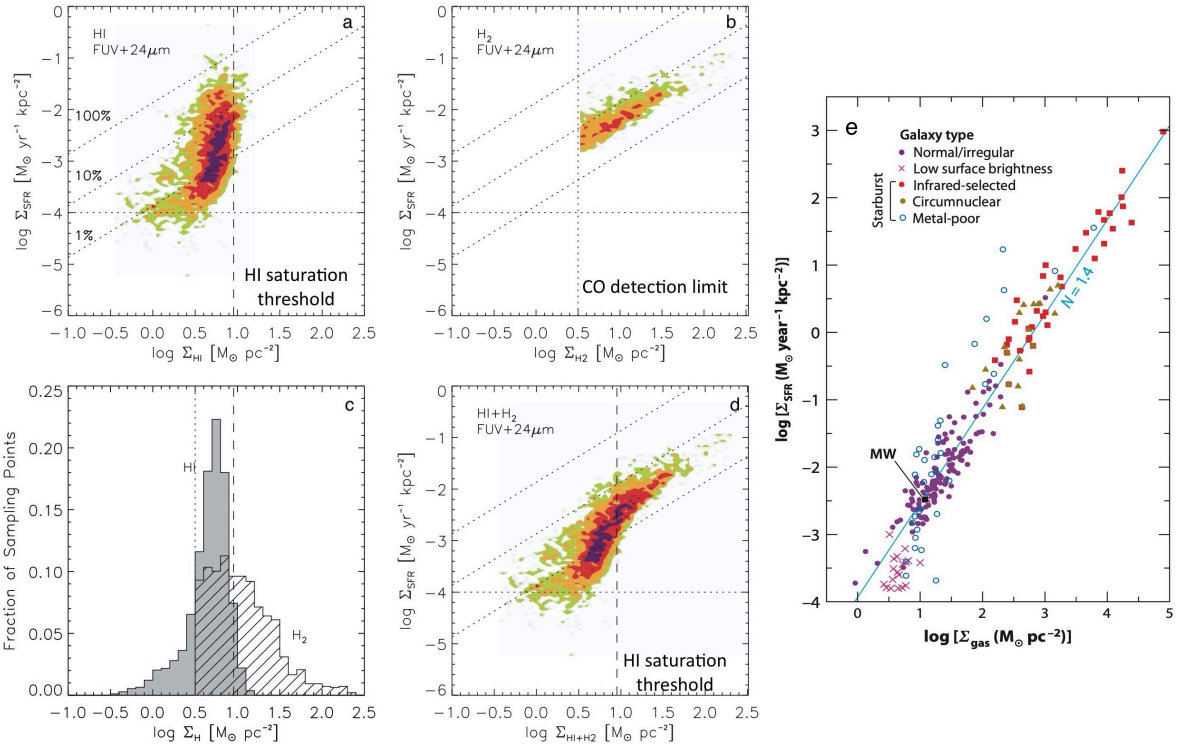

Fig. 1.12: **Left:** Spatially resolved atomic (**a**), molecular (**b**) and total (**d**) gas – star formation law and gas column density distribution (**c**). Figures from Bigiel et al. (2008). **Right:** Disk averaged total gas – star formation law (**d**). Figure from Kennicutt and Evans (2012).

Combining with recent results of the high redshift galaxies, it is found that SFE increases very slightly with redshift and is only weakly dependent on stellar mass, as SFE $\sim (1 + z)^{0.6\sim1}$, about a factor of 2 from $z = 0$ to $z = 2.5$ (Tacconi et al., 2013; Tacconi et al., 2018). Compared with the long timescale to accumulate stellar mass in galaxies (M_{star}/SFR) indicated by the main sequence as mentioned in Section 1.2.2, the short molecular gas depletion timescale implies that external gas replenishment is needed to sustain star formation in galaxies. The cold stream framework proposed by simulations predict cold gas accretion rates proportional to the host halo mass and evolving with redshift (e.g, Dekel et al., 2009), that leads to an agreement with the observed galaxy main sequence behaviour. However, the cold streams, i.e., the cold gas inflows, has been extremely hard to observe. Tentative detections through extended Lyα emission in galaxy clusters have been obtained by Daddi et al. (2020) and Ao et al. (2020). Although it is hard to confirm whether such emission originates from collisionally excited gas infall, the study of such structures can still put valuable constraints on the presence of gas inflows.

1.3.3 Gas content

As mentioned in Chapter 1.2.2, for galaxies at a specific mass, their SFRs increase with redshift (Figure 1.4), i.e., the galaxy main sequence evolves with redshift, as sSFR $\propto (1+z)^3$ until $z \sim 2$, and sSFR $\propto (1+z)^{1.5}$ at $z > 2$ (Lilly et al., 2013), but saturates at $z \sim 4$ (Schreiber et al., 2015). As the fuel of star formation, the cosmic evolution of the gas content, which is related to both the specific SFR and the gas depletion time, $f_{\rm gas} \equiv \frac{\rm M_{gas}}{\rm M_{star}} = {\rm sSFR} \times \tau_{\rm dep}$, is also important for us to test theory and models of star formation in galaxies. The dependence of sSFR and $\tau_{\rm dep}$ on redshift lead to a steep increase of gas fraction until $z \sim 2-3$, from $f_{gas} \sim 10\%$ in the local Universe to the highest value of $f_{gas} \sim 60\%$ at $z \sim 3$ (Figure 1.13). We note that these are the averaged behaviour of galaxies, and individual galaxies can have higher or lower gas fractions. Tacconi et al. (2020) found that gas content not only evolves with redshift, but also is related to the starburstiness and stellar mass, $f_{gas} \propto (1+z)^{2.5} \times (\delta\, MS)^{0.52} \times (M_{\rm star})^{-0.36}$. They suggest that the drop of gas content seen in the high stellar mass end, as is also seen in sSFR, i.e., the fattening at the high mass end in galaxy main sequence, indicates a "mass" quenching process in the most massive galaxies.

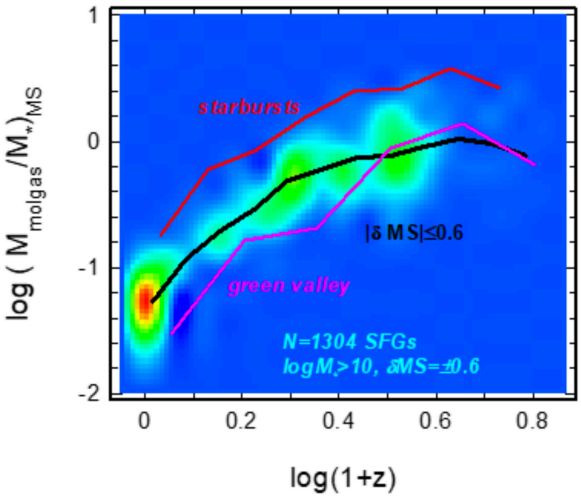

Fig. 1.13: Molecular gas fraction as a function of redshift. Figure from Tacconi et al. (2020).

1.4 Star formation as one of the energy sources of gas

1.4.1 Gas velocity dispersion and the energy sources

Galaxies at different cosmic epochs show quite distinct properties. Compared to their high-redshift counterparts at similar stellar masses, local star-forming galaxies are larger, and have relatively lower gas fractions and lower SFRs (Leroy et al., 2005; Daddi et al., 2010a; Tacconi et al., 2010; Madau and Dickinson, 2014). They are also less likely to experience violent events such as major mergers and gas accretion (Baugh et al., 1996; Genzel et al., 2008; Robotham et al., 2014). Despite of all the various properties, galaxy discs at all epochs tend to be in a state of marginal gravitational stability, which can be characterized by the close to unity Toomre (1964) Q parameter, as $Q = \kappa\sigma/\pi G\Sigma$, where κ is the epicyclic frequency of the galaxy's rotation, σ the velocity dispersion, represents the effect of

pressure, and Σ the mass surface density, represents the effect of gravity. However, many theoretical and observational studies suggest that gas in higher-z galaxies has larger random motions compared to gas in nearby galaxies. Galaxies at $z > 1$ have velocity dispersions in the range of 50–100 km s^{-1} (Nesvadba et al., 2006; Lehnert et al., 2009; Lehnert et al., 2013; Förster Schreiber et al., 2009; Wisnioski et al., 2015) and show an almost linear correlation with the SFR, while local galaxies show typical velocity dispersions of < 50 km s^{-1} (Varidel et al., 2016; Yu et al., 2019). On the other hand, both local and high-z galaxies show velocity dispersions higher than expected from only the thermal contribution of gas. The characteristic temperature of 10^4 K corresponds to a typical velocity dispersion of $\sim$9 km s^{-1} for the ionized gas emitting at Hα (Glazebrook, 2013).

The dominant energy source of the non-thermal turbulent motions is unclear. Numerous drivers have been proposed, including star formation feedback (Mac Low and Klessen, 2004; Krumholz and Matzner, 2009; Murray et al., 2010), radial transport of gas in discs due to gravitation (Krumholz and Burkhart, 2016; Krumholz et al., 2018), gas accretion from the intergalactic medium and minor mergers (Dekel et al., 2009; Glazebrook, 2013), galactic shear from the differential rotation in disc galaxies (Krumholz and Burkhart, 2015; Federrath et al., 2016; Federrath et al., 2017), etc. In Chapter 5, I studied the driver of turbulent motion of eight spatially-resolved nearby star-forming galaxies. The results show that star formation feedback is not the main energy source of the turbulent motions in galaxies with low SFR surface density. However, recent studies by Krumholz et al. (2018) and Varidel et al. (2020) on the global properties of galaxies found that the models taking into consideration of both the star formation feedback and the gravitational energy release from radial transport of gas can yield excellent agreement with the observations of galaxies with SFR ranging from 10^{-4} M$_\odot$ yr^{-1} to 10^3 M$_\odot$ yr^{-1}. The model predicts a transition from gravity-dominantly-driven turbulence in high-z galaxies to star-formation-driven turbulence in low-z galaxies, where SFR is lower. The distinct conclusions come from the different treatments of beam smearing effects, as will be explained below. This model also explains why galaxy bulges tend to form at high redshift and discs at lower redshift, and why galaxies tend to quench inside-out, because the gas accretion rate increases much faster with velocity dispersion, than SFR with velocity dispersion ($\dot{M}_{acc} \propto \sigma_{gas}^3$ vs. SFR $\propto \sigma_{gas}$) and then masses are transported more inward to a bulge in high-z galaxies and remain in the outskirts to form a disk in low-z galaxies (Krumholz et al., 2018).

1.4.2 Integral field unit (IFU), datacube and beam smearing effect

The integral field unit technique has been widely used in optical and near-IR to study galaxy kinematics. It allows us to obtain spatially resolved spectral information in the galaxies. In Chapter 5, I will present my work on the energy sources of the turbulent motions in local star-forming galaxies making use of the IFU survey, the SAMI Galaxy Survey (Croom et al., 2012; Bryant et al., 2015). The three dimensional information from such IFU observations are saved in the so-called datacubes (Figure 1.14). This is similar to the data product obtained from the interferometers at submillimeter to radio wavelengths.

Measurements of velocity dispersions from these datacubes are limited by the spectral and spatial resolution of the instruments. The observed emission line is broadened by the spectral resolution, but this can be addressed by convolving the line spread function into the emission line fitting. The limited spatial resolution blurs the spatial distribution of the intrinsic flux, the line of sight velocity profile, and

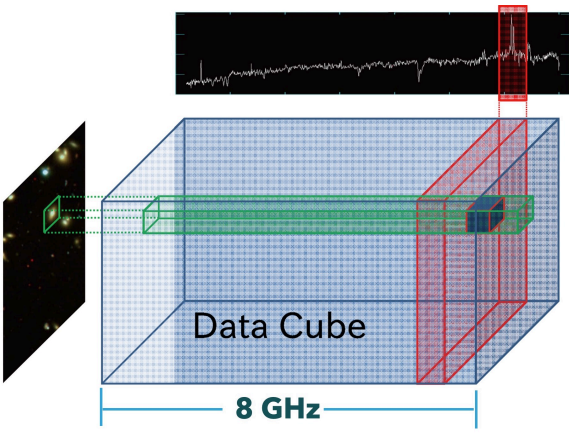

Fig. 1.14: Illustration of a datacube.

the line of sight velocity dispersion within the smallest resolved area. As a result, the observed velocity dispersion is elevated with the unresolved velocity gradient. This is the so-called beam smearing effect. Several tools have been developed to account for beam-smearing effect, e.g., ^{3D}BBAROLO[12] (DiTeodoro and Fraternali, 2015),GBKFIT[13] (Bekiaris et al., 2016), GALPAK^{3D} [14](Bouché et al., 2015), and BLOBBY3D (Varidel et al., 2019). They construct a 3D modelled cube for the galaxy and then spatially convolve the cube per spectral slice to simulate the effect of beam smearing. The convolved cube is finally compared to the observed data.

[12]Codes available at https://editeodoro.github.io/Bbarolo/.
[13]Codes available at https://supercomputing.swin.edu.au/portfolio/gbkfit/.
[14]Codes available at http://galpak3d.univ-lyon1.fr/.

2 Summary of the work done in this thesis

During the five years of my PhD, I have worked on several different projects described below. This thesis was done within a collaboration between Nanjing University, China and CEA-Saclay, France. I am also involved in several international research teams including GOODS-ALMA (PI: D. Elbaz), VANDELS (PIs: L. Pentericci and R. McLure) and SAMI (Team leader: S. Croom). I have published as first-author three papers and I have received the referee report of the forth paper while writing this manuscript. As principle or collaborating investigator, I have four observation projects accepted by ALMA, NOEMA and CFHT. I also presented my work in several international conferences with four talks and four posters. A full list of my publications, proposals and talks can be found in Appendix **??**.

A summary of my work done during this thesis is given as follows:

2.1 GOODS-ALMA

I have been working on the GOODS-ALMA survey (Project ID: 2015.1.00543.S, 2017.1.00543.S) during the last three years. This project aims at opening a new window on the dusty star formation of galaxies in the early Universe, by carrying out a wide (69 arcmin^2) and deep enough (180μJy at 0$''$.6) survey at 1.1 mm to detect dusty galaxies efficiently, as introduced in Section 1.2.4. Based on our analysis on the ALMA Cycle 3 data (2015.1.00543.S), the detections in the GOODS-ALMA survey show **1)** a population of optically dark galaxies that make up 17% of the detections and **2)** a high fraction, 40%, of AGNs (Franco et al., 2018).

Owing to the abundant ancillary data in the GOODS-South field, I made use of multi-wavelength observations to derive the properties of the optically dark galaxies and compiled the existing catalogs (ZFOURGE, CANDELS, CDFS-7Ms) to study the submillimeter emission of different galaxy populations by stacking.

2.1.1 Optically dark galaxies and their association with a proto-cluster in formation at $z \sim 3.5$

This work has been published in *Astronomy & Astrophysics* (Zhou et al., 2020), and is presented in Chapter 3.

I studied thoroughly the properties of the six optically dark galaxies detected in the GOODS-ALMA 1.1 mm continuum survey. None of them is listed in the deepest H-band based CANDELS catalog in the GOODS-*South* field. Five of them suffer from the confusion with bright neighboring galaxies even in the highly resolved optical to near-IR images. To retrieve information at these wavelengths, I performed a de-blending procedure with the method developed by one of the co-authors, C. Schreiber (Schreiber et al., 2018a, code). It turns out that after this deblending analysis two out of the six galaxies end up having H-band counterparts with magnitudes brighter than the detection limit determined by in the CANDELS team on their catalog. They were missed because they were considered as part of the neighboring galaxy because of the confusion limit as a drawback of the source extraction procedure. I fitted the optical-to-MIR SEDs of the optically dark galaxies and their neighbors respectively. The derived redshifts confirm the confusion due to a projection effect, meaning that the optically dark galaxies and their neighbors are at different redshifts.

As co-I, I contributed to a spectroscopic follow-up using ALMA (2018.1.01079.S, PI: M. Franco) to identify the exact redshifts of these optically dark galaxies. I analyzed the data with `CASA` and `GILDAS` and found that one emission line was detected in two of the galaxies.

To study the environment where these galaxies reside in, I constructed the surface number density map of galaxies in the GOODS-*South* field based on the ZFOURGE catalog. We choose ZFOURGE rather than CANDELS because the ZFOURGE catalog is based on detections extracted from the near-IR K_s band images, where galaxies at higher redshift appear brighter than they are in the optical images. We present evidence that nearly 70 % of the optically dark galaxies belong to the same over-density of galaxies at $z \sim 3.5$. We also found that the most massive one of the optically dark galaxies is also the most massive galaxy at $z > 3$ in the GOODS-ALMA field after excluding galaxies hosting a luminous AGN potentially responsible for an overestimation of their stellar mass. This galaxy, AGS24, falls at the very center of the peak of the galaxy surface density. This suggests that the surrounding over-density is a proto-cluster in the process of virialization and this massive galaxy is the candidate progenitor of the future Brightest Cluster Galaxy (BCG).

These optically dark galaxies unveiled by ALMA are good tracers of such large-scale structures in the early Universe and they can serve to test current theories on the formation of the most massive galaxies during the first billin years of the Universe.

2.1.2 Data compilation

The ALMA Cycle 5 data (2017.1.00543.S) fully arrived at the end of my PhD. The Cycle 3 and the Cycle 5 data share almost the same observation settings but the angular resolutions, meaning that they both reach a sensitivity of $\sim 128\,\mu$Jy at their natural resolutions of $\sim 0\farcs2$ and $\sim 1\farcs4$, respectively. Our preliminary analysis has shown that in the low resolution image (Cycle 5), there are apparently more detections than in the high resolution image (Cycle 3). However, most of the new detections are galaxies at lower redshift $z \lesssim 2$. Source extraction on the new data is led by another team member, C. Gomez Guijarro. I took part in merging the two sets of GOODS-ALMA data to push down the sensitivity to $\sim 85\,\mu$Jy at the combined natural resolution of $\sim 0\farcs45$. The preliminary flux measurements in the low resolution data and the merged data also show differences compared with those obtained

in the high resolution data from Cycle 3. We tried to taper this merged image to different resolutions to see the variance of flux of the detections. Further analysis is led by M. Xiao in our team. In addition to the two sets of GOODS-ALMA data, there are also ALMA archive data overlapping this field including deep surveys like ASPECS (PI: F. Walter), ASAGAO (PI: K. Kohno), HUDF (PI: J. Dunlop). I have also contributed to develop the procedure to create a "wedding cake" map combining all these observations.

ALMA being an interferometer, it provides us with 3D-datacubes, where spectroscopic information is also available at all the sky positions of the mosaic image. I have collaborated with the ASPECS team to search for emission lines in the ALMA data when I started to work on GOODS-ALMA. However, the source extraction from spectra always requires much higher sensitivity than that from continuum and indeed the Cycle 3 data alone is far from enough to retrieve meaningful information. With the "wedding cake" 3D map, we can start from the brightest detections in the dust continuum and try again to search for line emission. This is also one of my future plans.

2.1.3 Nascent AGNs in GOODS-ALMA

Despite the high fraction of AGNs, 40%, found in the detections in the GOODS-ALMA field, we notice that half of the AGNs show very high infrared to radio flux ratios, which goes against the existence of AGNs. The contradiction leads to two different paths – a) These AGNs at high redshift are so heavily attenuated that the re-emission by dust makes them more visible by ALMA. b) A larger amount of X-ray binaries are produced during star formation in the galaxies at high redshift and emit significantly in the X-ray domain, so the galaxies are confounded as AGNs.

Studies on the X-ray and infrared properties of star-forming galaxies are limited to galaxies at $z \lesssim 2$ (Mineo et al., 2012; Symeonidis et al., 2014; Rodighiero et al., 2019). The high angular resolution and sensitivity of the GOODS-ALMA data enable us to perform stacking to study more distant galaxies. Taking into account both the ZFOURGE catalog, which is more comprehensive on the high-redshift galaxies, and the CDFS-7Ms catalog, I compared the star-forming galaxies with and without an AGN at $2 < z < 4$. My first attempt with the Cycle 3 data alone did not yield meaningful results. However, with the merged image (Cycle 3 and Cycle 5), I found that AGNs have up to 50% higher flux densities at 1.1 mm than purely star-forming galaxies with similar stellar masses. This indicates that AGNs do not decrease the SFRs hence do not quench these star-forming galaxies, since even at these redshifts the 1.1 mm flux is largely dominated by dust heated by young and massive stars. We note that these are not QSO's, and their FIR SEDs are typical of those of star-forming galaxies. This is comparable to the excess of AGNs among starbursts at $z = 2$ in Rodighiero et al. (2019). I will keep working on that to see the correlation between X-ray and infrared emission in these galaxies.

2.1.4 Contribution as third author

I have contributed to several papers as co-author. In particular, I have contributed as third author in Franco et al. (2020a) and Franco et al. (2020b) on GOODS-ALMA. In Franco et al. (2020a), we created a supplementary catalog using IRAC (mid-IR) and VLA (radio) priors to identify detections from $4.8\,\sigma$

down to 3.5 σ. In Franco et al. (2020b), we studied the properties of the detections. One of the main results is that the submillimeter sizes of the GOODS-ALMA detections are smaller than their H-band sizes which are compatible with the typical $z \sim 2$ elliptical galaxies at similar masses. This indicates that compact bulges are forming in these galaxies.

2.2 Extremely metal-poor galaxies

The low dust content of the local extremely metal poor galaxies is similar to the normal star-forming galaxies found at high-z (z>5, e.g. Walter et al. 2012; Capak et al. 2015), which makes them ideal local analogs to study the first galaxies in the early Universe.

2.2.1 Spatially resolved dust emission

This work has been published in the *Monthly Notices of the Royal Astronomical Society* (Zhou et al., 2016), and is presented in Chapter 6.

I started my PhD with the study of the spatially resolved dust emission of extremely metal-poor galaxies. Our spatially resolved images from *Herschel* reveal higher dust temperatures and lower emissivity indices (β; using the single modified blackbody (MMB) model) compared to that of Spirals. And the two MMB fits with a fixed β=2 show that at 100 μm, about half of the emission comes from warm (50 K) dust, in contrast to the cold ($\sim$20 K) dust component. The far-IR colours are all related to the surface densities of young stars as traced by far-UV, 24 μm and SFRs, but not to the stellar mass surface densities. This suggests that the dust emitting at wavelengths from 70 to 350 μm is primarily heated by radiation from young stars.

2.2.2 Gas content in IZw18

I submitted a letter to *Astronomy & Astrophysics* to report this work. The referee report has been recently returned. This work is presented in Chapter 4.

The predicted CO flux in high-z normal star forming galaxies is in the order of μJy, challenging even with ALMA. Therefore, detailed studies on the metal-poor interstellar medium (ISM) rely on their local analogs. As co-I, I observed the CO J=2-1 emission in one of the most metal poor galaxies, IZw18, with NOEMA (W17BT, W18CA). I performed the data reduction with `GILDAS` and `CASA`. Based on the observation from the upgraded NOEMA Interferometer, we obtain an upper limit on the CO J=2-1 emission for IZw18 of $L'_{\mathrm{CO}(2-1)} < 7.64 \times 10^3$ K km s^{-1} pc^{-2}, ten times lower than previous studies (e.g., Leroy et al. 2007). As one of the most metal poor galaxies, IZw18 shows extremely low CO content despite its vigorous star formation activity. Such low CO content relative to its infrared luminosity, star formation rate and [C II] luminosity, compared to other galaxies, indicates a drastic change in the structure of the ISM at around a few percentages of Solar metallicity. Especially, the high [C II] luminosity relative to CO implies a larger molecular reservoir than the CO emitter in IZw18.

2.3 The SAMI Integral field Units (IFU) Survey

Similar to ALMA, IFU observations also produce 3D datacubes. Then we can associate the physical properties extracted from spectra, with their spatial information to understand the underlying physical processes. I collaborated with F. Bian, T. Yuan, C. Federrath, A. Melding and other members in the SAMI survey team to study spatially resolved nearby star-forming galaxies.

2.3.1 Energy source of turbulence in star-forming galaxies

This work has been published in *Monthly Notices of the Royal Astronomical Society* (Zhou et al., 2017) and is presented in Chapter 5.

I studied the energy sources of the turbulent velocity dispersion in spatially resolved local star-forming galaxies based on the SAMI survey. We found that on sub-kpc scales, our galaxies display a flat distribution of ionized gas velocity dispersions as a function of SFR surface density. A major fraction of our galaxies shows higher velocity dispersions than the predictions by feedback-driven models, especially at the low SFR surface density end. Our results suggest that additional sources beyond star formation feedback contribute to driving random motions of the interstellar medium in star-forming galaxies.

2.4 Observations

At the same time, I proposed as principle and collaborating investigator several observation projects to state-of-the-art telescopes. The results obtained from some of these proposals (ALMA: 2018.1.01079.S; NOEMA: W17BT, W18CA) have already been presented in some of the publications as mentioned above (Zhou et al., 2020, Zhou et al. submitted). In the following, I briefly describe the remaining proposals that I am involved in.

ALMA: Upon the discovery of the optically dark galaxies, we have been trying to propose ALMA observations to obtain spectroscopic redshifts for these galaxies. We have obtained one emission line in two galaxies from our first spectroscopic follow-up of the optically dark galaxies (2018.1.01079.S). Now that we have made a solid case that four (maybe even five) of them fall in the same large-scale structure, we will propose to observe the brightest line, [C II] of these galaxies to derive precise redshifts and study the properties associated with this line, e.g, the SFR-[C II] relation, the possible molecular gas content indicated by this line and the spatial distribution of [C II] emission since the observation would cover the entire overdensity.

VLA: I have attempted to obtain redshifts as well from the CO(1-0) emission in the optically dark galaxies with VLA. However, VLA was not ideal for redshift measurements as it does not cover as wide a frequency range as ALMA. The proposal was finally rejected. Once we have the accurate spectroscopic redshifts, we will come back to request CO(1-0) observations, as this transition traces better the molecular gas content than the higher-J transitions available in the ALMA windows. In

addition, Ginolfi et al. (2017) already showed evidence of a CO gas stream surrounding one of the optically-detected galaxies in this structure. We expect the existence of molecular gas in not only the galaxies, but also across the entire structure.

CFHT: In order to understand the low star formation efficiency in extremely metal poor galaxies, we need information on the molecular gas content in such galaxies. I proposed to observe the hot H_2 emission in Sextans A with WIRCam of CFHT. If detected, we may also study its spatial distribution and the interaction with the star formation activity within the galaxy. This proposal was approved on May 5, 2020 and graded as second quartile.

3 GOODS-ALMA: optically-dark ALMA galaxies shed light on a cluster in formation at $z = 3.5$

Thanks to its outstanding angular resolution, the Atacama Large Millimeter/submillimeter Array (ALMA) has recently unambiguously identified a population of optically dark galaxies with redshifts greater than $z = 3$, which play an important role in the cosmic star formation in massive galaxies.

In this chapter, I study the properties of the six optically dark galaxies detected in the 69 arcmin^2 GOODS-ALMA 1.1mm continuum survey. While none of them are listed in the deepest H-band based CANDELS catalog in the GOODS-*South* field down to $H = 28.16$ AB, we were able to de-blend two of them from their bright neighbor and measure an H-band flux for them. I present the spectroscopic scan follow-up of five of the six sources with ALMA band 4. All are detected in the 2 mm continuum with signal-to-noise ratios higher than eight. One emission line is detected in AGS4 ($\nu_{obs} = 151.44$ GHz with a $S/N = 8.58$) and AGS17 ($\nu_{obs} = 154.78$ GHz with a $S/N = 10.23$), which we interpret in both cases as being due to the CO(6–5) line at $z_{spec}^{\rm AGS4} = 3.556$ and $z_{spec}^{\rm AGS17} = 3.467$, respectively. These redshifts match both the probability distribution of the photometric redshifts derived from the UV to near-infrared spectral energy distributions (SEDs) and the far-infrared SEDs for typical dust temperatures of galaxies at these redshifts. We note that even though our galaxies are extremely faint at H band and are always blended with the neighbouring galaxies in the images at longer wavelengths, we manage to extract the photometries with the de-blending procedure and put constraints on the UV to near-infrared SEDs. We present evidence that nearly 70 % (4/6 of galaxies) of the optically dark galaxies belong to the same overdensity of galaxies at $z \sim 3.5$. The most massive one, AGS24 ($M_\star = 10^{11.32^{+0.02}_{-0.19}}$ M$_\odot$), is the most massive galaxy without an active galactic nucleus (AGN) at $z > 3$ in the GOODS-ALMA field. It falls in the very center of the peak of the galaxy surface density, which suggests that the surrounding overdensity is a proto-cluster in the process of virialization and that AGS24 is the candidate progenitor of the future brightest cluster galaxy (BCG).

3.1 Introduction

The discovery of bright submm-selected galaxies (SMGs; S(850 μm) > 5mJy; e.g., Blain et al., 2002) opened up a window on the formation of the most intense episodes of star-formation in massive distant galaxies. It is now widely accepted that understanding the nature of SMGs is a prerequisite to understand the formation of local massive ellipticals and Brightest Cluster Galaxies (BCGs) at the center of the most massive virialized structures. Defining starbursts as galaxies above the star-formation main sequence (MS, star formation rate vs. stellar mass, SFR - M$_\star$ correlation; Noeske et al. (2007); Elbaz

et al. (2007); Elbaz et al. (2011); Daddi et al. (2007); Rodighiero et al. (2011)), it has been found that some SMGs fall in the starburst category while some are MS galaxies (massive MS galaxies at $z = 3-5$ exhibit very high SFR, Schreiber et al. (2015)), some exhibit compact others extended star-formation (see e.g., **Hodge19**; Elbaz et al. (2018); Rujopakarn et al. (2016); Rujopakarn et al. (2019)).

Using ALMA to follow-up 63 optically-dark galaxies located in the three Southern hemisphere CANDELS fields (totalizing 600 arcmin^2 in the COSMOS, EGS and GOODS-South fields), Wang et al. (2019) showed that these galaxies contribute ten times more than equivalently massive ultraviolet-bright galaxies to the cosmic star-formation rate density at $z > 3$. Despite being bright – although 3 to 10 times fainter than the classical SMG population – in the sub-millimeter (here 870 μm), these galaxies unseen in the deepest UV to near-infrared surveys were selected as H-dropouts with an IRAC counterpart brighter than 24 AB at 4.5 μm. Thanks to the angular resolution of ALMA (0$''$.6 here), it is indisputable that these galaxies exhibit no counterpart from the UV to the H-band. While in the observations from single dish telescopes such as SCUBA,LABOCA, and the IRAM 30 m, LMT, several optical sources can play the role of candidate counterparts due to the large beam size. It took 14 years (Walter et al., 2012b) to identify the galaxy responsible for the brightest Submillimetre Common-User Bolometer Array (SCUBA) source in the HUDF (Hughes et al., 1998, HDF850.1). The H-dropout (or optically-dark) galaxies followed-up by ALMA experience lower, hence more normal, star-formation activity than the more classical SMGs such as those followed-up by ALMA as part of the ALESS project (see e.g. da Cunha et al. (2015), Swinbank et al. (2014)). The ALMA detected ones exhibit <SFR> = 200 $M_\odot$ yr^{-1} typical of MS galaxies at these redshifts although with a large scatter, whereas the undetected ones experience much lower SFR (Wang et al., 2019).

The clustering properties of these H-dropout galaxies – derived from their cross-correlation with H-detected galaxies with similar redshifts and masses – shows that they inhabit massive dark matter haloes ($M_h \sim 10^{13\pm0.3} h^{-1} M_\odot$ at $z = 4$) and constitute excellent candidate progenitors of the most massive galaxies presently located in the center of massive groups and galaxy clusters (Wang et al., 2019). Recent simulations strengthen this hypothesis by showing that galaxies in (proto)clusters at $z > 3$ may produce as much as 50 % of the cosmic SFR density (Chiang et al., 2017). Numerical simulations can be used to trace back the positions of the galaxies that will end up in a present-day galaxy cluster. Chiang et al. (2013) followed-up these galaxies in the stage preceding virialization, which they called the proto-cluster phase. They defined a useful reference effective radius encompassing 65% of the mass that will end up in the cluster, i.e. 65% of the proto-cluster mass as well. At a redshift of $z \sim 3$, that will be of interest in our analysis, this radius ranges from 5 comoving-Mpc (hereafter cMpc) for a $M(z = 0) = 3 \times 10^{14}\, M_\odot$ bound halo to >8 cMpc for a Coma-like $M(z = 0) = 10^{15}\, M_\odot$ halo. This is in line with the enclosed sizes, which contain 90% of the stellar mass in proto-clusters, found in Muldrew et al. (2015). Identifying a proto-cluster from observations is much more complex since it is difficult to determine the future of any given over-density of galaxies. However, when studying galaxy over-densities the effective radius defined from numerical simulations may be used as a reference size for a potential proto-cluster. Based on the standard hierarchical models of galaxy formation, numerical simulations demonstrate that massive galaxies at high redshifts are useful tracers of over-dense regions since they preferentially form within the peaks in the density field (Springel et al., 2005; De Lucia and Blaizot, 2007). At the same time, recent ALMA surveys have revealed that ALMA is a powerful tool in detecting massive galaxies at high redshift (Dunlop et al., 2017; Hatsukade et al., 2018; Franco et al., 2018) taking advantage of its high sensitivity and high spatial-resolution. As a result, not only can such

a population represent a unique probe of star-formation at cosmic epochs when dust attenuation is largely unknown, i.e., at $z > 3$, but it can also be seen as potential beacons to identify clusters at the epoch of their formation. Studying the connection of optically-dark ALMA galaxies with the formation of large-scale structures is the main goal of the present paper.

The study on how galaxy clusters form and evolve across cosmic time is critical to test models of large-scale structure formation. The formation of galaxy clusters is related to the collapse of the gravitationally bound over-densities originating from the peaks in the initial density fluctuations since the Big Bang (Kravtsov and Borgani, 2012). It is also well-known that galaxies evolve differently in different environments at early times: galaxies in denser regions tend to form earlier and evolve faster, as indicated by their ages and enhanced SFR, than galaxies in less dense regions (Thomas et al., 2005; Elbaz et al., 2007; Gobat et al., 2008). Therefore, by exploring the assembly of the most massive dark matter halos we hope to better understand how massive galaxies formed, in the framework of large-scale structure formation.

Various techniques have been developed to search for high-redshift galaxy clusters. However, a complete search for galaxy clusters at high redshift ($\gtrsim$2) becomes more difficult as the cluster properties evolve dramatically at an early age. Some galaxy clusters are mature systems with evidence of quiescent galaxies dominating the center (Papovich et al., 2012; Newman et al., 2014; Willis et al., 2020), while others still show substantial star formation activities in the center (Brodwin et al., 2013; Webb et al., 2015; Wang et al., 2016a). As a result, infrared/submilimeter (infrared/submm) surveys can be beneficial in revealing the over-densities (Daddi et al., 2009; Capak et al., 2011; Miller et al., 2018; Oteo et al., 2018; Gómez-Guijarro et al., 2019; Castignani et al., 2020), and extensive in-depth deep surveys from Atacama Large Millimeter Array (ALMA) can make significant contributions.

In this paper, we present the physical properties of six optically-dark galaxies detected in the GOODS-ALMA field based on the new ALMA data obtained from the spectroscopic follow-up of five of these galaxies. We also discuss the connection between their optically dark nature and the dense environment they reside in.

The GOODS-ALMA survey makes use of the 69 arcmin^2 ALMA image covering the deepest region of the Great Observatories Origins Deep Survey South (GOODS–*South*) field. In this large blind survey, massive (>$10^{10.5}$ $M_\odot$) and dust-rich galaxies at high redshift are efficiently detected due to their low surface number density in the early Universe. For more details of this survey we refer the readers to (Franco et al. (2018), hereafter F18).

We use cosmological parameters of H_0 = 70 km s^{-1} Mpc^{-1}, Ω_M = 0.3, and Ω_Λ = 0.7. A Salpeter (1955) initial mass function (IMF) is adopted to derive stellar masses and SFRs. We convert values obtained by other studies from a Chabrier (2003) IMF to a Salpeter (1955) IMF by multiplying SFR and stellar masses by the same factor 1.74.

3.2 Data and observations

3.2.1 ALMA data and observations

3.2.1.1 GOODS-ALMA survey data

We use data from GOODS-ALMA, a 1.1mm cosmological survey of 69 arcmin^2 ($69\times10'$) in the GOODS–*South* field (program 2015.1.00543.S, PI: D.Elbaz). GOODS-ALMA reaches an rms sensitivity of $\sigma \simeq 0.18$ mJy beam^{-1} in the $0''.60$ tapered mosaic (F18). The comparison between the redshift distribution of the detections in the GOODS-ALMA survey (F18; F20a) and the one in the smaller pencil beam ALMA survey of the *Hubble* Ultra Deep Field (4.5 arcmin^2, Dunlop et al. (2017)) shows that, for the same total observing time of about 20 hours, the shallower but 15 times wider GOODS-ALMA survey enables the detection of systematically more distant galaxies (F18; F20a). This is a natural consequence of the fact that high-redshift dusty galaxies are found to be massive. The combination of the low surface density and brightness of these galaxies then favors shallower and wider surveys.

A total of 35 galaxies have been detected above 3.5σ in GOODS-ALMA (Franco et al. (2020), hereafter F20a). These include 19 galaxies detected above the 4.8σ limit from a blind detection approach (F18) and 16 galaxies within 3.5 and 4.8σ detected using ancillary information, mainly *Spitzer*-IRAC prior positions (F20a). The median redshift and stellar mass of the S/N $\geq$ 4.8 sources are $z = 2.73$ and $M_\star = 1.0 \times 10^{11}$ M$_\odot$, whereas the sources with a 4.8 $>$ S/N $\geq$ 3.5, are both slightly closer ($z = 2.40$) and less massive ($M_\star = 7.2 \times 10^{10}$ M$_\odot$).

3.2.1.2 ALMA follow-up observations of five optically-dark galaxies

Out of the 35 ALMA galaxies presented in Section 3.2.1.1, an ensemble of six galaxies are optically-dark, or also called HST-dark since they are not detected in the optical to near-infrared HST images down to a 5σ *H*-band detection limit (HST-WFC3/F160W) of $H = 28.16$ AB mag (Guo et al., 2013). (12.5 %; F20a), for a global fraction of 17 % of optically dark galaxies. As a result, about 17% of the sources detected above 3.5σ in the GOODS-ALMA blind survey are optically dark (and 21% above 4.8σ). Out of these six sources initially classified as optically dark, we will show in Section 3.4.1 and 3.5.3.2 that two are associated with an H-band counterpart. They were missed from the H-band catalog due to blending.

We have obtained ALMA spectroscopic follow-up data for five of these optically-dark galaxies (AGS4, 11, 15, 17, 24) that we discuss in Section 3.4. The sixth one, AGS25, was identified after the ALMA call hence no follow-up data have been obtained for this one.

We followed-up these five optically-dark sources with ALMA band 4 using the spectroscopic scan mode in Cycle 7 (project 2018.1.01079.S PI: M. Franco). The band 4 observations were performed by combining four tunings to cover a total frequency range of 137.2–165.8 GHz that ensures a broad redshift coverage from $z = 2$ to $z = 5$, with at least one line detected among the possible CO transitions from $J = 4$ to $J = 7$, CI and H_2O. The observations were carried out with the array configuration C43-4, with a synthesized beam of $\sim 0''.88$. Each source was observed for 13 min on-source time in each tuning, reaching a typical rms sensitivity of 0.2 mJy per 400 km s^{-1}. We reduced the raw data using the standard ALMA pipeline with Common Astronomy Software Application package (CASA, McMullin

et al., 2007). Then we converted the data into *uvfits* format and performed analysis with the IRAM GILDAS tool (Gildas Team, 2013) using the same method as in Jin et al. (2019).

3.2.2 Ancillary data

GOODS-ALMA benefits from abundant ancillary data. We summarize in the following Sections the data that we use in the present study. For more details we refer the reader to Franco et al. (2018, Section 2.4.).

3.2.2.1 Optical/near-infrared data

We use the data from the Cosmic Assembly Near-IR Deep Extragalactic Legacy Survey (CANDELS; Grogin et al. (2011)) obtained using images from the Wide Field Camera 3 (WFC3) and the Advanced Camera for Surveys (ACS) on-board the *Hubble Space Telescope* (HST) in the filters: Y_{125}, J_{125}, B_{435}, V_{606}, i_{775}, i_{814} and z_{850}.

We also use images from the VLT, obtained in the U-band with VIMOS (Nonino et al., 2009), and in the K_s-band with ISAAC (Retzlaff et al., 2010) and HAWK-I (Fontana et al., 2014) and the associated CANDELS multiwavelength catalog (Guo et al., 2013). In the near-infrared, we also use images and data from the FourStar galaxy evolution survey (ZFOURGE, PI: I. Labbé; Straatman et al. (2016)). These include narrow-band filter images in the J (J_1, J_2, J_3) and H (H_s, H_l) bands useful for the photometric redshift determination. The ZFOURGE team produced the deepest K_s-band detection image by combining images from the survey itself together with images from previous surveys and reaching a 5σ limiting depth of 26.2 $\sim$ 26.5 AB mag in the whole Chandra Deep Field South (Giacconi et al., 2002, CDFS).

3.2.2.2 Mid-infrared data

We use *Spitzer* Infrared Array Camera (IRAC) images at 3.6 and 4.5 μm, reaching a depth of 26.5 AB mag, from the ultradeep mosaics of the IRAC Ultra Deep Field (Labbé et al., 2015, IUDF). These were obtained by combining the observations from the IUDF (PI: Labbé) and IRAC Legacy over GOODS (IGOODS, PI: Oesch) programs, together with archival data from GOODS (PI: Dickinson), S-CANDELS (PI: Fazio), ERS (PI: Fazio), and UDF2 (PI: Bouwens).

3.2.2.3 Radio data

We use radio images at 3 GHz and 6 GHz from the Karl G. Jansky Very Large Array (VLA; PI: W. Rujopakarn) which cover the entire GOODS-ALMA field. The 6 GHz map has an angular resolution of $0\farcs31 \times 0\farcs61$. The exposure time is in total 177 hours reaching an rms noise at the pointing center of 0.32 μJy beam^{-1}. The 3 GHz map has an angular resolution of $1\farcs19 \times 0\farcs59$ and an average rms noise of 1.03 μJy beam^{-1}. At 3 GHz, AGS4, 17 and 24 are detected with a S/N of 10.4, 9.9, and 5.6 using `PyBDSF`[1] (Rujopakarn et al. in prep.). We examined the image and noticed that the peak fluxes of

[1] https://www.astron.nl/citt/pybdsf/

AGS11, 15 and 25 are at $3 < S/N < 5$. At 6 GHz, only AGS4 is detected with $S/N > 5$ using PyBDSF[1], AGS17, 24 and 25 show peak fluxes at at $3 < S/N < 5$ in the image. We list the fluxes in Table 3.1 .

3.2.2.4 X-ray data

We use the catalog of Luo et al. (2017) obtained from the 7 Msec X-ray data in the CDFS field observed in three bands: 0.5-7.0 keV, 0.5-2.0 keV, and 2-7 keV. This catalog includes a classification of candidate X-ray active galactic nuclei (AGN) that we discuss in the following of the paper.

3.2.3 Origin of the redshifts and stellar masses

In total, 11621 galaxies located in the GOODS-ALMA field have been attributed either a photometric redshift (92 % of the sample) or a spectroscopic redshift (894 galaxies). We discuss below the origin of these redshifts, including the newly obtained ones from the VANDELS survey that we use to improve the contrast on the $z \sim 3.5$ structure that we will discuss in the following sections.

3.2.3.1 Photometric redshifts and stellar masses

The photometric redshifts used in the present study come from the catalog generated by the ZFOURGE team (Straatman et al., 2016; Forrest et al., 2017). We use the redshift maximizing the likelihood (minimized χ^2), z_{peak}, as derived by fitting the observed SEDs with the code EAzY (Brammer et al., 2008). These photometric redshifts present an excellent agreement with existing spectroscopic redshifts with $\sigma_z = 0.020$ at $z > 1.5$ (Straatman et al., 2016), where σ_z is the normalized median absolute deviation (NMAD) of $\Delta z/(1+z)$, i.e., 1.48 $\times$ the median absolute deviation (MAD) of $|z_{phot} - z_{spec}|/(1+z_{spec})$.

We adopt the stellar masses of the ZFOURGE catalog which were derived with Bruzual and Charlot (2003) stellar population synthesis models (Straatman et al., 2016) assuming exponentially declining star formation histories (SFH) and a Calzetti et al. (2000) dust attenuation law.

3.2.3.2 Spectroscopic redshifts

The spectroscopic redshifts are both from the literature, as compiled in the ZFOURGE catalog, and from the latest data release from the VANDELS survey (DR3[2]). VANDELS targets star-forming galaxies at $5.5 \geq z \geq 2.5$ and massive passive galaxies at $2.5 \geq z \geq 1.0$ in the CANDELS CDFS and UDS fields. It is an ultra-deep spectroscopic survey of high-redshift galaxies with exposure times ranging from 20 to 80 hours per source (Pentericci et al., 2018; McLure et al., 2018). In total, we obtain 132 new spectroscopic redshifts, z_{spec}, in the GOODS-ALMA field from VANDELS and 83 of them fall in the redshift range $4 \geq z \geq 3$.

3.2.4 Derived parameters of the optically dark galaxies

[2]VANDELS DR3: http://archive.eso.org/cms/eso-archive-news/new-data-release-of-spectra-and-catalog-from-vandels.html; http://vandels.inaf.it/db/query_catalogs.jsp.

3.2.4.1 Redshifts

To derive the photometric redshifts, we first de-blend[3] AGS4, 15, and 24 from their neighbors in the observed optical to mid-infrared images (ancillary data in Section 3.2.2), as to be discussed in detail in Section 3.4. The photometric data are then used to measure the redshifts by fitting the optical to mid-infrared (rest-frame UV to near-infrared) SEDs with EAzY (Brammer et al., 2008). The photometric redshift of AGS25 comes from its K_s-band counterpart in the ZFOURGE catalog, $\mathrm{ID}_{\mathrm{ZFOURGE}} = 11353$. AGS11 and 17 are either too faint or too close to a bright emitter in the images to be de-blended properly and derive meaningful redshifts, therefore we do not have photometric redshifts for these two galaxies.

The spectroscopic redshifts of AGS4 and AGS17 are obtained based on the detected emission lines in the ALMA spectroscopic follow-up and their SEDs at UV to near-infrared and far-infrared (rest-frame), which will be discussed in detail in Section 3.3.

3.2.4.2 Stellar masses

The stellar masses of AGS4, 15 and 24 are derived from the observed optical to mid-infrared SED fitted with FAST++[4] assuming a delayed exponentially declining SFH and a Calzetti et al. (2000) attenuation law. The stellar masses of AGS11 and 17 are calculated based only on the IRAC emission. The stellar mass of AGS25 comes from its K_s-band counterpart in the ZFOURGE catalog.

3.2.4.3 Infrared luminosities

Infrared luminosities are measured by the SED fitting of the *Herschel* and ALMA flux densities for AGS4 and AGS17 using CIGALE (Boquien et al., 2019) as in F20b. The other four galaxies are not detected by *Herschel*, then their infrared luminosity was derived by fitting the ALMA 1.1mm point with the SED templates in Schreiber et al. (2018), as described in F20b.

3.2.4.4 SFRs

The star formation rates are measured in Franco et al. (2020a, hereafter,), as $\mathrm{SFR}_{\mathrm{tot}} = \mathrm{SFR}_{\mathrm{IR}} + \mathrm{SFR}_{\mathrm{UV}}$. $\mathrm{SFR}_{\mathrm{IR}}$ is calculated based on the correlation between infrared luminosity and SFR in Kennicutt (1998b) and $\mathrm{SFR}_{\mathrm{UV}}$ contributes only 1% to SFR in the GOODS-ALMA detections (F20b), therefore it is negligible.

All six galaxies are detected in the radio at 3GHz with flux densities ranging from 4 μJy to 40 μJy (Table. 3.1). This allows us to estimate a radio SFR. With such extremely faint flux densities, they are not expected to present a radio excess that could be attributed to an AGN, but we checked this as

[3] By applying the de-blending method described in Schreiber et al. (2018b), also see code developed by Corentin Schreiber: https://github.com/cschreib/qdeblend.

[4] FAST++: https://github.com/cschreib/fastpp, a version of the code FAST Kriek et al. (2009) fully rewritten that can handle much larger parameter grids and offers additional features.

follows. We calculated the luminosity at 1.4GHz (restframe) from the flux at 3GHz assuming a radio spectral index of $\alpha = \alpha_{1.4\mathrm{GHz}}^{3\mathrm{GHz}} = -0.8$, the typical value for galaxies at $z > 2$ (Delhaize et al., 2017):

$$L_{1.4\,\mathrm{GHz}}\,(\mathrm{W\ Hz^{-1}}) = \frac{4\pi D_L^2}{(1+z)^{\alpha+1}} \left(\frac{1.4}{3}\right)^{\alpha} S_{3\mathrm{GHz}}. \tag{3.1}$$

where D_L is the luminosity distance to the object. The results are listed in Table 3.1. Then we compared the ratio $L_{1.4\mathrm{GHz}}$/SFR with the radio excess threshold as in Delvecchio et al. (2017). All the six optically dark galaxies have $L_{1.4\mathrm{GHz}}$/SFR well below threshold, with the one of AGS24 being five time lower and the others at least ten times lower. This is fully consistent with star-forming galaxies at $z \sim 3.5$. A radio AGN contribution cannot be ruled out, but it must be contributing for a very small fraction to the total radio emission. Nevertheless, due to vigorous star formation dominating the total radio emission at low resolution, only Very Long Baseline Interferometry (VLBI) observations could unambiguously shed light on the possible presence of radio AGN activity on circum-nuclear (< 100pc) scales.

We also checked in the CDFS 7Ms catalog (Luo et al., 2017) and found that an X-ray source is located equally close to AGS4 and another galaxy, $\mathrm{ID_{ZFOURGE}} = 12333$. Therefore, it is not clear whether this X-ray source is associated with our optically dark source, AGS4. A detailed study of the AGN contamination to the SFR of AGS4 is presented in F20b where it is found to be negligible.

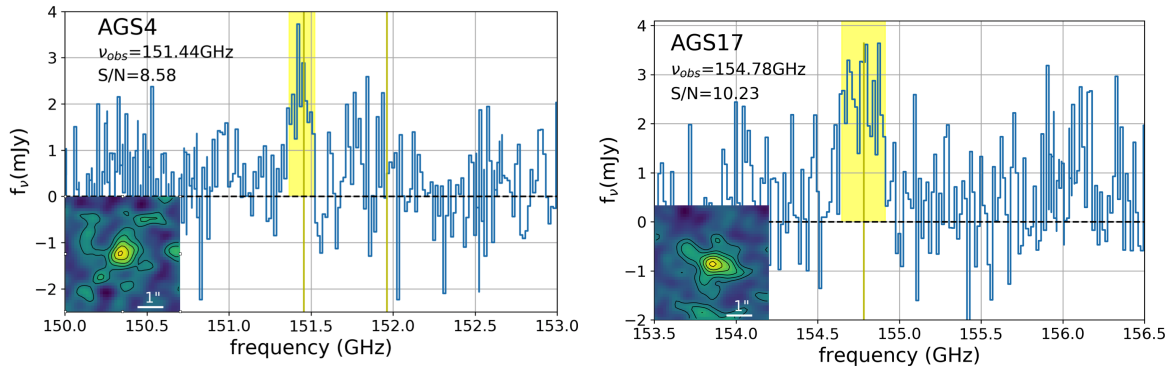

Fig. 3.1: ***Left:*** Part of the spectrum obtained from the ALMA band 4 observation of AGS4. The yellow shade highlights the detected emission line. The emission line map is shown in the bottom-left corner. The contours denote 1 to 5σ, with the step of 1σ. ***Right:*** Same as on the left, but for AGS17. The contours in the map denote 1 to 6σ, with the step of 1σ.

3.3 Results of the ALMA spectroscopic follow-up

In this section, we present the results of the ALMA spectroscopic follow-up. As introduced in Section 3.2.1.2, five of the six optically dark galaxies are followed up, as AGS25 was identified after the ALMA call. One emission line is detected in AGS4 and AGS17, and we constrained the upper limits for AGS11, 15 and 24.

3.3.1 AGS4

The spectrum of AGS4 shows a clear line detection with a $S/N = 8.58$ at $\nu_{obs} = 151.44$ GHz (see Fig. 3.1-*Left*). One ALMA spectral line alone is not sufficient to obtain a definitive spectroscopic redshift for AGS4. However, out of the various possible lines that may be responsible for the one that is detected, only three lines can be reconciled with the 4000 Å break that is seen in the optical to near-infrared SED of AGS4 (Fig. 3.3-*Top-left*, see more discussion on the SED in Section 3.4.1), namely the CO(6-5), CO(7-6) and $H_2O(2_{11}\text{-}2_{02})$ lines.

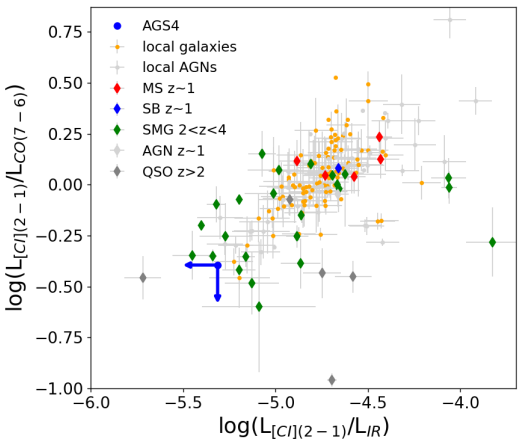

Fig. 3.2: Upper limit of the [CI](2-1)/CO(7-6) flux ratio of AGS4 (blue arrows), compared with existing observations of local and high-redshift MS galaxies, starburst galaxies and AGNs (data compiled in Valentino et al. (2018); Valentino et al. (2020)). If the detected emission line is indeed CO(7-6), then the flux ratio would fall at the lower end of the trend shown by the existing observations.

Another reason to favor these lines comes from the far-infrared SED (Fig.22 in F18). Being one of the brightest GOODS-ALMA sources, AGS4 is detected in five *Herschel* bands (at 100, 160, 250, 350 and 500 μm), which together with the ALMA measurements, allowed F18 to obtain a robust identification of the peak of the far-infrared SED which falls close to 350 μm. Redshifts below $z = 2$ (such as the one obtained for the 4-3 CO transition) would lead to dust temperatures (peak around 120 μm) much colder than typical $z\sim2$ galaxies (see Schreiber et al. (2018)).

We exclude $H_2O(2_{11}\text{-}2_{02})$ since it is typically less bright or as bright (Yang et al., 2016, flux ratio from 0.4 to 1.1) as the neighboring high-J CO transition lines (7–6 or 6–5) and we do not find any evidence for a second line in the ALMA spectrum that can be comparable to the 8.7σ detection.

The CO(7-6) line with a rest-frame frequency of $\nu_{\rm RF} = 806.7$ GHz provides a spectroscopic redshift of $z_{spec}^{AGS4} = 4.326$ which agrees with one of the two peaks of the probability distribution function (PDF) of the optical photometric redshift. We note that the [CI](2-1) ($\nu_{\rm rf} = 809.3$ GHz) line falls very close to the CO(7-6) line and is not detected here with a 3.5σ limit of 0.7 mJy which corresponds to a [CI](2-1)/CO(7-6) ratio of 0.40. This flux ratio falls at the lower end of the trend defined by the MS galaxies, starburst galaxies and AGNs in the local universe and at high-z (data compiled and described in Valentino et al., 2018; Valentino et al., 2020a), as shown in Fig. 3.2. Chance is small to have AGS4 to be an extreme case of the [CI](2-1)/CO(7-6) flux ratio. The CO(6-5) line with a rest-frame frequency

of $\nu_{\rm RF}$ = 806.7 GHz gives a z_{spec}^{AGS4} = 3.566 which agrees with the 4000 Å discontinuity in the optical SED. Therefore, we adopt the redshift to be z_{spec}^{AGS4} = 3.556 assuming the line to be CO(6-5).

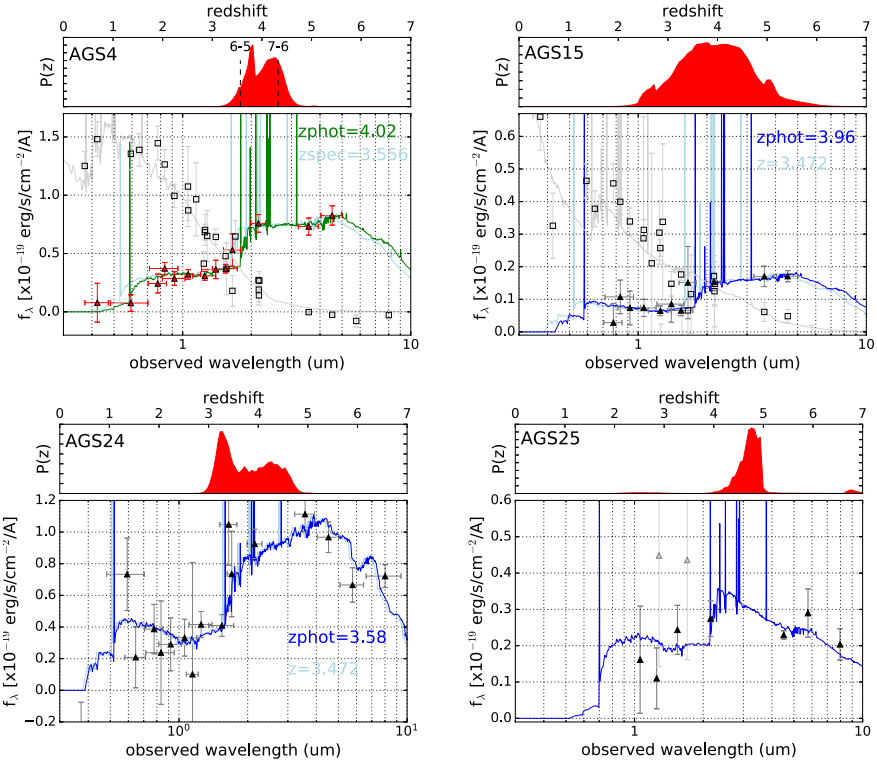

Fig. 3.3: ***Top-left:*** The SED of AGS4. Top: Photometric redshift probability distribution function derived by EAzY (Brammer et al., 2008). Bottom: The SED fittings. The green curve shows the best-fit of AGS4 at z_{phot} = 4.02 using EAzY, and we shift the SED to the spectroscopic redshift (z_{spec} = 3.556) of AGS4 in light blue for comparison. The grey curve shows the SED of the optically-bright neighbor, $\mathrm{ID_{ZFOURGE}}$ = 12333. ***Top-right:*** The SED of AGS15. The blue curve shows the best-fit at z_{phot} = 3.96 derived by EAzY and we shift the SED to the redshift peak of the over-density, at z = 3.472, in light blue for comparison. The grey curve shows the SED of the optically-bright neighbor, $\mathrm{ID_{CANDELS}}$ = 3818. ***Bottom-left:*** The SED of AGS24. Same as AGS15. ***Bottom-right:*** The SED of AGS25 at z_{phot} = 4.70, fitted by EAzY with the photometry retrieved from the ZFOURGE catalog.

3.3.2 AGS17

Our spectroscopic scan follow-up of AGS17 shows an emission line at 154.78 GHz with a S/N = 10.23. The far-infrared SED in this region peaks at around 400 μm (F18, Fig.22). Taking this far-infrared SED into account, the detected line is likely to be CO(5-4) or CO(6-5) or CO(7-6) since the higher-J or lower-J transitions give redshifts leading to unrealistic dust temperatures with dust emission peaking at λ < 67 μm or at λ > 134 μm, restframe. We checked the three $L_{\rm IR}$–$L_{\rm CO}$ relation for the three transitions. We found that the ALMA flux of AGS17 and the corresponding $L_{\rm IR}$ for the three different redshifts, which are z = 2.723, 3.467, 4.212, will bring the galaxy to the positions which are consistent with the $L_{\rm IR} - L_{\rm CO}$ relations of the three transitions (Liu et al., 2015). Therefore, we cannot disentangle these possibilities based on the single line.

However, if we assume the line to correspond to the CO(7-6) transition ($\nu_{\rm rf}$ = 806.7 GHz), a second line, [CI] ($\nu_{\rm rf}$ = 809.3 GHz), is supposed to be detected at similar significance (Valentino et al., 2020a) and it is not the case for AGS17. We are then left with two possibilities: a spectroscopic redshift of $z_{spec}^{\rm AGS17}$ = 2.723 in the case of the CO(5-4) transition and the other of $z_{spec}^{\rm AGS17}$ = 3.467 for the CO(6-5) transition. The second redshift of $z_{spec}^{\rm AGS17}$ = 3.467 turns out to fall within a redshift peak in the redshift distribution of the galaxies in the field which also exhibits a concentration of galaxies right around AGS17, as we will discuss in more details in Section 3.5.3. For that reason, despite the fact that we cannot strictly rule out the possibility that we are here observing the CO(5-4) transition, we decided to favor the CO(6-5) transition from a purely probabilistic point of view. A mild confirmation of this choice comes from the dust temperature that we obtain when assuming one or the other transition and redshift. If the transition is CO(5-4), the spectroscopic redshift $z_{spec}^{\rm AGS17}$ = 2.723 implies a dust temperature $T_{\rm dust} \sim$ 30 K, using a simple conversion of the peak of the SED at around 400 μm to the dust temperature. This is lower than the typical temperature $T_{\rm dust} \sim$ 38 K for the main sequence galaxies at this redshift (Schreiber et al., 2018a). Instead, if we assume the transition to be CO(6-5), the $z_{spec}^{\rm AGS17}$ = 3.467 indicates a dust temperature $T_{\rm dust} \sim$ 37 K which is close to the typical dust temperature $T_{\rm dust} \sim$ 40 K at z = 3.5 (Schreiber et al., 2018a) and is consistent with the mean dust temperature, $T_{\rm dust}$ = 37 K, of the 39 optically dark galaxies in Wang et al. (2019). We note that we also tried to obtain an independent confirmation of the redshift of AGS17 from its UV to near-IR SED as we did for AGS4. However, as we will discuss in Section 3.5.3.2 and as shown in Fig. 3.8-*Bottom*, the optical emission of AGS17 suffers from a strong blending with bright neighbors that prevents us from extracting a meaningful SED that we could use to obtain a robust, or even tentative, model fit and photometric redshift derivation.

3.3.3 Upper limits of AGS11, AGS15 and AGS24

Our spectroscopic scan follow-up of AGS11, AGS15 and AGS24 does not show emission line detections higher than 5σ. Based on their assumed redshifts, as will be discussed in Section 3.5.3, the ALMA spectroscopic scans encompass the position of the CO (6-5) emission line in the three galaxies. At the assumed redshifts, the infrared luminosities can be converted to CO(6-5) luminosities using the relation defined by Liu et al. (2015) and then to CO(6-5) fluxes accordingly. We find that the non-detection of the CO(6-5) line agrees with the dispersion of the $L_{\rm IR}$-$L'_{\rm CO\,6-5}$ relation with values below 3σ for the three galaxies (2.8σ, 2.3σ, 0.7σ for AGS11, AGS15 and AGS24 respectively).

3.4 GOODS-ALMA optically-dark galaxies

As described in Section 3.2.1.1, six out of the 35 GOODS-ALMA detections do not have counterparts in the CANDELS catalog (Guo et al., 2013). Despite their non detection in the H-band images, we are able to measure the residual emission in the optical to near-infrared images after subtracting the contribution of neighboring galaxies and to use the resulting measurements to obtain photometric redshift determinations as discussed in the next sections. After a careful analysis of the H-band images of these galaxies, we realized that in two cases, AGS4 and AGS15, there was a clear association in the H-band image that was matching the ALMA contours. In both cases, the H-band detection was close to a bright H-band neighbor and both objects were interpreted in the CANDELS catalog as a

single object, hence neglecting the ALMA source. If we were to extrapolate our small number statistics to the population of optically-dark galaxies at these depths, this would imply that about 35 % of the optically-dark sources are mistaken as such due to confusion. We note however, that these galaxies are detected here because of the very deep H-band image since their AB magnitudes are $H = 25.23$ and 27.11 AB for AGS4 and AGS15, respectively.

All four of the optically-dark galaxies detected from a blind detection above 4.8σ are detected with IRAC and listed in the catalog of Ashby et al. (2015). These galaxies are AGS4, 11, 15 and 17. The remaining two optically-dark galaxies, AGS24 and AGS25, were detected in the ALMA image using IRAC priors in F20a. However, they were not listed in the catalog of Ashby et al. (2015). In both cases, F20a (see also Section 3.5.3.1) noticed that despite being well above the IRAC detection limit, these two galaxies were missed because of the presence of a bright neighbor due to confusion (see Fig. 3.7). After carefully subtracting the surrounding neighbors, the flux densities measured at 3.5 μm for both galaxies are $F_{3.6\mu m}$(AGS24) = 4.7 ± 0.5 μJy and $F_{3.6\mu m}$(AGS25) = 1.5 ± 0.1 μJy.

Five of the GOODS-ALMA optically-dark galaxies (AGS4, 11, 15, 17 and 24) were followed-up with ALMA band 4 (see Section 3.2.1.2) and all are confirmed with a S/N of 14.7, 16.8, 15.3, 15.9 and 8.7 in the 2 mm continuum. AGS25 was not included in the ALMA proposal because the list of sources below the 4.8σ limit that includes it was still under construction at the time. All the six optically dark galaxies are also detected above 4.5σ at 870 μm continuum (Cowie et al., 2018). Hence there is no doubt that they are all real.

Another confirmation of the robustness of four of the optically-dark galaxies – AGS4, 17 and 24– comes from their detection in the radio with the VLA at 3 GHz with a S/N of 10.4, 9.9, and 5.6, respectively. AGS11, 15 and 25 are not detected with S/N higher than 5 (Rujopakarn et al. in prep.). The first two of the detected galaxies, AGS4 and AGS17, are the only optically-dark galaxies in the sample that are also detected with *Herschel* and their far-infrared SED is well-measured with no less than five *Herschel* data points from 100 to 500 μm in the observed frame. We discuss in the following two sections the properties of AGS4 and AGS25.

3.4.1 AGS4, an extremely massive galaxy at z=3.556 and a case of blending in the Hubble H-band image

AGS4 is detected in GOODS-ALMA with a $S/N = 9.7$ at 1.1 mm (F18, see also red solid contours in Fig. 3.4). Using the ALMA follow-up observations presented in Section 3.3.1, we now have a confirmation of the robustness of this source through its detection with ALMA at 2 mm with an even higher $S/N = 14.7$ (green dashed contours in Fig. 3.4).

AGS4 is an illustration of what we may call spectral de-confusion. The two catalogs CANDELS and ZFOURGE have identified a single object associated with this position on the sky. The CANDELS position is close to the center of the bright optical emitter whereas the ZFOURGE position is close to the bright K_s-band near-infrared emitter. The position of the ALMA detection exhibits a clear offset with respect to the bright optical emitter and falls on the North-West blob that is the brightest in the near-infrared. As shown in Fig. 3.4, AGS4 is at 0.″5 from a bright optical emitter. They are considered as

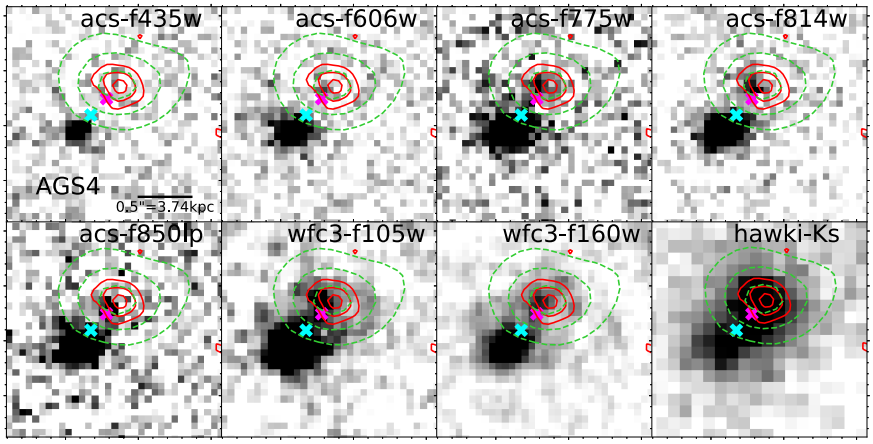

Fig. 3.4: Images of AGS4 from the observed B (435 nm, rest-frame UV) to near-infrared observed K_s (2.2 μm, rest-frame B) bands. The red contours denote the ALMA detection at 1.1mm at the resolution of 0.″29. The green dashed contours denote the ALMA detection at 2mm at the resolution of 0.″88. The astrometric corrections between ALMA and HST images are applied throughout this work. The cyan "x" denotes the optical bright neighbor, $\mathrm{ID_{CANDELS}} = 8923$ ($z_{phot} = 0.24$). The magenta "x" denotes the detection by ZFOURGE based on the K_s-band image, $\mathrm{ID_{ZFOURGE}} = 12333$ ($z_{phot} = 3.76$). If not stated otherwise, the images in this paper are all oriented with the North up and East to the left.

two regions of the same galaxy ($\mathrm{ID_{CANDELS}} = 8923$, $z_{phot} = 0.24$, cyan "x" in Fig. 3.4) in the CANDELS catalog (Guo et al., 2013). The ZFOURGE position is at 0.″16 ($\mathrm{ID_{ZFOURGE}} = 12333$) to AGS4 (magenta "x" in Fig. 3.4), and the photometic redshift derived by the ZFOURGE team is $z_{phot}^{12333} = 3.76$.

As discussed above, AGS4 exhibits an H-band counterpart well above the WFC3 detection limit in GOODS-*South* of $H = 25.23$ AB that was missed due to blending with a bright neighbor. Therefore, despite being truly optically-dark in the optical bands, AGS4 is not strictly speaking an optically-dark galaxy since it is detected in the H-band. After de-blending[3] both emitters – none of which corresponds to the centroid of the CANDELS or ZFOURGE positions which are both in between the two emitters – we can clearly see two different SEDs (Fig. 3.3-*Top-left*). We note that the two ALMA detections at 1.1mm and 2mm are well-centered on the North-West emitter. The photometric redshift associated to this object, once deconvolved from the bright optical emitter, is $z_{phot}^{AGS4} = 4.02^{+0.36}_{-0.60}$. We note that the optical source identified in the CANDELS catalog ($\mathrm{ID_{CANDELS}} = 8923$) is clearly offset from the ALMA contours, leaving little doubt that these are two separate galaxies. It is only in the low resolution K_s-band image that some confusion takes place. Being near-IR based, the ZFOURGE catalog identified the position of the peak K_s emission which matches the ALMA galaxy and attributed to it a photometric redshift of $z_{phot}^{\mathrm{ZFOURGE}}$=3.76 ($\mathrm{ID_{ZFOURGE}} = 12333$). The SED fittings of the photometric points associated to the CANDELS (grey) and ZFOURGE (green) galaxies are both shown in Fig. 3.3-*Top-left*. The grey SED does not leave any doubt on the fact that this is a very nearby galaxy ($z_{phot}^{\mathrm{CANDELS}}$=0.24), with a clear drop of the emission above 0.8 μm, whereas the green SED exhibits a break around 1.6 μm ($z_{phot}^{\mathrm{ZFOURGE}}$=3.76). The very strong difference between the SEDs of the CANDELS and ZFOURGE sources clearly show that they cannot be considered as two sides of the same galaxy, one visible in the optical the other one in the near to far infrared. These two redshifts suggest that there are indeed two galaxies in projection here.

Our ALMA spectral-scan follow-up presented in Section 3.3.1 provides complementary evidence for this spectral de-confusion between two super-imposed galaxies with a clear line detection that matches the CO(6-5) transition at a redshift of $z_{spec} = 3.566$ (see Fig. 3.1-*Left*), well within the range of possibilities of our photometric redshift estimate. Adopting the redshift at $z_{spec}^{AGS4} = 3.556$, the stellar mass of AGS4 is $M_\star = 10^{11.09\pm0.08}\,M_\odot$ which makes AGS4 one of the most massive galaxies in the early Universe. Note that adopting $z_{spec}^{AGS4} = 4.326$, as for CO(7-6), the stellar mass that we obtain for AGS4 is $M_\star = 10^{11.45\pm0.20}\,M_\odot$, which would make AGS4 the most massive galaxies known in the Universe above $z = 4$.

We investigated the possibility that the stellar mass of AGS4 may be contaminated by the presence of the continuum from an AGN, but we did not find any evidence of a power-law continuum emission in the SED presented in the Fig. 23 of F18 (also in F20b), nor any radio emission associated to it. There is an X-ray detected AGN that is associated with its neighbor ($ID_{ZFOURGE} = 12333$) which could potentially affect the measurement if attributed to the wrong counterpart, but again we do not see any clear signature of such effect. The q_{TIR}-parameter (see Eq. 3.2) measuring the infrared to radio flux ratio parameter is equal to $q_{TIR} = 2.49\pm0.06$, higher than the typical value for star-forming galaxies at $z\sim3.5$ proposed by Delhaize et al. (2017), $q_{TIR} = 2.16\pm0.06$, indicating no radio excess of this galaxy.

$$q_{TIR} = \log\left(\frac{L_{TIR}}{3.75\times10^{12}\,Hz}\right) - \log\left(\frac{L_{1.4\,GHz}}{W\,Hz^{-1}}\right). \tag{3.2}$$

where L_{TIR} is total infrared luminosity ($8-1000\ \mu$m) in unit W, and the $L_{1.4\,GHz} = 2.73\times10^{24}\,W\,Hz^{-1}$ is derived from the 10.4σ detection of AGS4 at 3 GHz assuming a radio spectral index of $\alpha = \alpha_{1.4GHz}^{3GHz} = -0.8$, the typical value for galaxies at $z > 2$ (Delhaize et al., 2017), using Eq. 3.1.

3.4.2 AGS25, the most distant optically-dark galaxy in GOODS-ALMA

AGS25 is the only optically-dark galaxy in the sample that is identified in the ZFOURGE catalog and is not confused with a neighboring galaxy. The counterpart of AGS25 in the K_s-band image is clearly visible in Fig. 3.5 (middle panel). It is associated with the ZFOURGE galaxy $ID_{ZFOURGE} = 11353$ at z_{phot}^{AGS25}=4.64. We fitted its photometric measurements as listed in the ZFOURGE catalog using the code `EAzY` for consistency with the other galaxies, and found a PDF of the photometric redshift well peaked at the redshift given in the ZFOURGE catalog (Fig. 3.3-*Bottom-right*). We find a peak redshift of $z_{phot}^{AGS25} = 4.71^{+0.24}_{-0.24}$ that encompasses the value from ZFOURGE that we keep for consistency with F20a. This makes AGS25 the most distant optically-dark galaxy in GOODS-ALMA. The IRAC emission of the galaxy is polluted by the contribution of a bright neighbor at a distance of 3 arcsec (outside of the postage stamps shown in Fig. 3.5). This explains why the galaxy is not listed in the IRAC S-CANDELS catalog (Ashby et al., 2015). After de-convolution of the bright neighbor, a clear IRAC detection is obtained (see Fig. 3.5 right panel) that was used to determine its flux density in F20a. The stellar mass of AGS25 at this redshift is $M_\star = 10^{10.39^{+0.12}_{-0.29}}\,M_\odot$ (F20a). AGS25 is not detected by Herschel, hence its $SFR = 839\pm131\,M_\odot\,yr^{-1}$ was derived in F20a by adjusting the SED of Schreiber et al. (2018) to the

1.1mm ALMA flux density corresponding to 195 μm in the rest-frame, which is not far from the peak of the far-infrared SED.

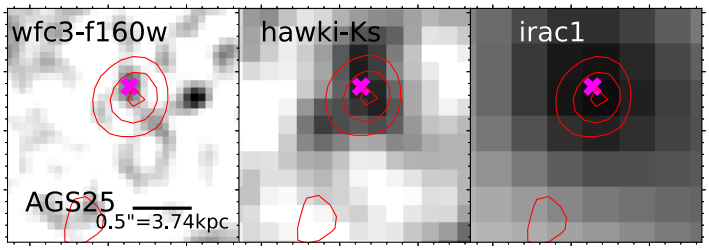

Fig. 3.5: Images of AGS25 in the H-band (1.6 μm), K_s-band (2.2 μm) and IRAC1-band (3.6 μm). The contribution of a 3″ distant bright neighbor of AGS25 was subtracted to produce the IRAC image as in F20a. The red contours denote the ALMA detection at 1.1mm at the resolution of 0″.60. The magenta "x" is the ZFOURGE counterpart $\mathrm{ID}_{\mathrm{ZFOURGE}} = 11353$.

3.5 An over-density at $z \sim 3.5$ in GOODS-ALMA

3.5.1 Clustering properties of optically dark galaxies

A large statistical sample of IRAC detected optically-dark galaxies in the CANDELS fields studied by Wang et al. (2019) shows that the optically-dark galaxies are the most massive galaxies in the early Universe and are probably the progenitors of the most massive galaxies we see in the groups or clusters of galaxy in the local Universe.

Here in the 69 arcmin^2 GOODS-ALMA field, four of the six optically dark galaxies reside in a small region of 5 arcmin^2 only. We calculate that the probability to have four out six galaxies randomly falling in such a small area is only 0.4% from four million Monte Carlo mock realizations. In addition, all the four optically-dark galaxies present a redshift consistent with $z = 3.5$ where field galaxies demonstrate a clear peak in their redshift distribution.

3.5.2 A clear peak at $z \sim 3.5$ in the redshift distribution

The redshift distribution of the galaxies with either a photometric or a spectroscopic redshift in the $6.9' \times 10'$ GOODS-ALMA field presents a peak at $z \sim 3.5$ (Fig. 3.6). This peak is at a 3.5σ significance among the 1373 galaxies at $3 \leq z \leq 4$ (Fig. 3.6). The redshift bin size is taken to be 0.03 to optimize the peak in the redshift distribution, which was previously identified in Straatman et al. (2016, Fig. 23) using the ZFOURGE catalog.

Here we increase by a factor of three the total number of galaxies with a spectroscopic redshift that fall within the redshift range $3 \leq z \leq 4$ in GOODS-ALMA. As many as 83 new spectroscopic redshifts have recently been measured and released in the data release 3 (DR3) of the VANDELS survey (McLure et al., 2018; Pentericci et al., 2018) that fall within $3 \leq z \leq 4$ in GOODS-ALMA. The VANDELS redshifts

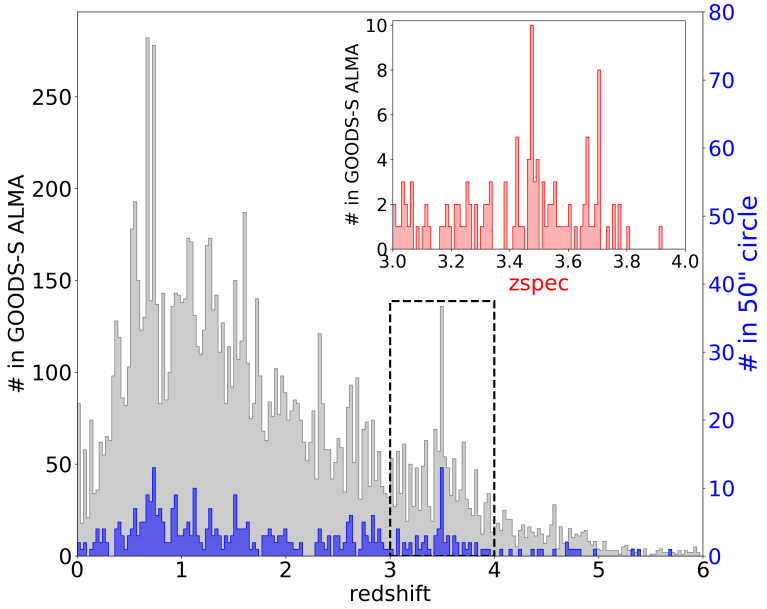

Fig. 3.6: Redshift distribution of the 11674 galaxies with a redshift (either photometric or spectroscopic) located within the $6.9' \times 10'$ GOODS-ALMA field (grey). The sub-sample of 395 galaxies located within $50''$ of the most massive galaxy in the field at $z > 3$, AGS24, are shown in blue. The insert shows the distribution of the spectroscopic redshifts of the 121 galaxies at $3 \leq z_{spec} \leq 4$ over the GOODS-ALMA field. Ten galaxies fall in the redshift bin $3.470 \leq z_{spec} \leq 3.480$. The mean redshift of the ten galaxies is $z_{spec} = 3.472$. The redshifts are from the ZFOURGE (Straatman et al., 2016) and VANDELS DR3 (McLure et al., 2018; Pentericci et al., 2018) catalogs.

supplement the already existing 38 spectroscopic redshifts originally listed in the ZFOURGE catalog and used by Straatman et al. (2016).

The 121 galaxies with spectroscopic redshifts at $3 \leq z_{spec} \leq 4$ show a clear peak at $3.470 \leq z_{spec} \leq 3.480$ containing ten galaxies (Fig. 3.6). These ten galaxies have a mean redshift at $z_{spec} = 3.472$. This is consistent with the peak at $z \sim 3.5$ shown by the 1373 galaxies with either spectroscopic or photometric redshifts.

3.5.3 Optically-dark galaxies at $z \sim 3.5$

We find that four out of the six optically-dark galaxies exhibit a redshift that is consistent with being located in the same redshift peak at $z \sim 3.5$, which corresponds to an over-density centered on the most massive of them, AGS24, as to be discussed below. We may even count five out of the six if we include AGS4, which is at $z_{spec} = 3.556$ and at a distance of $3'$ from AGS24. Accounting for the redshifts of the sources, this corresponds to 70.8 cMpc (comoving) and 15.5 pMpc (proper). The comoving distance is typical of those found in distant super-clusters while the proper distance is consistent with those of proto-clusters, which suggests that AGS4 could potentially be a member of the proto-cluster as well. We start by describing in detail the properties of AGS24, because it is the most massive of all the optically-dark galaxies in GOODS-ALMA and even among all GOODS-*South* galaxies at $z > 3$ and constitutes an excellent candidate for a future BCG galaxy. The remaining three optically-dark galaxies at $z \sim 3.5$ are discussed in the next section.

Tab. 3.1: Properties of the optically dark galaxies.

ID	RA [deg]	Dec [deg]	z_{phot}	z_{spec}	assumed z	log $M_\star$ log [$M_\odot$]	log $L_{\rm IR}$ log [$L_\odot$]	SFR [$M_\odot$ yr^{-1}]	$R_{\rm SB}$	$F_{1.1\rm mm}$ [mJy]	$F_{2\rm mm}$ [mJy]	log $L_{\rm CO}$ log [$L_\odot$]	H [mag]	$F_{3\rm GHz}$ [μJy]	$F_{6\rm GHz}$ [μJy]	$L_{1.4\rm GHz}$ [WHz^{-1}]
(1)	(2)	(3)	(4)	(5)	(6)	(7)	(8)	(9)	(10)	(11)	(12)	(13)	(14)	(15)	(16)	(17)
AGS4	53.148839	-27.821192	–	3.556	3.556	$11.09^{+0.06}_{-0.18}$	12.93±0.02	1435^{+76}_{-83}	$3.8^{+1.9}_{-0.5}$	1.72±0.20	0.29±0.02	4.95±0.93	25.23	17.28±1.66	8.64±0.77	2.73×10^{24}
AGS11	53.108818	-27.869055	–	–	3.472	$10.24^{+0.75}_{-0.00}$	12.94±0.07	1492^{+252}_{-253}	$28.7^{+0.1}_{-23.6}$	1.34±0.25	0.30±0.02	–	–	4.48±1.06	–	6.72×10^{23}
AGS15	53.074847	-27.875880	$3.96^{+0.80}_{-0.78}$	–	3.472	$10.56^{+0.01}_{-0.41}$	12.78±0.08	1034^{+180}_{-179}	$9.5^{+11.2}_{-1.7}$	1.21±0.11	0.32±0.02	–	27.11	5.38±1.06	–	8.08×10^{23}
AGS17	53.079374	-27.870770	–	3.467	3.467	$10.52^{+0.40}_{-0.06}$	13.08±0.02	2070^{+112}_{-117}	$20.9^{+3.1}_{-12.6}$	2.30±0.44	0.35±0.02	5.22±1.01	–	39.00±3.94	1.16±0.32	5.86×10^{24}
AGS24	53.087178	-27.840217	$3.58^{+0.49}_{-0.38}$	–	3.472	$11.32^{+0.02}_{-0.19}$	12.31±0.11	353^{+80}_{-82}	$0.6^{+0.5}_{-0.1}$	0.88±0.22	0.19±0.02	–	–	12.43±2.19	1.41±0.32	1.87×10^{24}
AGS25	53.183710	-27.836515	4.64	–	4.64	10.39	12.68±0.07	832^{+126}_{-135}	$8.0^{+1.3}_{-1.3}$	0.82±0.19	–	–	–	3.92±1.06	1.07±0.32	5.90×10^{23}

Columns: **(1)** Source names; **(2) (3)** Coordinates in the ALMA image (J2000): see F18 and F20a; **(4)** Photometric redshifts: see Section 3.2.4.1; **(5)** Spectroscopic redshifts: The spectroscopic redshifts of AGS4 and AGS17 are derived from the CO(6-5) line measured in our ALMA spectroscopic scan follow-up, see Section 3.3; **(6)** Assumed redshifts: We assign the redshift of AGS11, AGS15 and AGS24 to be the same as the central position of the redshift peak that presents an over-density centered on AGS24, z_{peak} =3.472, as discussed in section 3.5.2 and 3.5.3, which is consistent with their photometric redshifts. For each galaxy, all the properties are measured assuming the redshift listed here; **(7)** Stellar masses: see Section 3.2.4.2; **(8)** Infrared luminosities: see Section 3.2.4.3; **(9)** SFRs: see Section 3.2.4.4; **(10)** Starburstness: As in F20a, $R_{\rm SB}$ = SFR/SFR$_{MS}$, where SFR$_{MS}$ is the average SFR of MS galaxies as defined in Schreiber et al. (2018); **(11)** Flux densities at 1.1 mm: Peak fluxes measured using `Blobcat` as in F18 and the fluxes of AGS15 and AGS17 are updated in F20a; **(12)** Peak fluxes at 2 mm from the ALMA band4 follow-up; **(13)** CO luminosities: the CO(6-5) line detected in our ALMA spectroscopic scan follow-up; **(14)** H-band AB magnitudes: After de-blending, AGS4 and AGS15 turn out to have H-band magnitudes higher than the detection limit; **(15)** Flux densities at 3GHz: the flux densities of AGS4, 17 and 24 are the peak flux derived using PyBDSF[1](Rujopakarn et al. in prep.), flux densities of AGS11, 15 and 25 are the peak flux densities in the 3GHz image; **(15)** Flux densities at 6 GHz: the flux density of AGS4 is the peak flux derived using PyBDSF[1], flux densities of AGS17, 24 and 25 are the peak flux densities in the 6GHz image, AGS11 and AGS15 don't have peak flux density higher than 3σ; **(17)** Luminosity at 1.4GHz: derived from the flux density at 3GHz using Eq. 3.1.

Tab. 3.2: Information of the neighbors of AGS24.

ID	z_{spec}	z_{phot}	$M_\star$ $[10^{10} \times M_\odot]$	SFR $[M_\odot\ yr^{-1}]$
ZFOURGE10672	–	3.53	5.88	30.2
ZFOURGE10627	3.478	3.48	2.63	14.8
CDFS007493	3.482	–	0.41	–

3.5.3.1 AGS24, the most massive galaxy at $z > 3$ in GOODS-*South*

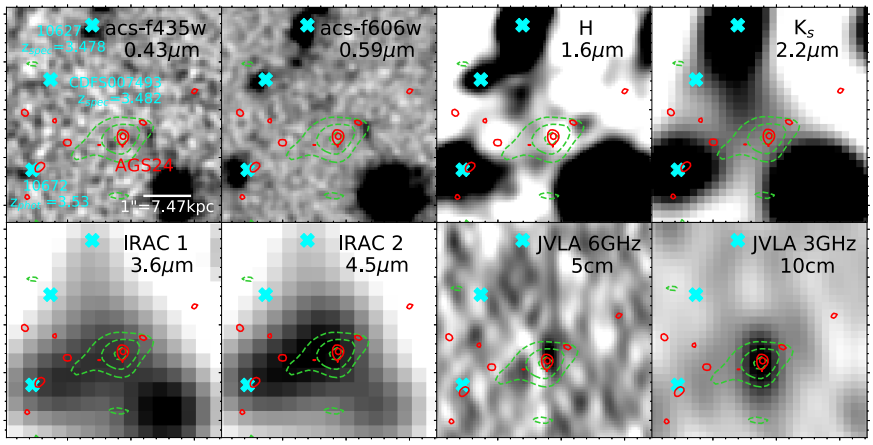

Fig. 3.7: Images of AGS24 in the *B*, *V*, *H* and K_s band, IRAC 3.6 and 4.5μm, JVLA 6 GHz (3.7σ) and 3 GHz (5.7σ). The contours are the same as in Fig. 3.4 but for AGS24. The three neighbor galaxies are labeled with $ID_{ZFOURGE}$ or ID_{CDFS} and their redshift separately.

AGS24 has been detected with a signal-to-noise-ratio of 4.9σ and 8.7σ in the GOODS-ALMA 1.1mm image and in the 2 mm continuum image of the ALMA spectroscopic scan follow-up (red and green contours in Fig. 3.7). This galaxy exhibits a lower S/N ratio in the GOODS-ALMA image tapered at 0.″6 (3.9σ) than in the image at the original resolution of 0.″29 (4.9σ), which suggests that the dust emission is very compact. This optically-dark galaxy exhibits a clear radio counterpart at 6 GHz (3.7σ) and 3 GHz (5.7σ). Despite being absent from the list of IRAC sources in the field given in the S-CANDELS catalog (Ashby et al., 2015), this source does exhibit clear IRAC emission at 3.6 and 4.5 μm that is partly blended with the three surrounding very nearby galaxies that are clearly detected in the *H* and K_s bands. The emission of AGS24 in the *H* and K_s bands is marginal but was estimated after de-blending the contribution from the three neighboring sources and used to determine its photometric redshift.

After de-blending[3], we derive a photometric redshift of $z_{\rm AGS24} = 3.58^{+0.49}_{-0.38}$. Assuming this redshift, the excess emission in the *V* band may correspond to the Lyα emission line (Fig. 3.3-*Bottom-left*). However, we analyzed the VLT/MUSE data obtained in this region but did not find any evidence for Lyα emission despite the high sensitivity of MUSE ($rms = 4\times10^{20}$ erg s^{-1} cm^{-2} A^{-1} Herenz et al., 2017). We conclude that the excess V band emission remains uncertain and may be due to noise fluctuation.

The three neighboring galaxies are located at similar distances of $\sim$1.″5 (equivalent to 11.3 kpc at $z \sim 3.5$) from AGS24 (Fig. 3.7 and Table 3.2). They all have a redshift of $z\sim$3.5, including two spectroscopic redshifts – $ID_{ZFOURGE} = 10627$, $z_{spec} = 3.478$ and $ID_{CDFS} = 007493$, $z_{spec} = 3.482$ (VANDELS DR3) – and one photometric redshift – $ID_{ZFOURGE} = 10672$, $z_{phot} = 3.53$ (Straatman et al., 2016). As a

result, the group of four galaxies appears to be physically connected and makes a dense and compact association of galaxies typical of what can be found at the center of distant proto-clusters (Springel et al., 2005; De Lucia and Blaizot, 2007).

Altogether, the following reasons suggest that AGS24 is located at the redshift of $z\sim$3.472 (Section 3.5.2) of the proto-cluster: *(i)* the three neighbors of AGS24 have $z\sim$3.472, *(ii)* the photometric redshift of AGS24 is consistent with this redshift, *(iii)* AGS24 belongs to the highly improbable association of optically-dark galaxies that fall in the region of the $z\sim$3.472 proto-cluster.

Assuming this redshift, we estimate the total infrared luminosity of AGS24 to be $L_{\rm IR} = 10^{12.31\pm0.11}\,{\rm L}_\odot$ fitting the rest-frame 195, 245, 490 μm emission of the galaxy that corresponds to the observed 870 μm, 1.13 and 2 mm using the typical far-infrared SED of a MS galaxy at this redshift (Schreiber et al., 2015). We also checked that we obtained a consistent total infrared luminosity after fitting these measurements with a Draine et al. (2007) SED, which gives the same result within 10%.

Assuming $z = 3.472$, the stellar mass of AGS24 is $M_\star = 10^{11.32^{+0.02}_{-0.19}}\,{\rm M}_\odot$ (adopting the Calzetti et al. (2000) attenuation law and a delayed exponentially declining SFH). It is $\sim$ 10 times more massive than the galaxy presented in Ginolfi et al. (2017) which used to be the most massive galaxy at $z = 3\sim4$ in this field. We note that the stellar mass was derived by fitting the near UV to near-infrared photometry, similar to the method we used for our galaxies. In order to test the robustness of the value of the stellar mass of AGS24, we recompute it assuming various star formation histories (SFH) to see whether this mass could fall down by a large amount. We use the SED fitting code FAST++[4] to test a delayed exponentially declining and an exponentially declining SFH as well as a truncated SFH, with the possibility to add a second burst. We also test the impact of varying the attenuation law using the code CIGALE (Boquien et al., 2019) with the attenuation laws from Calzetti et al. (2000), Charlot and Fall (2000), and the modified Charlot and Fall (2000) law in MAGPHYS (da Cunha et al., 2008). The results are listed in Table 3.3. They show that despite these wide variety of SFH and attenuation laws, the stellar mass of AGS24 remains within $10^{11.31}$ and $10^{11.52}\,{\rm M}_\odot$.

With a redshift of $z\sim3.5$, AGS24 is the most massive galaxy in the GOODS-ALMA field above $z = 3$. The other similarly massive candidate galaxies in this redshift range either have a strong AGN potentially contaminating the estimate of the stellar mass or highly unreliable redshifts. Two galaxies without an AGN at $z > 3$ have similarly large stellar masses in the GOODS-ALMA field ($\rm ID_{ZFOURGE} = 11505$ and 16410, marginally detected in the K_s-band with S/N = 5.0, 5.5, at $z_{phot} = 5.36$, 4.73). They both have very high χ^2 values of 126.6 and 43.0 associated with their photometric redshifts. Only 3% and 19% of the ZFOURGE galaxies have photometric redshifts with such high χ^2 values. Therefore, we consider the redshifts of these two galaxies not reliable.

We inspect the possible contamination of an AGN on the near- and mid-infrared emission which may result in an overestimation of the stellar mass. We calculate the infrared to radio flux ratio, $q_{\rm TIR} = 2.05\pm0.18$ (see Eq. 3.2), where the 1.4GHz luminosity, $L_{1.4\,\rm GHz} = 1.87\times10^{24}\,{\rm W\,Hz^{-1}}$, is converted from the JVLA 3GHz emission (5.7σ) of AGS24 assuming a radio spectral index of $\alpha = -0.8$, as we did for AGS4. Within the rms, the infrared to radio flux ratio agrees with the value $q_{\rm TIR} = 2.16 \pm 0.06$ for star-forming galaxies at redshift $z\sim3.5$ by Delhaize et al. (2017), indicating no radio excess of this galaxy. We also checked that AGS24 does not have a counterpart in the deepest Chandra 7Ms

Tab. 3.3: Stellar masses of AGS24 assuming different SFHs and attenuation laws.

FAST++[4]: Calzetti et al. (2000) attenuation law + vary SFHs	
Models	$\log M_\star$ [$\log M_\odot$]
delayed exponentially declining	$11.37^{+0.01}_{-0.23}$
exponentialy declining	$11.31^{+0.11}_{-0.19}$
truncated	$11.40^{+0.00}_{-0.28}$
a second burst	$11.33^{+0.04}_{-0.18}$
CIGALE: delayed exponentially declining SFH + vary attenuation laws	
Models	$\log M_\star$ [$\log M_\odot$]
Calzetti et al. (2000)	11.52 ± 0.57
Charlot and Fall (2000)	11.41 ± 0.21
MAGPHYS[a]	11.44 ± 0.22

[a] A modified Charlot and Fall (2000) law that is used in MAGPHYS (da Cunha et al., 2008)

source catalog (Luo et al., 2017). We searched for extended diffuse emission in the Chandra 7Ms image but found no robust evidence for such emission that could be associated with an intra-cluster medium. Therefore, we conclude that AGS24 is the most massive galaxy at $z>3$ without an AGN in the GOODS-ALMA field. Forrest et al. (2019) recently spectroscopically confirmed ($z_{spec}=3.493$) a similarly extremely massive quiescent galaxy in the VIDEO XMM-Newton field (Annunziatella et al., in prep.) that is spectroscopically confirmed ($z_{spec}=3.493$) and interpreted as experiencing a rapid downfall of star formation.

The predicted number of galaxies that are as massive or more massive than AGS24 in the GOODS-ALMA field at $3<z<4.5$ is 1.15, based on the galaxy stellar mass function (SMF) derived from the observations in the COSMOS field (Davidzon et al., 2017). Pillepich et al. (2018) compared the SMF of Davidzon et al. (2017) to the one from the IllustrisTNG simulation and found them consistent. Thus the existence of one massive galaxy, AGS24, is consistent with the existing observation and simulation.

3.5.3.2 Physical properties of the optically-dark galaxies AGS11, AGS15 and AGS17 at $z\sim3.5$

- AGS11 is detected at 1.1mm with a $S/N=5.71$ in F18 (also see red solid contours in Fig. 3.8-*Top*) and 2 mm with a $S/N=16.8$ (green dashed contours in Fig. 3.8-*Top*). A neighboring galaxy is identified in ZFOURGE that matches the K_s and IRAC emission (magenta "x" in Fig. 3.8-*Top*). This object is located at 0.″45 from the ALMA detection. It has been attributed with a photometric redshift of $z_{phot}^{7589}=4.82$ in the ZFOURGE catalog. However, this redshift is highly uncertain with flag $\mathtt{use}=0$, hence highly unreliable. Data at hand do not allow us to determine whether this object is the counterpart of the ALMA detection, AGS11, or like several other optically dark sources studied here, an independent galaxy seen in projection. The optical emission at the ALMA detection position is within the noise fluctuation. Therefore, we do not attributed the ZFOURGE ID and the associated redshift to AGS11. Instead, we consider the association of the optically dark galaxies with the over-density at $z\sim3.5$ as potential evidence that AGS11 has a redshift matching this over-density. In Table 3.1 we decided to attribute AGS11 with the $z_{peak}=3.472$

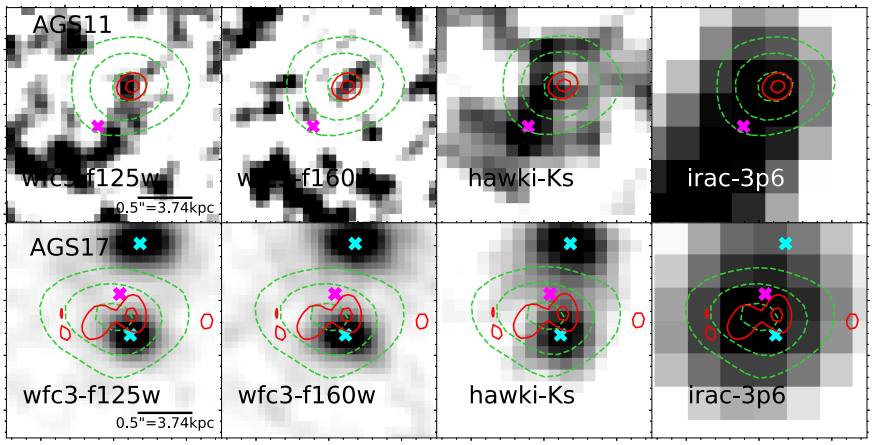

Fig. 3.8: ***Top:*** Images of AGS11 in the *J* band, *H* band, K_s band and IRAC 3.6 μm . The magenta "x" denotes the detection in K_s-band by ZFOURGE, $\mathrm{ID}_{\mathrm{ZFOURGE}} = 7589$ ($z_{phot} = 4.82$). ***Bottom:*** Same as above, but for AGS17. The cyan "x"s denote the optical bright neighbors, $\mathrm{ID}_{\mathrm{CANDELS}} = 4414$ ($z_{phot} = 0.03$, below) and $\mathrm{ID}_{\mathrm{CANDELS}} = 4436$ ($z_{phot} = 0.95$, above). The magenta "x" denotes the detection in K_s-band by ZFOURGE, $\mathrm{ID}_{\mathrm{ZFOURGE}} = 6964$ ($z_{phot} = 1.85$).

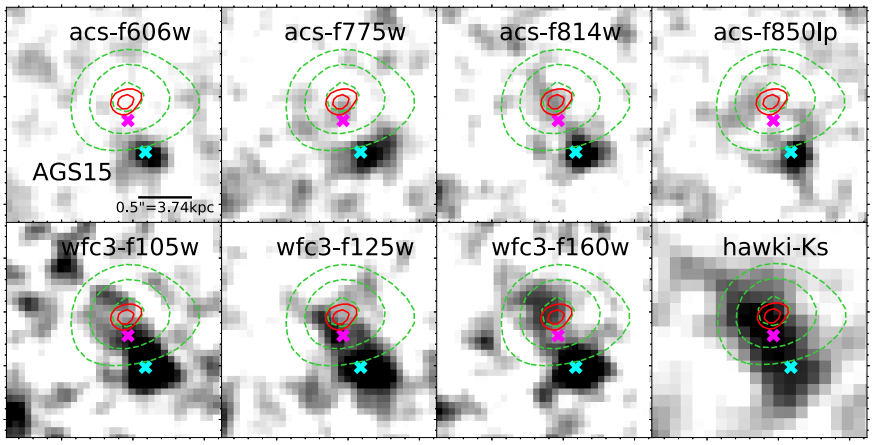

Fig. 3.9: Same as in Fig. 3.4, but for AGS15. The cyan "x" denotes the optical bright neighbor, $\mathrm{ID}_{\mathrm{CANDELS}} = 3818$ ($z_{phot} = 4.27$). The magenta "x" denotes the detection in K_s-band by ZFOURGE, $\mathrm{ID}_{\mathrm{ZFOURGE}} = 6755$ ($z_{phot} = 3.47$).

of the over-density. Assuming $z_{\rm AGS11} = 3.472$, the infrared luminosity we derived for AGS11 is $L_{\rm IR} = 10^{12.94\pm0.07}\,{\rm L}_\odot$.

- AGS15 is located at 0″.59 to a optically bright galaxy ($\rm ID_{CANDELS} = 3818$, cyan "x" in Fig. 3.9). It is detected at 5.22σ in the 1 mm image (F18, see also red contours in Fig. 3.9). This detection is further confirmed in the 2 mm continuum at 15.3σ in the follow up ALMA spectroscopic scan (green dashed contours in Fig. 3.9). In the K_s-band image, the infrared emission from AGS15 and from the optically bright galaxy is blended, and the two galaxies are confused as one ($\rm ID_{ZFOURGE} = 6755$, magenta "x" in Fig. 3.9) in the ZFOURGE catalog. The redshift derived by the ZFOURGE team is $z_{phot}^{6755} = 3.46$ and the stellar mass is $M_\star = 10^{9.86}\,{\rm M}_\odot$. We notice that there is a high uncertainty in the SED fitting by the ZFOURGE team, with $\chi^2 = 45.4$ which is higher than 84% of all the galaxies in the ZFOURGE catalog. If it is the counterpart of AGS15, then the low stellar mass will make AGS15 an extreme case, i.e., 10 times less massive compared to the other ALMA detections. After de-blending AGS15 and the optically bright galaxy, as shown in Fig. 3.9 and Fig. 3.3-*Top-right*, we find that in fact AGS15 has an H band magnitude higher than the detection limit, $H = 27.11$ AB. We fit the SED with `EAzY` (Brammer et al., 2008) and `FAST++`[4] to derive the photometric redshift and the stellar mass. The $z_{\rm peak}$ derived for AGS15 is at $z_{phot}^{\rm AGS15} = 3.96^{+0.80}_{-0.78}$. Hence the galaxy has, within the uncertainties on the photometry, a photometric redshift that encompasses the redshift peak at $z_{peak} = 3.472$. Assuming this redshift, we obtain the infrared luminosity of AGS15 to be $L_{\rm IR} = 10^{12.78\pm0.08}\,{\rm L}_\odot$, the SFR to be ${\rm SFR} = 1042^{+181}_{-183}\,{\rm M}_\odot\,{\rm yr}^{-1}$ and the stellar mass to be $M_\star = 10^{10.56^{+0.01}_{-0.41}}\,{\rm M}_\odot$.

- AGS17 is detected at 1.1 mm with a $S/N = 5.01$ (F18, also see red solid contours in Fig. 3.8-*Bottom*) and with a $S/N = 15.9$ in the 2 mm continuum (green dashed contours in Fig. 3.8-*Bottom*). It is located between two bright optical emitters, $\rm ID_{CANDELS} = 4414$, ($z_{phot}^{4414} = 0.03$, Pannella et al., 2015) at 0″.27, and $\rm ID_{CANDELS} = 4436$, ($z_{phot}^{4436} = 0.95$, fitted with `EAzY`) at 0″.57 (cyan "x"s in Fig. 3.8-*Bottom*). These two emitters are also clearly seen in the K_s-band image, however, they are not resolved in the ZFOURGE catalog (magenta "x" in Fig. 3.8-*Bottom*, $\rm ID_{ZFOURGE} = 6964$). The redshift derived from this blended emission is $z_{phot}^{6964} = 1.85$ which is not consistent with either the redshifts of the optical emitters.

  Assuming that the emission line detected in our ALMA spectroscopic follow-up is the CO(6-5) transition as discussed in Section 3.3.2, AGS17 has a spectroscopic redshift $z_{spec}^{\rm AGS17} = 3.467$, which puts it at a distance of 4.30 cMpc from AGS24, assuming $z^{\rm AGS24} = z_{peak} = 3.472$. Hence it falls inside the proto-cluster as the distance is shorter than the typical size of a proto-cluster ($\sim$14.5 cMpc) at $z \sim 3.5$ in simulations (Muldrew et al., 2015). The low probability to have a galaxy fall in projection with the structure that is located at the redshift corresponding to the CO(6-5) transition makes us favor this transition. Then the stellar mass is $M_\star = 10^{10.59^{+0.29}_{-0.19}}\,{\rm M}_\odot$ based on the IRAC band emission and the infrared luminosity derived from the SED fitting using Herschel and ALMA data is $L_{\rm IR} = 10^{13.08\pm0.02}\,{\rm L}_\odot$.

3.5.4 Spatial distribution of galaxies at $z \sim 3.5$ in the GOODS-ALMA field

3.5.4.1 Local over-density (δ) of individual galaxies

We calculate the over-density ($\delta = \rho / \bar{\rho}$) of the 364 galaxies at $3.42 \leq z \leq 3.57$ in GOODS-ALMA. This redshift range covers a distance of 125 cMpc which is consistent with the size of a large scale structure, a (proto-)supercluster of $\sim 60 \times 60 \times 150$ cMpc at $z \sim 2.45$, identified by Cucciati et al. (2018). We derive a dispersion of $\sigma(\delta) = 0.20$ among the 364 galaxies. We do that by comparing the projected local galaxy density within 2 cMpc (ρ) of a galaxy, to the average number density over the GOODS-ALMA field ($\bar{\rho} = 1.32\,\mathrm{cMpc}^{-2}$ or $5.13\,\mathrm{arcmin}^{-2}$).

Seven of the detections in the GOODS-ALMA field reside in this narrow redshift range, AGS1, 4, 5, 11, 15, 17, and 24, five (underlined) out of the seven are optically-dark. The $z_{spec}^{\mathrm{AGS1}} = 3.442$ of AGS1 comes from VANDELS DR3, zflag = 1, i.e., 50% probability to be correct, while we note that it is recorded as $z_{spec}^{\mathrm{AGS1}} = 2.309$ in F18. AGS5 has a photometric redshift of $z_{phot}^{\mathrm{AGS5}} = 3.46$ (Straatman et al., 2016). As mentioned in Section 3.4.1, AGS4 has a redshift of $z_{spec}^{AGS4} = 3.556$.

At the same time, eight massive galaxies fall in this redshift range in the ZFOURGE catalog. They have a stellar mass, $\log[\mathrm{M}_\star/\mathrm{M}_\odot] > 10.5$, which is equivalently massive as the ALMA detections (F18). They have a median stellar mass of $M_\star = 10^{10.82}\,\mathrm{M}_\odot$. These eight massive galaxies, as well as the seven ALMA detections all show a local over-density ($\delta > 1$). Out of the 15 massive galaxies, AGS24 shows the most prominent clustering, $\delta_{\mathrm{AGS24}} = 2.06$, hence a $> 5\sigma$ excess with respect to the average galaxy surface density. Hence AGS24 is both the most massvie galaxy at $z > 3$ in the GOODS-ALMA field with no AGN and it is located in the densest surface density peak at $z \sim 3.5$. This makes it an excellent candidate for a future BCG as we discuss in Section 3.5.5. The degree of over-density of the four other HST-dark galaxies are $\delta_{\mathrm{AGS11}} = 1.46$ ($> 2\sigma$ excess), $\delta_{\mathrm{AGS15}} = 1.64$ ($> 3\sigma$ excess), $\delta_{\mathrm{AGS17}} = 1.76$ ($\sim 4\sigma$ excess), $\delta_{\mathrm{AGS4}} = 1.39$ ($\sim 2\sigma$ excess), and for the other two ALMA detection with optical counterparts, it is $\delta_{\mathrm{AGS1}} = 1.21$, $\delta_{\mathrm{AGS5}} = 1.03$.

Regardless of mass, when focusing on the galaxies in the densest regions, i.e., $\delta > 5\sigma(\delta)$, we found in total 12 galaxies in the ZFOURGE catalog. It turns out that they all lie within 50″ of AGS24 (red circle in Fig. 3.11) and the barycenter of these galaxies falls exactly at AGS24. The most massive of the 12 galaxies is $\mathrm{ID}_{\mathrm{ZFOURGE}} = 10672$, $M_\star = 10^{10.76}\,\mathrm{M}_\odot$. It is at 1.″5 from AGS24.

In Fig. 3.10, we show the over-density as a function of stellar mass of the 364 galaxies at $3.42 < z < 3.57$ in the GOODS-ALMA field and the ALMA detected galaxies. We can see that as the stellar mass increases, the galaxies tend to fall in denser regions, which is in line with what Muldrew et al. (2015) found in Millennium Simulation (Springel et al., 2005) on galaxies at $z = 2$. They conclude that the most massive galaxies at high redshift reside in proto-clusters given the little difference in the environments of only proto-cluster galaxies and those of all the massive galaxies. Besides, the ALMA detections are the most massive ones in the field and reside in the densest regions. AGS24, as the most massive one in the field, resides in the densest region in the field. Therefore, these optically dark galaxies revealed by ALMA make up for what has been missed from optical observations. The relation between their dusty and massive nature and the dense environment they reside in provides evidence of environmental effects on galaxy evolution.

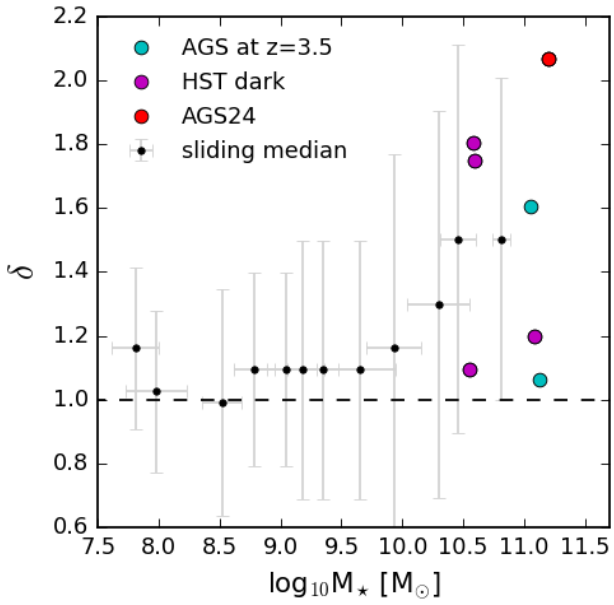

Fig. 3.10: Local over-density (δ) of individual galaxies in the GOODS-ALMA field at $3.42 < z < 3.57$. The black dots show the sliding medians of δ at different stellar masses. The filled circles indicate all the ALMA detections. The purple circles are the HST dark galaxies and the red circle indicates AGS24.

3.5.4.2 Projected density map over the GOODS-ALMA field

We construct the projected galaxy density in Fig. 3.11. Similar to the method used in Forrest et al. (2017), we create a grid with a cell size of $0\farcs9 \times 0\farcs9$ in the GOODS-ALMA field and calculate the over-density ($\delta = \rho / \bar{\rho}$) for each cell. 364 galaxies (40 with z_{spec}) at $3.42 \leq z \leq 3.57$ are used to produce the map. The galaxies with spectroscopic redshifts are marked as white dots in Fig. 3.11. An overdense region comes out in the South-East region as indicated by the zoom-in box in Fig. 3.11. The 4σ peak of this over-density happens to be very close to AGS24, the galaxy with the strongest over-density ($\delta_{\rm AGS24} = 2.06$) this is consistent with the fact that it is in a highly clustered environment. Out of the 364/40 (redshift/z_{spec}) galaxies in the 69 arcmin^2 field, 126/18 reside in this 15 arcmin^2 box, and 26/3 galaxies in this redshift slice fall within 50″ (2 arcmin^2) of AGS24.

We notice that the over-density shown in the projected density map encompasses four out of the six HST-dark galaxies detected by ALMA (AGS 11, 15, 17, 24, stars in Fig. 3.11). The overlap of an over-density of ALMA detected optically-dark galaxies and an over-density of optically detected galaxies shows that these ALMA detected galaxies are good tracers of structures in the early Universe.

This over-density has been classified as a proto-cluster in previous publications. Franck and McGaugh (2016) identified it in a list of proto-clusters at $2.74 < z < 3.71$ built out of $\sim$ 14000 spectroscopic redshifts (with 604 of them finally used). They defined proto-clusters as galaxy densities greater than the field density by a factor 7 within a radius of 2′ and a redshift range of $\delta z < 0.03$. One of their proto-clusters, CCPC-z34-002, has a redshift of $z = 3.476$, hence consistent with the redshift peak of $z = 3.472$ studied here. We note that the CCPC-z34-002 density peak, roughly estimated from the distribution of only 23 galaxies within a radius of 20 cMpc, does not correspond to the location of AGS24 but falls only 10″

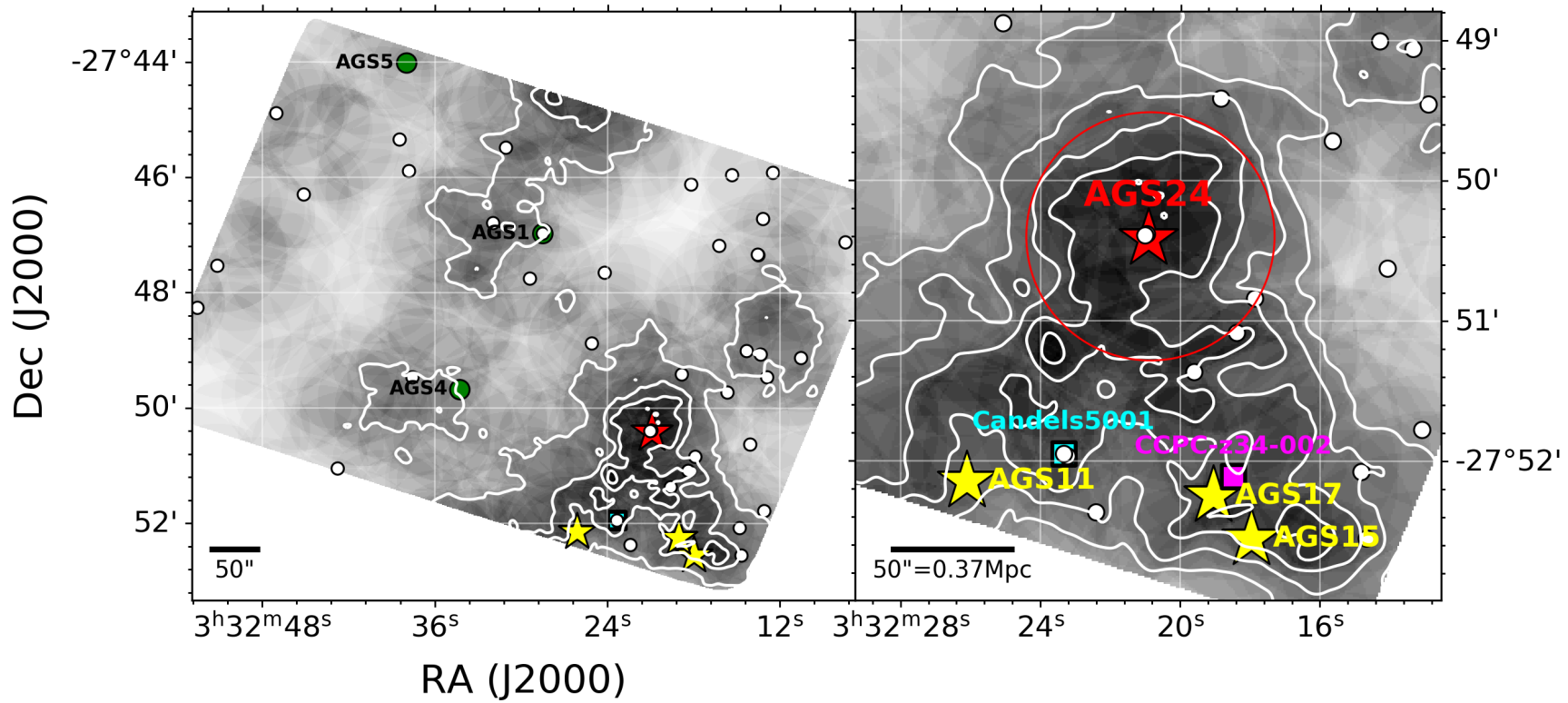

Fig. 3.11: Projected density of 364 galaxies (40 with z_{spec}) at $3.42 \leq z \leq 3.57$. The contours show 1,2,3,4σ level of the over-density. ***Left*** panel covers the field observed in GOODS-*South* ALMA. ***Right*** panel shows the zoom-in of the extended structure in the bottom right corner of GOODS-ALMA field, which encompasses 126(18) galaxies over 15 arcmin^2. The red star indicates the position of AGS24. The red circle indicates a 50″ radius region (2 arcmin^2) including 26(3) galaxies. The yellow stars refer to the HST-galaxies AGS 11, 15 and 17 located also in this larger structure. The green circles represent the AGS 1 and 5 which are also in this redshift range but not optically-dark. The white circles show the 40 galaxies with spectroscopic redshifts. We note that the two white circles falling on the red star of AGS24 are two galaxies dissociated from AGS24. The magenta square denotes the center of the proto-cluster CCPC-z34-002 identified by Franck and McGaugh (2016). The cyan square denotes Candels5001, which used to be the most massive galaxy at $3 < z < 4$ in this field (Ginolfi et al., 2017). The 50″ scale in the figure is equivalent to a proper distance of 0.37 Mpc at $z = 3.5$.

from AGS17, and the typical diameter of the proto-clusters studied by Franck and McGaugh (2016) of 4 arcmin matches the zoom shown in Fig. 3.11-*Right*. In the following, we will consider as a members of a candidate proto-cluster the galaxies of the redshift peak that fall in this area. This structure encompasses four out of six, hence 67 %, of the optically-dark galaxies identified in the GOODS-ALMA field.

This over-density was also identified by Forrest et al. (2017) who used a population of extreme emission line galaxies, with low stellar masses and by the VANDELS survey with a three-dimensional algorithm (Guaita et al., 2020). Moreover, only nine out of 131 the Lyα-emitting galaxies selected from the VANDELS survey reside in their 13 detected over-densities at $z > 2$, indicating that Lyα-emitting galaxies are not ideal tracers of over-densities. Finally, we note that Ginolfi et al. (2017) observed the molecular gas content of the galaxy CANDELS-5001 (blue square in Fig. 3.11, $M_\star = 10^{10.27^{+0.38}_{-0.11}}$ M$_\odot$, $z_{spec} = 3.473$) and found that this galaxy was surrounded by an extended emission of molecular gas spanning 40 kpc traced by the CO(4-3) transition. Furthermore they detect nine additional CO systems within a radius of 250 kpc from the massive galaxy and mostly distributed in the same direction as the CO elongated structure found in the central 40 kpc which they interpret as evidence for large-scale gas accretion on the galaxy. This large-scale accretion might be enhanced by the larger scale dark matter halo of the structure (see e.g. Rosdahl and Blaizot (2012)).

We calculate the distance between AGS1, 4, 5 and AGS24 to be 40.5 cMpc, 70.8 cMpc and 25.5 cMpc respectively. Despite their larger distance, AGS1 and 5 might be involved in a wider structure than the proto-cluster that includes AGS11, 15, 17, 24 and potentially also AGS4. This wider structure may be compared to the superclusters at high redshift discussed in Cucciati et al. (2018) and Toshikawa et al. (2020).

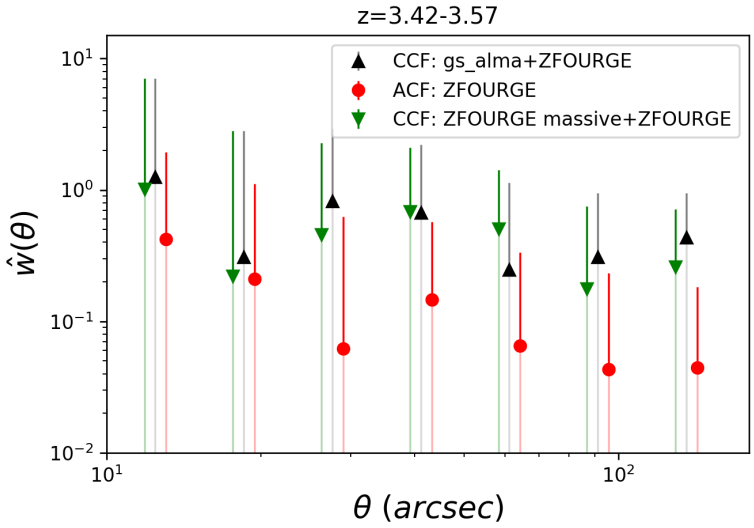

Fig. 3.12: Comparison of the auto-correlation function (ACF) of the 364 galaxies at $3.42 \leq z \leq 3.57$ in the ZFOURGE catalog (red dots), the cross-correlation function (CCF) between these galaxies and the ALMA detections (black triangles), and the cross-correlation function between these galaxies and the galaxies which are equivalently massive as the ALMA detections (green triangles), i.e., $M_\star > 10^{10.5}$ M$_\odot$.

3.5.4.3 Two point correlation function (2PCF)

We calculated the auto-correlation function of the 364 galaxies (40 with z_{spec}) at $3.42 \leq z \leq 3.57$ using a uniformly generated random sample in the GOODS-ALMA field, independent of mass (red dots in Fig. 3.12), the cross-correlation function between these 364 galaxies and the ALMA detections (black triangles in Fig. 3.12), and the cross-correlation function between these 364 galaxies and the massive galaxies which are equivalently massive as the ALMA detections, i.e., $M_\star > 10^{10.5}\,M_\odot$ out of the 364, (green triangles in Fig. 3.12). A Landy and Szalay (1993) estimator is adopted. Error bars are estimated from 1000 bootstrap samples. Despite of the large error bars, the two cross-correlations both show systematically higher excess possibility compared to the auto-correlation of the 364 galaxies in this redshift range. This indicates a clustering feature of the ALMA detected optically dark galaxies, as well as the equivalently massive galaxies.

3.5.5 Dynamical state of the proto-cluster at $z \sim 3.5$

As discussed in Section 3.5.3.1, AGS24 is the most massive galaxy in the field at $z > 3$ ($M_\star = 10^{11.32^{+0.02}_{-0.19}}\,M_\odot$) and in particular at $z \sim 3.5$, making it a good candidate for the future BCG of the over-density of galaxies if it becomes a galaxy cluster. The fact that it is surrounded by three galaxies with the same redshift of $z \sim 3.5$ within 1.″5 from AGS24 (11.3 kpc at $z \sim 3.5$) strengthens this hypothesis (Fig. 3.7 and Table 3.2).

To estimate the dark matter mass of this structure, we first calculated the total stellar mass of all the galaxies within 50″ of AGS24 and then determined an upper limit of M_h=$10^{15.0}\,M_\odot$ to the dark matter mass based on the relation in Behroozi et al. (2013), assuming that this structure is already virialized. We also determined a lower limit of M_h=$10^{13.3}\,M_\odot$ by summing up the individual halo masses of the each galaxy within 50″ of AGS24.

We note that the projected number density profile of the galaxies in the structure do not follow the slope expected for the NFW profile (Navarro et al., 1996) of a gravitationally bound cluster, but instead exhibit a shallow slope (Fig. 3.13). We show for comparison the projected number density profile of the most distant galaxy cluster to our knowledge, CL J1001+0220 at $z = 2.506$ (Wang et al., 2016a).

However, the structure shown in the density map (Fig. 3.11), as well as the fact that AGS24 is the most massive galaxy which falls at the density peak and has a reduced SFR compared to MS galaxies, suggests that this structure is in the process of viralization and that such an environment is influencing the evolution of AGS24, diminishing its star formation activity. Galaxies like AGS24 have been missed by previous studies given their dusty nature, despite being the most massive candidate galaxies that can be used as a beacon to trace the barycenter of the proto-clusters in the process of virialization.

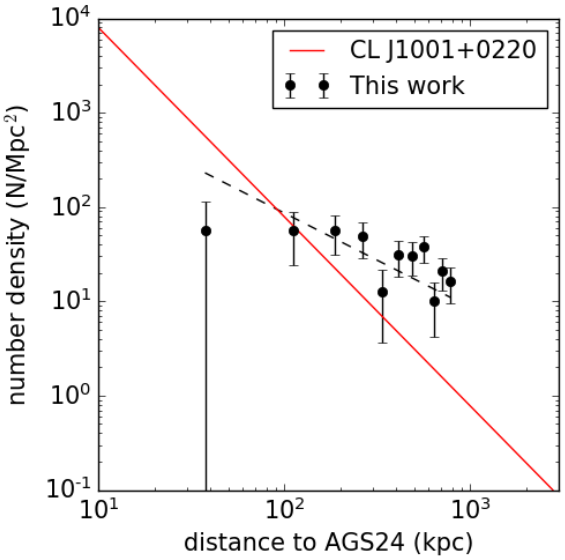

Fig. 3.13: Projected numbers of galaxies in the over-density as a function of their distance to AGS24 (black circles) and the black dashed line is the linear fitting to the profile. The red line shows the best-fit projected NFW profile (Navarro et al., 1996) of a galaxy cluster at $z = 2.506$, CL J1001+0220 (Wang et al., 2016a).

3.6 Conclusions

We have analyzed the properties of an ensemble of six optically dark galaxies, AGS4, 11, 15, 17, 24 and 25 identified in the GOODS-ALMA survey. They do not have optical counterparts in the deepest H-band based catalog down to $H = 28.16$ AB.

Out of the six sources initially classified as optically dark, a careful analysis revealed that two were associated with an H-band counterpart that was not identified in the H-band catalog missed due to blending. AGS4 and AGS15, that were identified as optically dark in F18, are extremely close to a bright optical source at 0.″50 and 0.″27 respectively, and as such they were wrongly considered as parts of the bright neighbor. However we showed that their SED can be used to perform a spectral de-confusion of the sources at very different redshifts. We note that the H-band magnitude of these galaxies is extremely faint since it is 25.2 AB and 27.1 AB for AGS4 and AGS15 respectively. The second one is below the detection limit of most H-band images. The definition of HST-dark or optically-dark is obviously a function of the depth of the HST images. All of six sources except AGS24 do exhibit a counterpart in the K_s-band image but they were mistakenly associated with a bright neighbor, hence none was listed in the ZFOURGE catalog.

We performed a spectroscopic scan follow-up of five of them with ALMA (AGS4, 11, 15, 17 and 24). All five exhibit a clear 2 mm counterpart in the continuum with $S/N = 14.7$, 16.8, 15.3, 15.9 and 8.7 respectively, which reinforces their robustness. We detected one emission line for AGS4 ($\nu_{obs} = 151.44$ GHz with a $S/N = 8.58$) and for AGS17 ($\nu_{obs} = 154.78$ GHz with a $S/N = 10.23$). Taking into consideration the PDF of the photometric redshifts derived from the optical to near-infrared SEDs and the far-infrared SEDs as well as the infrared luminosities, we conclude that the spectroscopic redshifts of the two galaxies match the CO(6-5) transition and are $z_{spec}^{\rm AGS4} = 3.556$ and $z_{spec}^{\rm AGS17} = 3.467$.

Existing spectroscopic confirmation of optically dark sources have been so far limited to a few sources, e.g., $z = 5.183$: Walter et al. (2012); $z = 3.717$: Schreiber et al. (2018); $z = 3.097$ & 5.113: Wang et al. (2019).

Close to 70 % (4/6) of the optically-dark galaxies reside in an over-density of galaxies at $z \sim 3.5$ (AGS11, 15, 17 and 24, Fig. 3.11). In Wang et al. (2019), the HST-dark galaxies exhibit a highly heterogeneous spatial distribution illustrated by their strong clustering measured by the cross-correlation functions. This is consistent with the present finding of a strong association of most of the blindly detected optically-dark galaxies in GOODS-ALMA of four out of six galaxies located in the same proto-cluster. In addition, the redshifts of these galaxies are all consistent with this over-density (Table. 3.1), indicating that these galaxies are tracing a galaxy cluster in formation.

We also notice that AGS24 is not only in the barycenter of the structure at $z \sim 3.5$ but also the most massive galaxy in this structure ($M_\star = 10^{11.32^{+0.02}_{-0.19}}$ $M_\odot$), suggesting that AGS24 is a candidate BCG in formation. In fact, AGS24 is the most massive galaxy without an AGN at $z > 3$ in the GOODS-ALMA field. Compared to the other five optically dark galaxies with high starburstness, AGS24 is the only main sequence galaxy (Table 3.1) indicating that it is influenced by the environment it resides in. The fact that AGS24 is a is a candidate BCG also indicates that the proto-cluster is in the process of virialization.

4 Extremely weak CO emission in IZw 18

Local metal-poor galaxies are ideal analogs of primordial galaxies with interstellar medium (ISM) barely enriched with metals. However, it is unclear whether carbon monoxide remains to be a good tracer and coolant of molecular gas at low metallicity.

Based on the observation with the upgraded NOEMA Interferometer, I report in this chapter an upper limit of CO J=2-1 emission in IZw18, pushing down the detection limit to be $L'_{\mathrm{CO}(2-1)} < 7.64 \times 10^3\,\mathrm{K\,km\,s^{-1}\,pc^{-2}}$, ten times lower than previous studies. As one of the most metal poor galaxy, IZw18 shows extremely low CO content despite its vigorous star formation activities. Such low CO content relative to its infrared luminosity, star formation rate (SFR) and [C II] luminosity, compared to other galaxies, indicates a drastic change in the structure of the ISM at around a few percentages of Solar metallicity. Especially, the high [C II] luminosity relative to CO implies a larger molecular reservoir than the CO emitter in IZw18. I also obtain an upper limit of the 1.3 mm continuum overlapping the H I emission peak. This upper limit excludes a submilimeter excess in IZw18.

4.1 Introduction

Star formation takes place in molecular gas dominated by H_2, except perhaps for that in the early universe. However, H_2 can only be excited at a temperature above 100 K, hence it cannot be observed directly in the cold molecular gas that fuels star formation. The second most abundant molecule, CO, has been demonstrated to be a powerful tracer of the molecular clouds in galaxies, but this application becomes complicated in metal-poor environments (see Bolatto et al., 2013, for a review).

In the early Universe, first galaxies form in the primordial gas with little elements heavier than hydrogen. Observationally, at $z \gtrsim 5$, normal star-forming galaxies with star formation rates (SFRs) of ten to a few hundred solar masses per year indeed have a low dust content (Walter et al., 2012a; Capak et al., 2015), comparable to local metal-poor galaxies. Nevertheless, the predicted CO flux in these high-z galaxies is in the order of μJy and remains challenging with the state-of-the-art submilimeter array, ALMA. Detailed study on the metal-poor interstellar medium (ISM) relies on their local analogs.

Despite extensive search for CO emission in local dwarf galaxies (Leroy et al., 2007; Schruba et al., 2012; Cormier et al., 2014; Hunt et al., 2015a; Warren et al., 2015; Shi et al., 2015a), the detection rate decreases sharply in galaxies at metallicity lower than 1/5 Solar metallicity ($Z_\odot$)[1]. The extremely faint CO emission poses questions on the existence of molecular gas in such galaxies. On the other hand, CO may not be an ideal tracer of molecular gas (Grenier et al., 2005; Wolfire et al., 2010; Shi et al., 2016) in low-metallicity environments. Because of the low dust content, the radiation field in

[1] Here we adopt solar metallicity as $12 + \log(\mathrm{O/H}) = 8.7$ (Asplund et al., 2009)

metal-poor galaxies are enhanced. In this case, H_2 molecules self-shield while CO can be disscociated easily. Low CO content is then expected in metal-poor galaxies. On the other hand, exposed to the hard radiation field, CO molecules can be easily photodissociated and produce ionized carbon, [CII]. [CII] could come from ionized gas as well as neutral gas and the surface of photodissociation regions (PDRs). However, the fractions of [CII] emission from ionized gas derived from observation constraints are systematically lower than the one from simulations (Accurso et al., 2017b; Cormier et al., 2019). Hence it's still unclear if it is feasible to use [CII] to trace H_2 gas.

So far, among the galaxies below 10% $Z_\odot$, only Sextans B (7% $Z_\odot$), has a robust CO detection (Shi et al., 2016; Shi et al., 2020). The impact of low metal abundance on the star formation requires further exploration of the most metal poor galaxies. In this work, we used the upgraded NOEMA Interferometer to observe the CO J=2-1 emission in IZw18, one of the galaxies with the lowest metallicity in the local universe ($\sim$3% $Z_\odot$, Izotov and Thuan, 1999a). IZw18 is a proto-type of blue compact dwarfs located at a distance of 18.2 Mpc (Aloisi et al., 2007a). The active star formation therein (Hunt et al., 2005) indicates the presence of molecular gas. Leroy et al. (2007) obtained an upper limit of the CO(1-0) emission ($L'_{\rm CO} < 10^5$ K km s^{-1} pc^2) using the IRAM plateau de Bure interferometer, which however is not deep enough to conclude whether IZw 18 has a normal CO content relative to other physical properties. Here we put further constraints on the CO content in IZw18 by pushing down the detection limit of $L'_{\rm CO}$ by 10 times using NOEMA Interferometer after its Phase II upgrade.

4.2 Observations

The observations of IZw18 were carried out with the NOEMA Interferometer on 2017 December 24 (obs-17) and 2019 March 23 (obs-18) for a total of 16 hrs (11.6 hrs on source) with configuration D. We processed the data at IRAM/Grenoble using the `GILDAS` package. The final CO J = 2-1 datacubes of obs17, obs18 and the merge of the two, have beam sizes of $1''.83 \times 1''.60$ (obs-17), $1''.71 \times 1''.41$ (obs-18) and $1''.71 \times 1''.48$ (merged), respectively, a frequncy resolution of 0.2MHz (0.26 km s^{-1} at 230 GHz), and rms of 4.7 mJy/beam, 5.9 mJy/beam and 4.6 mJy/beam, respectively. IZw18 was entirely covered by the 22″ (FWHM) primary beam.

4.3 Results

4.3.1 CO J=2-1

We smoothed the data to a velocity resolution of 3 km s^{-1}, consistent with the CO line width found in the most metal poor galaxies in the literature (Shi et al., 2016). We found one marginal detection ($\alpha = 9^{\rm h}34^{\rm m}02^{\rm s}.00$, $\delta = 55°14'28''.81$) at the peak of the stellar emission, as indicated by the red contour superimpose on the HST V-band image (Fig. 4.1-Left). It covers an area defined by the 3-σ contour of $\sim 1''.52 \times 1''.52$, approximately the size of the synthesized beam. We plot the spectra from the merged, obs-17 and obs-18 data cubes in Fig. 4.1-Right. A spectral signal at 3-σ is seen at 46 km s^{-1}, as a tentative detection. The peak fluxes derived from the peak channels have signal-to-noise ratios of 3.47,

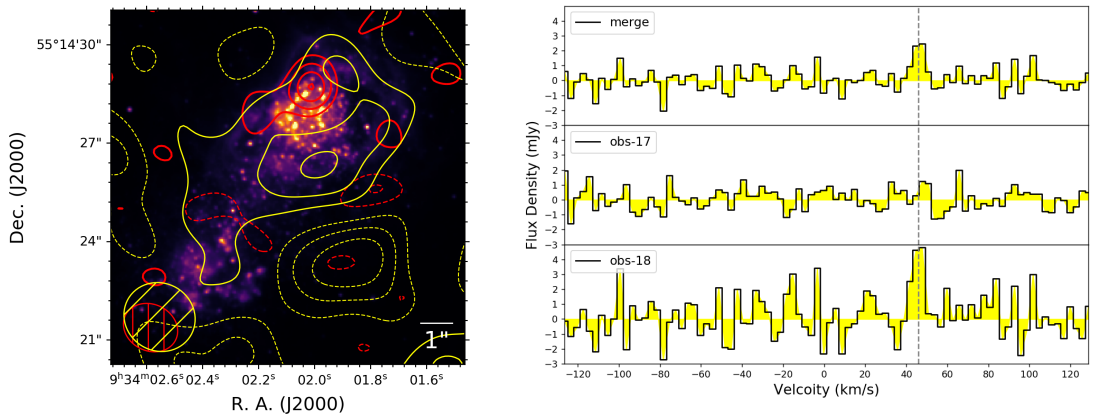

Fig. 4.1: **Left:** CO J=2-1 emission and 1.3 mm continuum superimposed on HST V-band image. The red contours denote the CO J=2-1 detection at the resolution of $1''.71 \times 1''.48$, starting from $2\,\sigma$, in increments of $1\,\sigma$ (3.3 mJy/beam) significance. The yellow contours denote the continuum detection at 1.3 mm at the resolution of $2''.21 \times 2''.06$, starting from $1\,\sigma$, in increments of $1\,\sigma$ significance (0.024 mJy/beam). Dashed contours are in negative. **Right:**The CO J=2-1 spectra with a velocity resolution of 3 km s^{-1} from the merged, obs-17 and obs18 data cubes, extracted from the area defined by the 3-σ contour as shown in Figure 4.1-Left. The $1\,\sigma$ uncertainty is 0.72, 0.72, 1.39 mJy, respectively. The grey dash line denotes the marginal detection at $\sim$46 km s^{-1}.

2.73 and 3.45 for the merged, obs-17 and obs-18 data cubes. Hereafter we use the result from the merged data cube, and treat this marginal signal as an upper limit.

The 3-σ upper limit of the CO J=2-1 flux is $S_{\mathrm{CO}(2-1)} = 2.48$ mJy and the corresponding CO luminosity is then derived to be $L'_{\mathrm{CO}(2-1)} = 7.64 \times 10^3$ K km s^{-1} pc^{-2} using the formulation of Solomon and Vanden Bout (2005). The CO emission tends to reside in small clumps as what was found in another extremely metal poor galaxy, Sextans A (Shi et al., 2020). We expect the missing diffuse emission should not contribute much to the upper limit, since most CO clumps are very compact at low metallicity conditions (Glover et al., 2010; Glover and Mac Low, 2011).

4.3.2 1.3 mm continuum

We created a continuum map after removing channels with covering emission. The continuum map is smoothed to have an angular resolution of $2''.21 \times 2''.06$ with an rms noise of 24 μJy. The peak flux of 77 μJy falls at $\alpha = 9^{\mathrm{h}}34^{\mathrm{m}}02^{\mathrm{s}}00$, $\delta = 55°14'26''.30$ which is only $\sim 1''$ from the flux peak of the HI emission of IZw18 (Lelli et al., 2012). This is the only 3σ signal within the primary beam.

4.4 Discussion

In this section, we discuss how the upper limits of the CO luminosity and the 1.3 mm continuum flux would constrain our current understanding on the star formation process in the extremely metal poor environment in IZw18.

We compare IZw18 to the star-forming regions in four extremely metal poor galaxies ($12 + \log(\mathrm{O/H}) < 8$) from Shi et al. (2015a) and Shi et al. (2016), seven metal poor dwarf galaxies from the *Herschel* Dwarf Galaxy Survey (DGS Cormier et al., 2014, compiled in), 16 nearby dwarf galaxies in Schruba et al. (2012) and nearby galaxies compiled therein, eight metal poor galaxies from Hunt et al. (2015a), local galaxies with stellar mass higher than $10^9\,M_\odot$ from the xCOLD GASS survey (Saintonge et al., 2017), and massive, infrared bright, local star-forming galaxies at Solar metallicity from Gao and Solomon (2004).

4.4.1 SED and Submilimetre excess

We first investigate the Spectral Energy Distribution (SED) of IZw18 taking into account the 3-σ upper limit at 1.3 mm. All other photometric data are taken from Hunt et al. (2015a). We performed the SED fitting with CIGALE (Noll et al., 2009) adopting a delayed star formation history, a Draine et al. (2007) dust model, which is consistent with the method used for the star-forming regions in Shi et al. (2015a) and Shi et al. (2016), and a radio component. The infrared luminosity derived from the fit is $2.2 \times 10^7\,L_\odot$, consistent with the one from Hunt et al. (2015a), the stellar mass is $4.33 \times 10^6\,M_\odot$, within the uncertainty of the stellar masses derived from stellar mass-to-light ratios at K band and R band (Fumagalli et al., 2010; Lelli et al., 2012).

We also explore the existence of the excess at submilimeter wavelengths (e.g., Galliano et al., 2003; Lisenfeld et al., 2002; Galametz et al., 2011; Rémy-Ruyer et al., 2013a) in IZw18. It does not have detections at the far-IR wavelengths longer than 160 μm. The 3σ upper limit at 1.3 mm places a strong constraint on the (sub)milimeter end of the dust emission. We fitted the far-IR SED with the modified blackbody model and derived a lower limit of the dust emissivity β to be 2.1, which suggests no submilimetre excess in IZw18.

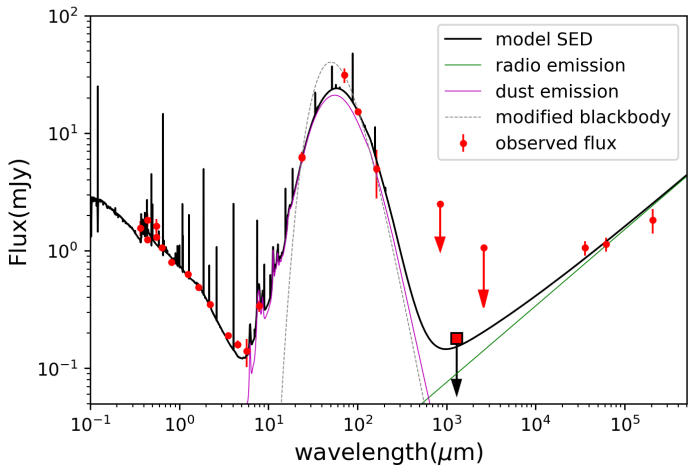

Fig. 4.2: SED of IZw18, with CIGALE best fit adopting a delayed star formation history, a Draine et al. (2007) dust model, and a radio component. A modified blackbody fit is shown with a grey dotted line. The 1.3 mm continuum 3σ upper limit is shown as in the black box.

4.4.2 Infrared luminosity and SFR versus $L'_{\rm CO}$

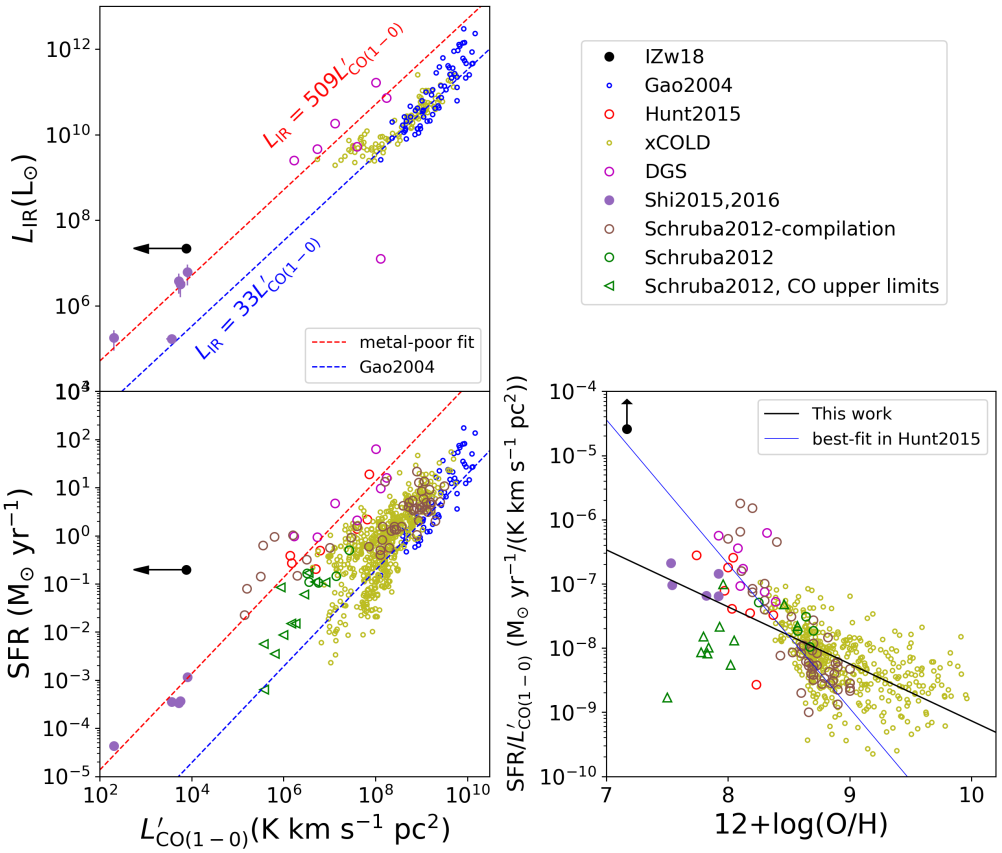

Fig. 4.3: The infrared luminosity and SFR (*Top-left*) versus $L'_{\rm CO(1-0)}$ (*Bottom-left*) as well as the SFR/$L'_{\rm CO(1-0)}$ as a function of metallicity. The upper limit of IZw18 is show as a black circle with an arrow, in comparison with the galaxies described in Section 5.4. In the two panels on the left, the blue dashed lines show the linear correlation by Gao and Solomon (2004) and the red dashed lines show the linear fit of the metal poor galaxies (Shi et al., 2015a; Shi et al., 2016; Hunt et al., 2015a; Cormier et al., 2014, DGS). In the right panel, the blue solid line denote the best fit of the metal poor galaxies in Hunt et al. (2015a) where galaxies in Schruba et al. (2012) are also included. The black solid line shows a power law fitting all the galaxies in the plot.

In Fig. 4.3, we plot the total infrared luminosity (8 – 1000 μm) versus $L'_{\rm CO(1-0)}$ and SFR versus $L'_{\rm CO(1-0)}$. These two correlations have been well estabilished in massive star-forming galaxies (e.g., Gao and Solomon, 2004) as CO molecules and $L_{\rm IR}$ trace H_2 molecular clouds and star formation in clouds, respectively. We assume optically thick and thermalized CO emission, then $L'_{\rm CO(1-0)} = L'_{\rm CO(2-1)}$. We note that CO tend to become warm and optically thin as CO is exposed to the interstellar radiation in metal poor galaxies. Schruba et al. (2012) adopted $R_{21} = 0.7$ which is the average value from HERACLES galaxies (Rosolowsky et al., 2015) for the nearby dwarf galaxies. Saintonge et al. (2011) studied the 523 galaxies in xCOLD GASS survey and gave an average value of 0.79±0.03 with larger scatter at $L'_{\rm CO(1-0)} < 10^8$ K km s^{-1} pc^2. Therefore, the choice of R_{21} may lead to the derived $L'_{\rm CO(1-0)}$ a factor of 1.4 different the one from our assumption. SFR is derived from the combination of far-UV and 24 μm emission for all the galaxies except the infrared bright galaxies for which the SFR is derived from the infrared luminosity.

Compared to star-forming galaxies at Solar metallicity, metal poor galaxies show higher $L_{\rm IR}/L'_{\rm CO(1-0)}$ and SFR/$L'_{\rm CO(1-0)}$ ratios. The $L_{\rm IR}/L'_{\rm CO(1-0)}$ ratio of metal poor galaxies is on average 15.4 times higher than the one of the massive, normal star-forming galaxies at Solar luminosity. IZw18 shows even higher $L_{\rm IR}/L'_{\rm CO(1-0)}$ and SFR/$L'_{\rm CO(1-0)}$ ratios, which are $\gtrsim$5.7 and $\gtrsim$119 times higher than those of other metal poor galaxies (Fig. 4.3-*Top left*), respectively. CO molecules are hard to form in metal poor environments because there is fewer raw material and there is little dust to protect the already scarce CO molecules from UV radiation. The higher ratios are a natural result of this. The SFR/$L'_{\rm CO(1-0)}$ ratio of metal poor galaxies increases as the metallicity decreases (Fig. 4.3-*Bottom right*). Hunt et al. (2015a) found a significant correlation when fitting their dwarf galaxies, detections in Schruba et al. (2012) and the compilation therein. However, when including all galaxies in the regression and comparing with IZw 18, we see a shallower trend, especially in the star-forming in the extremely metal poor galaxies (Shi et al., 2015a; Shi et al., 2016), we see a shallower trend. On the other hand, the SFR/$L'_{\rm CO(1-0)}$ ratio of IZw18, which is at 12 + log(O/H) = 7.17 (Izotov and Thuan, 1999a), increases dramatically and does not follow the trend defined by the other galaxies. This suggests a drastic change in the CO distribution/content of galaxies at a few percentages of Solar metallicity.

SFR and $L'_{\rm CO(1-0)}$ can be derived from observations, but the molecular gas mass, $M_{\rm H_2} = \alpha_{\rm CO} \times L'_{\rm CO(1-0)}$, is the key quantity of interest. The observed SFR/$L'_{\rm CO(1-0)}$ ratio is related to both the depletion time ($\tau_{\rm dep}$) and the CO-to-H_2 conversion factor ($\alpha_{\rm CO}$) as SFR/$L'_{\rm CO(1-0)}$ = SFR/($M_{\rm H_2}/\alpha_{\rm CO}$) = $\alpha_{\rm CO}/\tau_{\rm dep}$. Many studies have shown that $\alpha_{\rm CO}$ increases rapidly as low metallcity theoretically and observationally (Israel, 1997; Glover and Mac Low, 2011; Leroy et al., 2011; Narayanan et al., 2012; Elmegreen et al., 2013; Shi et al., 2016). If $\tau_{\rm dep}$ is constant as is found for the nearby disk galaxies (Leroy et al., 2008b; Bigiel et al., 2011), then the dependence of SFR/$L'_{\rm CO(1-0)}$ ratio on metallicity is the direct consequence of the variation of $\alpha_{\rm CO}$. However, $\tau_{\rm dep}$ in dwarf galaxies remains uncertain and tends to be longer at lower mass and at lower specific SFR (sSFR; Saintonge et al., 2011; Shi et al., 2014a). IZw18, as a dwarf galaxy with low sSFR, is likely to have higher $\tau_{\rm dep}$. This, together with the high SFR/$L'_{\rm CO(1-0)}$ ratio of IZw18, would lead to an even higher $\alpha_{\rm CO}$, as $\alpha_{\rm CO} = \tau_{\rm dep} \times \frac{\rm SFR}{L'_{\rm CO(1-0)}}$. Further constraints on the conversion factor ($\alpha_{\rm CO}$) is beyond the scope of this paper.

4.4.3 The structure of the interstellar medium

Bolatto et al. (1999) and Röllig et al. (2006) modeled the photodissociation regions (PDRs) and found that as the [CII] regions expand at low metallicity, the $L_{\rm [CII]}/L_{\rm CO(1-0)}$ ratio increases, which is confirmed in observations (Madden, 2000; Cormier et al., 2014). Cormier et al. (2015) detected the bright [CII] emission in IZw18. We plot $L_{\rm [CII]}/L_{\rm CO(1-0)}$ ratio as a function of metallicity and specific SFR in Fig. 4.4. IZw18 generally follows the trend defined by the DGS and xCOLD galaxies but shows ratios several times higher than the prediction of the regression fits. Cormier et al. (2019) modeled the mid and far-IR emission of the DGS galaxies and found that the covering factor of PDRs decreases at decreasing metallicity which indicates an increase of the ISM porosity. Then the extreme case of IZw18 reinforces the drastic change of the structure of the ISM in systems at a few percentages of Solar metallicity and may have similar implications for such systems in the early Universe.

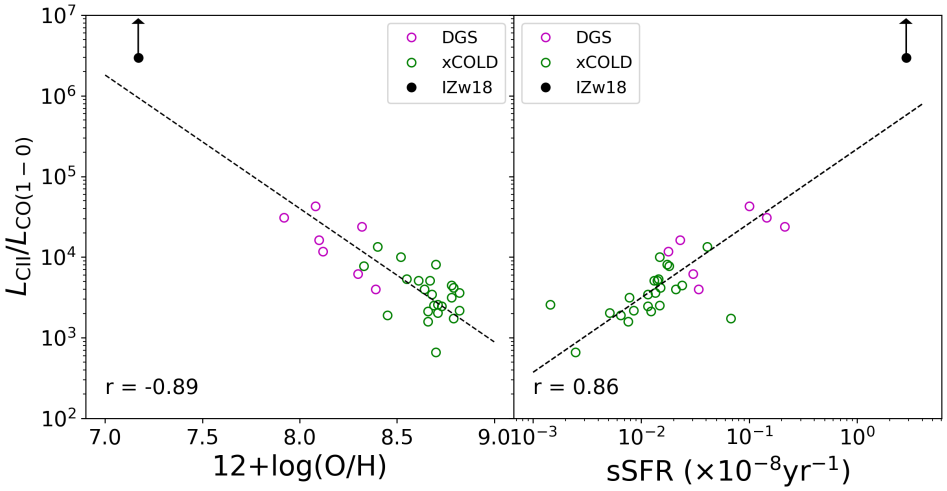

Fig. 4.4: $L_{\rm CII}/L_{\rm CO(1-0)}$ ratio as a function of metallicity (*Left*) and specific SFR (*Right*). The Pearson correlation coefficients of the regression fits are shown in the bottom left corners in each panel.

4.5 Conclusion

In this letter, we report an upper limit of CO J=2-1 in IZw18, using the observation from NOEMA Interferometer after its Phase II upgrade. We push down the detection limit of $L'_{\rm CO}$ to be $L'_{\rm CO(2-1)} < 7.64 \times 10^3$ K km s^{-1} pc^{-2}, ten times lower than that of Leroy et al. (2007). As one of the most metal poor galaxy, IZw18 shows $L_{\rm IR}/L'_{\rm CO(1-0)}$ and SFR/$L'_{\rm CO(1-0)}$ ratios much higher than those of galaxies with higher metal abundance. Particularly, the SFR/$L'_{\rm CO(1-0)}$ constraints the CO-to-H_2 conversion factor to rise considerably at metallicity lower than 5% $Z_\odot$. The high $L_{\rm [CII]}/L_{\rm CO(1-0)}$ ratio indicates a drastic change in the structure of the extremely metal-poor ISM of IZw18. An upper limit of the continuum emission at 1.3 mm is also obtained to constrain the Rayleigh Jeans tail of the SED and a submilimeter excess in IZw18 is excluded.

5

The SAMI Galaxy Survey: energy sources of the turbulent velocity dispersion in spatially-resolved local star-forming galaxies

In this chapter, I investigate the energy sources of random turbulent motions of ionised gas from Hα emission in eight local star-forming galaxies from the Sydney-AAO Multi-object Integral field spectrograph (SAMI) Galaxy Survey. These galaxies satisfy strict pure star-forming selection criteria to avoid contamination from active galactic nuclei (AGN) or strong shocks/outflows. Using the relatively high spatial and spectral resolution of SAMI, we find that – on sub-kpc scales our galaxies display a flat distribution of ionised gas velocity dispersion as a function of star formation rate (SFR) surface density. A major fraction of our SAMI galaxies shows higher velocity dispersion than predictions by feedback-driven models, especially at the low SFR surface density end. Our results suggest that additional sources beyond star formation feedback contribute to driving random motions of the interstellar medium (ISM) in star-forming galaxies.

5.1 Introduction

The kinematics, structure and star formation activity of a galaxy depend on a combination of complex physical processes such as gravity, turbulence, magnetic fields, radiation, heating/cooling, feedback, accretion, operating both interior to and exterior to the galaxy. The relative importance of these processes is expected to depend on cosmic evolution and galactic environment. Galaxies at different cosmic epochs show quite distinct properties. Compared to their high-redshift counterparts at similar stellar masses, local star-forming galaxies are larger, and have relatively lower gas fractions and lower SFRs (Leroy et al., 2005; Daddi et al., 2010a; Tacconi et al., 2010; Madau and Dickinson, 2014). They are also less likely to experience violent events such as major mergers and gas accretion (Baugh et al., 1996; Genzel et al., 2008; Robotham et al., 2014).

Many theoretical and observational studies suggest that gas in higher redshift galaxies has larger random motions compared to gas in low-redshift galaxies (Nesvadba et al., 2006; Lehnert et al., 2009; Lehnert et al., 2013; Förster Schreiber et al., 2009; Wisnioski et al., 2015). These random, turbulent motions may play a crucial role in regulating the formation of stars (Green et al., 2010; Federrath and Klessen, 2012; Padoan et al., 2014). However, the origin and energy source of the turbulence remains poorly understood. External mechanisms like gas accretion from the intergalactic medium and minor mergers (Glazebrook, 2013), and internal mechanisms such as star formation feedback

(stellar winds, supernovae), cloud-cloud collisions in the disc (Tasker and Tan, 2009), the release of gravitational energy via accretion of cold gas streams from the halo or the inspiral of clumps (Klessen and Hennebelle, 2010), galactic shear from the differential rotation in disc galaxies (Krumholz and Burkhart, 2015), spiral-arms shocks in spiral galaxies (Tamburro et al., 2009) and others can poteintially drive such turbulence (Mac Low and Klessen, 2004; Elmegreen, 2009; Federrath et al., 2016; Federrath et al., 2017).

Several studies have been carried out to explore the energetic drivers of the turbulence in both high and low redshift disc galaxies, e.g., Elmegreen and Scalo (2004), Scalo and Elmegreen (2004), Tamburro et al. (2009), and Gritschneder et al. (2009). Green et al. (2014) found that the gas velocity dispersion increases with SFR in star-forming galaxies both locally and at high redshift. Based on observations and analytic considerations, Lehnert et al. (2009) and Lehnert et al. (2013) speculated that there is a relation between velocity dispersion and SFR surface density ($\Sigma_{\rm SFR}$) in active star-forming galaxies at $z \sim 1$–3, and that it is the intense star formation that supports the high velocity dispersion and thus balances the gravitational pressure. In contrast, Genzel et al. (2011) found that the velocity dispersion correlates only weakly with $\Sigma_{\rm SFR}$ in their study of giant star-forming clumps in five galaxies at $z \sim 2$ together with other rotation-dominant star-forming galaxies, lensed galaxies, and dispersion-dominated galaxies at $z \sim 2$. They suggest that a large-scale release of gravitational energy could induce the global large random motions in high-redshift galaxies, and that local star formation feedback triggering outflows and stirring up the interstellar medium (ISM) drives the local variation of turbulent, random motions.

Spatially resolved information is vital to understand the details of the physical processes that drive different interactions within galaxies. The three-dimensional (3D) spectra of galaxies uncover the distribution of the physical properties and give clues to how the internal physical processes shape the galaxies by connecting the spectral information with its position in the galaxy. Integral field spectroscopy (IFS) enables us to obtain this crucial spatial information. More importantly, IFS gives us both spectral and kinematic information; i.e., the intensity-weighted gas velocity and velocity dispersion along the line of sight. Taking advantage of this, IFS surveys such as the Calar Alto Legacy Integral Field Area Survey (CALIFA; Sánchez et al., 2012), the SAMI Survey (Croom et al., 2012; Bryant et al., 2015), and the Mapping Nearby Galaxies at Apache Point Observatory (MaNGA) Survey (Bundy et al., 2015) have made significant progress in this area. SAMI has a higher instrumental resolution σ = 29 km s^{-1} at 6250 – 7350 Å (Sharp et al., 2015) than the other IFS surveys mentioned above, which have instrumental resolution > 80 km s^{-1} at a similar wavelength range (Sánchez, 2015). In this work we investigate the properties of the ISM in star-forming galaxies using data from the SAMI Galaxy Survey. We measure maps of $\Sigma_{\rm SFR}$ and gas velocity dispersion, and use these maps to derive the relation between $\Sigma_{\rm SFR}$ and gas velocity dispersion. We further include $\Sigma_{\rm SFR}$ and velocity dispersion data from the literature, and determine the dependence of velocity dispersion on redshift, up to $z \sim 3$.

Section 5.2 presents the sample selection criteria and data reduction including the signal-to-noise ratio criteria, the data source and their reduction strategy, and the estimation of the magnitude of beam smearing effect. In Section 5.3, our results and comparison with high-redshift and Hα luminous local star-forming galaxies are presented. We further discuss the main source(s) of the turbulence in star-forming galaxies in Section 5.4. Section 5.5 summarzies the conclusions of this work. A standard cosmology of H_0 = 70 km s^{-1} Mpc^{-1}, $\Omega_{\rm m}$ = 0.3, Ω_Λ = 0.7 is assumed throughout.

Tab. 5.1: Red and blue data cubes from LZIFU.

data cube	$\lambda^{\dagger}$	R‡	σ^{*}
Blue	3700 – 5700 Å	1730	74 km s^{-1}
Red	6250 – 7350 Å	4500	29 km s^{-1}

† Wavelength range.
‡ Spectral resolution. Full width half maximum (FWHM) = c/R.
* Velocity resolution according to spectral resolution.

5.2 Sample and data analysis

5.2.1 Sample selection

5.2.1.1 The SAMI Galaxy Survey

We use the SAMI Galaxy Survey (Croom et al., 2012) to select local star-forming galaxies. The SAMI Survey will observe in total $\sim$ 3400 galaxies. It covers a broad range of galaxies in stellar mass and environment. The sample targets redshifts 0.004 – 0.095, Petrosian magnitudes $r_{\rm pet}$ < 19.4 [1], stellar masses 10^7 – 10^{12} $M_{\odot}$ and environments from isolated field galaxies through group galaxies to cluster galaxies (Bryant et al., 2015; Owers et al., 2017).

SAMI is mounted at the prime focus on the Anglo-Australian Telescope. It has a 1 degree diameter field of view and uses 13 fused fibre bundles (Hexabundles, Bland-Hawthorn et al., 2011; Bryant et al., 2014) with a high (75%) fill factor. Each of the bundles contains 61 fibres of 1.6 arcsec diameter which results in diameter of 15 arcsec in each integral field unit (IFU). The IFUs, together with 26 sky fibres, are inserted into pre-drilled plates using magnetic connectors. SAMI fibres are fed to the double-beam AAOmega spectrograph (Sharp et al., 2006). AAOmega provides a range of different resolutions and wavelength ranges. For the SAMI Galaxy Survey, the 570V grating at 3700 – 5700 Å is used to give a resolution of R = 1730 (σ = 74 km s^{-1}), and the R1000 grating from 6250 – 7350 Å for a resolution of R = 4500 (σ = 29 km s^{-1}) (Table 5.1) (Sharp et al., 2015). Therefore, each SAMI object has one blue and one red data cube. Early reduced datacubes are included in the first public data release (Allen et al., 2015, Green et al. in prep.). All datacubes are constructed on spatial grids where each grid cell has a size of $0.5\,\mathrm{arcsec} \times 0.5\,\mathrm{arcsec}$ corresponding to a physical scale of $\sim$ 0.5 $\times$ 0.5 kpc^2 for our sample of local star-forming galaxies ($z \sim 0.05$). Note that the spatial resolution of SAMI data is determined by the average seeing in observations ($\sim 2.5\mathrm{arcsec}$), corresponding to a physical scale of 2.5 kpc (z $\sim$ 0.05).

The spectral fitting pipeline of SAMI galaxies, LZIFU (Ho et al., 2014; Ho et al., 2016), is designed to extract two-dimensional emission line flux maps and kinematic maps to investigate the dynamics of gas in galaxies. LZIFU uses up to three Gaussian profiles to fit emission lines, separating up to three different kinematic components contributing to the emission lines.

Maps of SFR and SFR surface density (Medling et al., 2018) are also available in the SAMI database. Briefly, these maps are calculated from extinction-corrected Hα flux maps using the calibration in

[1] Extinction-corrected SDSS DR7 Petrosian mag.

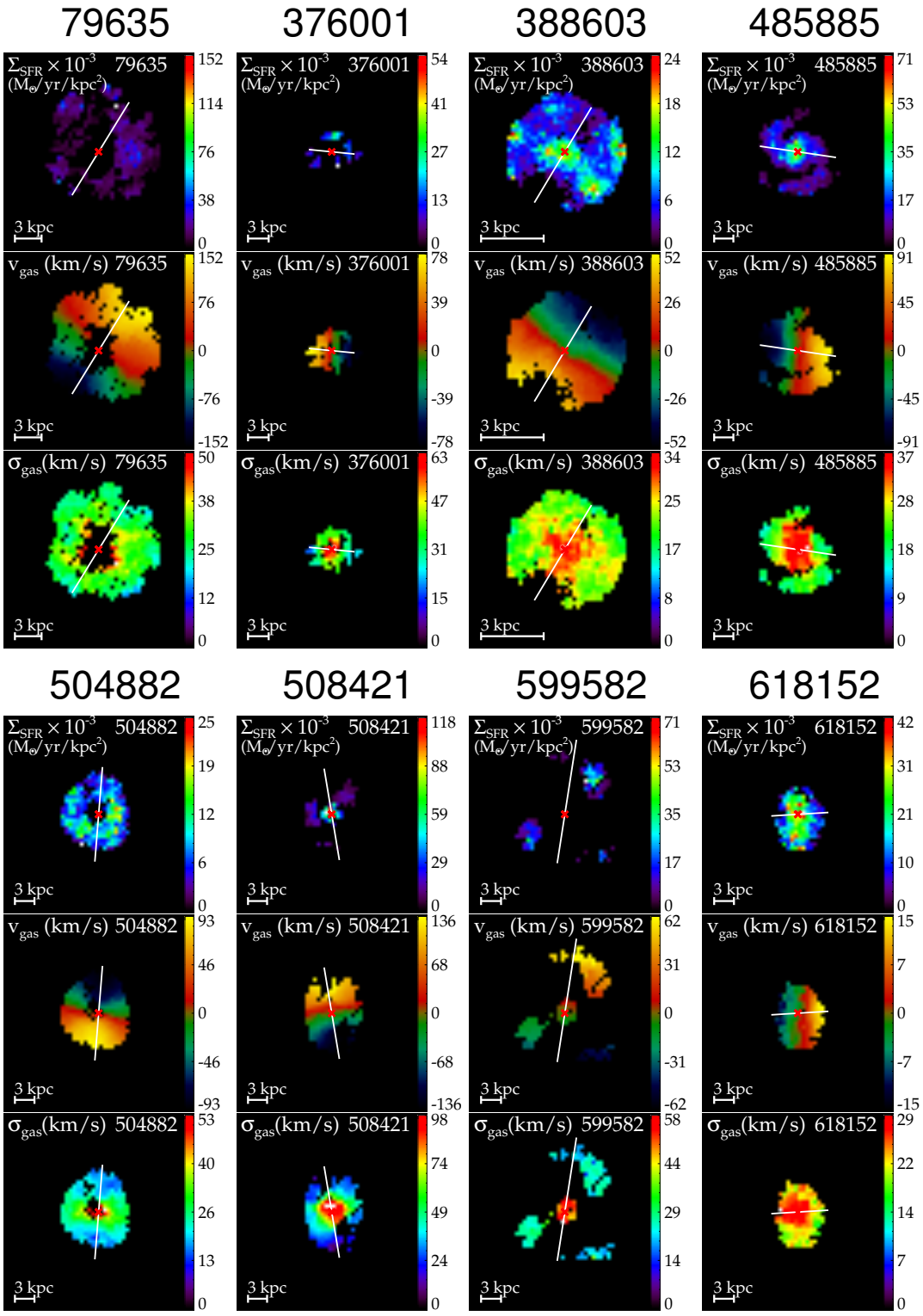

Fig. 5.1: Images of different components of each galaxy. Top: SFR surface density (extinction corrected) in $M_\odot$ yr^{-1} kpc^{-2}. Middle: ionised gas velocity in km s^{-1}. Bottom: ionised gas velocity dispersion in km s^{-1}. In all images, we only display spaxels with S/N > 34 (see Section 5.2.2.2 for the choice of S/N). The red crosses are the centres of the galaxies. The white solid lines are the major axes (see Section 5.2.2.1).

Tab. 5.2: Properties of the eight star-forming galaxies in our final sample of star-forming SAMI galaxies.

CATID	RA	DEC	redshift	stellar mass[1]	radius[2]		ellip[3]	i[4]	$\sigma_{\rm gas}$[5]	$\Sigma_{\rm SFR}$[6]
	[hh: mm: ss]	[dd: mm: ss]		[$M_\odot$]	[arcsec]	[kpc]		[°]	[km s^{-1}]	[$M_\odot$ yr^{-1} kpc^{-2}]
79635	14 50 03.3	00 05 51.0	0.040	2.9×10^{10}	9.13	7.8	0.40	55.0	28 ± 4	0.019 ± 0.009
376001	08 46 31.3	01 29 00.0	0.051	1.8×10^{10}	2.41	2.7	0.07	22.4	31 ± 9	0.022 ± 0.007
388603	09 23 08.1	02 29 09.9	0.017	6.3×10^{9}	14.3	5.2	0.12	28.6	24 ± 4	0.009 ± 0.003
485885	14 31 01.9	-01 43 02.0	0.055	1.8×10^{10}	5.04	6.0	0.16	33.6	24 ± 4	0.014 ± 0.005
504882	14 30 15.3	-01 55 56.2	0.054	1.3×10^{10}	3.80	4.4	0.19	37.0	20 ± 2	0.010 ± 0.003
508421	14 27 57.4	-01 37 52.3	0.055	2.5×10^{10}	3.74	4.5	0.26	43.0	87 ± 44	0.076 ± 0.016
599582	08 48 45.6	00 17 29.5	0.053	6.2×10^{10}	9.60	11	0.32	48.6	26 ± 5	0.020 ± 0.009
618152	14 18 05.5	00 13 38.6	0.053	1.0×10^{10}	3.56	4.1	0.29	46.1	24 ± 3	0.023 ± 0.010

[1] Stellar masses are from the GAMA survey (Taylor et al., 2011).
[2] Effective radius, i.e., half light radius, also from the GAMA survey (Kelvin et al., 2012).
[3] Ellipticity is from the GAMA survey (http://www.gama-survey.org/dr2/tools/sov.php). We use the GAL_ELLIP_R to get the R-band axis ratio. The relation between minor-to-major axis ratio and ellipticity is: *b/a* = 1 - ellipticity.
[4] Inclination angle. The calculation is based on classical Hubble formula: $\cos^2 i = ((b/a)^2 - q_0^2)/(1 - q_0^2))^{1/2}$, where *b/a* is the minor-to-major axis ratio, *i* is the inclination angle and q_0 = 0.2 (i = 90° for $b/a < q_0$).
[5] Flux weighted global gas velocity dispersion. Only the pixels with $\sigma_{\rm gas} > 2\ v_{\rm grad}$ are considered (see more in Section 5.2.2.3).
[6] Flux weighted SFR surface density. Only the pixels with $\sigma_{\rm gas} > 2\ v_{\rm grad}$ are considered (see more in Section 5.2.2.3).

Kennicutt et al. (1994). Extinction corrections are calculated using the Balmer decrement, and flux is converted to luminosity using distances calculated from the flow-corrected redshifts of the GAMA Survey Catalog (Baldry et al., 2012).

5.2.1.2 Our sample

To select star-forming galaxies from the parent SAMI sample, we use optical emission line diagnostic diagrams, so-called 'BPT/VO' diagrams (Baldwin et al., 1981; Veilleux and Osterbrock, 1987) with multi-component emission line fits. In the following analysis of the chosen star-forming galaxies, we use single component fits, which are sufficient to describe star-forming galaxies. In the most conservative way, we select those galaxies with all detected spaxels lying below the theoretical extreme starburst lines in all the three BPT/VO87 diagrams, i.e., [NII]λ6583/Hα *vs.* [OIII]λ5007/Hβ, [SII]λ6717,λ6731/Hα *vs.* [OI]λ6300/Hβ and [NII]λ6583/Hα *vs.* [OIII]λ5007/Hβ (Baldwin et al., 1981; Veilleux and Osterbrock, 1987; Kewley et al., 2001). Thus we minimise the contamination of AGNs, outflows, and shock contamination. We note that there are a few spaxels with elevated non-thermal-ratios suggestive of shocks in 508421. Because these spaxels are few in numbers and lie below the theoretical extreme starburst lines in all the three BPT/VO diagrams, we still keep this galaxy.

We find that eight out of 756 SAMI galaxies satisfy our complete selection criteria. By the time of this work, 756 of the 3400 SAMI galaxies have had reduced data cubes available with the required analysis products. We find 22 star-forming galaxies meeting the criteria, but 11 of them are cluster galaxies which may be influenced by their environments. We choose not to discuss cluster galaxies, in order to focus on turbulence induced locally through accretion and/or galaxy-internal processes such as star formation feedback. Among the remaining 11 galaxies, two lack the information of stellar velocity dispersion (van de Sande et al., 2017, this will be relevant for a follow-up paper to determine the Toomre Q and that we want to use the same set of eight galaxies for this and the follow-up paper) and another lacks enough spaxels with high enough signal-to-noise ratio. Table 6.1 lists the basic information of the eight galaxies in our final sample. Our eight star-forming galaxies are at redshifts ranging from 0.017 to 0.055, most of them at the high end. Their stellar masses range from 6.3 $\times 10^9$

$M_\odot$ to 6.2 $\times 10^{10}$ $M_\odot$ and the median stellar mass is 2.5 $\times 10^{10}$ $M_\odot$, similar to most of the galaxies in SAMI sample (Bryant et al., 2015).

5.2.2 Gas kinematic information

5.2.2.1 Definition of the major axis

To define the major axis, we first define the centre of each galaxy as the centre of each datacube. We note that this is consistent with the photometric and kinematic centres of each galaxy in our sample. The major axis of each galaxy is determined based on the velocity field of the galaxy. The centre velocity ($v_{\rm centre}$) of each galaxy is measured by averaging the central four pixels; gas velocity is given as: $v_{\rm gas} = v - v_{\rm centre}$.

5.2.2.2 Velocity and Velocity dispersion

Ionised gas velocity ($v_{\rm gas}$) and gas velocity dispersion ($\sigma_{\rm gas}$) are measured from the emission lines by the LZIFU pipeline. The velocity dispersions in the datacubes have removed instrument resolutions, i.e., $\sigma_{\rm gas} = (\sigma^2_{\rm obs} - \sigma^2_{\rm instr})^{1/2}$, where $\sigma_{\rm instr}$ is the instrumental velocity dispersion and $\sigma_{\rm obs}$ is the observed velocity dispersion). We emphasise that the error of the line width can be underestimated because of the limitation of the instrument resolution. Thus we make an estimation of the lower limit of the reliable velocity dispersion. Given that $\sigma_{\rm instr}$ = 29 km $\rm s^{-1}$ (assuming the instrument resolution for the Hα line is fixed and exactly 29 km $\rm s^{-1}$), if we want to resolve an intrinsic velocity dispersion of 12 km $\rm s^{-1}$ with signal to noise ratio (S/N) of 5 (i.e., $(S/N)_{\rm true} \equiv \frac{\sigma_{\rm gas}}{d\sigma_{\rm gas}}$ = 5, $\sigma_{\rm gas}$ is the intrinsic velocity dispersion in the datacubes), then we can derive:

$$\sigma^2_{\rm gas} = \sigma^2_{\rm obs} - \sigma^2_{\rm instr};$$
$$\mathrm{d}\sigma^2_{\rm gas} = \mathrm{d}\sigma^2_{\rm obs} - \mathrm{d}\sigma^2_{\rm instr}\,,$$
$$(\mathrm{d}\sigma^2_{\rm instr} = 2\mathrm{d}\sigma_{\rm instr} = 0\,,\ \sigma_{\rm instr} = 29\ \mathrm{km\ s^{-1}});$$
$$2\sigma_{\rm gas}\mathrm{d}\sigma_{\rm gas} = 2\sigma_{\rm obs}\mathrm{d}\sigma_{\rm obs};$$
$$\text{dividing both sides with } \sigma^2_{\rm gas}:$$
$$\frac{\mathrm{d}\sigma_{\rm gas}}{\sigma_{\rm gas}} = \frac{\mathrm{d}\sigma_{\rm obs}}{\sigma_{\rm obs}}\,\frac{\sigma^2_{\rm obs}}{\sigma^2_{\rm gas}};$$
$$\text{rearranging this equation and substituting } \sigma^2_{\rm obs} \text{ with } \sigma^2_{\rm gas} + \sigma^2_{\rm instr}:$$
$$\frac{\sigma^2_{\rm obs}}{\sigma^2_{\rm gas}} = \frac{\sigma^2_{\rm gas} + \sigma^2_{\rm instr}}{\sigma^2_{\rm gas}} = \frac{\sigma_{\rm obs}}{\mathrm{d}\sigma_{\rm obs}} \Big/ \frac{\sigma_{\rm gas}}{\mathrm{d}\sigma_{\rm gas}} \equiv \frac{(\mathrm{S/N})_{\rm obs}}{(\mathrm{S/N})_{\rm true}};$$
$$\frac{\sigma_{\rm obs}}{\mathrm{d}\sigma_{\rm obs}} = \frac{\sigma_{\rm gas}}{\mathrm{d}\sigma_{\rm gas}}\left(\frac{\sigma^2_{\rm instr}}{\sigma^2_{\rm gas}} + 1\right),\ \text{i.e.,}$$
$$(\mathrm{S/N})_{\rm obs} = (\mathrm{S/N})_{\rm true}\left(\frac{\sigma^2_{\rm instr}}{\sigma^2_{\rm gas}} + 1\right) = 5 \times \left(\frac{29^2}{12^2} + 1\right) = 34.$$

Then observed emission line S/N needs to be 34, i.e., $(S/N)_{\rm obs} \equiv \frac{\sigma_{\rm obs}}{d\sigma_{\rm obs}}$ = 34. This criterion translates to a measured velocity dispersion S/N cut that depends on velocity dispersion: $(S/N)_{\rm true}$ = $(S/N)_{\rm obs}$ /

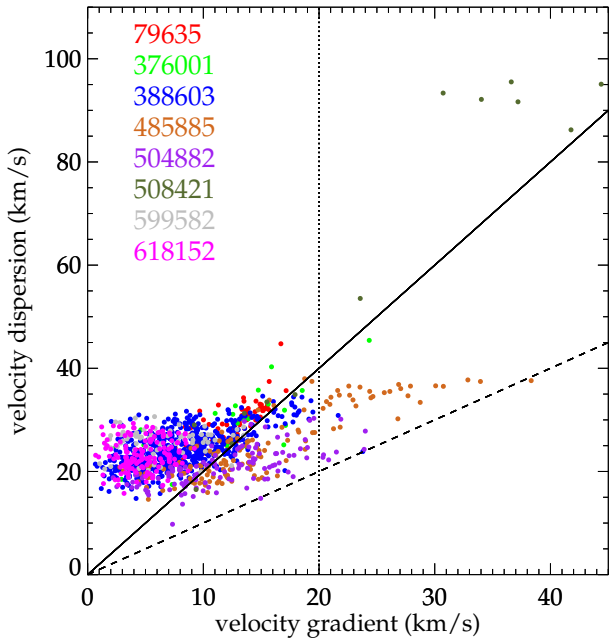

Fig. 5.2: Dependence of gas velocity dispersion ($\sigma_{\rm gas}$) on velocity gradient ($v_{\rm grad}$, Equation 5.1). Points in each individual galaxy are labeled by colour. The solid line refers to $\sigma_{\rm gas}$ = 2 $v_{\rm grad}$ and the dashed line refers to $\sigma_{\rm gas}$ = $v_{\rm grad}$. The dotted line denotes the velocity gradient at 20 km s^{-1}. These three different lines represent the three different criteria that we tested to account for beam smearing (Section 5.2.2.3).

($\sigma^2_{\rm instr}/\sigma^2_{\rm gas}$ + 1). Therefore, in order to resolve velocity dispersion down to 12 km s^{-1} (corresponding to the thermal broadening velocity of ionised gas) with S/N > 5, we select only spaxels with S/N > 34 for velocity dispersion. Given that the velocity dispersion we are measuring is lower than the spectral resolution, we do simple Monte Carlo simulations to see if there is a systematic overestimation. The simulations test (S/N)$_{\rm obs}$ from 10 to 34 and a range of line widths between 5 km s^{-1} and 40 km s^{-1}. They confirm the scaling predicted by our very simple analytic model: indeed, in order to measure $\sigma_{\rm gas}$ (with a target intrinsic S/N) one needs a much larger S/N on the observed. Assuming a velocity sampling of 5 km/s, we obtain an excellent fit to our simple analytic formula above, i.e., a (S/N)$_{\rm obs}$ > 34 is required for 12 km s^{-1} with (S/N)$_{\rm true}$ > 5. However, the absolute S/N requirement eventually depends on the specifics of the instrument, and a separate publication fully dedicated to these Monte Carlo simulations is in preparation.

Maps of gas velocity ($v_{\rm gas}$) and gas velocity dispersion ($\sigma_{\rm gas}$) together with $\Sigma_{\rm SFR}$ are shown in Figure 5.1.

5.2.2.3 Beam smearing effect

The measured velocity dispersion may be overestimated in the presence of a velocity gradient within the scale of one beam; this is what we call beam smearing. The magnitude of beam smearing increases

with increasing local velocity gradient. We use the velocity gradient ($v_{\rm grad}$) across a spaxel (Varidel et al., 2016),

$$v_{\rm grad} = \sqrt{(v[x+1,y] - v[x-1,y])^2 + (v[x,y+1] - v[x,y-1])^2}. \quad (5.1)$$

to estimate the magnitude of the beam smearing (*x, y* are the image grid cell indices). We use the upper, lower, left and right neighbours of each spaxel to measure $v_{\rm grad}$. These 5 pixels make up the central cross in a 3 $\times$ 3 binned spaxel, which is roughly equivalent to the size of the seeing limited FWHM of $\sim$2.5$\rm arcsec$. Therefore, $v_{\rm grad}$ is indicative of the beam smearing effect within the size of the beam FWHM. A higher $v_{\rm grad}$ can indicate a larger beam smearing effect and thus a higher observed velocity dispersion. In order to account for the effect of beam smearing in the following analysis, we remove the spaxels whose line-width may have been primarily caused by a velocity gradient due to beam smearing. Note that the boundary spaxels don't have enough necessary neighbouring spaxels to calculate velocity gradient, we choose to also remove boundary spaxels.

In Figure 5.2, we show the measured velocity dispersion as a function of the velocity gradient for each spaxel and galaxy. We tried three different criteria to account for the beam smearing effect. We exclude spaxels with:

1. $v_{\rm grad}$ > 0.5 $\sigma_{\rm gas}$ (solid line),

2. $v_{\rm grad}$ > $\sigma_{\rm gas}$ (dashed line),

3. $v_{\rm grad}$ > 20 km s^{-1} (dotted line).

We find that our results do not depend on the particular choice of the beam-smearing cut. All three selection criteria yield consistent results. A flat but elevated distribution of gas velocity dispersion (see more in Section 5.3.2.1) is shown in all of the three cases. We choose to preserve only the spaxels with $\sigma_{\rm gas}$ > 2 $v_{\rm grad}$ (those above the black solid line) in the following analysis. Our method here is similar to the simple analytic calculation in Bassett et al. (2014, equation (1)).

5.2.3 Spatial resolution

We compare our sample with high redshift surveys and local Hα luminous galaxies. The data in Lehnert et al. (2013) has FWHM $\sim$0.6$\rm arcsec$ and pixel scale 0.25$\rm arcsec$ corresponding to 5 kpc and 2 kpc at $z \sim$ 2. The seeing limit of our sample is $\sim$ 2.5$\rm arcsec$ and the pixel scale is 0.5$\rm arcsec$, which correspond to 2.5 kpc and 0.5 kpc at $z \sim$ 0.05. Genzel et al. (2017) has FWHM up to 0.2$\rm arcsec$ corresponding to $\sim$ 1.5 kpc at $z \sim$ 0.76 – 2.65. Green et al. (2014) has spatial resolutions of 1 – 3 kpc. We reach similar resolutions as Genzel et al. (2011) and Green et al. (2014) and better than Lehnert et al. (2013). All the works above either construct models or use simulations to remove the beam smearing effect.

5.3 Results

We investigate the relation between $\Sigma_{\rm SFR}$ and $\sigma_{\rm gas}$ spaxel by spaxel (locally), and within individual galaxies (globally), to see if star formation drives the velocity dispersion in these local star-forming galaxies.

5.3.1 The spatial distribution of $\Sigma_{\rm SFR}$, $v_{\rm gas}$, and $\sigma_{\rm gas}$

In Figure 5.1, we show the maps of $\Sigma_{\rm SFR}$, gas velocity and gas velocity dispersion for each of our eight galaxies. The major axes and galaxy centres are labeled in the images. We see:

a) The $\Sigma_{\rm SFR}$ maps have various distributions. There are often multiple peaks and rings, and some of the peaks are not at the centre, indicating local structures such as spiral arms, star-forming clumps, etc.

b) All galaxies show clear velocity gradients indicating rotation.

c) All galaxies show a gas velocity dispersion peak at the centre.

d) The distribution of gas velocity dispersion does not always follow the distribution of $\Sigma_{\rm SFR}$ (i.e. the peaks in $\sigma_{\rm gas}$ do not always correlate with those in $\Sigma_{\rm SFR}$). This is self-consistent because regions of intense mechanical or radiative energy injections (e.g., star-forming regions) are over-pressured and compact while over-pressurized gas is over a much larger scale.

5.3.2 The $\sigma_{\rm gas}$ – $\Sigma_{\rm SFR}$ relation in local and high redshift star-forming galaxies

5.3.2.1 Local (spaxel-by-spaxel) analysis

After removing the spaxels with high $v_{\rm grad}$ (keeping those with $\sigma_{\rm gas} > 2\ v_{\rm grad}$), we compare the spatially resolved relation between $\sigma_{\rm gas}$ and $\Sigma_{\rm SFR}$ in our local galaxies with that in high redshift galaxies (Lehnert et al., 2009) in Figure 5.3. We also insert a zoom-in of our SAMI data with a logarithmic y-axis.

As shown by the filled circles, the velocity dispersion of our local star-forming galaxies is almost constant around 20 km s^{-1}, covering a $\Sigma_{\rm SFR}$ range of over an order of magnitude. As discussed in Section 5.2.2.2, SAMI is able to detect $\sigma_{\rm gas}$ below 15 km s^{-1} for a sufficiently high S/N (here 34), therefore the cut-off at $\sim$15 km s^{-1} represents a physical cut-off. The flat and tight distribution of $\sigma_{\rm gas}$ in our local star-forming galaxies does not present an obvious correlation with $\Sigma_{\rm SFR}$. There are some outliers with $\sigma_{\rm gas} > 40$ km s^{-1} that may result from a shocked component in 508421 as mentioned in Section 5.2.1.2 and 5.2.2.3.

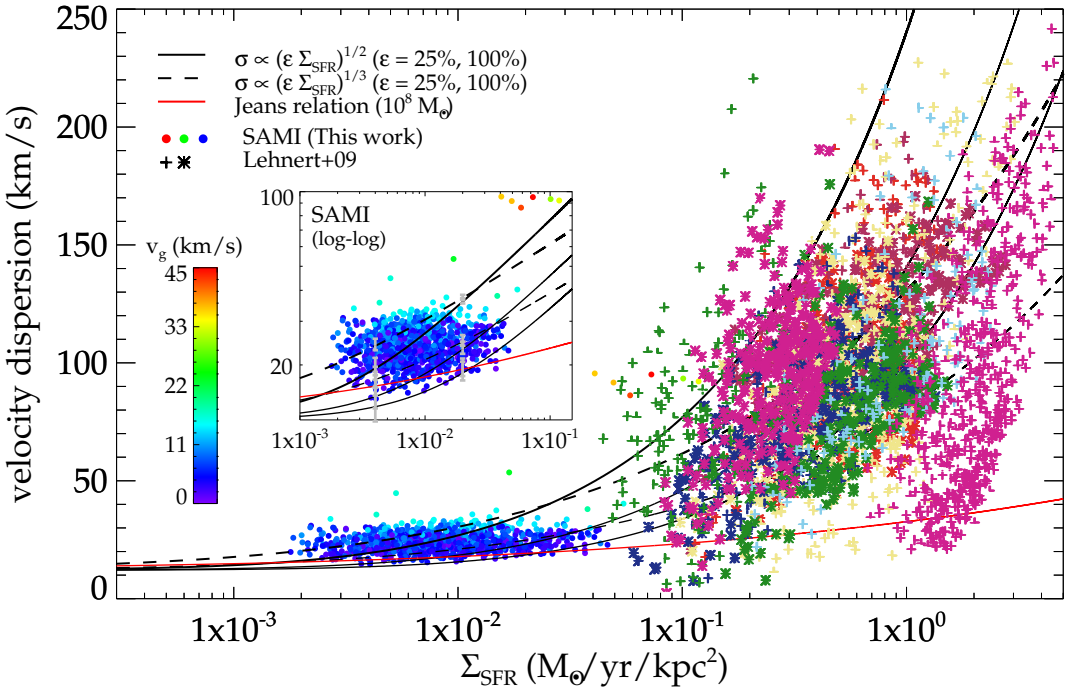

Fig. 5.3: Spatially resolved dependence of $\sigma_{\rm gas}$ on $\Sigma_{\rm SFR}$. We remove pixels with $v_{\rm grad} > 0.5\ \sigma_{\rm gas}$ to account for beam smearing effects (see Figure 5.2 and Section 5.2.2). Our eight SAMI galaxies are compared to Lehnert et al. (2009, Figure 12 therein). Each filled circle refers to one spaxel in each galaxy and is colour-coded with the magnitude of velocity gradient ($v_{\rm grad}$, Equation 5.1). The crosses and asterisks in different colours refer to the 11 actively star-forming galaxies at $z \sim 2$ in Lehnert et al. (2009). The solid black curves show $\sigma \propto (\epsilon \dot{E})^{1/2}$, where $\dot{E}$ is the energy injection due to star formation, and ϵ is the coupling efficiency of the energy injected into the ISM. The dashed curves show $\sigma \propto (\epsilon \dot{E})^{1/3}$ assuming that velocity dispersions correspond to energy dissipation due to turbulent motions. The red solid curve shows the velocity dispersion of a 10^8 $M_\odot$ clump assuming a simple Jeans relation. A zoom-in of our SAMI galaxies with a logarithmic y-axis is also shown here. All of the models have included the typical thermal broadening of Hα of 12 km s^{-1}. The error bars in the zoom-in figure show the maximum range of the thermal broadening of 10 –15 km s^{-1}. The colourbar on the left shows the magnitude of the velocity gradient (v_g).

We also connect the behaviour of the gas in star-forming galaxies from low-z to high-z by superimposing our data onto the results in Figure 12 from Lehnert et al. (2009). The crosses and asterisks in different colours refer to the 13 actively star-forming galaxies at $z \sim 2$ in Lehnert et al. (2009). The high redshift galaxies in Lehnert et al. (2009) show higher velocity dispersion with larger scatter than our local star-forming galaxies. They are also more or less positively correlated with $\Sigma_{\rm SFR}$, however, with substantial scatter. This may indicate that star formation feedback plays a more important role in high redshift star-forming galaxies than in their local counterparts. High redshift star-forming galaxies, as shown in Genzel et al. (2011) and Genzel et al. (2014), are mostly irregular and clumpy while local galaxies are stable and rotationally supported, as seen in Figure 5.1. Therefore, juvenile high redshift galaxies could be more easily affected by their intense star formation activity and mature local galaxies could be more sensitive to galactic-scale dynamics like cloud-cloud collisions, galactic shear and self-gravity than to star formation feedback. We discuss this further in Section 5.4.

Theoretical models for $\sigma_{\rm gas}$

The curves in Figure 5.3 denote different models proposed by Lehnert et al. (2009) to explain the relation between $\sigma_{\rm gas}$ and $\Sigma_{\rm SFR}$.

If the dissipated energy comes from star formation, and star formation induces high pressures, then a simple scaling relation is expected. This is indicated by the solid black curves, in the form $\sigma \propto (\epsilon \dot{E})^{1/2}$, where $\dot{E}$ is the energy injection rate due to star formation, and ϵ is the coupling efficiency between the injected energy and the ISM. According to Dib et al. (2006), when modelling the ISM with a coupling efficiency of 25% (a conservative value), quiescent galaxies may switch to a starburst mode at $\Sigma_{\rm SFR}$ = $10^{-2.5}$ to 10^{-2} $M_\odot$ yr^{-1} kpc^{-2}. The bottom two black solid lines are derived from such models using these two values, showing $\sigma_{\rm gas} = 100\Sigma_{\rm SFR}^{1/2}$ and $\sigma_{\rm gas} = 140\Sigma_{\rm SFR}^{1/2}$ ($\sigma_{\rm gas}$ is in km s^{-1}, $\Sigma_{\rm SFR}$ is in $M_\odot$ yr^{-1} kpc^{-2}, the same below). The third curve at the top shows $\sigma_{\rm gas} = 240\Sigma_{\rm SFR}^{1/2}$, using coupling efficiencies of 100% (an extreme and unrealistic value).

If the energy is dissipated through incompressible turbulence, another scaling relation would be expected. This is shown by the dashed curves in the form of $\sigma_{\rm gas} \propto (\epsilon \dot{E})^{1/3}$ where $\dot{E}$ is the energy dissipated through turbulence. The two black dashed curves show $\sigma_{\rm gas} = 80\Sigma_{\rm SFR}^{1/3}$ and $\sigma_{\rm gas} = 130\Sigma_{\rm SFR}^{1/3}$, using coupling efficiencies of 25%, 100%, and a primary injection scale of 1 kpc.

If the turbulence is powered by gravity, assuming a simple Jeans relationship between mass and velocity dispersion, Lehnert et al. (2009) derived the relation in the form of $\sigma_{\rm gas} \sim M_J^{1/4} G^{1/2} \Sigma_{\rm gas}^{1/4}$ = 54 km s^{-1} $M_{J,9}^{1/4} \Sigma_{\rm SFR}^{0.18}$, where G is the gravitational constant, $\Sigma_{\rm gas}$ is the gas mass surface density in $M_\odot$ pc^{-2}, $M_{J,9}$ is the Jeans mass in units of 10^9 $M_\odot$ and $\Sigma_{\rm SFR}$ is in $M_\odot$ kpc^{-2} yr^{-1}. The red solid curve shows the velocity dispersion as a function of $\Sigma_{\rm SFR}$ of a 10^8 $M_\odot$ giant molecular cloud (GMC). Given the mass of our local star-forming galaxies are similar to the Milky Way, there is not any molecular cloud more massive than 10^8 $M_\odot$ (Roman-Duval et al., 2010), which means that the red curve represents an upper limit for the velocity dispersion obtained via the Jeans relation proposed by Lehnert et al. (2009)

Due to a characteristic temperature of 10^4 K (Andrews and Martini, 2013), the Hα emission line has a typical thermal broadening of $\sim$ 12 km s^{-1}. In addition, the temperature distribution in an HII region is

not uniform, so we estimate a maximum range of 10 – 15 km s^{-1} (Andrews and Martini, 2013). Here in all of the models we include the intrinsic thermal broadening of 12 km s^{-1}, but we also display the maximum range with the error-bars in the zoom-in figure.

None of the models can properly explain our local star-forming galaxies. $\sigma \propto (\epsilon \dot{E})^{1/2}$ and $\sigma \propto (\epsilon \dot{E})^{1/3}$ are consistent with some of the spaxels in our SAMI galaxies. However, all of the relations predict lower velocity dispersion than seen in a significant number of spaxels. Most of the data points of our galaxies are significantly above the bottom two black solid lines and the bottom black dashed line, which correspond to a realistic coupling efficiency of 25% (Dib et al., 2006) in the two models. Even if we consider the most extreme (and unrealistic) cases with coupling efficiencies of 100%, as shown by the top black solid line and the top black dashed line, the datapoints at the lower $\Sigma_{\rm SFR}$ end cannot be well explained. The same is true with the Jeans instability relation. Even if we assume extreme GMC masses as high as as 10^8 $\rm M_\odot$, it still underestimates the velocity dispersion of our galaxies. Moreover, the error bars in the zoom-in figure indicate that the uncertainty induced by the thermal broadening has minor influence on the distribution of the models. Therefore, simply considering energy injection from star formation, dissipation of incompressible turbulence, or release of gravitational energy alone as the source of velocity dispersion is not enough to explain the distribution of gas velocity dispersion in local star-forming galaxies.

5.3.2.2 Global (galaxy-averaged) analysis

In Figure 5.4, we look at the global behaviour of the gas in star-forming galaxies. We include the local Hα luminous galaxies from Green et al. (2014) as green diamonds, and the z > 1 star-forming galaxies and star-forming clumps with good data quality[2], for comparison. The area used to calculate the $\Sigma_{\rm SFR}$ of galaxies in Green et al. (2014) are from the radii based on an exponential model fit. Given their various sizes, they span a very large range of $\Sigma_{\rm SFR}$. The global $\Sigma_{\rm SFR}$s and velocity dispersions of our eight galaxies are listed in Table 6.1. The global $\Sigma_{\rm SFR}$s and velocity dispersions are the flux weighted averages of spaxels within individual galaxies. Only the spaxels with $\sigma_{\rm gas}$ > 2 $v_{\rm grad}$ are considered in the measurement. All these works derive velocity dispersion from the Hα emission lines. The grey contour denotes the distribution of local star forming galaxies with $\sigma_{\rm gas}$ derived from HI (Dib et al., 2006), and we include the intrinsic thermal broadening of 12 km s^{-1} here. The difference in velocity dispersions between HI and Hα comes from the thermal broadening of warm ionised gas at $\sim 10^4$ K.

Comparing our eight SAMI galaxies to the high redshift galaxies, we see similar behaviour to the spatially resolved data (c.f. Figure 5.3). When taking the 67 Hα luminous galaxies from Green et al. (2014) into account, we find that it can well connect the local and high-redshift galaxies. In Figure 5.4, we see that their distribution at the lower $\Sigma_{\rm SFR}$ end agrees with the distribution of our eight galaxies and the higher $\Sigma_{\rm SFR}$ end follows the distribution of the high redshift galaxies as well. Green et al. (2014)'s local star-forming galaxies are chosen to have similar properties to the high redshift galaxies, such as high gas fraction and high Hα luminosities ($\gtrsim 10^{42}$ erg s^{-1}). Note that we calculate the $\Sigma_{\rm SFR}$ of

[2]which includes – a) $z \sim 2$ star-forming clumps (Genzel et al., 2011) as black filled squares; b) $z \sim$ 2–3 low mass ($\sim 10^9$ $\rm M_\odot$) lensed star-forming galaxies (Jones et al., 2010) as dark green triangles; c) $z \sim$ 1.5–3 low mass ($\sim$ 0.3–3 $\times 10^{10}$ $\rm M_\odot$), compact but well-resolved with adaptive optics "dispersion dominated" star-forming galaxies (Law et al., 2009) as red open squares; **d)** $z \sim$ 1.5–2.5 disks from the SINS survey (Cresci et al., 2009; Förster Schreiber et al., 2009) as blue open circles.

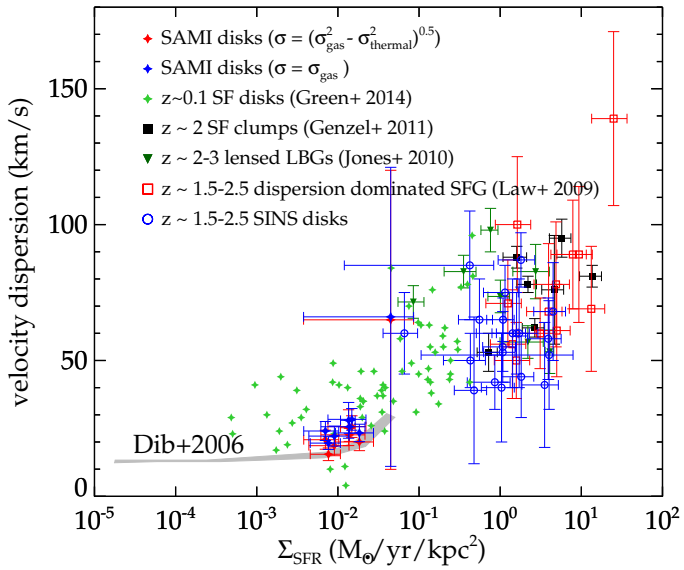

Fig. 5.4: Global dependence of $\sigma_{\rm gas}$ on $\Sigma_{\rm SFR}$. Our eight SAMI galaxies compared to local high Hα luminosity galaxies from Green et al. (2014) and z > 1 star-forming galaxies and clumps (see Section 5.3.2.2 for further details). Each blue (red) filled diamond shows one entire galaxy in our sample including (excluding) the contribution from thermal broadening ($\sigma_{\rm thermal} \sim 12$ km s^{-1}, Glazebrook, 2013). For the measurement of $\sigma_{\rm gas}$ and $\Sigma_{\rm SFR}$, see footnotes in Table 6.1. Green diamonds refer to the Hα luminous galaxies in Green et al. (2014). The black filled squares, dark green triangles, red open squares and blue open circles refer to the z > 1 star-forming galaxies and clumps. The grey contour denotes the distribution of local star-forming galaxies with gas velocity dispersion derived from HI (Dib et al., 2006), and we include the intrinsic thermal broadening of 12 km s^{-1} here.

Tab. 5.3: Spearman correlation coefficient (r_s).

	$\sigma_{\rm gas}$ vs. $\Sigma_{\rm SFR}$	
	r_s	P*
SAMI + Green†	0.72	$\ll$0.01
SAMI + high-z‡	0.53	$\ll$0.01
SAMI + Green†+ high-z‡	0.76	$\ll$0.01

† Hα luminous galaxies in Green et al. (2014).
‡ z >1 star-forming galaxies and star-forming clumps. See Section 5.3.2.2 for further detail.
* Significance level of the Spearman correlation coefficient.

galaxies in Green et al. (2014) without flux weighting, so the $\Sigma_{\rm SFR}$ may be underestimated compared to other galaxies.

We measure the Spearman correlation coefficients between gas velocity dispersion and $\Sigma_{\rm SFR}$, for three different groups of the three sets of data. The results are listed in Table 5.3. Our eight SAMI galaxies together with Green et al. (2014)'s Hα luminous galaxies show strong correlation between velocity dispersion and $\Sigma_{\rm SFR}$ (r_s = 0.72). When we include the high-z galaxies, the correlations become a bit stronger (r_s = 0.76). However, when combining our eight SAMI galaxies with only the high-z galaxies, the correlation becomes moderate (r_s = 0.53). Note that the global $\Sigma_{\rm SFR}$ are flux weighted. Therefore this result comes from relatively more active star-forming regions, which is not contrary to the conclusion we draw from the spatially resolved analysis in Section 5.3.2.1. Stellar feedback alone is insufficient to drive the observed $\sigma_{\rm gas}$, especially at low SFR surface density (Section 5.3.2.1), while it can become dominant when SFR surface density is high enough (Section 5.3.2.2).

5.4 Discussion

5.4.1 Main driver(s) of velocity dispersion

As mentioned in Section 5.3.2.1, the flat and elevated (compared to the model predictions) distribution of spaxels of our SAMI galaxies shown in Figure 5.3 indicates that the star formation feedback is unlikely to dominate the gas velocity dispersion at the scale of $\sim$ 0.5 $\times$ 0.5 kpc^2. Thus, additional drivers of turbulence must be acting in these local, low $\Sigma_{\rm SFR}$ galaxies. As indicated by the flatness of the distribution, such sources need to be common among galaxies and not vary much within galaxies.

The drivers of turbulence can either compress the gas (compression processes) or directly excite solenoidal motions of gas (stirring processes) (Federrath et al., 2016; Federrath et al., 2017).

Stellar feedback like stellar winds of OB stars and Wolf Rayet stars, supernova explosions, as well as accretion processes (such as accretion onto a galaxy) and gravitational contraction are able to compression the gas, and then increase gas velocity dispersion and induce star formation at the same time. Therefore, SFR (or $\Sigma_{\rm SFR}$) may not be directly related to gas velocity dispersion. Both SFR (or $\Sigma_{\rm SFR}$) and gas velocity dispersion can be affected simultaneously by the same sources (e.g. accretion, gravity etc.), but to different degree.

Krumholz and Burkhart (2016) proposed that the turbulence in the ISM is driven by gravity rather than stellar feedback. The higher (than expected) velocity dispersion in Figure 5.3 may be due to the release of gravitational energy. However, Krumholz and Burkhart (2016)'s conclusion comes from the constraint of rapid star-forming, high velocity dispersion galaxies. Their models do not show any apparent difference at low velocity dispersion. Moreover, they investigate the relation with SFR rather than $\Sigma_{\rm SFR}$ and on entire galaxies rather than on spatially resolved regions. On the other hand, Lehnert et al. (2009)'s models in Figure 5.3 reveal that – (i) self-gravity is not sufficient even if the model (red solid curve) adopts an extremely massive the star-forming clump as 10^8 M$_\odot$, which is too big for local

star-forming galaxies; (ii) turbulence can be driven by the bulk motions induced by energy injection from star formation, and then cascade, redistribute and dissipate the energy down to smallest scales. Star formation powers the turbulence of galaxies with high velocity dispersions in complex ways, but star formation alone is insufficient to explain the gas velocity dispersions in our local star-forming galaxies. Generally, both gravity and star formation can power the turbulence but dominate at different redshifts and/or in different environments.

Stirring processes like galactic shear, jets and/or outflows can induce solenoidal motions, i.e., increase the velocity dispersion, but suppress the star formation. Shear is a typical driver of the turbulence in the centres of our galaxy and possibly other galaxies (Krumholz and Kruijssen, 2015; Kruijssen, 2016; Federrath et al., 2016; Federrath et al., 2017). Compared to compressive stirring mechanisms, solenoidal stirring processes have less influence on the density distribution (Federrath et al., 2008; Federrath et al., 2010). Therefore, solenoidal driving mechanisms reduce the SFR compared to compressive sources of $\sigma_{\rm gas}$ (Federrath and Klessen, 2012). Solenoidal drivers (such as shear) may be able to provide an explanation for the distribution of our SAMI galaxies in Figure 5.3: suppressed $\Sigma_{\rm SFR}$ but relatively higher gas velocity dispersion than expected from star formation feedback.

Note that the velocity modes (solenoidal and compressible) do not grow independently of one another (for a detailed analysis in the case of compressive and solenoidal driving of the turbulence, see Federrath et al. (2010, Fig. 14) and Federrath et al. (2011, Fig. 3 bottom panel)). However, what we are referring to here when we talk about solenoidal and compressive modes, are the modes in the acceleration field (not the resulting velocity field) that drives the turbulence. A summary of the differences and implications of solenoidally- and compressively-driven turbulence and their implications for star formation is presented in Federrath et al. (2017) and the main theoretical framework as well as comparison to observations are presented in Federrath and Klessen (2012).

5.4.2 Caveats

5.4.2.1 The medium being observed

Hα emission traces ionized gas and gives information on the turbulences in HII regions. We may miss out the tracers showing the star formation feedback and effects of turbulence driven by galaxy dynamics (such as shear) by just analysing the ionized gas (and not including the atomic and molecular phases). Studies such as Stilp et al. (2013) find two component fits are necessary for HI lines in nearby galaxies, and the broad components are mainly related to the star-formation intensity, which support the idea of star formation supporting the turbulence and gravitational instability/shear. Here we are limited to strong emission line data, but we have applied for ALMA time to follow-up a subset of our galaxies to study the velocity dispersion in the cold/molecular gas as well.

5.4.2.2 Removing the inner regions of the galaxies

In this paper, circum-nuclear regions of our galaxies are removed because of the strong influence of beam-smearing. However, circum-nuclear regions are very interesting and important in order to

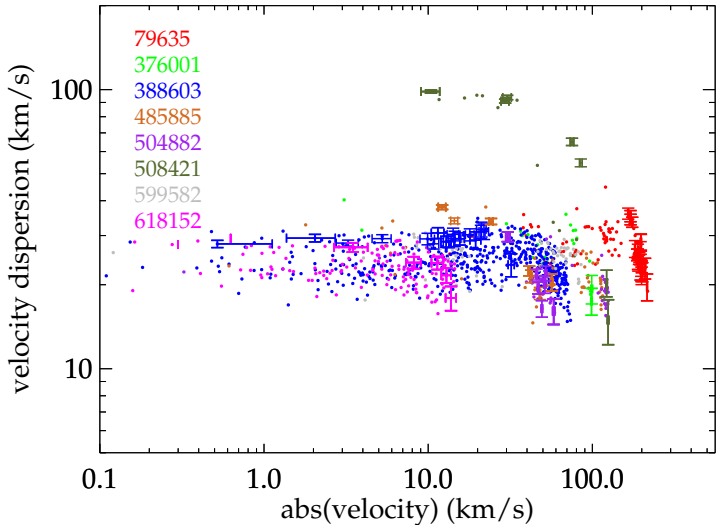

Fig. 5.5: Velocity dispersion as a function of velocity. Spaxels along the major axis are plotted with errorbars. Points in each individual galaxy are labeled by colour.

develop a complete picture of turbulence injection across a galaxy. The influence of the rotation curve could be especially important in circum-nuclear regions, providing a strong test of the gravitational shear/instability arguments. The broadest molecular lines are also found in the circum-nuclear gas of galaxies suggesting that star formation is playing a crucial role there (e.g. Wilson et al., 2011). Here we chose to exclude the inner regions, where beam smearing significantly affects our data. Future studies that attempt to correct for beam smearing will be needed to investigate the turbulence in the circum-nuclear regions in detail.

5.4.2.3 Removing the galaxies that show any evidence for shocks

Shock driven turbulence contains important information about the connection between star formation feedback and turbulence. However, it is difficult to disentangle the contribution of star formation from possible AGN activity to extract actual SFRs accurately from the shock-heated gas. We would likely overestimate SFRs and thus overestimate the effect of star formation feedback. Thus, in a conservative way, we chose not to include any galaxies with signatures of shock-excited emission and focus on purely star-forming galaxies.

5.4.2.4 Dependence of velocity dispersion on rotational velocity

Figure 5.5 shows the dependence of velocity dispersion on rotational velocity. Overall, we see no strong dependence. However, we see some trends of decreasing velocity dispersion with increasing velocity, especially along the major axes (labeled with errorbars). The beam smearing effect would be higher in the center than the outside. For our galaxies, we have already removed the highly affected spaxels, thus the circum-nuclear regions are removed (Section 5.4.2.2).

5.5 conclusion

Random, turbulent motions are important in regulating the star formation in the galaxies, but the energy source of turbulent motions remains unclear. We investigate the random motions of the ionised gas in local star-forming galaxies. After very strict selection to avoid the possible contamination by AGN, shocks and outflows, we find eight SAMI galaxies satisfying the pure star-forming criteria based on emission line diagnostic diagrams. We minimise the influence of beam smearing by removing the spaxels with $\sigma_{\rm gas} < 2\ v_{\rm grad}$ before further analysis (Figure 5.2). The spatially resolved images and high spectral resolution of the SAMI Galaxy Survey shows that, on scales of 0.5×0.5 kpc^2, turbulence within local star-forming galaxies is not exclusively driven by star formation feedback. The flat but elevated (compared to model predictions) distribution of gas velocity dispersion as a function of $\Sigma_{\rm SFR}$ (Figure 5.3) implies that there must be some additional energy source(s) besides star formation feedback, especially at the low $\Sigma_{\rm SFR}$ end. Such source(s) need to be common among local star-forming galaxies and do not vary spatially across galaxies. The difference with the high-redshift galaxies and Hα luminous galaxies (Figures 5.3 and 5.4) indicates that the low SFR in these local galaxies is too weak to explain the random motions of the ionised gas. Juvenile high redshift galaxies could be more sensitive to their intense star formation activity while mature local galaxies could be more influenced by galactic-scale dynamics like gravity, and galactic shear than by star formation feedback.

6 Spatially resolved dust emission of extremely metal poor galaxies[1]

In this chapter, I present infrared (IR) spectral energy distributions (SEDs) of individual star-forming regions in four extremely metal poor (EMP) galaxies with metallicity $Z \lesssim Z_{\odot}/10$ as observed by the *Herschel* Space Observatory. With the good wavelength coverage of the SED, it is found that these EMP star-forming regions show distinct SED shapes as compared to those of grand design Spirals and higher metallicity dwarfs: they have on average much higher $f_{70\mu m}/f_{160\mu m}$ ratios at a given $f_{160\mu m}/f_{250\mu m}$ ratio; single modified black-body (MBB) fittings to the SED at $\lambda \geq 100$ μm still reveal higher dust temperatures and lower emissivity indices compared to that of Spirals, while two MBB fittings to the full SED with a fixed emissivity index (β = 2) show that even at 100 μm about half of the emission comes from warm (50 K) dust, in contrast to the cold ($\sim$20 K) dust component. Our spatially resolved images further reveal that the far-IR colors including $f_{70\mu m}/f_{160\mu m}$, $f_{160\mu m}/f_{250\mu m}$ and $f_{250\mu m}/f_{350\mu m}$ are all related to the surface densities of young stars as traced by far-UV, 24 μm and SFRs, but not to the stellar mass surface densities. This suggests that the dust emitting at wavelengths from 70 μm to 350 μm is primarily heated by radiation from young stars.

6.1 Introduction

Stars born within primordial galaxies in the early universe form out of gas with no or little metals. These distant galaxies are, however, difficult to detect. Nearby extremely metal poor (EMP) star-forming galaxies are chemically unevolved, and thus offer important astrophysical laboratories for our understandings of the interstellar medium (ISM) and star formation in the low metallicity environments (Kunth and Östlin, 2000; Rémy-Ruyer et al., 2013b; Shi et al., 2014b; Shi et al., 2015b). Dust grains play a vital role in galaxy formation and evolution. Characterizing the dust properties by investigating the infrared (IR) emission is a powerful way to understanding the ISM and evolution of dwarf galaxies (Feldmann, 2015).

The integrated dust properties of dwarfs have been investigated with $Spitzer$ Space Telescope. It is found that aromatic features are absent in the metal poor galaxies. Engelbracht et al. (2005) pointed out that the ratio $f_{8\mu m}/f_{24\mu m}$ depends strongly on the metallicity (where f_{λ} is the flux density at wavelength λ), with significantly lower values (mean ratio 0.08 $\pm$ 0.04) for galaxies below one-third of the Solar metallicity than those at higher metallicities (mean ratio 0.70 $\pm$ 0.53).[2] Draine and Li (2007) confirmed no polycyclic aromatic hydrocarbons (PAH) emission in low-metallicity galaxies, as well as other works (e.g. Wu et al., 2006; Rosenberg et al., 2008). The HI-to-dust mass ratio as studied by Engelbracht

[2]Engelbracht et al. (2005) adopted Solar metallicity as 12 + log(O/H) = 8.7(Allende Prieto et al., 2001). Here in this paper, we define Solar metallicity to be 8.7 as well. Thus one-third of the Solar metallicity is around 8.2.

et al. (2008) is shown to increase with the decreasing metallicity to 12+log(O/H)∼8, as $\sim Z^{-2.5}$, and flattens out at lower oxygen abundances. They also found an anti-correlation between dust temperature [3] and metallicity up to 12+log(O/H)∼8, from T∼23 K near the Solar metallicity to T∼40 K at lower metallicity, but a positive relation at lower metallicities.

The *Herschel* Space Observatory further extends the wavelength coverage into the far-IR and sub-millimeter wavelengths, which combined with the *Spitzer* photometry significantly improves the measurement of the dust properties. The total gas-to-dust ratio as revealed by *Herschel* increases the decreasing metallicity. The slope of the relationship is -1 at higher metallicity (12+log(O/H) > 8) and becomes even steeper at the lower metallicity end (Rémy-Ruyer et al., 2014). It is also found that the metal content may not be the only factor affecting the dust properties of dwarfs. For example, the dust to stellar mass ratio of IZw 18 and SBS 0335-052, which have similar metallicities to the other EMP galaxies in Table 6.1, are very different (10^{-6} to 10^{-5}, and 10^{-3} to 10^{-2}, respectively) as estimated by Fisher et al. (2014) and Hunt et al. (2014), respectively. The ratio for IZw 18 is extremely low, while that for SBS 0335-052 is comparable to that found for normal Spiral galaxies (Hunt et al., 2014).

While significant progresses have been made in understanding the integrated dust properties of EMP galaxies, spatially resolved investigations of dust properties of these galaxies are still rare, and thus the dependence of dust properties on the local condition is largely unconstrained in the EMP galaxies. In this study, we aim to benefit from the high spatial resolution of the $Herschel$ Space Observatory to investigate the IR emission of individual star-forming regions of four EMP galaxies, with focus on the IR SED shapes and their relations to the local conditions.

6.2 Sample, observations and data analysis

6.2.1 The sample

Our sample of EMP galaxies contains four objects including Sextans A, ESO 146-G14, DDO 68 and Holmberg II (Ho II). Sextans A is a dwarf irregular at 1.4 Mpc with 12+log(O/H)=7.49 based on the direct method (Kniazev et al., 2005). ESO 146-G14 with a direct method based 12+log(O/H)=7.61 (Bergvall and Ronnback, 1995) is a blue low surface brightness galaxy at a distance of 21.4 Mpc. DDO 68 with a direct method based 12+log(O/H)=7.21 (Pustilnik et al., 2005) is a blue compact dwarf at a distance of 5.9 Mpc. Ho II is a Magellanic irregular dwarf at a distance of 3.3 Mpc (McCall et al., 2012), with a direct method based 12+log(O/H)=7.92 (Croxall et al., 2009).

We also compared our results to the integrated measurements of the KINGFISH sample (Kennicutt et al., 2011), the DGS (Dwarf Galaxy Survey) sample (Madden et al., 2013), and other two EMP galaxies (I Zw 18 & SBS 0335-052). These properties are listed in Table 6.1.

Tab. 6.1: Properties of our four EMP galaxies along with additional two galaxies from the literature

Name	Distance [Mpc]	Metallicity 12+log(O/H)	Morphology
SextansA	1.4	7.49	dIrr
ESO146-G14	21.4	7.61	LSB
DDO 68	5.9	7.21	BCD
HoII	3.3	7.92	dIrr
I Zw 18	18.2[a]	7.14[b]	BCD
SBS 0335-052	56.0[c]	7.25[d]	BCD

[a] Aloisi et al. (2007b);
[b] Izotov and Thuan (1999b);
[c] Madden et al. (2013);
[d] Izotov et al. (1997).

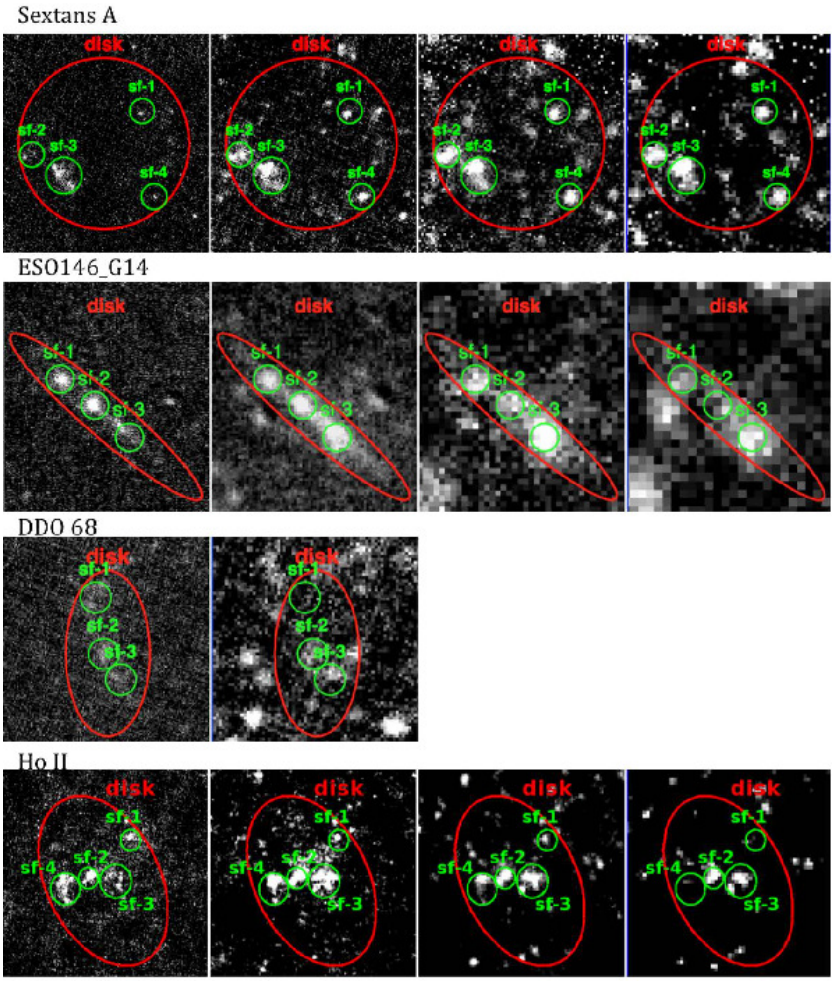

Fig. 6.1: The Herschel images of our galaxies at 70, 160, 250 and 350 μm from left to right. The large ellipses indicate the extension of the whole star-forming disk and small circles are those individual dusty star-forming regions.

Tab. 6.2: Exposure time of *Herschel* data used in this paper.

Name	PACS	SPIRE
	70, 160 μm	250, 350, 500 μm
SextansA	1.9 hr	6 min
ESO146-G14	1.6 hr	6 min
DDO 68	2.7 hr	10 min

6.2.2 Observations

Herschel broad-band images (PI: Y. Shi, PID: OT2_yshi_3) of Sextans A, ESO 146-G14 and DDO 68 were taken at 70 and 160 μm through the scan map modes of PACS (Poglitsch et al., 2010), and 250, 350 and 500 μm through the small map modes with SPIRE (Griffin et al., 2010). The exposure time (excluding overheads) in the two PACS bands is 1.9 hr, 1.6 hr and 2.7 hr for Sextans A, ESO 146-G14 and DDO 68, respectively, and in the three SPIRE bands is 6 min, 6 min and 10 min, respectively. The data of Sextans A and ESO 146-G14 have been partly published in Shi et al. (2014b) where the detailed data reduction was given, while the data of DDO 68 is newly presented here. DDO 68 has low S/N, which may cause large uncertainties on the color (§ 6.3). The PACS and SPIRE integration times of the observations are also listed in in Table 6.2. The Herschel data of Ho II was taken from the KINGFISH project (Kennicutt et al., 2011).

In addition to the Herschel data, the Spitzer IR data at 24 μm and GALEX far-UV data at 1516Å were also retrieved from the archive.

6.2.3 Photometric measurements

As detailed in Shi et al. (2014b), the star-forming disk of each galaxy is defined as an ellipse/circle to closely follow the 10σ contour of the far-UV emission, as shown in Fig. 6.1. Note that for DDO 68 we excluded the tidal tail to better focus on the main disk, although the tail is formally above the 10σ detection threshold. Individual dusty star-forming clumps within a star-forming disk were identified as circle regions with elevated far-UV and 160 μm IR emission which is 3σ above the fluctuations of the disk emission. The defined star-forming regions are listed in Table 6.3. For the flux measurements, the underlying sky emission is estimated within a sky annuli between 1.1 and 1.5 times the disk aperture. For flux error estimates, the *Herschel* flux uncertainty is given by the following sources: the first is the uncertainty of the photon noise within the aperture we defined; the second is the uncertainty from the sky background subtraction; the third represents the uncertainty introduced by the offset from the accurate PSF position when we defined the aperture for each source; and the system uncertainty is also included. For more details please see Shi et al. (2014b). The measurements of fluxes at other wavelengths basically follow the same procedure. The photometric results of these star-forming regions are listed in Table 6.3.

In order to compare images among different resolutions, aperture corrections are performed on all the star forming clumps based on their PSFs. We have tested that the aperture correction method has almost the same effect as convolving images to the same resolution when fitting SEDs (e.g.,

[3] Temperatures are derived from modified blackbody, with the emissivity index β fixed to be 2.

Tab. 6.3: Photometry Of Individual Star-forming Regions In Metal Poor Galaxies

Region[a]	Position (J2000)[b]	$m_a \times m_b$[c] [arcsec^2]	f_{FUV}[d] [μJy]	$f_{3.6\mu m}$ [mJy]	$f_{4.5\mu m}$ [mJy]	$f_{24\mu m}$ [mJy]	$f_{70\mu m}$ [mJy]	$f_{100\mu m}$ [mJy]	$f_{160\mu m}$ [mJy]	$f_{250\mu m}$ [mJy]	$f_{350\mu m}$
SextansA/sf-1	10:10:56.9 -04:40:27.0	22x22	960 ±0.4	1.64±0.009	1.05±0.008	1.06±0.14	41±2		56±7	55±3	32±3
SextansA/sf-2	10:11:10.0 -04:41:44.5	22x22	660 ±0.4	1.65±0.009	1.36±0.008	3.22±0.33	72±3		147±18	111±4	52±4
SextansA/sf-3	10:11:6.20 -04:42:22.5	32x32	4300 ±0.6	2.78±0.013	2.20±0.011	6.30±0.64	267±4		297±24	164±5	89±4
SextansA/sf-4	10:10:55.5 -04:42:59.4	22x22	260 ±0.4	1.14±0.009	0.69±0.008	0.94±0.13	21±2		69±8	62±3	34±3
ESO146-G14/sf-1	22:13:6.0 -62:03:32.5	10x10	150 ±0.2	0.33±0.003	0.24±0.003	1.02±0.16	28±4		38±6	29±4	16±3
ESO146-G14/sf-2	22:13:2.5 -62:03:51.6	10x10	260 ±0.2	0.38±0.003	0.28±0.003	1.23±0.18	36±5		52±8	28±3	11±3
ESO146-G14/sf-3	22:12:59.0 -62:04:14.3	10x10	90 ±0.2	0.74±0.003	0.50±0.003	0.91±0.16	15±2		57±9	49±6	31±4
DDO68/sf-a	09:56:46.6 +28:50:16.6	10x10	340 ±0.1	0.08±0.004	0.08±0.006	0.71±0.08	11±1		<2	<5	<5
DDO68/sf-b	09:56:46.2 +28:49:39.6	10x10	370 ±0.1	0.41±0.004	0.25±0.006	0.36±0.05	10±1		9±1	<5	<5
DDO68/sf-c	09:56:45.3 +28:49:22.6	10x10	350 ±0.1	0.60±0.004	0.43±0.006	0.33±0.05	10±1		8±1	7±1	<5
HoII/sf-1	08:18:48.5 +70:44:40.1	28x28	880 ±0.5	1.34±0.008	1.09±0.012	16.69±1.67	319±6	165±5	144± 14	79±4	51±4
HoII/sf-2	08:19:13.3 +70:42:56.3	28x28	2610 ±0.5	20.41±0.008	14.19±0.012	46.32±4.63	471±7	497±5	407± 39	205±4	103±4
HoII/sf-3	08:18:57.2 +70:42:48.4	46x46	4740 ±0.8	12.31±0.014	8.40±0.020	17.91±1.80	449±7	751±8	630± 19	345±7	196±6
HoII/sf-4	08:19:26.9 +70:42:27.0	43x43	4780 ±0.7	10.44±0.013	7.99±0.018	63.18±6.32	765±7	892±7	387± 16	247±6	105±5

[a] Star-forming regions we defined in our EMP galaxies;
[b] RA & DEC of the center of each region;
[c] Major axis and minor axis of each region in arcsecond;
[d] Flux density at far-UV of each region, the same with $f_{3.6\mu m}$, $f_{4.5\mu m}$, $f_{70\mu m}$, $f_{160\mu m}$, $f_{250\mu m}$, $f_{350\mu m}$.

Tab. 6.4: Pixel sizes of *Herschel* data used in this paper.

Instrument	Wavelength	Pixel size	Resolution
Herschel/PACS	70, 160 μm	1 arcsec, 2 arcsec	5 arcsec, 13 arcsec
Herschel/SPIRE	250, 350, 500 μm	4 arcsec, 6 arcsec, 8 arcsec	18 arcsec, 25 arcsec, 36 arcsec
Spitzer/IRAC	3.6, 4.5μm	0.75 arcsec[a], 0.75 arcsec	2.5 arcsec, 2.5 arcsec
Spitzer/MIPS	24μm	1.5 arcsec	6 arcsec
GALEX/FUV	1516Å	1.5 arcsec	4.5 arcsec

[a] The pixel size of the 3.6 image of ESO146-G14 is 0.6arcsec.

see Casasola et al., 2015). Pixel sizes and resolutions of images at each wavelength are listed in Table 6.4.

6.3 The far-IR SEDs

6.3.1 The color-color diagrams

Fig. 6.2-Left shows the $f_{70\mu m}/f_{160\mu m}$ vs $f_{160\mu m}/f_{250\mu m}$ color-color diagram of our individual EMP regions along with those integrated measurements of the KINGFISH and DGS galaxies. The predictions of single modified black-body (MBB) models are overlaid as grids where the solid line represents a constant emissivity index, β, with the temperature ranging from 10 to 100 K in decrements of 5 K from the left-bottom to the upper-right, and the dashed lines represent constant temperatures with β ranging from 0.0 to 3.0 in steps of 0.5 from the left-bottom to the upper-right. The included DGS galaxies are those with Z/Z above $\sim$10%, because those EMP ones in their sample lack the enough S/N ($\geq$ 3) to be included. As indicated by Fig. 6.2-Left, our sample shows a quite different behavior as compared to the DGS and KINGFISH Spirals. The majority of the KINGFISH locates in the region with $f_{70\mu m}/f_{160\mu m} < 1.5$ and $f_{160\mu m}/f_{250\mu m} < 2.5$, and the DGS ranges from the bottom-left to the upper-right, confined by the overlaid gray-body curves. In contrast, our EMP regions mainly occupy the left side of the plot, with $f_{160\mu m}/f_{250\mu m} < 2$ but $f_{70\mu m}/f_{160\mu m}$ covers a range from 0 to 2.5. At given $f_{160\mu m}/f_{250\mu m}$ our sample shows a much larger scatter in $f_{70\mu m}/f_{160\mu m}$, and more dramatically, a large fraction of our sample has $f_{70\mu m}/f_{160\mu m}$ above the limit of a single modified black-body with β=0 (that is the black-body emission) for a given $f_{160\mu m}/f_{250\mu m}$. When compared with the trend of star forming galaxies predicted by empirical models of Dale et al. (2014), the median behavior of KINGFISH and DGS basically follow the trend, while star-forming regions of our EMP galaxies lie systematically above the trend. A reasonable explanation for the large $f_{70\mu m}/f_{160\mu m}$ ratio is an excess of $f_{70\mu m}$ emission contributed by an additional source of heating. The stochastically heated small grains may be responsible for the excess 70 μm emission (Draine and Li, 2001). The requirement of a second heating component when performing a fit to the 70-500 μm photometry has been widely seen in all types of galaxies (Galametz et al., 2012; Rémy-Ruyer et al., 2013b), while our sample seems to be the extreme case in which about half of our sample has $f_{70\mu m}/f_{160\mu m}$ higher than the black-body curve for a given $f_{160\mu m}/f_{250\mu m}$ color.

Similar to Fig. 6.2-Left, Fig. 6.2-Right presents another color-color plot that is $f_{160\mu m}/f_{250\mu m}$ vs. $f_{250\mu m}/f_{350\mu m}$. Again, our EMP regions occupy a different area of the diagram, when compared with the other two sample. The KINGFISH Spirals and DGS galaxies span a similar range of $f_{250\mu m}/f_{350\mu m}$

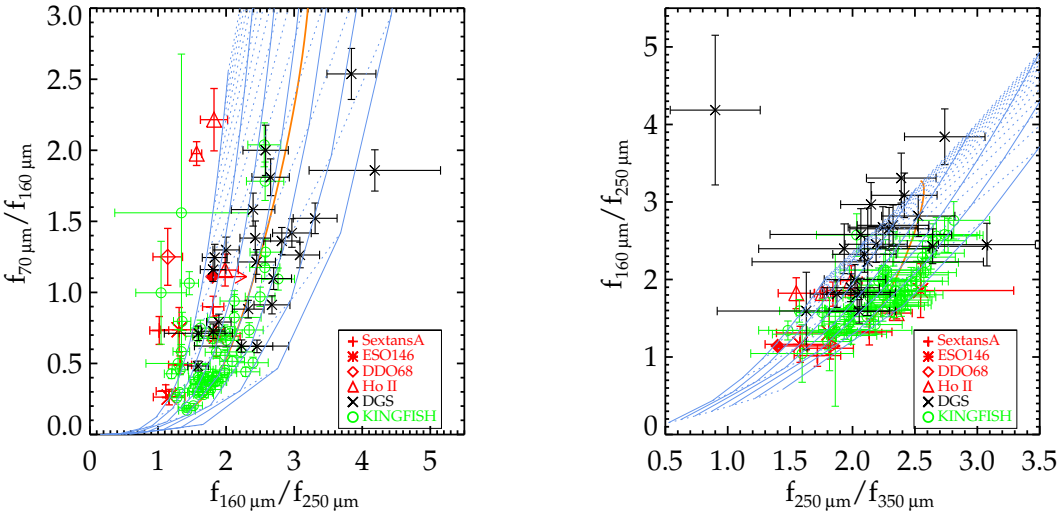

Fig. 6.2: **Left**: The distribution of EMP star-forming regions, and integrated measurements of galaxies from DGS and KINGFISH in the $f_{70\mu m}/f_{160\mu m}$ vs. $f_{160\mu m}/f_{250\mu m}$ color-color diagram. The grid is a single modified black-body with a range of temperatures and emissivity indices. The solid line represents a constant emissivity index, β, with the temperature ranging from 10 to 100 K in a decrement of 5 K from the left-bottom to the upper-right. Dashed lines represent constant temperature with β ranging from 0.0 to 3.0 in a step of 0.5 from the left-bottom to the upper-right. The brown line is the trend of star forming galaxies predicted by the model of Dale et al. (2014). **Right**: Same as left but using $f_{160\mu m}/f_{250\mu m}$ vs. $f_{250\mu m}/f_{350\mu m}$.

but the latter shows larger $f_{160\mu m}/f_{250\mu m}$ at given $f_{250\mu m}/f_{350\mu m}$ compared to the former. In contrast, our EMP regions mainly occupy the locus toward the bottom-left corner with smaller $f_{160\mu m}/f_{250\mu m}$ and $f_{250\mu m}/f_{350\mu m}$. In the figure there is one object (UM 461) that deviates significantly from the trend. It is difficult to explain such a strange SED. We double checked the photometric measurements and obtained consistent values with those in the literature of Rémy-Ruyer et al. (2013b) as used in the figure. But we did notice that the centroids of the 250 and 350 um images are significantly offset (14″) from those of the 70 and 160 μm, indicating possible significant contamination by a background source at these two wavelengths.

6.3.2 Modified black-body fitting

To further characterize the SED shape and understand the dust emission of EMP star-forming regions, the MBB fittings are carried out. A single MBB model fitting to the full SED is not appropriate as a single photon heating dust component may contaminate significantly the 70 μm or even the 100 μm emission. We first performed a single MBB fitting to the photometry $\geq$ 100 μm by assuming at these longer wavelengths the contribution from the hot dust component was negligible. The MBB model is determined by the dust temperature T and the dust emissivity index β from $S_\nu = A * B_\nu(T)\lambda^{-\beta}$, where S_ν was the flux density at frequency ν, A was a constant that is related to the column density of the dust, and $B_\nu(T)$ was the Planck function. This method assumed an optically thin condition at the observed far-IR wavelengths with the dust mass derived from $M_{\rm dust} = \frac{S_\nu {\rm D}^2}{\kappa_\nu {\rm B}_\nu(T)}$, where κ_ν was the

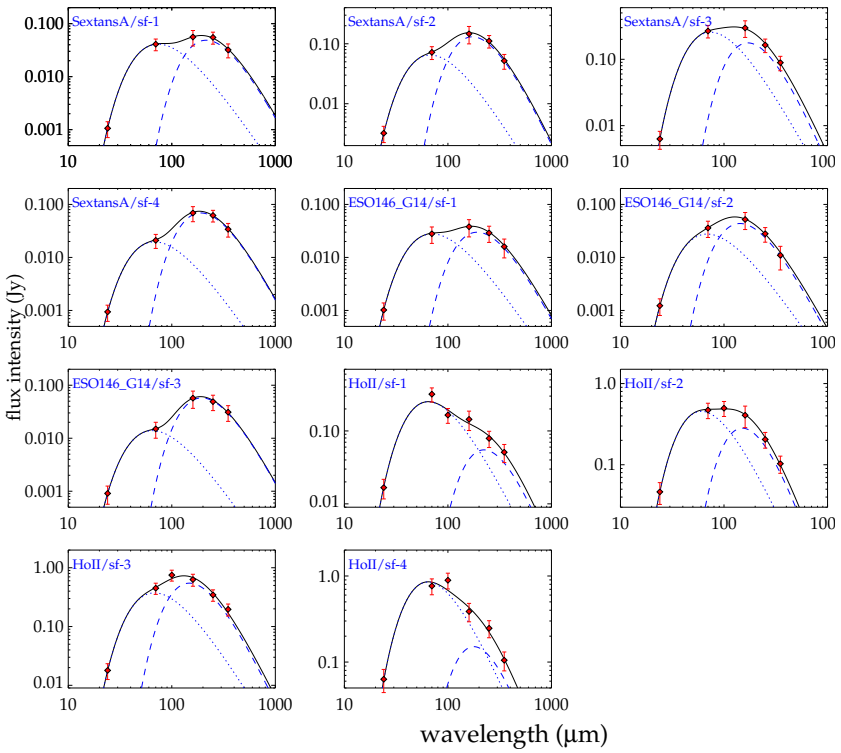

Fig. 6.3: The two modified black-body fitting to the SEDs. Reds dots are the flux density at different wavelength within each star-forming region. Black solid lines are the 2T MMB best fits with blue dotted lines the best fits of the warm dust components and blue dashed lines the best fits of the cold dust components.

dust opacity, and D was the distance to the galaxy. We took κ_ν = 1.9 cm^2 g^{-1} at λ = 350μm [7], and calculated the dust mass at λ=350μm as this band was less sensitive to temperature than shorter wavelengths, and had lower uncertainties than those at longer wavelengths. As listed in Table 6.5, the single MBB fitting gave a $\beta \sim 1$ and $T \sim$ 20-50 K. The temperature may be underestimated for Sextans A and ESO 146-G14 as there is no 100 μm photometry.

The two-MBB fitting is more reasonable by taking the advantage of the full SED, which is carried out with the equation $S_\nu = A_w * B_\nu(T_w)\lambda^{-\beta_w} + A_c * B_\nu(T_c)\lambda^{-\beta_c}$, where A_w, T_w and β_w describe the hot component of the dust emission while A_c, T_c and β_c are for the cold component. Here we fixed β_w = 1 to represent the hot small grains and β_c = 2 for the cold large grains, similar to the study of Zhu et al. (2009). The results are shown in Fig. 6.3 and listed in Table 6.6. The dust mass is derived in the same way as the single MBB fitting. If the cold component dust indices β_c decrease from 2.0 to 1.7, 1.5 and 1.3, the derived T_c increases and the derived dust mass drops by 10%, 25% and 50%, respectively.

Our two MBB fits give cold dust with $T_\mathrm{c} \sim$ 15-20 K and warm dust with $T_\mathrm{w} \sim$ 50-60 K. Fig. 6.3 indicates that the warm dust emission is significant for these EMP star-forming regions, in contrast to those of Spirals (Galametz et al., 2012). To further characterize the importance of the hot dust emission, we performed similar fittings to the integrated SEDs of the DGS sample (Rémy-Ruyer et al., 2013b) and investigated the fraction of the emission from the warm dust MBB at 100 μm $(f_\mathrm{warm}/f_\mathrm{total})_{100\mu m}$ as a function of the oxygen abundance. The result is shown in Figure 6.4. It indicates that the fraction

[7] http://www.astro.princeton.edu/∼draine/dust/dustmix.html, (Milky Way, R_V = 3.1)

Tab. 6.5: Results of Single MBB Fits to the SEDs at $\geq$ 100 μm

Region	T [K]	β	M_{dust} [$M_\odot$]
SextansA/sf-1	19± 8	0.99±1.22	1.34×10^3
SextansA/sf-2	25± 9	1.02±0.78	1.31×10^3
SextansA/sf-3	37± 17	0.59±0.56	9.93×10^2
SextansA/sf-4	21± 9	1.00±1.12	1.21×10^3
ESO146-G14/sf-1	23± 22	0.90±2.24	1.00×10^5
ESO146-G14/sf-2	30± 5	1.14±0.64	4.51×10^4
ESO146-G14/sf-3	22± 16	0.80±1.94	2.11×10^5
HoII/sf-1	47± 13	0.07±0.44	1.98×10^3
HoII/sf-2	37± 4	0.70±0.24	6.03×10^3
HoII/sf-3	33± 1	0.82±0.06	1.30×10^4
HoII/sf-4	41± 1	0.95±0.06	5.42×10^3

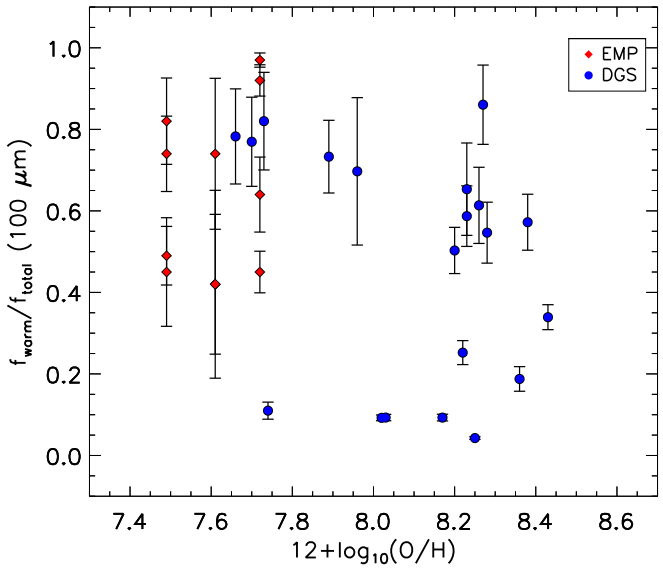

Fig. 6.4: The fraction of warm dust emission at 100 μm as a function of the Oxygen abundance based on the two modified black-body fitting. The red diamonds are the EMP star-forming regions, and blue circles are for the integrated dwarf galaxies from the DGS.

$(f_{\rm warm}/f_{\rm total})_{100\mu m}$ increases on average with decreasing metallicities: around the Solar abundance, the warm dust emission is small ($<$ 20%) but reaches above 50% below one tenth of the Solar metallicity. Such a high warm dust contribution cautions the single MBB fitting to the photometry for EMP galaxies when the data at $\lambda \leq$ 100 μm are included. As shown in Figure 6.3, our two-MBB fittings with β=2 for the cold component also provide good fittings, while the single MBB requires a lower β. This suggests that the result about β is sensitive to the way how the MBB fitting is performed, and the β of metal poor galaxies can be underestimated as a result of a large warm dust contribution up to 100 μm.

6.3.3 Spatial variations of SEDs and dust heating Mechanism

Spatially resolved IR data allow to investigate the spatial variation of the IR SEDs among different star-forming regions in our EMP galaxy sample. As shown in Fig. 6.2-Left, the variation in the color $f_{70\mu m}/f_{160\mu m}$ among different EMP regions for a given galaxy seems to be smaller as compared to the

Tab. 6.6: Results of two MBB Fits to the Photometry

Region	T_{cold} [K]	T_{warm} [K]	M_{warm} [$M_\odot$]	M_{cold} [$M_\odot$]	M_{warm}/M_{cold}	$f_{warm}/f_{total}(100\mu m)$	$L_{8-1000\mu m}$ [$L_\odot$]
SextansA/sf-1	13±2	49±2	2.22×10^{1}	3.33×10^{3}	6.7×10^{-3}	0.82	1.93×10^{5}
SextansA/sf-2	16±2	54±3	2.49×10^{1}	3.00×10^{3}	8.3×10^{-3}	0.49	4.09×10^{5}
SextansA/sf-3	17±3	49±2	1.43×10^{2}	3.72×10^{3}	3.8×10^{-2}	0.74	1.11×10^{6}
SextansA/sf-4	15±1	53±3	7.74×10^{0}	2.62×10^{3}	3.0×10^{-3}	0.45	1.53×10^{5}
ESO146-G14/sf-1	15±2	52±2	2.78×10^{3}	2.60×10^{5}	1.0×10^{-2}	0.74	2.98×10^{7}
ESO146-G14/sf-2	20±4	53±5	2.50×10^{3}	8.64×10^{4}	2.9×10^{-2}	0.42	3.77×10^{7}
ESO146-G14/sf-3	14±2	56±3	1.00×10^{3}	5.35×10^{5}	1.9×10^{-3}	0.42	2.66×10^{7}
HoII/sf-1	13±3	56±2	4.19×10^{2}	2.39×10^{4}	1.8×10^{-2}	0.97	5.46×10^{6}
HoII/sf-2	19±3	60±4	5.81×10^{2}	1.69×10^{4}	3.4×10^{-3}	0.64	1.21×10^{7}
HoII/sf-3	19±2	53±3	7.68×10^{2}	3.04×10^{4}	2.5×10^{-2}	0.45	1.17×10^{7}
HoII/sf-4	16±4	57±2	1.36×10^{3}	2.11×10^{4}	6.4×10^{-2}	0.92	1.88×10^{7}

overall scatter of the integrated color. The $f_{70\mu m}/f_{160\mu m}$ spans an overall range from about 0.2 to 2.5. In contrast, four EMP regions in Sextans A have $f_{70\mu m}/f_{160\mu m}$ between 0.5 and 1.0, four regions of Ho II span the color range from 0.7 to 2.3, and three regions of ESO 146-G14 show the color from 0.2 to 0.7. As shown in Fig. 6.2-Right, the variation in the color $f_{160\mu m}/f_{250\mu m}$ among different EMP regions within a given galaxy is also smaller than the overall scatter among integrated quantities of galaxies.

With the spatially resolved images, we can further study the color as a function of local conditions in the 2-D. In Fig. 6.5, the far-IR color of individual EMP regions is investigated as a functions of far-UV surface brightness, 24 μm surface brightness, SFRs and stellar masses[9]. All surface brightness/densities as listed in Table. 6.7 are inclination corrected with angles of 0°, 50°, 54° and 30° for Sextans A, ESO 146-G14, DDO 68 and Ho II, respectively. As indicated by the figure, the far-UV surface brightness of our EMP regions are between about 0.01 and 0.1 MJy/sr, which is within the range of Spirals (Gil de Paz et al., 2007; Shi et al., 2011). The SFR surface densities of our EMP regions are between $10^{-3.5}$ and 10^{-2} $M_\odot$/yr/kpc^2. This is also within the range of star-forming regions of local Spirals (Bigiel et al., 2008). The stellar mass surface densities of EMP regions are between 5 and 15 $M_\odot$/pc^2, which is several times lower than those of Spirals (e.g. Shi et al., 2011).

Fig. 6.5 shows that all three IR colors including $f_{70\mu m}/f_{160\mu m}$, $f_{160\mu m}/f_{250\mu m}$ and $f_{250\mu m}/f_{350\mu m}$ increase on average with the increasing far-UV surface brightness, 24μm surface brightness and SFR surface densities, with the best relationships with the SFR surface densities. While all these three surface brightness/densities are associated with young stars, the SFR derived here includes both the unobscured component as traced by the far-UV and the obscured one as traced by the 24 μm. Fig. 6.5 further shows that there are no trends between the IR colors and the stellar mass surface densities. Unlike the SFR, the stellar mass is better related to old stars. Investigations of the relationships between the far-IR colors and the tracers can be used to constrain if the dust is mainly heated by the radiation from the young stars or the interstellar radiation field from the old stars. As argued by Bendo et al. (2015), such investigations show many advantages in understanding the dust heating mechanism as compared to other methods such as the dust SED fitting and radiative transfer that relies on assumptions of dust grain properties, SED shapes of heating source etc. The results of Fig. 6.5 thus support that young stars are the main heating source of dust radiating at wavelengths from 70 μm to $\geq$ 250 μm in EMP star-forming regions. Investigations of the heating source of dust in Spirals by

[9] SFRs and stellar masses are estimated following Leroy et al. (2008a)'s formula. SFR from Leroy et al. (2008a) is calibrated from Spiral galaxies and combines both UV (unobsured) and IR (obscured) maps, which is applicable to low-metallicity galaxies (Calzetti et al., 2007; Salim et al., 2007). For one galaxy (Sextans A), we collected the broad-band photometry (FUV, NUV, V-band, 3.6 μm and 4.5 μm) and derived stellar masses based on the SED fitting. The result is not that different from the one based on Leroy et al. (2008a)'s method, with the difference < 20%.

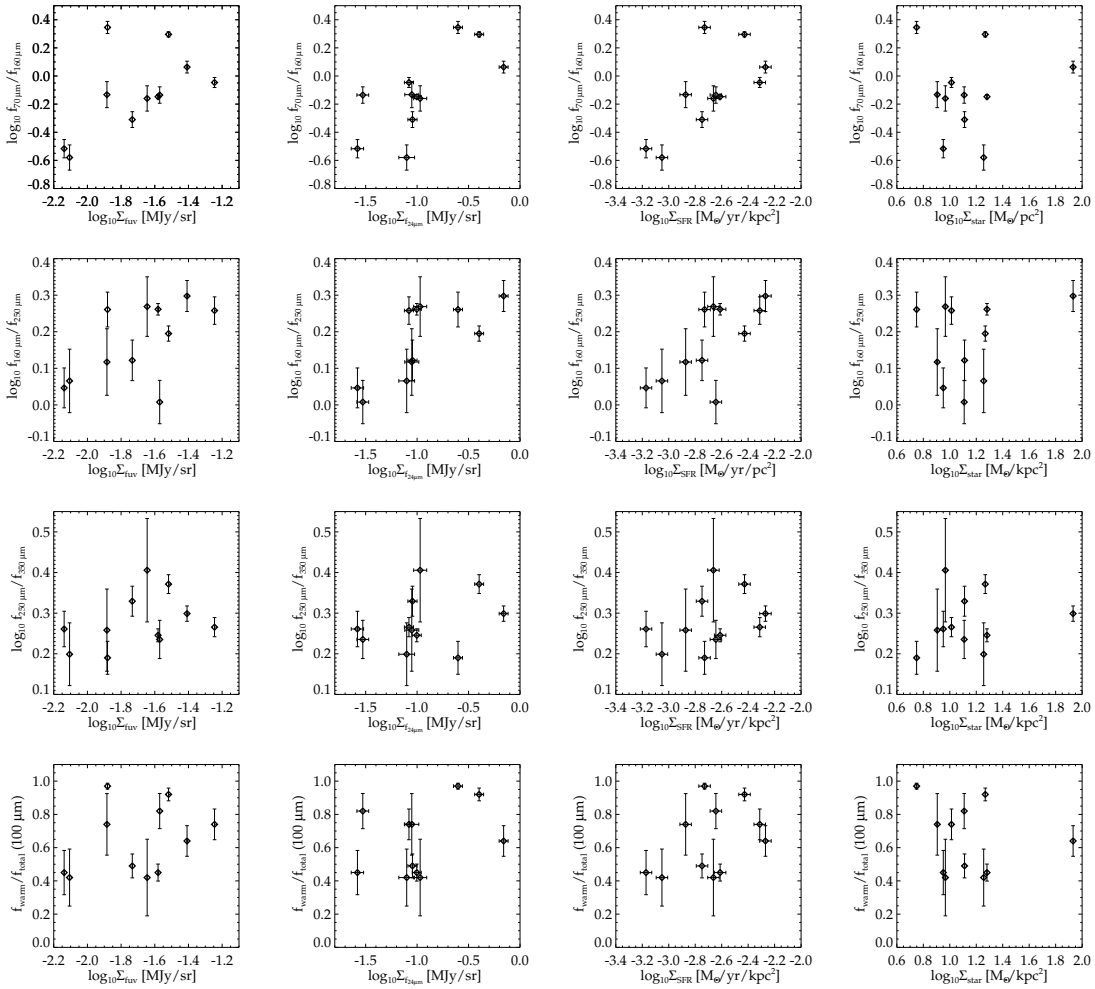

Fig. 6.5: The IR colors as functions far-UV surface brightness, 24 μm surface brightness, SFR surface densities and stellar mass surface densities from left to right.

Bendo et al. (2015) found that in only 3 out of 24 galaxies, the $f_{160\mu m}/f_{250\mu m}$ and $f_{250\mu m}/f_{350\mu m}$ are better related to the SFRs than old stars while in the remaining the $f_{250\mu m}/f_{350\mu m}$ color is driven by both.

The above result suggests that the dust of emission at 70 μm up to 350 μm in EMP regions is heated by young stars instead of diffuse stellar radiation from old stars. The underlying cause for this needs further investigations. As discussed above, the SFR surface densities of our EMP regions are not that different from those in Spirals, indicating the radiation fields from young stars are not enhanced in EMP regions compared to star-forming regions in Spirals. But the SFR relative to the stellar mass, i.e. the specific SFR (sSFR), in these EMP regions is enhanced, with the median of log(sSFR[Gyr^{-1}]) around -0.82 and a standard deviation of 0.36. In contrast, the star-forming regions of 12 Spirals in Shi et al. (2011) have the median log(sSFR[Gyr^{-1}]) of -1.28 and a standard deviation of 0.32. Compared to the sSFRs of dwarf galaxies as studied by Hunt et al. (2015b), our galaxies lie below their trend, but still within the scatter (0.01 – 30 Gyr^{-1}, around metallicities of our galaxies). This difference could be due to the fact that our galaxies are mostly dwarf irregulars and low-surface-brightness galaxies, while the sample of Hunt et al. (2015b) contains many blue compact dwarf galaxies that are known to be compact with enhanced SFRs and have higher sSFRs due to interactions.

The properties of dust grains in EMP galaxies may be systematically different from those in Spirals, making the heating from young stars important to the dust emission all the way up to 350 μm. For example, if small dust grains in EMP galaxies are abundant, they could be heated to higher temperatures without requiring an enhanced radiation field. It is observationally difficult to quantify the size of dust grains. Studies of extinction curves point out that metal poor dwarfs in the local group, SMC and LMC, show more steeply rising extinction at UV wavelengths, suggesting smaller dust grains in these two galaxies (for a review, see Li et al., 2015). A simple extrapolation of this result into the EMP regime would naturally expect the dust in EMP galaxies to be smaller due to the lack of raw material for grain growth. Small grains could offer more surface area for the formation of molecular hydrogen that is likely abundant in EMP galaxies as indicated by several tracers including dust (e.g. Shi et al., 2014b), warm H_2 (e.g. Hunt et al., 2010) and [CII] 158 μm (e.g. Madden et al., 1997; Madden et al., 2013) although CO is very weak (e.g. Shi et al., 2015b). However, it is impossible with current facilities to obtain the measurements of the extinction curve for these relatively distant EMP galaxies, and thus to conclude the size of dust grains in EMP galaxies.

6.4 Dust-to-stellar mass ratio

In Fig. 6.6, the dust-to-stellar mass ratio of our EMP regions are plotted against the oxygen abundance, 12+log(O/H), along with the integrated quantities from the DGS. The dust masses of both samples are measured using the same method, i.e. the two MBB fitting (see §6.3.2), which could avoid the artificial effects of different dust mass estimates on the relationship. As shown in the figure, there does not seem to exist any correlation between these two quantities. Hunt et al. (2014) also found that two EMP galaxies (IZw 18 and SBS 0335-052) show very different dust-to-stellar mass ratio although both are similarly very metal poor, and their ratios lie within the overall scatter of spiral and other dwarfs at higher metallicities. Our significantly increased number of the data-points in the EMP regime as compared to the work of Hunt et al. (2014) allows us to derive conclusive results that the dust-to-stellar

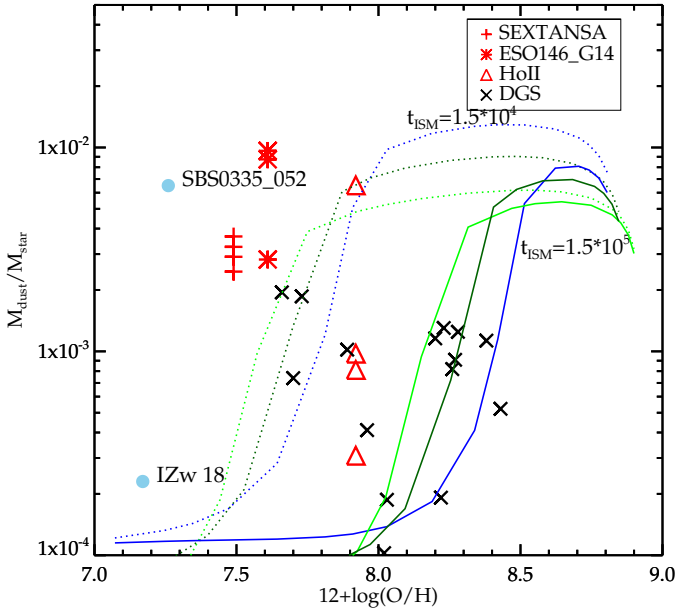

Fig. 6.6: The dust-to-stellar mass ratio of our EMP star-forming regions and integrated galaxies of the DGS. The lines are the model predictions by Feldmann (2015). t_{ISM} is the dust growth time-scale which can be computed from basic collision theory (Weingartner and Draine, 1999) (solid or dashed lines). Q_{MS} denotes the (multiplicative) offset of a given galaxy from the main sequence (blue: 1/3, cyan: 1, green: 3). The data for IZw 18 and SBS 0335-052 are from Hunt et al. (2014).

mass ratio is not related to the metallicity. The figure further indicates that even within a given galaxy, the dust-to-stellar mass ratio of individual EMP regions could show large scatters, e.g. EMP regions in Ho II span the whole range from roughly 10^{-4} to 10^{-2} while EMP regions in Sextans A and ESO 146-G14 have much smaller scatters.

The overlaid lines in Fig. 6.6 are the predictions of the model by Feldmann (2015, private communication), where t_{ISM} is the dust growth time-scale which can be derived from Weingartner and Draine (1999)'s basic collision theory (solid or dashed lines). Blue, cyan and green lines refer to $Q_{MS} = \frac{1}{3}$, 1, 3, which denote the (multiplicative) offset of a given galaxy from the main sequence. While the normalization of the trend depends on the methodology used for dust mass and metallicity measurements, the model-predicted sharp drop between 1/10 and 1/5 solar abundance is clearly not seen in Fig. 6.6. The model of Feldmann (2015) invokes gas outflow, inflow and star formation in an equilibrium state in order to reproduce the observed dust-to-gas mass ratio as a function of metallicity as well as many other observed galaxy properties. The model is motivated to explain the observed sharp drop in the dust-to-gas mass ratio vs. the metallicity around 20% solar metallicity (Rémy-Ruyer et al., 2014; Shi et al., 2014b). Fig. 6.6 indicates that although a sharp drop may occur in the dust-to-gas ratio, a similar drop in the trend of the dust-to-stellar ratio as a function of metallicity is not seen. The model argues that the dust content in EMP galaxies is mainly regulated by the galactic outflow, whose efficiency may be overestimated so that too much dust is removed relative to the stellar content. Our results further suggest that if outflows regulate the dust-to-stellar mass ratio, they must vary greatly on scales of 100 – 1000 pc.

Tab. 6.7: Measurements of 2-D Densities of EMP Star-Forming Regions

Region	$\Sigma_{\rm fuv}$ [MJy/sr]	$\Sigma_{24\mu m}$ [MJy/sr]	$\Sigma_{\rm SFR}$ $[M_\odot/yr/kpc^2]$	$\Sigma_{\rm star}$ $[M_\odot/pc^2]$	$\Sigma_{\rm dust}$ $[M_\odot/kpc^2]$
SextansA/sf-1	(2.69±0.018)×10^{-2}	(2.97±0.39)×10^{-2}	(2.27±0.23)×10^{-3}	(1.28±0.007)×10^{1}	(4.72± 0.47)×10^{4}
SextansA/sf-2	(1.85±0.026)×10^{-2}	(9.01±0.92)×10^{-2}	(1.78±0.18)×10^{-2}	(1.29±0.007)×10^{1}	(3.75± 0.38)×10^{4}
SextansA/sf-3	(5.69±0.061)×10^{-2}	(8.33±0.85)×10^{-2}	(4.87±0.49)×10^{-3}	(1.03±0.005)×10^{1}	(3.85± 0.39)×10^{4}
SextansA/sf-4	(7.27±0.668)×10^{-3}	(2.63±0.36)×10^{-2}	(6.73±0.67)×10^{-4}	(8.93±0.070)×10^{0}	(3.79±0.38)×10^{4}
ESO146-G14/sf-1	(1.31±0.058)×10^{-2}	(8.88±0.22)×10^{-2}	(1.34±0.13)×10^{-3}	(8.04±0.073)×10^{0}	(9.84±0.98)×10^{4}
ESO146-G14/sf-2	(2.26±0.033)×10^{-2}	(1.07±0.24)×10^{-1}	(2.18±0.22)×10^{-3}	(9.26±0.073)×10^{0}	(3.59±0.36)×10^{4}
ESO146-G14/sf-3	(7.83±0.096)×10^{-3}	(7.92±0.22)×10^{-2}	(8.88±0.89)×10^{-4}	(1.80±0.007)×10^{1}	(1.80±0.18)×10^{5}
HoII/sf-1	(1.32±0.025)×10^{-2}	(2.50±0.29)×10^{-1}	(1.87±0.29)×10^{-3}	(5.61±0.034)×10^{0}	(6.50±0.65)×10^{5}
HoII/sf-2	(3.90±0.008)×10^{-2}	(6.93±0.80)×10^{-1}	(5.38±0.54)×10^{-3}	(8.55±0.003)×10^{1}	(4.01±0.40)×10^{4}
HoII/sf-3	(2.63±0.007)×10^{-2}	(9.93±0.12)×10^{-2}	(2.45±0.25)×10^{-3}	(1.91±0.002)×10^{1}	(3.38±0.34)×10^{4}
HoII/sf-4	(3.03±0.006)×10^{-2}	(4.01±0.46)×10^{-1}	(3.74±0.37)×10^{-3}	(1.85±0.002)×10^{1}	(2.76±0.28)×10^{4}

6.5 Conclusions

We present IR SEDs of individual star-forming regions in four EMP galaxies observed by *Herschel*. The main conclusions are:

(1) As compared to spirals and higher metallicity dwarfs, EMP star-forming regions have on average much higher $f_{70\mu m}/f_{160\mu m}$ ratios at given $f_{160\mu m}/f_{250\mu m}$ ratios. In addition, single MBB fits to the SED at $\lambda \geq 100$ μm show higher dust temperatures and lower emissivity indices, while two-MBB fits with a fixed emissivity index show that even at 100 μm about half of the emission comes from warm ($\sim$ 50 K) dust, unlike that seen in Solar metallicity spiral galaxies.

(2) Our spatially resolved images further reveal that the far-IR colors including $f_{70\mu m}/f_{160\mu m}$, $f_{160\mu m}/f_{250\mu m}$ and $f_{250\mu m}/f_{350\mu m}$ are all related to the surface densities of young stars (far-UV, 24 μm and SFRs), but not with the stellar mass surface densities. This suggests that the dust emitting at wavelengths from 70 μm all the way up to the 350 μm is heated by radiation from young stars instead of old stars.

(3) Our EMP regions cover a large range in the dust-to-stellar mass ratio, indicating the importance of local conditions, such as outflows etc., in regulating the dust content.

7 Conclusion and perspectives

7.1 Conclusion

In this thesis, I focus on the large-scale ($\sim$kpc) star formation of galaxies, taking advantage of the data from *Herschel*, ALMA, NOEMA, and the SAMI IFU survey.

Based on the GOODS-ALMA survey, the largest cosmological survey with the large ALMA interferometer at 1.1 mm, I studied the six optically-dark galaxies (i.e., undetected in the observed U to H-bands) uncovered by this survey. We present evidence that four out of the six optically-dark galaxies belong to the same overdensity of galaxies at $z \sim 3.5$. One of them, AGS24 ($M_\star = 10^{11.32^{+0.02}_{-0.19}}$ M$_\odot$), is the most massive galaxy without an AGN at $z > 3$ in the GOODS-ALMA field, and it falls in the very center of the galaxy surface density peak. This suggests that the surrounding overdensity is a proto-cluster in the process of virialization and that AGS24 is the candidate progenitor of the future brightest cluster galaxy. This further indicates that wide but moderately shallow surveys at submilimeter wavelengths are a powerful tool to unveil massive galaxies which tend to reside at the bottom of the potential well of large-scale structures, leading us to follow up the properties of such galaxies in the context of their environments.

The nearby extremely metal-poor galaxies can be considered as analogs of the high-z galaxies which also form stars out of gas with very low metal content. They serve as ideal laboratories to study the formation and evolution of galaxies in the early Universe. I studied the molecular gas content in IZw18, one of the most metal poor galaxies. The upper limit of CO J=2-1 emission is ten times lower than previous studies despite the vigorous star formation activity of IZw18. Such low CO content indicates a drastic change in the structure of the ISM at around a few percentages of Solar metallicity. Especially, the high [C II] luminosity relative to CO implies a larger molecular gas reservoir than inferred from CO in IZw18. I also studied the resolved dust emission in four extremely metal-poor galaxies observed by *Herschel*. They show higher dust temperatures and lower emissivity indices compared to those of spiral galaxies. The high contribution from warm (50 K) dust to the far-IR emission and the correlation between the far-infrared colours and the surface densities of young stars suggest that the dust emission of these galaxies is primarily heated by radiation from young stars.

The SAMI IFU survey provides 3D information on galaxy kinematics. My work shows that on sub-kpc scales, local star-forming galaxies display a flat distribution of ionized gas velocity dispersion as a function of star formation rate surface density. However, the velocity dispersion is higher than the prediction of star-formation-driven models, implying additional sources to drive random motions of the interstellar medium in star-forming galaxies.

In summary, the work done in my thesis has put more constraints on the understanding of galaxy evolution: The first galaxies with little heavy elements may have very different ISM structures, very likely to be more porous, compared the local galaxies. And the study on the gas content in such galaxies requires tracers such as [C II] (Madden et al., 2020) other than CO, which can be easily destroyed without the shielding by dust. The radiation field is more exposed to the ISM due to the low dust content. Then it's harder to increase the density of molecular clouds. This may lead to the low star formation efficiency in these galaxies (Shi et al., 2014b). As galaxies gradually grow massive, their high masses make it easier to sustain the dust content hence they form stars more efficiently. Galaxies reside in dense environments tend to experience an accelerated growth and end up to be more massive than those in isolated systems, as they may have had more abundant gas reservoir to form stars and/or more interactions with other galaxies. This could be the case of the massive galaxies we found in the protocluster at $z \sim 3.5$, which are rare and extremely faint in the optical to near-IR due to the high dust content. However, an early mature may indicate an early death since the rapid growth can exhaust the fuel of star formation very shortly, which is the case of the massive quiescent galaxies observed at $z \sim 2$. The establishment of this evolution path requires more statistics. The star-forming galaxies are in the balance between the gravity and pressure. The energy sources to support the pressure in distant and local galaxies are not the same, with the former from the star formation feedback and the later from the gravitational energy release of gas radial transportation. The transition between the two can be also related to the morphological transformation where the bulges form early in compact distant galaxies and discs seen in the local galaxies form later (Krumholz et al., 2018).

7.2 Perspective

7.2.1 More on the optically dark galaxies

Spectroscopic redshifts and the ISM properties of the optically dark galaxies in the protocluster: The redshift measurements in Chapter 3 are based on the analysis of optical-to-near-IR SED, far-IR SED, as well as the one emission line detected in two of the optically-dark galaxies. It is necessary to obtain the precise redshifts spectroscopically by observing the bright [C II] line, which is considered as the main coolant in high-z galaxies, emitting $\sim$0.1%-1% of the far-IR continuum. The [C II]/$L_{\rm FIR}$ ratio shows an anticorrelation with $L_{\rm FIR}$, but with a large scatter. Meanwhile, recent studies argue that [C II]/$L_{\rm FIR}$ exhibits a tighter relation with dust temperature (e.g., Malhotra et al., 2017). The high frequency of the [C II] line also enables a wider redshift range search in comparison with the CO lines, given the limited observing frequency range of ALMA. A follow-up observation of [C II] with ALMA would allow us to confirm the redshift of these galaxies and study the properties of the ISM in these galaxies. Once the redshifts are confirmed, we would request to detect their CO emission by VLA or ALMA. Ginolfi et al. (2017) already showed evidence of a CO gas stream surrounding one of the optically-detected galaxies in this structure. We expect to see the molecular gas not only in the optically dark galaxies fueling the star formation but also across the entire large-scale structure supporting the continuous growth of the galaxies therein.

Environments of a larger sample of optically dark galaxies: The overdensities of dusty star-forming galaxies (DSFGs) haven been discovered since ALMA revealed the multiplicities of the

brightest *Herschel* and JCMT/SCUBA2 sources. These dusty galaxies always show extremely active star formation. The existence of DSFGs challenges current models, and whether proto-clusters traced by these galaxies are rare or common is still under debate. Our team has identified a large sample of optically dark galaxies in three CANDELS fields based on their H - [4.5] color (Wang et al., 2016b), see also Section 1.2.1. These optically dark galaxies generally fall in the galaxy main sequence, in contrast to those bright DSFGs. Owing to the abundant ancillary data in the CANDELS fields, we can construct galaxy number densities for these galaxies to see the environments they reside in as we did in Zhou et al. (2020). The difference shown by the proto-clusters traced by the bright DSFGs and by the main sequence optically-dark galaxies would constrain how dense environments affect the evolution of the galaxies therein.

In the era of the JWST: accurate measurements of stellar properties of the optically dark galaxies: Because of the extreme faintness of the optically dark galaxies, the stellar mass measurements have been limited to the photometries from the marginal detections or blended images, let alone the size measurements of their stellar component. With the high sensitivity and high angular resolution of the near-to-mid IR instruments on the upcoming JWST telescope, it is possible to obtain images with high enough quality to derive the stellar properties of these galaxies.

7.2.2 AGN feedback on high-z star-forming galaxies

As mentioned in 2.1.3, with the newly arrived GOODS-ALMA data (Cycle 5), I stacked the star-forming galaxies with and without AGNs using the merged GOODS-ALMA image (Cycle 3 and Cycle 5). I found that AGNs galaxies have up to 50% higher flux densities at 1.1 mm, indicating that AGNs do not decrease the SFRs hence do not quench these star-forming galaxies. This is not contradictary to the high AGN fraction found in the GOODS-ALMA detections (Franco et al., 2018) and is comparable to the excess of AGNs among starbursts at $z = 2$ in Rodighiero et al. (2019). I will keep working on the influence of AGNs on high-z star-forming galaxies.

Acknowledgement

It came as a surprise when I got to know that I could also do a joint-PhD at Université de Paris Saclay and it was already such a great pleasure to come to CEA as a visiting student for two years, thanks to everyone at CEA as a host and the financial support from China Scholar Council.

During the two years in France, I have gained a lot of knowledge not only from academia but also from everyone I met.

First of all, thank you, David. Thanks for hosting me at CEA and for mentoring me in this thesis. Your passion for science inspires me. It reminds me that being a researcher is not only a way to make a living, but more essentially a lifestyle. A lifestyle to stay curious about everything, to observe what is happening around us, to crack down what is behind what we see. It reminds me of how I was originally fascinated about science: to think, to ask questions originated from my daily life and finally to describe, to explain, and to predict these phenomena. I am grateful for your patience with me, for explaining to me the big pictures and for so much help with my life in France.

Thanks Emanuele for always taking so much time for the Journal Club and for the valuable discussions, your door is always open when I need help. Thanks also to many other people, Jérôme, Alain, Pascale, Laure, Tao, Corentin, Benjamin, Frederic, Emeric, Koryo for always being so warm-hearted, I have learnt a lot from you.

And all the friends at CEA, my two years at CEA would not have been so fruitful and unforgettable without you. Max, my office mate, you have been always helping me in the most critical time. You offered me valuable suggestions when I got stuck at work. And our tea/coffee breaks, bicycle trips, cheese and wine... Chiara, I feel so lucky to have had you by my side during all these adventures (the opening day, the D-day, the interviews with the committees... and our trip to Giverny, hanging out in Paris). Antonello, you are one of the old friends since I came to CEA for a short internship three years ago. You have been always sharing your good ideas with me. I am so grateful for your immediate help after my laptop was stolen. Anna, you always have the magic to make the atmosphere so lively and cheerful. Ivan, you are so organized and taking care of everyone of us. Baptise and Solène, you introduced to me the French culture and shared with me so many fun facts about life in France. Dangning, thanks to you, our "2019 Chinese New Year's Eve dinner" was such a success. You also offered me so many useful tips as an experienced "Chinese in France". And many other friends I met at CEA: Rose, Maud, Valeska, Benjamin, Antigone, Anita, Daizhong, Francesco, Jeremy.

And my life at the center of the world, Gif-sur-Yvette: Thank you, Judica, for hosting me at your place. You have been like a mother to teach me how to take care of myself in your own special way, and have shown me how to think critically, how to take actions actively to solve problems efficiently.

Thank you, Pascale. You have never regarded me as an outsider, and have always kindly invited me to all kinds of activities. This makes me feel integrated to the life in France and so much less lonely when I was in France.

And many thanks to all my friends, my teachers and my family back in China, what I want to say to you are included in the Chinese version of my thesis. Thanks Mum and Dad for your unconditional support of all time.

Merci Anoine. Mille mercis pour ton grand soutien lors de ma thèsis et l'écriture de ce manuscript. Merci d'être toujours là et de me motiver. Merci d'être venu dans ma vie.

Bibliography

Accurso, G., A. Saintonge, T. G. Bisbas, and S. Viti (Jan. 2017a). "Radiative transfer meets Bayesian statistics: where does a galaxy's [C II] emission come from?" In: MNRAS 464.3, pp. 3315–3330. arXiv: 1607.03488 [astro-ph.GA] (cit. on p. 15).

Accurso, G., A. Saintonge, B. Catinella, et al. (Oct. 2017b). "Deriving a multivariate α_{CO} conversion function using the [C II]/CO (1-0) ratio and its application to molecular gas scaling relations". In: MNRAS 470.4, pp. 4750–4766. arXiv: 1702.03888 [astro-ph.GA] (cit. on p. 58).

Allen, J. T., S. M. Croom, I. S. Konstantopoulos, et al. (Jan. 2015). "The SAMI Galaxy Survey: Early Data Release". In: MNRAS 446, pp. 1567–1583. arXiv: 1407.6068 (cit. on p. 67).

Allende Prieto, Carlos, David L. Lambert, and Martin Asplund (July 2001). "The Forbidden Abundance of Oxygen in the Sun". In: ApJ 556.1, pp. L63–L66. arXiv: astro-ph/0106360 [astro-ph] (cit. on p. 83).

Aloisi, A., G. Clementini, M. Tosi, et al. (Oct. 2007a). "I Zw 18 Revisited with HST ACS and Cepheids: New Distance and Age". In: ApJ 667.2, pp. L151–L154. arXiv: 0707.2371 [astro-ph] (cit. on p. 58).

– (Oct. 2007b). "I Zw 18 Revisited with HST ACS and Cepheids: New Distance and Age". In: ApJ 667.2, pp. L151–L154. arXiv: 0707.2371 [astro-ph] (cit. on p. 85).

Andrews, B. H. and P. Martini (Mar. 2013). "The Mass-Metallicity Relation with the Direct Method on Stacked Spectra of SDSS Galaxies". In: ApJ 765, 140, p. 140. arXiv: 1211.3418 (cit. on pp. 75, 76).

Ao, Yiping, Zheng Zheng, Christian Henkel, et al. (Mar. 2020). "Infalling gas in a Lyman-α blob". In: Nature Astronomy 4, pp. 670–674. arXiv: 2003.06099 [astro-ph.GA] (cit. on p. 17).

Ashby, M. L. N., S. P. Willner, G. G. Fazio, et al. (June 2015). "S-CANDELS: The Spitzer-Cosmic Assembly Near-Infrared Deep Extragalactic Survey. Survey Design, Photometry, and Deep IRAC Source Counts". In: ApJS 218, 33, p. 33. arXiv: 1506.01323 (cit. on pp. 38, 40, 44).

Asplund, Martin, Nicolas Grevesse, A. Jacques Sauval, and Pat Scott (Sept. 2009). "The Chemical Composition of the Sun". In: ARA&A 47.1, pp. 481–522. arXiv: 0909.0948 [astro-ph.SR] (cit. on p. 57).

Baldry, I. K., S. P. Driver, J. Loveday, et al. (Mar. 2012). "Galaxy And Mass Assembly (GAMA): the galaxy stellar mass function at z 0.06". In: MNRAS 421, pp. 621–634. arXiv: 1111.5707 (cit. on p. 69).

Baldry, Ivan K., Karl Glazebrook, Jon Brinkmann, et al. (Jan. 2004). "Quantifying the Bimodal Color-Magnitude Distribution of Galaxies". In: ApJ 600.2, pp. 681–694. arXiv: astro-ph/0309710 [astro-ph] (cit. on pp. 3, 4).

Baldwin, J. A., M. M. Phillips, and R. Terlevich (Feb. 1981). "Classification parameters for the emission-line spectra of extragalactic objects". In: PASP 93, pp. 5–19 (cit. on p. 69).

Bassett, R., K. Glazebrook, D. B. Fisher, et al. (Aug. 2014). "DYNAMO - II. Coupled stellar and ionized-gas kinematics in two low-redshift clumpy discs". In: MNRAS 442, pp. 3206–3221. arXiv: 1405.6753 (cit. on p. 72).

Baugh, C. M., S. Cole, and C. S. Frenk (Dec. 1996). "Evolution of the Hubble sequence in hierarchical models for galaxy formation". In: MNRAS 283, pp. 1361–1378. eprint: astro-ph/9602085 (cit. on pp. 18, 65).

Behroozi, Peter S., Risa H. Wechsler, and Charlie Conroy (2013). “The Average Star Formation Histories of Galaxies in Dark Matter Halos from z = 0-8”. In: ApJ 770.1, 57, p. 57. arXiv: 1207.6105 [astro-ph.CO] (cit. on p. 53).

Bekiaris, G., K. Glazebrook, C. J. Fluke, and R. Abraham (Jan. 2016). “Kinematic modelling of disc galaxies using graphics processing units”. In: MNRAS 455.1, pp. 754–784. arXiv: 1510.01815 [astro-ph.IM] (cit. on p. 20).

Bell, Eric F., Christian Wolf, Klaus Meisenheimer, et al. (June 2004). “Nearly 5000 Distant Early-Type Galaxies in COMBO-17: A Red Sequence and Its Evolution since z∼1”. In: ApJ 608.2, pp. 752–767. arXiv: astro-ph/0303394 [astro-ph] (cit. on pp. 3, 4).

Bendo, G. J., M. Baes, S. Bianchi, et al. (Mar. 2015). “The identification of dust heating mechanisms in nearby galaxies using Herschel 160/250 and 250/350 μm surface brightness ratios”. In: MNRAS 448.1, pp. 135–167. arXiv: 1409.1815 [astro-ph.GA] (cit. on pp. 92, 94).

Bergvall, Nils and Jari Ronnback (Apr. 1995). “ESO 146-G14, a retarded disc galaxy”. In: MNRAS 273.3, pp. 603–614 (cit. on p. 84).

Béthermin, Matthieu, Emanuele Daddi, Georgios Magdis, et al. (Jan. 2015). “Evolution of the dust emission of massive galaxies up to z = 4 and constraints on their dominant mode of star formation”. In: A&A 573, A113, A113. arXiv: 1409.5796 [astro-ph.GA] (cit. on p. 7).

Bigiel, F., A. Leroy, F. Walter, et al. (Dec. 2008). “The Star Formation Law in Nearby Galaxies on Sub-Kpc Scales”. In: AJ 136.6, pp. 2846–2871. arXiv: 0810.2541 [astro-ph] (cit. on pp. 16, 17, 92).

Bigiel, F., A. K. Leroy, F. Walter, et al. (Apr. 2011). “A Constant Molecular Gas Depletion Time in Nearby Disk Galaxies”. In: ApJ 730.2, L13, p. L13. arXiv: 1102.1720 [astro-ph.CO] (cit. on pp. 17, 62).

Blain, Andrew W., Ian Smail, R. J. Ivison, J. P. Kneib, and David T. Frayer (2002). “Submillimeter galaxies”. In: Physics Reports 369.2, pp. 111–176. arXiv: astro-ph/0202228 [astro-ph] (cit. on pp. 11, 27).

Bland-Hawthorn, J., J. Bryant, G. Robertson, et al. (Jan. 2011). “Hexabundles: imaging fiber arrays for low-light astronomical applications”. In: Optics Express 19, p. 2649 (cit. on p. 67).

Bolatto, Alberto D., James M. Jackson, and James G. Ingalls (Mar. 1999). “A Semianalytical Model for the Observational Properties of the Dominant Carbon Species at Different Metallicities”. In: ApJ 513.1, pp. 275–286. arXiv: astro-ph/9812181 [astro-ph] (cit. on p. 62).

Bolatto, Alberto D., Mark Wolfire, and Adam K. Leroy (Aug. 2013). “The CO-to-H_2 Conversion Factor”. In: ARA&A 51.1, pp. 207–268. arXiv: 1301.3498 [astro-ph.GA] (cit. on pp. 15, 16, 57).

Boquien, M., D. Burgarella, Y. Roehlly, et al. (2019). “CIGALE: a python Code Investigating GALaxy Emission”. In: A&A 622, A103, A103. arXiv: 1811.03094 [astro-ph.GA] (cit. on pp. 33, 45).

Bouché, N., H. Carfantan, I. Schroetter, L. Michel-Dansac, and T. Contini (Sept. 2015). “GalPak^{3D}: A Bayesian Parametric Tool for Extracting Morphokinematics of Galaxies from 3D Data”. In: AJ 150.3, 92, p. 92. arXiv: 1501.06586 [astro-ph.IM] (cit. on p. 20).

Bouwens, R. J., G. D. Illingworth, P. A. Oesch, et al. (Aug. 2012). “UV-continuum Slopes at z ∼4-7 from the HUDF09+ERS+CANDELS Observations: Discovery of a Well-defined UV Color-Magnitude Relationship for z >= 4 Star-forming Galaxies”. In: ApJ 754.2, 83, p. 83. arXiv: 1109.0994 [astro-ph.CO] (cit. on p. 5).

Brammer, G. B., P. G. van Dokkum, and P. Coppi (Oct. 2008). “EAZY: A Fast, Public Photometric Redshift Code”. In: ApJ 686, pp. 1503–1513. arXiv: 0807.1533 (cit. on pp. 32, 33, 36, 48).

Brinchmann, J., S. Charlot, S. D. M. White, et al. (July 2004). “The physical properties of star-forming galaxies in the low-redshift Universe”. In: MNRAS 351.4, pp. 1151–1179. arXiv: astro-ph/0311060 [astro-ph] (cit. on p. 5).

Brodwin, M., S. A. Stanford, A. H. Gonzalez, et al. (Dec. 2013). “The Era of Star Formation in Galaxy Clusters”. In: ApJ 779, 138, p. 138. arXiv: 1310.6039 (cit. on p. 29).

Bruzual, G. and S. Charlot (Oct. 2003). “Stellar population synthesis at the resolution of 2003”. In: MNRAS 344, pp. 1000–1028. eprint: astro-ph/0309134 (cit. on p. 32).

Bryant, J. J., J. Bland-Hawthorn, L. M. R. Fogarty, J. S. Lawrence, and S. M. Croom (Feb. 2014). “Focal ratio degradation in lightly fused hexabundles”. In: MNRAS 438, pp. 869–877. arXiv: 1311.6865 [astro-ph.IM] (cit. on p. 67).

Bryant, J. J., M. S. Owers, A. S. G. Robotham, et al. (Mar. 2015). “The SAMI Galaxy Survey: instrument specification and target selection”. In: MNRAS 447, pp. 2857–2879. arXiv: 1407.7335 (cit. on pp. 19, 66, 67, 70).

Bundy, K., M. A. Bershady, D. R. Law, et al. (Jan. 2015). “Overview of the SDSS-IV MaNGA Survey: Mapping nearby Galaxies at Apache Point Observatory”. In: ApJ 798, 7, p. 7. arXiv: 1412.1482 (cit. on p. 66).

Calzetti, D., L. Armus, R. C. Bohlin, et al. (Apr. 2000). “The Dust Content and Opacity of Actively Star-forming Galaxies”. In: ApJ 533, pp. 682–695. eprint: astro-ph/9911459 (cit. on pp. 32, 33, 45, 46).

Calzetti, D., R. C. Kennicutt, C. W. Engelbracht, et al. (Sept. 2007). “The Calibration of Mid-Infrared Star Formation Rate Indicators”. In: ApJ 666.2, pp. 870–895. arXiv: 0705.3377 [astro-ph] (cit. on p. 92).

Capak, P. L., C. Carilli, G. Jones, et al. (June 2015). “Galaxies at redshifts 5 to 6 with systematically low dust content and high [C II] emission”. In: Nature 522.7557, pp. 455–458. arXiv: 1503.07596 [astro-ph.GA] (cit. on p. 57).

Capak, P. L., D. Riechers, N. Z. Scoville, et al. (Feb. 2011). “A massive protocluster of galaxies at a redshift of z˜5.3”. In: Nature 470, pp. 233–235. arXiv: 1101.3586 [astro-ph.CO] (cit. on p. 29).

Casasola, Viviana, Leslie Hunt, Françoise Combes, and Santiago García-Burillo (May 2015). “The resolved star-formation relation in nearby active galactic nuclei”. In: A&A 577, A135, A135. arXiv: 1503.00280 [astro-ph.GA] (cit. on p. 88).

Casey, Caitlin M., Desika Narayanan, and Asantha Cooray (Aug. 2014). “Dusty star-forming galaxies at high redshift”. In: Phys. Rep. 541.2, pp. 45–161. arXiv: 1402.1456 [astro-ph.CO] (cit. on pp. 10–12).

Castignani, G., F. Combes, and P. Salomé (Mar. 2020). “Environmental processing in cluster core galaxies at z = 1.7”. In: A&A 635, L10, p. L10. arXiv: 2001.05776 [astro-ph.GA] (cit. on p. 29).

Chabrier, G. (July 2003). “Galactic Stellar and Substellar Initial Mass Function”. In: PASP 115, pp. 763–795. eprint: astro-ph/0304382 (cit. on p. 29).

Charlot, S. and S. M. Fall (Aug. 2000). “A Simple Model for the Absorption of Starlight by Dust in Galaxies”. In: ApJ 539, pp. 718–731. eprint: astro-ph/0003128 (cit. on pp. 45, 46).

Chiang, Yi-Kuan, Roderik Overzier, and Karl Gebhardt (Dec. 2013). “Ancient Light from Young Cosmic Cities: Physical and Observational Signatures of Galaxy Proto-clusters”. In: ApJ 779.2, 127, p. 127. arXiv: 1310.2938 [astro-ph.CO] (cit. on p. 28).

Chiang, Yi-Kuan, Roderik A. Overzier, Karl Gebhardt, and Bruno Henriques (2017). “Galaxy Protoclusters as Drivers of Cosmic Star Formation History in the First 2 Gyr”. In: The Astrophysical Journal 844.2, L23, p. L23. arXiv: 1705.01634 [astro-ph.GA] (cit. on pp. 14, 28).

Cibinel, A., E. Daddi, F. Bournaud, et al. (Aug. 2017). “ALMA constraints on star-forming gas in a prototypical z = 1.5 clumpy galaxy: the dearth of CO(5-4) emission from UV-bright clumps”. In: MNRAS 469.4, pp. 4683–4704. arXiv: 1703.02550 [astro-ph.GA] (cit. on p. 11).

Cimatti, A., P. Cassata, L. Pozzetti, et al. (Apr. 2008). “GMASS ultradeep spectroscopy of galaxies at z ∼2. II. Superdense passive galaxies: how did they form and evolve?” In: A&A 482.1, pp. 21–42. arXiv: 0801.1184 [astro-ph] (cit. on p. 11).

Cooray, Asantha (Mar. 2016). “Extragalactic background light measurements and applications”. In: Royal Society Open Science 3.3, p. 150555. arXiv: 1602.03512 [astro-ph.CO] (cit. on p. 10).

Cormier, D., N. P. Abel, S. Hony, et al. (June 2019). “The Herschel Dwarf Galaxy Survey. II. Physical conditions, origin of [C II] emission, and porosity of the multiphase low-metallicity ISM”. In: A&A 626, A23, A23. arXiv: 1904.08434 [astro-ph.GA] (cit. on pp. 15, 58, 62).

Cormier, D., S. C. Madden, V. Lebouteiller, et al. (Apr. 2014). “The molecular gas reservoir of 6 low-metallicity galaxies from the Herschel Dwarf Galaxy Survey. A ground-based follow-up survey of CO(1-0), CO(2-1), and CO(3-2)”. In: A&A 564, A121, A121. arXiv: 1401.0563 [astro-ph.GA] (cit. on pp. 57, 60–62).

Cormier, D., S. C. Madden, V. Lebouteiller, et al. (June 2015). “The Herschel Dwarf Galaxy Survey. I. Properties of the low-metallicity ISM from PACS spectroscopy”. In: A&A 578, A53, A53. arXiv: 1502.03131 [astro-ph.GA] (cit. on pp. 15, 62).

Cowie, L. L., J. González-López, A. J. Barger, et al. (2018). “A Submillimeter Perspective on the GOODS Fields (SUPER GOODS). III. A Large Sample of ALMA Sources in the GOODS-S”. In: ApJ 865.2, 106, p. 106. arXiv: 1805.09424 [astro-ph.GA] (cit. on p. 38).

Cresci, G., E. K. S. Hicks, R. Genzel, et al. (May 2009). “The SINS Survey: Modeling the Dynamics of z ˜ 2 Galaxies and the High-z Tully-Fisher Relation”. In: ApJ 697, pp. 115–132. arXiv: 0902.4701 [astro-ph.CO] (cit. on p. 76).

Croom, S. M., J. S. Lawrence, J. Bland-Hawthorn, et al. (Mar. 2012). “The Sydney-AAO Multi-object Integral field spectrograph”. In: MNRAS 421, pp. 872–893. arXiv: 1112.3367 (cit. on pp. 19, 66, 67).

Croxall, Kevin V., Liese van Zee, Henry Lee, et al. (Nov. 2009). “Chemical Abundances of Seven Irregular and Three Tidal Dwarf Galaxies in the M81 Group”. In: ApJ 705.1, pp. 723–738. arXiv: 0910.3162 [astro-ph.GA] (cit. on p. 84).

Cucciati, O., B. C. Lemaux, G. Zamorani, et al. (Nov. 2018). “The progeny of a cosmic titan: a massive multi-component proto-supercluster in formation at z = 2.45 in VUDS”. In: A&A 619, A49, A49. arXiv: 1806.06073 [astro-ph.CO] (cit. on pp. 49, 52).

da Cunha, E., S. Charlot, and D. Elbaz (Aug. 2008). “A simple model to interpret the ultraviolet, optical and infrared emission from galaxies”. In: MNRAS 388, pp. 1595–1617. arXiv: 0806.1020 (cit. on pp. 45, 46).

da Cunha, E., F. Walter, I. R. Smail, et al. (2015). “An ALMA Survey of Sub-millimeter Galaxies in the Extended Chandra Deep Field South: Physical Properties Derived from Ultraviolet-to-radio Modeling”. In: ApJ 806.1, 110, p. 110. arXiv: 1504.04376 [astro-ph.GA] (cit. on pp. 11, 28).

Daddi, E., F. Bournaud, F. Walter, et al. (Apr. 2010a). “Very High Gas Fractions and Extended Gas Reservoirs in z = 1.5 Disk Galaxies”. In: ApJ 713, pp. 686–707. arXiv: 0911.2776 (cit. on pp. 7, 18, 65).

Daddi, E., A. Cimatti, A. Renzini, et al. (Dec. 2004). “A New Photometric Technique for the Joint Selection of Star-forming and Passive Galaxies at 1.4 <∼z <∼2.5”. In: ApJ 617.2, pp. 746–764. arXiv: astro-ph/0409041 [astro-ph] (cit. on p. 4).

Daddi, E., H. Dannerbauer, D. Stern, et al. (Apr. 2009). “Two Bright Submillimeter Galaxies in a z = 4.05 Protocluster in Goods-North, and Accurate Radio-Infrared Photometric Redshifts”. In: ApJ 694, pp. 1517–1538. arXiv: 0810.3108 (cit. on pp. 5, 29).

Daddi, E., M. Dickinson, G. Morrison, et al. (2007). “Multiwavelength Study of Massive Galaxies at z∼2. I. Star Formation and Galaxy Growth”. In: ApJ 670.1, pp. 156–172. arXiv: 0705.2831 [astro-ph] (cit. on pp. 5, 28).

Daddi, E., D. Elbaz, F. Walter, et al. (May 2010b). “Different Star Formation Laws for Disks Versus Starbursts at Low and High Redshifts”. In: ApJ 714.1, pp. L118–L122. arXiv: 1003.3889 [astro-ph.CO] (cit. on p. 16).

Daddi, E., F. Valentino, R. M. Rich, et al. (June 2020). “Three Lyman-alpha emitting filaments converging to a massive galaxy group at z=2.91: a case for cold gas infall”. In: arXiv e-prints, arXiv:2006.11089, arXiv:2006.11089. arXiv: 2006.11089 [astro-ph.GA] (cit. on p. 17).

Dale, Daniel A., George Helou, Georgios E. Magdis, et al. (Mar. 2014). “A Two-parameter Model for the Infrared/Submillimeter/Radio Spectral Energy Distributions of Galaxies and Active Galactic Nuclei”. In: ApJ 784.1, 83, p. 83. arXiv: 1402.1495 [astro-ph.GA] (cit. on pp. 88, 89).

Danielson, A. L. R., A. M. Swinbank, Ian Smail, et al. (May 2017). “An ALMA Survey of Submillimeter Galaxies in the Extended Chandra Deep Field South: Spectroscopic Redshifts”. In: ApJ 840.2, 78, p. 78. arXiv: 1705.03503 [astro-ph.GA] (cit. on p. 11).

Davidzon, I., O. Ilbert, C. Laigle, et al. (2017). “The COSMOS2015 galaxy stellar mass function . Thirteen billion years of stellar mass assembly in ten snapshots”. In: A&A 605, A70, A70. arXiv: 1701.02734 [astro-ph.GA] (cit. on p. 46).

De Lucia, G. and J. Blaizot (Feb. 2007). “The hierarchical formation of the brightest cluster galaxies”. In: MNRAS 375, pp. 2–14. eprint: astro-ph/0606519 (cit. on pp. 28, 45).

Decarli, Roberto, Fabian Walter, Jorge Gónzalez-López, et al. (Sept. 2019). “The ALMA Spectroscopic Survey in the HUDF: CO Luminosity Functions and the Molecular Gas Content of Galaxies through Cosmic History”. In: ApJ 882.2, 138, p. 138. arXiv: 1903.09164 [astro-ph.GA] (cit. on pp. 12, 13).

Dekel, A., Y. Birnboim, G. Engel, et al. (Jan. 2009). “Cold streams in early massive hot haloes as the main mode of galaxy formation”. In: Nature 457.7228, pp. 451–454. arXiv: 0808.0553 [astro-ph] (cit. on pp. 1, 17, 19).

Delhaize, J., V. Smolčić, I. Delvecchio, et al. (June 2017). “The VLA-COSMOS 3 GHz Large Project: The infrared-radio correlation of star-forming galaxies and AGN to z 6”. In: A&A 602, A4, A4. arXiv: 1703.09723 (cit. on pp. 34, 40, 45).

Delvecchio, I., V. Smolčić, G. Zamorani, et al. (June 2017). “The VLA-COSMOS 3 GHz Large Project: AGN and host-galaxy properties out to z $\lesssim$ 6”. In: A&A 602, A3, A3. arXiv: 1703.09720 [astro-ph.GA] (cit. on p. 34).

Díaz-Santos, T., L. Armus, V. Charmandaris, et al. (Sept. 2013). “Explaining the [C II]157.7 μm Deficit in Luminous Infrared Galaxies—First Results from a Herschel/PACS Study of the GOALS Sample”. In: ApJ 774.1, 68, p. 68. arXiv: 1307.2635 [astro-ph.CO] (cit. on p. 7).

Dib, S., E. Bell, and A. Burkert (Feb. 2006). “The Supernova Rate-Velocity Dispersion Relation in the Interstellar Medium”. In: ApJ 638, pp. 797–810. eprint: astro-ph/0506339 (cit. on pp. 75–77).

DiTeodoro, E. M. and F. Fraternali (Aug. 2015). “^{3D} BAROLO: a new 3D algorithm to derive rotation curves of galaxies”. In: MNRAS 451.3, pp. 3021–3033. arXiv: 1505.07834 [astro-ph.GA] (cit. on p. 20).

Dole, H., G. Lagache, J. L. Puget, et al. (May 2006). “The cosmic infrared background resolved by Spitzer. Contributions of mid-infrared galaxies to the far-infrared background”. In: A&A 451.2, pp. 417–429. arXiv: astro-ph/0603208 [astro-ph] (cit. on p. 11).

Draine, B. T., D. A. Dale, G. Bendo, et al. (July 2007). “Dust Masses, PAH Abundances, and Starlight Intensities in the SINGS Galaxy Sample”. In: ApJ 663.2, pp. 866–894. arXiv: astro-ph/0703213 [astro-ph] (cit. on pp. 15, 45, 60).

Draine, B. T. and Aigen Li (Apr. 2001). “Infrared Emission from Interstellar Dust. I. Stochastic Heating of Small Grains”. In: ApJ 551.2, pp. 807–824. arXiv: astro-ph/0011318 [astro-ph] (cit. on p. 88).

– (Mar. 2007). “Infrared Emission from Interstellar Dust. IV. The Silicate-Graphite-PAH Model in the Post-Spitzer Era”. In: ApJ 657.2, pp. 810–837. arXiv: astro-ph/0608003 [astro-ph] (cit. on p. 83).

Dunlop, J. S., R. J. McLure, A. D. Biggs, et al. (Apr. 2017). “A deep ALMA image of the Hubble Ultra Deep Field”. In: MNRAS 466, pp. 861–883. arXiv: 1606.00227 (cit. on pp. 12, 13, 28, 30).

Elbaz, D., E. Daddi, D. Le Borgne, et al. (June 2007). “The reversal of the star formation-density relation in the distant universe”. In: A&A 468, pp. 33–48. eprint: astro-ph/0703653 (cit. on pp. 5, 27, 29).

Elbaz, D., M. Dickinson, H. S. Hwang, et al. (Sept. 2011). “GOODS-Herschel: an infrared main sequence for star-forming galaxies”. In: A&A 533, A119, A119. arXiv: 1105.2537 (cit. on pp. 5, 7, 28).

Elbaz, D., R. Leiton, N. Nagar, et al. (Aug. 2018). “Starbursts in and out of the star-formation main sequence”. In: A&A 616, A110, A110. arXiv: 1711.10047 (cit. on pp. 11, 28).

Elmegreen, B. G. (Mar. 2009). “Star Formation in Disks: Spiral Arms, Turbulence, and Triggering Mechanisms”. In: The Galaxy Disk in Cosmological Context. Ed. by J. Andersen, Nordströara, B. m, and J. Bland-Hawthorn. Vol. 254. IAU Symposium, pp. 289–300. arXiv: 0810.5406 (cit. on p. 66).

Elmegreen, B. G. and J. Scalo (Sept. 2004). “Interstellar Turbulence I: Observations and Processes”. In: ARA&A 42, pp. 211–273. eprint: astro-ph/0404451 (cit. on p. 66).

Elmegreen, Bruce G., Monica Rubio, Deidre A. Hunter, et al. (Mar. 2013). “Carbon monoxide in clouds at low metallicity in the dwarf irregular galaxy WLM”. In: Nature 495.7442, pp. 487–489. arXiv: 1310.4322 [astro-ph.GA] (cit. on p. 62).

Engelbracht, C. W., K. D. Gordon, G. H. Rieke, et al. (July 2005). “Metallicity Effects on Mid-Infrared Colors and the 8 μm PAH Emission in Galaxies”. In: ApJ 628.1, pp. L29–L32. arXiv: astro-ph/0506214 [astro-ph] (cit. on p. 83).

Engelbracht, C. W., G. H. Rieke, K. D. Gordon, et al. (May 2008). “Metallicity Effects on Dust Properties in Starbursting Galaxies”. In: ApJ 678.2, pp. 804–827. arXiv: 0801.1700 [astro-ph] (cit. on p. 83).

Event Horizon Telescope Collaboration, Kazunori Akiyama, Antxon Alberdi, et al. (Apr. 2019). “First M87 Event Horizon Telescope Results. I. The Shadow of the Supermassive Black Hole”. In: ApJ 875.1, L1, p. L1. arXiv: 1906.11238 [astro-ph.GA] (cit. on p. 2).

Federrath, C., G. Chabrier, J. Schober, et al. (2011). “Mach Number Dependence of Turbulent Magnetic Field Amplification: Solenoidal versus Compressive Flows”. In: Phys. Rev. Lett. 107 (11), p. 114504 (cit. on p. 79).

Federrath, C. and R. S. Klessen (Dec. 2012). “The Star Formation Rate of Turbulent Magnetized Clouds: Comparing Theory, Simulations, and Observations”. In: ApJ 761, 156, p. 156. arXiv: 1209.2856 [astro-ph.SR] (cit. on pp. 65, 79).

Federrath, C., R. S. Klessen, and W. Schmidt (Dec. 2008). “The Density Probability Distribution in Compressible Isothermal Turbulence: Solenoidal versus Compressive Forcing”. In: ApJ 688, L79, p. L79. arXiv: 0808.0605 (cit. on p. 79).

Federrath, C., J. M. Rathborne, S. N. Longmore, et al. (Dec. 2016). “The Link between Turbulence, Magnetic Fields, Filaments, and Star Formation in the Central Molecular Zone Cloud G0.253+0.016”. In: ApJ 832, 143, p. 143. arXiv: 1609.05911 (cit. on pp. 19, 66, 78, 79).

– (Jan. 2017). “The link between solenoidal turbulence and slow star formation in G0.253+0.016”. In: The Multi-Messenger Astrophysi Ed. by R. M. Crocker, S. N. Longmore, and G. V. Bicknell. Vol. 322. IAU Symposium, pp. 123–128. arXiv: 1609.08726 [astro-ph.SR] (cit. on pp. 19, 66, 78, 79).

Federrath, C., J. Roman-Duval, R. S. Klessen, W. Schmidt, and M.-M. Mac Low (Mar. 2010). “Comparing the statistics of interstellar turbulence in simulations and observations. Solenoidal versus compressive turbulence forcing”. In: A&A 512, A81, A81. arXiv: 0905.1060 [astro-ph.SR] (cit. on p. 79).

Feldmann, Robert (May 2015). “The equilibrium view on dust and metals in galaxies: Galactic outflows drive low dust-to-metal ratios in dwarf galaxies”. In: MNRAS 449.3, pp. 3274–3292. arXiv: 1412.2755 [astro-ph.GA] (cit. on pp. 83, 95).

Fisher, David B., Alberto D. Bolatto, Rodrigo Herrera-Camus, et al. (Jan. 2014). “The rarity of dust in metal-poor galaxies”. In: Nature 505.7482, pp. 186–189 (cit. on p. 84).

Fontana, A., J. S. Dunlop, D. Paris, et al. (Oct. 2014). “The Hawk-I UDS and GOODS Survey (HUGS): Survey design and deep K-band number counts”. In: A&A 570, A11, A11. arXiv: 1409.7082 (cit. on p. 31).

Forrest, B., K.-V. H. Tran, A. Broussard, et al. (Mar. 2017). “Discovery of Extreme [O III]+Hβ Emitting Galaxies Tracing an Overdensity at z
3.5 in CDF-South”. In: ApJ 838, L12, p. L12. arXiv: 1703.03814 (cit. on pp. 32, 50, 52).

Forrest, Ben, Marianna Annunziatella, Gillian Wilson, et al. (2019). “An Extremely Massive Quiescent Galaxy at $z = 3.493$: Evidence of Insufficiently Rapid Quenching Mechanisms in Theoretical Models”. In: arXiv e-prints, arXiv:1910.10158, arXiv:1910.10158. arXiv: 1910.10158 [astro-ph.GA] (cit. on p. 46).

Förster Schreiber, N. M., R. Genzel, N. Bouché, et al. (Dec. 2009). “The SINS Survey: SINFONI Integral Field Spectroscopy of z ˜ 2 Star-forming Galaxies”. In: ApJ 706, pp. 1364–1428. arXiv: 0903.1872 [astro-ph.CO] (cit. on pp. 19, 65, 76).

Franck, J. R. and S. S. McGaugh (2016). “The Candidate Cluster and Protocluster Catalog (CCPC) of Spectroscopically Identified Structures Spanning 2.74 < z < 3.71”. In: ApJ 817.2, 158, p. 158. arXiv: 1512.04956 [astro-ph.GA] (cit. on pp. 50–52).

Franco, M., D. Elbaz, M. Béthermin, et al. (2018). “GOODS-ALMA: 1.1 mm galaxy survey. I. Source catalog and optically dark galaxies”. In: A&A 620, A152, A152. arXiv: 1803.00157 [astro-ph.GA] (cit. on pp. 12, 21, 28–31, 35, 36, 38, 40, 43, 46, 48, 49, 54, 99).

Franco, M., D. Elbaz, L. Zhou, et al. (May 2020a). “GOODS-ALMA: The slow downfall of star-formation in z = 2-3 massive galaxies”. In: arXiv e-prints, arXiv:2005.03043, arXiv:2005.03043. arXiv: 2005.03043 [astro-ph.GA] (cit. on pp. 11, 23, 33, 34, 40).

Franco, M., D. Elbaz, L. Zhou, et al. (May 2020b). “GOODS-ALMA: Using IRAC and VLA to probe fainter millimeter galaxies”. In: arXiv e-prints, arXiv:2005.03040, arXiv:2005.03040. arXiv: 2005.03040 [astro-ph.GA] (cit. on pp. 12, 13, 23, 24, 30, 38, 40, 41, 43).

Fumagalli, Michele, Mark R. Krumholz, and Leslie K. Hunt (Oct. 2010). “Testing Models for Molecular Gas Formation in Galaxies: Hydrostatic Pressure or Gas and Dust Shielding?” In: ApJ 722.1, pp. 919–936. arXiv: 1008.4137 [astro-ph.CO] (cit. on p. 60).

Galametz, M., R. C. Kennicutt, M. Albrecht, et al. (Sept. 2012). “Mapping the cold dust temperatures and masses of nearby KINGFISH galaxies with Herschel”. In: MNRAS 425.1, pp. 763–787. arXiv: 1207.1301 [astro-ph.CO] (cit. on pp. 88, 90).

Galametz, M., S. C. Madden, F. Galliano, et al. (Aug. 2011). “Probing the dust properties of galaxies up to submillimetre wavelengths. II. Dust-to-gas mass ratio trends with metallicity and the submm excess in dwarf galaxies”. In: A&A 532, A56, A56. arXiv: 1104.0827 [astro-ph.CO] (cit. on p. 60).

Galliano, F., S. C. Madden, A. P. Jones, et al. (Aug. 2003). “ISM properties in low-metallicity environments. II. The dust spectral energy distribution of NGC 1569”. In: A&A 407, pp. 159–176. arXiv: astro-ph/0306192 [astro-ph] (cit. on p. 60).

Gao, Yu and Philip M. Solomon (May 2004). “The Star Formation Rate and Dense Molecular Gas in Galaxies”. In: ApJ 606.1, pp. 271–290. arXiv: astro-ph/0310339 [astro-ph] (cit. on pp. 60, 61).

Genzel, R., A. Burkert, N. Bouché, et al. (Nov. 2008). “From Rings to Bulges: Evidence for Rapid Secular Galaxy Evolution at z ˜ 2 from Integral Field Spectroscopy in the SINS Survey”. In: ApJ 687, 59-77, pp. 59–77. arXiv: 0807.1184 (cit. on pp. 18, 65).

Genzel, R., N. M. Förster Schreiber, P. Lang, et al. (Apr. 2014). “The SINS/zC-SINF Survey of z ˜ 2 Galaxy Kinematics: Evidence for Gravitational Quenching”. In: ApJ 785, 75, p. 75. arXiv: 1310.3838 (cit. on p. 75).

Genzel, R., S. Newman, T. Jones, et al. (June 2011). “The Sins Survey of z ˜ 2 Galaxy Kinematics: Properties of the Giant Star-forming Clumps”. In: ApJ 733, 101, p. 101. arXiv: 1011.5360 (cit. on pp. 66, 72, 75, 76).

Genzel, R., N. M. Förster Schreiber, H. Übler, et al. (Mar. 2017). “Strongly baryon-dominated disk galaxies at the peak of galaxy formation ten billion years ago”. In: Nature 543.7645, pp. 397–401. arXiv: 1703.04310 [astro-ph.GA] (cit. on p. 72).

Genzel, R., L. J. Tacconi, D. Lutz, et al. (Feb. 2015). “Combined CO and Dust Scaling Relations of Depletion Time and Molecular Gas Fractions with Cosmic Time, Specific Star-formation Rate, and Stellar Mass”. In: ApJ 800.1, 20, p. 20. arXiv: 1409.1171 [astro-ph.GA] (cit. on pp. 7, 15).

Giacconi, R., A. Zirm, J. Wang, et al. (Apr. 2002). “Chandra Deep Field South: The 1 Ms Catalog”. In: ApJS 139, pp. 369–410 (cit. on p. 31).

Gil de Paz, Armando, Samuel Boissier, Barry F. Madore, et al. (Dec. 2007). “The GALEX Ultraviolet Atlas of Nearby Galaxies”. In: ApJS 173.2, pp. 185–255. arXiv: astro-ph/0606440 [astro-ph] (cit. on p. 92).

Gildas Team (May 2013). GILDAS: Grenoble Image and Line Data Analysis Software. ascl: 1305.010 (cit. on p. 31).

Ginolfi, M., R. Maiolino, T. Nagao, et al. (July 2017). “Molecular gas on large circumgalactic scales at z = 3.47”. In: MNRAS 468, pp. 3468–3483. arXiv: 1611.07026 (cit. on pp. 26, 45, 51, 52, 98).

Glazebrook, K. (Nov. 2013). “The Dawes Review 1: Kinematic Studies of Star-Forming Galaxies Across Cosmic Time”. In: PASA 30, e056, e056. arXiv: 1305.2469 (cit. on pp. 19, 65, 77).

Glover, S. C. O., C. Federrath, M. M. Mac Low, and R. S. Klessen (May 2010). “Modelling CO formation in the turbulent interstellar medium”. In: MNRAS 404.1, pp. 2–29. arXiv: 0907.4081 [astro-ph.SR] (cit. on p. 59).

Glover, S. C. O. and M. M. Mac Low (Mar. 2011). “On the relationship between molecular hydrogen and carbon monoxide abundances in molecular clouds”. In: MNRAS 412.1, pp. 337–350. arXiv: 1003.1340 [astro-ph.GA] (cit. on pp. 59, 62).

Gobat, R., P. Rosati, V. Strazzullo, et al. (2008). “Star formation histories of early-type galaxies at z = 1.2 in cluster and field environments”. In: A&A 488.3, pp. 853–860. arXiv: 0806.4537 [astro-ph] (cit. on p. 29).

Gómez-Guijarro, C., D. A. Riechers, R. Pavesi, et al. (Feb. 2019). “Confirming Herschel Candidate Protoclusters from ALMA/VLA CO Observations”. In: ApJ 872.2, 117, p. 117. arXiv: 1905.08813 [astro-ph.GA] (cit. on p. 29).

González-López, Jorge, Mladen Novak, Roberto Decarli, et al. (July 2020). “The ALMA Spectroscopic Survey in the HUDF: Deep 1.2 mm Continuum Number Counts”. In: ApJ 897.1, 91, p. 91. arXiv: 2002.07199 [astro-ph.GA] (cit. on pp. 11, 13).

Green, A. W., K. Glazebrook, P. J. McGregor, et al. (Oct. 2010). “High star formation rates as the origin of turbulence in early and modern disk galaxies”. In: Nature 467, pp. 684–686. arXiv: 1010.1262 [astro-ph.GA] (cit. on p. 65).

Green, A. W., K. Glazebrook, P. J. McGregor, et al. (Jan. 2014). “DYNAMO - I. A sample of Hα-luminous galaxies with resolved kinematics”. In: MNRAS 437, pp. 1070–1095. arXiv: 1310.6082 (cit. on pp. 66, 72, 76–78).

Grenier, Isabelle A., Jean-Marc Casandjian, and Régis Terrier (Feb. 2005). “Unveiling Extensive Clouds of Dark Gas in the Solar Neighborhood”. In: Science 307.5713, pp. 1292–1295 (cit. on p. 57).

Griffin, M. J., A. Abergel, A. Abreu, et al. (July 2010). “The Herschel-SPIRE instrument and its in-flight performance”. In: A&A 518, L3, p. L3. arXiv: 1005.5123 [astro-ph.IM] (cit. on p. 86).

Gritschneder, M., T. Naab, S. Walch, A. Burkert, and F. Heitsch (Mar. 2009). “Driving Turbulence and Triggering Star Formation by Ionizing Radiation”. In: ApJ 694, pp. L26–L30. arXiv: 0901.2113 [astro-ph.SR] (cit. on p. 66).

Grogin, N. A., D. D. Kocevski, S. M. Faber, et al. (Dec. 2011). “CANDELS: The Cosmic Assembly Near-infrared Deep Extragalactic Legacy Survey”. In: ApJS 197, 35, p. 35. arXiv: 1105.3753 (cit. on p. 31).

Gruppioni, C., F. Pozzi, G. Rodighiero, et al. (June 2013). “The Herschel PEP/HerMES luminosity function - I. Probing the evolution of PACS selected Galaxies to z 4”. In: MNRAS 432.1, pp. 23–52. arXiv: 1302.5209 [astro-ph.CO] (cit. on p. 10).

Guaita, L., E. Pompei, M. Castellano, et al. (July 2020). “The VANDELS survey: Discovery of massive overdensities of galaxies at z>2”. In: arXiv e-prints, arXiv:2007.12314, arXiv:2007.12314. arXiv: 2007.12314 [astro-ph.GA] (cit. on p. 52).

Guo, Y., H. C. Ferguson, M. Giavalisco, et al. (Aug. 2013). “CANDELS Multi-wavelength Catalogs: Source Detection and Photometry in the GOODS-South Field”. In: ApJS 207, 24, p. 24. arXiv: 1308.4405 (cit. on pp. 14, 30, 31, 37, 39).

Hatsukade, Bunyo, Kotaro Kohno, Yuki Yamaguchi, et al. (2018). “ALMA twenty-six arcmin^2 survey of GOODS-S at one millimeter (ASAGAO): Source catalog and number counts”. In: PASJ 70.6, 105, p. 105. arXiv: 1808.04502 [astro-ph.GA] (cit. on pp. 12, 13, 28).

Hauser, M. G., R. G. Arendt, T. Kelsall, et al. (Nov. 1998). “The COBE Diffuse Infrared Background Experiment Search for the Cosmic Infrared Background. I. Limits and Detections”. In: ApJ 508.1, pp. 25–43. arXiv: astro-ph/9806167 [astro-ph] (cit. on p. 10).

Heckman, Timothy M. and Philip N. Best (Aug. 2014). “The Coevolution of Galaxies and Supermassive Black Holes: Insights from Surveys of the Contemporary Universe”. In: ARA&A 52, pp. 589–660. arXiv: 1403.4620 [astro-ph.GA] (cit. on p. 1).

Heinis, S., V. Buat, M. Béthermin, et al. (Feb. 2013). “HERMES: unveiling obscured star formation - the far-infrared luminosity function of ultraviolet-selected galaxies at z $\sim$ 1.5”. In: MNRAS 429.2, pp. 1113–1132. arXiv: 1211.4336 [astro-ph.CO] (cit. on p. 5).

Herenz, Edmund Christian, Tanya Urrutia, Lutz Wisotzki, et al. (Sept. 2017). “The MUSE-Wide survey: A first catalogue of 831 emission line galaxies”. In: A&A 606, A12, A12. arXiv: 1705.08215 [astro-ph.GA] (cit. on p. 44).

Ho, I., A. M. Medling, B. Groves, et al. (July 2016). “LZIFU: an emission-line fitting toolkit for integral field spectroscopy data”. In: ArXiv e-prints. arXiv: 1607.06561 (cit. on p. 67).

Ho, I.-T., L. J. Kewley, M. A. Dopita, et al. (Nov. 2014). “The SAMI Galaxy Survey: shocks and outflows in a normal star-forming galaxy”. In: MNRAS 444, pp. 3894–3910. arXiv: 1407.2411 (cit. on p. 67).

Hodge, J. A., I. Smail, F. Walter, et al. (2019). “ALMA Reveals Potential Evidence for Spiral Arms, Bars, and Rings in High-redshift Submillimeter Galaxies”. In: ApJ 876.2, 130, p. 130. arXiv: 1810.12307 [astro-ph.GA] (cit. on p. 11).

Hodge, Jacqueline A. and Elisabete da Cunha (Apr. 2020). “High-redshift star formation in the ALMA era”. In: arXiv e-prints, arXiv:2004.00934, arXiv:2004.00934. arXiv: 2004.00934 [astro-ph.GA] (cit. on p. 11).

Hubble, E. P. (Dec. 1926). “Extragalactic nebulae.” In: ApJ 64, pp. 321–369 (cit. on pp. 2, 3, 5).

Hubble, Edwin and Milton L. Humason (July 1931). “The Velocity-Distance Relation among Extra-Galactic Nebulae”. In: ApJ 74, p. 43 (cit. on p. 4).

Hughes, David H., Stephen Serjeant, James Dunlop, et al. (1998). “High-redshift star formation in the Hubble Deep Field revealed by a submillimetre-wavelength survey”. In: Nature 394.6690, pp. 241–247. arXiv: astro-ph/9806297 [astro-ph] (cit. on pp. 13, 28).

Hunt, L. K., K. K. Dyer, and T. X. Thuan (June 2005). “The radio continuum of the extremely metal-poor blue compact dwarf galaxy I Zw 18”. In: A&A 436.3, pp. 837–844 (cit. on p. 58).

Hunt, L. K., S. García-Burillo, V. Casasola, et al. (Nov. 2015a). “Molecular depletion times and the CO-to-H_2 conversion factor in metal-poor galaxies”. In: A&A 583, A114, A114. arXiv: 1509.04870 [astro-ph.GA] (cit. on pp. 57, 60–62).

– (Nov. 2015b). “Molecular depletion times and the CO-to-H_2 conversion factor in metal-poor galaxies”. In: A&A 583, A114, A114. arXiv: 1509.04870 [astro-ph.GA] (cit. on p. 94).

Hunt, L. K., L. Testi, V. Casasola, et al. (Jan. 2014). “ALMA observations of cool dust in a low-metallicity starburst, SBS 0335-052”. In: A&A 561, A49, A49. arXiv: 1312.0944 [astro-ph.GA] (cit. on pp. 84, 94, 95).

Hunt, Leslie K., Trinh X. Thuan, Yuri I. Izotov, and Marc Sauvage (Mar. 2010). “The Spitzer View of Low-Metallicity Star Formation. III. Fine-Structure Lines, Aromatic Features, and Molecules”. In: ApJ 712.1, pp. 164–187. arXiv: 1002.0991 [astro-ph.CO] (cit. on p. 94).

Israel, F. P. (Dec. 1997). “H_2 and its relation to CO in the LMC and other magellanic irregular galaxies”. In: A&A 328, pp. 471–482. arXiv: astro-ph/9709194 [astro-ph] (cit. on p. 62).

Izotov, Yuri I. and Trinh X. Thuan (Feb. 1999a). “Heavy-Element Abundances in Blue Compact Galaxies”. In: ApJ 511.2, pp. 639–659. arXiv: astro-ph/9811387 [astro-ph] (cit. on pp. 58, 62).

– (Feb. 1999b). “Heavy-Element Abundances in Blue Compact Galaxies”. In: ApJ 511.2, pp. 639–659. arXiv: astro-ph/9811387 [astro-ph] (cit. on p. 85).

Izotov, Yuri I., Trinh X. Thuan, and Valentin A. Lipovetsky (Jan. 1997). “The Primordial Helium Abundance: Systematic Effects and a New Determination”. In: ApJS 108.1, pp. 1–39 (cit. on p. 85).

Jin, S., E. Daddi, G. E. Magdis, et al. (Dec. 2019). “Discovery of Four Apparently Cold Dusty Galaxies at z=3.62—5.85 in the COSMOS Field: Direct Evidence of Cosmic Microwave Background Impact on High-redshift Galaxy Observables”. In: ApJ 887.2, 144, p. 144. arXiv: 1906.00040 [astro-ph.GA] (cit. on p. 31).

Jones, T. A., A. M. Swinbank, R. S. Ellis, J. Richard, and D. P. Stark (May 2010). “Resolved spectroscopy of gravitationally lensed galaxies: recovering coherent velocity fields in subluminous z ˜ 2-3 galaxies”. In: MNRAS 404, pp. 1247–1262. arXiv: 0910.4488 (cit. on p. 76).

Kauffmann, Guinevere, Timothy M. Heckman, Simon D. M. White, et al. (May 2003). “Stellar masses and star formation histories for 10^5 galaxies from the Sloan Digital Sky Survey”. In: MNRAS 341.1, pp. 33–53. arXiv: astro-ph/0204055 [astro-ph] (cit. on p. 4).

Kelvin, L. S., S. P. Driver, A. S. G. Robotham, et al. (Apr. 2012). “Galaxy And Mass Assembly (GAMA): Structural Investigation of Galaxies via Model Analysis”. In: MNRAS 421, pp. 1007–1039. arXiv: 1112.1956 (cit. on p. 69).

Kennicutt Robert C., Jr. (Jan. 1998a). “Star Formation in Galaxies Along the Hubble Sequence”. In: ARA&A 36, pp. 189–232. arXiv: astro-ph/9807187 [astro-ph] (cit. on p. 2).

– (1998b). “The Global Schmidt Law in Star-forming Galaxies”. In: ApJ 498.2, pp. 541–552. arXiv: astro-ph/9712213 [astro-ph] (cit. on pp. 16, 33).

Kennicutt, R. C., D. Calzetti, G. Aniano, et al. (Dec. 2011). “KINGFISH—Key Insights on Nearby Galaxies: A Far-Infrared Survey with Herschel: Survey Description and Image Atlas”. In: PASP 123.910, p. 1347. arXiv: 1111.4438 [astro-ph.CO] (cit. on pp. 84, 86).

Kennicutt Jr., R. C., P. Tamblyn, and C. E. Congdon (Nov. 1994). “Past and future star formation in disk galaxies”. In: ApJ 435, pp. 22–36 (cit. on p. 69).

Kennicutt, Robert C. and Neal J. Evans (Sept. 2012). “Star Formation in the Milky Way and Nearby Galaxies”. In: ARA&A 50, pp. 531–608. arXiv: 1204.3552 [astro-ph.GA] (cit. on pp. 15–17).

Kewley, L. J., M. A. Dopita, R. S. Sutherland, C. A. Heisler, and J. Trevena (July 2001). “Theoretical Modeling of Starburst Galaxies”. In: ApJ 556, pp. 121–140. eprint: astro-ph/0106324 (cit. on p. 69).

Klessen, R. S. and P. Hennebelle (Sept. 2010). “Accretion-driven turbulence as universal process: galaxies, molecular clouds, and protostellar disks”. In: A&A 520, A17, A17. arXiv: 0912.0288 (cit. on p. 66).

Kniazev, Alexei Y., Eva K. Grebel, Simon A. Pustilnik, Alexander G. Pramskij, and Daniel B. Zucker (Oct. 2005). “Spectrophotometry of Sextans A and B: Chemical Abundances of H II Regions and Planetary Nebulae”. In: AJ 130.4, pp. 1558–1573. arXiv: astro-ph/0502562 [astro-ph] (cit. on p. 84).

Kormendy, John and Luis C. Ho (Aug. 2013). “Coevolution (Or Not) of Supermassive Black Holes and Host Galaxies”. In: ARA&A 51.1, pp. 511–653. arXiv: 1304.7762 [astro-ph.CO] (cit. on p. 1).

Kravtsov, A. V. and S. Borgani (Sept. 2012). “Formation of Galaxy Clusters”. In: ARA&A 50, pp. 353–409. arXiv: 1205.5556 (cit. on p. 29).

Kriek, M., P. G. van Dokkum, I. Labbé, et al. (July 2009). “An Ultra-Deep Near-Infrared Spectrum of a Compact Quiescent Galaxy at z = 2.2”. In: ApJ 700, pp. 221–231. arXiv: 0905.1692 [astro-ph.CO] (cit. on p. 33).

Kruijssen, J. M. D. (Sept. 2016). “Towards a multi-scale understanding of the gas-star formation cycle in the Central Molecular Zone”. In: ArXiv e-prints. arXiv: 1609.08158 (cit. on p. 79).

Krumholz, M. R. and B. Burkhart (Dec. 2015). “Is Turbulence in the Interstellar Medium Driven by Feedback or Gravity? An Observational Test”. In: ArXiv e-prints. arXiv: 1512.03439 (cit. on pp. 19, 66).

– (May 2016). “Is turbulence in the interstellar medium driven by feedback or gravity? An observational test”. In: MNRAS 458, pp. 1671–1677. arXiv: 1512.03439 (cit. on pp. 19, 78).

Krumholz, M. R. and J. M. D. Kruijssen (Oct. 2015). “A dynamical model for the formation of gas rings and episodic starbursts near galactic centres”. In: MNRAS 453, pp. 739–757. arXiv: 1505.07111 (cit. on p. 79).

Krumholz, Mark R., Blakesley Burkhart, John C. Forbes, and Roland M. Crocker (June 2018). “A unified model for galactic discs: star formation, turbulence driving, and mass transport”. In: MNRAS 477.2, pp. 2716–2740. arXiv: 1706.00106 [astro-ph.GA] (cit. on pp. 19, 98).

Krumholz, Mark R. and Christopher D. Matzner (Oct. 2009). “The Dynamics of Radiation-pressure-dominated H II Regions”. In: ApJ 703.2, pp. 1352–1362. arXiv: 0906.4343 [astro-ph.SR] (cit. on p. 19).

Kunth, D. and G. Östlin (Jan. 2000). “The most metal-poor galaxies”. In: A&A Rev. 10, pp. 1–79. arXiv: astro-ph/9911094 [astro-ph] (cit. on p. 83).

Labbé, I., P. A. Oesch, G. D. Illingworth, et al. (Dec. 2015). “Ultradeep IRAC Imaging Over the HUDF and GOODS-South: Survey Design and Imaging Data Release”. In: ApJS 221, 23, p. 23. arXiv: 1507.08313 (cit. on p. 31).

Landy, Stephen D. and Alexander S. Szalay (July 1993). “Bias and Variance of Angular Correlation Functions”. In: ApJ 412, p. 64 (cit. on p. 53).

Lang, Philipp, E. Schinnerer, Ian Smail, et al. (July 2019). “Revealing the Stellar Mass and Dust Distributions of Submillimeter Galaxies at Redshift 2”. In: ApJ 879.1, 54, p. 54. arXiv: 1905.06960 [astro-ph.GA] (cit. on pp. 11, 12).

Larson, Richard B. (Nov. 1974). “Effects of supernovae on the early evolution of galaxies”. In: MNRAS 169, pp. 229–246 (cit. on p. 1).

Law, D. R., C. C. Steidel, D. K. Erb, et al. (June 2009). “The Kiloparsec-scale Kinematics of High-redshift Star-forming Galaxies”. In: ApJ 697, pp. 2057–2082. arXiv: 0901.2930 (cit. on p. 76).

Le Floc’h, Emeric, Casey Papovich, Hervé Dole, et al. (Oct. 2005). “Infrared Luminosity Functions from the Chandra Deep Field-South: The Spitzer View on the History of Dusty Star Formation at 0 <∼z <∼1”. In: ApJ 632.1, pp. 169–190. arXiv: astro-ph/0506462 [astro-ph] (cit. on p. 10).

Lehnert, M. D., L. Le Tiran, N. P. H. Nesvadba, et al. (July 2013). “On the self-regulation of intense star-formation in galaxies at z = 1-3”. In: A&A 555, A72, A72. arXiv: 1304.7734 (cit. on pp. 19, 65, 66, 72).

Lehnert, M. D., N. P. H. Nesvadba, L. Le Tiran, et al. (July 2009). “Physical Conditions in the Interstellar Medium of Intensely Star-Forming Galaxies at Redshift˜2”. In: ApJ 699, pp. 1660–1678. arXiv: 0902.2784 [astro-ph.CO] (cit. on pp. 19, 65, 66, 73–75, 78).

Lelli, F., M. Verheijen, F. Fraternali, and R. Sancisi (Jan. 2012). “Dynamics of starbursting dwarf galaxies: I Zw 18”. In: A&A 537, A72, A72. arXiv: 1110.6042 [astro-ph.CO] (cit. on pp. 59, 60).

Lemaître, G. (Mar. 1931). “Expansion of the universe, A homogeneous universe of constant mass and increasing radius accounting for the radial velocity of extra-galactic nebulae”. In: MNRAS 91, pp. 483–490 (cit. on p. 4).

Leroy, A., A. D. Bolatto, J. D. Simon, and L. Blitz (June 2005). “The Molecular Interstellar Medium of Dwarf Galaxies on Kiloparsec Scales: A New Survey for CO in Northern, IRAS-detected Dwarf Galaxies”. In: ApJ 625, pp. 763–784. eprint: astro-ph/0502302 (cit. on pp. 18, 65).

Leroy, A. K., F. Walter, E. Brinks, et al. (Dec. 2008a). “The Star Formation Efficiency in Nearby Galaxies: Measuring Where Gas Forms Stars Effectively”. In: AJ 136, pp. 2782–2845. arXiv: 0810.2556 (cit. on p. 92).

Leroy, Adam, John Cannon, Fabian Walter, Alberto Bolatto, and Axel Weiss (July 2007). “The Low CO Content of the Extremely Metal-poor Galaxy I Zw 18”. In: ApJ 663.2, pp. 990–994. arXiv: 0704.0862 [astro-ph] (cit. on pp. 57, 58, 63).

Leroy, Adam K., Alberto Bolatto, Karl Gordon, et al. (Aug. 2011). “The CO-to-H_2 Conversion Factor from Infrared Dust Emission across the Local Group”. In: ApJ 737.1, 12, p. 12. arXiv: 1102.4618 [astro-ph.CO] (cit. on pp. 15, 62).

Leroy, Adam K., Fabian Walter, Elias Brinks, et al. (Dec. 2008b). “The Star Formation Efficiency in Nearby Galaxies: Measuring Where Gas Forms Stars Effectively”. In: AJ 136.6, pp. 2782–2845. arXiv: 0810.2556 [astro-ph] (cit. on p. 62).

Li, Aigen, Shu Wang, Jian Gao, and B. W. Jiang (2015). “Dust in the Local Group”. In: Lessons from the Local Group: A Conference in p. 85 (cit. on p. 94).

Lilly, Simon J., C. Marcella Carollo, Antonio Pipino, Alvio Renzini, and Yingjie Peng (Aug. 2013). “Gas Regulation of Galaxies: The Evolution of the Cosmic Specific Star Formation Rate, the Metallicity-Mass-Star-formation Rate Relation, and the Stellar Content of Halos”. In: ApJ 772.2, 119, p. 119. arXiv: 1303.5059 [astro-ph.CO] (cit. on p. 18).

Lisenfeld, U., F. P. Israel, J. M. Stil, and A. Sievers (Feb. 2002). “(Sub)millimetre emission from NGC 1569: An abundance of very small grains”. In: A&A 382, pp. 860–871. arXiv: astro-ph/0112212 [astro-ph] (cit. on p. 60).

Liu, Daizhong, Yu Gao, Kate Isaak, et al. (2015). “High-J CO versus Far-infrared Relations in Normal and Starburst Galaxies”. In: ApJ 810.2, L14, p. L14. arXiv: 1504.05897 [astro-ph.GA] (cit. on pp. 36, 37).

Luo, B., W. N. Brandt, Y. Q. Xue, et al. (Jan. 2017). “The Chandra Deep Field-South Survey: 7 Ms Source Catalogs”. In: ApJS 228, 2, p. 2. arXiv: 1611.03501 (cit. on pp. 32, 34, 46).

Mac Low, M.-M. and R. S. Klessen (Jan. 2004). “Control of star formation by supersonic turbulence”. In: Reviews of Modern Physics 76, pp. 125–194. eprint: astro-ph/0301093 (cit. on pp. 19, 66).

Madau, Piero and Mark Dickinson (2014). “Cosmic Star-Formation History”. In: Annual Review of Astronomy and Astrophysics 52, pp. 415–486. arXiv: 1403.0007 [astro-ph.CO] (cit. on pp. 8, 9, 18, 65).

Madden, S. C., D. Cormier, S. Hony, et al. (Sept. 2020). “Tracing the total molecular gas in galaxies: [CII] and the CO-dark gas”. In: arXiv e-prints, arXiv:2009.00649, arXiv:2009.00649. arXiv: 2009.00649 [astro-ph.GA] (cit. on pp. 15, 16, 98).

Madden, S. C., A. Poglitsch, N. Geis, G. J. Stacey, and C. H. Townes (July 1997). “[C II] 158 Micron Observations of IC 10: Evidence for Hidden Molecular Hydrogen in Irregular Galaxies”. In: ApJ 483.1, pp. 200–209 (cit. on p. 94).

Madden, S. C., A. Rémy-Ruyer, M. Galametz, et al. (June 2013). “An Overview of the Dwarf Galaxy Survey”. In: PASP 125.928, p. 600. arXiv: 1305.2628 [astro-ph.GA] (cit. on pp. 84, 85, 94).

Madden, Suzanne C. (July 2000). “Effects of massive star formation on the ISM of dwarf galaxies”. In: New A Rev. 44.4-6, pp. 249–256. arXiv: astro-ph/0002046 [astro-ph] (cit. on p. 62).

Magdis, G. E., D. Elbaz, E. Daddi, et al. (May 2010). “A Multi-wavelength View of the Star Formation Activity at z ~3”. In: ApJ 714.2, pp. 1740–1745. arXiv: 1003.5773 [astro-ph.CO] (cit. on p. 5).

Magdis, Georgios E., E. Daddi, M. Béthermin, et al. (Nov. 2012). “The Evolving Interstellar Medium of Star-forming Galaxies since z = 2 as Probed by Their Infrared Spectral Energy Distributions”. In: ApJ 760.1, 6, p. 6. arXiv: 1210.1035 [astro-ph.CO] (cit. on pp. 7, 15).

Magnelli, B., D. Lutz, A. Saintonge, et al. (Jan. 2014). “The evolution of the dust temperatures of galaxies in the SFR-M_* plane up to z $\sim$ 2”. In: A&A 561, A86, A86. arXiv: 1311.2956 [astro-ph.CO] (cit. on p. 7).

Magnelli, B., P. Popesso, S. Berta, et al. (May 2013). “The deepest Herschel-PACS far-infrared survey: number counts and infrared luminosity functions from combined PEP/GOODS-H observations”. In: A&A 553, A132, A132. arXiv: 1303.4436 [astro-ph.CO] (cit. on pp. 10, 15).

Malhotra, Sangeeta, James E. Rhoads, K. Finkelstein, et al. (Jan. 2017). “Herschel Extreme Lensing Line Observations: [CII] Variations in Galaxies at Redshifts z=1-3”. In: ApJ 835.1, 110, p. 110 (cit. on p. 98).

Martin, Crystal L. (Mar. 1999). “Properties of Galactic Outflows: Measurements of the Feedback from Star Formation”. In: ApJ 513.1, pp. 156–160. arXiv: astro-ph/9810233 [astro-ph] (cit. on p. 1).

McCall, M. L., O. Vaduvescu, F. Pozo Nunez, et al. (Apr. 2012). “Fundamentals of the dwarf fundamental plane”. In: A&A 540, A49, A49. arXiv: 1204.1074 [astro-ph.CO] (cit. on p. 84).

McLure, R. J., L. Pentericci, A. Cimatti, et al. (Sept. 2018). “The VANDELS ESO public spectroscopic survey”. In: MNRAS 479, pp. 25–42. arXiv: 1803.07414 (cit. on pp. 32, 41, 42).

McMullin, J. P., B. Waters, D. Schiebel, W. Young, and K. Golap (2007). “CASA Architecture and Applications”. In: Astronomical Data Analysis Software and Systems XVI. Ed. by R. A. Shaw, F. Hill, and D. J. Bell. Vol. 376. Astronomical Society of the Pacific Conference Series, p. 127 (cit. on p. 30).

Medling, Anne M., Luca Cortese, Scott M. Croom, et al. (Apr. 2018). “The SAMI Galaxy Survey: spatially resolving the main sequence of star formation”. In: MNRAS 475.4, pp. 5194–5214. arXiv: 1801.04283 [astro-ph.GA] (cit. on p. 67).

Miller, T. B., S. C. Chapman, M. Aravena, et al. (Apr. 2018). “A massive core for a cluster of galaxies at a redshift of 4.3”. In: Nature 556.7702, pp. 469–472. arXiv: 1804.09231 [astro-ph.GA] (cit. on p. 29).

Mineo, S., M. Gilfanov, and R. Sunyaev (Nov. 2012). “X-ray emission from star-forming galaxies - II. Hot interstellarmedium”. In: MNRAS 426.3, pp. 1870–1883. arXiv: 1205.3715 [astro-ph.HE] (cit. on p. 23).

Mo, Houjun, Frank C. van den Bosch, and Simon White (2010). Galaxy Formation and Evolution (cit. on p. 1).

Moran, Sean M., Richard S. Ellis, Tommaso Treu, et al. (Apr. 2006). “GALEX Observations of “Passive Spirals” in the Cluster Cl 0024+17: Clues to the Formation of S0 Galaxies”. In: ApJ 641.2, pp. L97–L100. arXiv: astro-ph/0603182 [astro-ph] (cit. on p. 3).

Muñoz Arancibia, A. M., J. González-López, E. Ibar, et al. (Dec. 2018). “The ALMA Frontier Fields Survey. IV. Lensing-corrected 1.1 mm number counts in Abell 2744, MACS J0416.1-2403 and MACS J1149.5+2223”. In: A&A 620, A125, A125. arXiv: 1712.03983 [astro-ph.GA] (cit. on p. 13).

Muldrew, Stuart I., Nina A. Hatch, and Elizabeth A. Cooke (2015). “What are protoclusters? - Defining high-redshift galaxy clusters and protoclusters”. In: MNRAS 452.3, pp. 2528–2539. arXiv: 1506.08835 [astro-ph.CO] (cit. on pp. 28, 48, 49).

Murray, Norman, Eliot Quataert, and Todd A. Thompson (Jan. 2010). “The Disruption of Giant Molecular Clouds by Radiation Pressure & the Efficiency of Star Formation in Galaxies”. In: ApJ 709.1, pp. 191–209. arXiv: 0906.5358 [astro-ph.GA] (cit. on p. 19).

Narayanan, Desika, Mark R. Krumholz, Eve C. Ostriker, and Lars Hernquist (Apr. 2012). “A general model for the CO-H_2 conversion factor in galaxies with applications to the star formation law”. In: MNRAS 421.4, pp. 3127–3146. arXiv: 1110.3791 [astro-ph.GA] (cit. on p. 62).

Navarro, Julio F., Carlos S. Frenk, and Simon D. M. White (1996). “The Structure of Cold Dark Matter Halos”. In: ApJ 462, p. 563. arXiv: astro-ph/9508025 [astro-ph] (cit. on pp. 53, 54).

Nesvadba, N. P. H., M. D. Lehnert, F. Eisenhauer, et al. (Oct. 2006). “Extreme Gas Kinematics in the z=2.2 Powerful Radio Galaxy MRC 1138-262: Evidence for Efficient Active Galactic Nucleus Feedback in the Early Universe?” In: ApJ 650, pp. 693–705. eprint: astro-ph/0606530 (cit. on pp. 19, 65).

Newman, A. B., R. S. Ellis, S. Andreon, et al. (June 2014). “Spectroscopic Confirmation of the Rich z = 1.80 Galaxy Cluster JKCS 041 using the WFC3 Grism: Environmental Trends in the Ages and Structure of Quiescent Galaxies”. In: ApJ 788, 51, p. 51. arXiv: 1310.6754 (cit. on p. 29).

Noeske, K. G., B. J. Weiner, S. M. Faber, et al. (2007). “Star Formation in AEGIS Field Galaxies since z=1.1: The Dominance of Gradually Declining Star Formation, and the Main Sequence of Star-forming Galaxies”. In: ApJ 660.1, pp. L43–L46. arXiv: astro-ph/0701924 [astro-ph] (cit. on pp. 5, 27).

Noll, S., D. Burgarella, E. Giovannoli, et al. (Dec. 2009). “Analysis of galaxy spectral energy distributions from far-UV to far-IR with CIGALE: studying a SINGS test sample”. In: A&A 507.3, pp. 1793–1813. arXiv: 0909.5439 [astro-ph.CO] (cit. on p. 60).

Nonino, M., M. Dickinson, P. Rosati, et al. (Aug. 2009). “Deep U Band and R Imaging of Goods-South: Observations, Data Reduction and First Results”. In: ApJS 183, pp. 244–260. arXiv: 0906.4250 [astro-ph.CO] (cit. on p. 31).

Oesch, P. A., G. Brammer, P. G. van Dokkum, et al. (Mar. 2016). “A Remarkably Luminous Galaxy at z=11.1 Measured with Hubble Space Telescope Grism Spectroscopy”. In: ApJ 819.2, 129, p. 129. arXiv: 1603.00461 [astro-ph.GA] (cit. on p. 9).

Oteo, I., R. J. Ivison, L. Dunne, et al. (Mar. 2018). “An Extreme Protocluster of Luminous Dusty Starbursts in the Early Universe”. In: ApJ 856.1, 72, p. 72. arXiv: 1709.02809 [astro-ph.GA] (cit. on p. 29).

Owers, M. S., J. T. Allen, I. Baldry, et al. (June 2017). “The SAMI Galaxy Survey: the cluster redshift survey, target selection and cluster properties”. In: MNRAS 468, pp. 1824–1849. arXiv: 1703.00997 (cit. on p. 67).

Padoan, P., C. Federrath, G. Chabrier, et al. (2014). “The Star Formation Rate of Molecular Clouds”. In: Protostars and Planets VI, pp. 77–100. arXiv: 1312.5365 (cit. on p. 65).

Pannella, M., C. L. Carilli, E. Daddi, et al. (June 2009). “Star Formation and Dust Obscuration at z $\approx$ 2: Galaxies at the Dawn of Downsizing”. In: ApJ 698.2, pp. L116–L120. arXiv: 0905.1674 [astro-ph.CO] (cit. on p. 5).

Pannella, M., D. Elbaz, E. Daddi, et al. (2015). “GOODS-Herschel: Star Formation, Dust Attenuation, and the FIR-radio Correlation on the Main Sequence of Star-forming Galaxies up to z 4”. In: ApJ 807.2, 141, p. 141. arXiv: 1407.5072 [astro-ph.GA] (cit. on pp. 5, 48).

Papovich, C., R. Bassett, J. M. Lotz, et al. (May 2012). “CANDELS Observations of the Structural Properties of Cluster Galaxies at z = 1.62”. In: ApJ 750, 93, p. 93. arXiv: 1110.3794 (cit. on p. 29).

Peacock, John A., Shaun Cole, Peder Norberg, et al. (Mar. 2001). “A measurement of the cosmological mass density from clustering in the 2dF Galaxy Redshift Survey”. In: Nature 410.6825, pp. 169–173. arXiv: astro-ph/0103143 [astro-ph] (cit. on p. 1).

Pentericci, L., R. J. McLure, B. Garilli, et al. (Sept. 2018). “The VANDELS ESO public spectroscopic survey: Observations and first data release”. In: A&A 616, A174, A174. arXiv: 1803.07373 (cit. on pp. 32, 41, 42).

Pillepich, Annalisa, Dylan Nelson, Lars Hernquist, et al. (2018). “First results from the IllustrisTNG simulations: the stellar mass content of groups and clusters of galaxies”. In: MNRAS 475.1, pp. 648–675. arXiv: 1707.03406 [astro-ph.GA] (cit. on p. 46).

Poglitsch, A., C. Waelkens, N. Geis, et al. (July 2010). “The Photodetector Array Camera and Spectrometer (PACS) on the Herschel Space Observatory”. In: A&A 518, L2, p. L2. arXiv: 1005.1487 [astro-ph.IM] (cit. on p. 86).

Polletta, M., M. Tajer, L. Maraschi, et al. (July 2007). “Spectral Energy Distributions of Hard X-Ray Selected Active Galactic Nuclei in the XMM-Newton Medium Deep Survey”. In: ApJ 663.1, pp. 81–102. arXiv: astro-ph/0703255 [astro-ph] (cit. on p. 3).

Popping, Gergö, Fabian Walter, Peter Behroozi, et al. (Mar. 2020). “The ALMA Spectroscopic Survey in the HUDF: A Model to Explain Observed 1.1 and 0.85 mm Dust Continuum Number Counts”. In: ApJ 891.2, 135, p. 135. arXiv: 2002.07180 [astro-ph.GA] (cit. on pp. 11, 13).

Puglisi, A., E. Daddi, D. Liu, et al. (2019). “The Main Sequence at z 1.3 Contains a Sizable Fraction of Galaxies with Compact Star Formation Sizes: A New Population of Early Post-starbursts?” In: ApJ 877.2, L23, p. L23. arXiv: 1905.02958 [astro-ph.GA] (cit. on p. 11).

Pustilnik, S. A., A. Y. Kniazev, and A. G. Pramskij (Nov. 2005). “Study of DDO 68: nearest candidate for a young galaxy?” In: A&A 443.1, pp. 91–102. arXiv: astro-ph/0507658 [astro-ph] (cit. on p. 84).

Rémy-Ruyer, A., S. C. Madden, F. Galliano, et al. (Sept. 2013a). “Revealing the cold dust in low-metallicity environments. I. Photometry analysis of the Dwarf Galaxy Survey with Herschel”. In: A&A 557, A95, A95. arXiv: 1309.1371 [astro-ph.CO] (cit. on p. 60).

– (Sept. 2013b). “Revealing the cold dust in low-metallicity environments. I. Photometry analysis of the Dwarf Galaxy Survey with Herschel”. In: A&A 557, A95, A95. arXiv: 1309.1371 [astro-ph.CO] (cit. on pp. 83, 88–90).

Rémy-Ruyer, A., S. C. Madden, F. Galliano, et al. (Mar. 2014). “Gas-to-dust mass ratios in local galaxies over a 2 dex metallicity range”. In: A&A 563, A31, A31. arXiv: 1312.3442 [astro-ph.GA] (cit. on pp. 84, 95).

Retzlaff, J., P. Rosati, M. Dickinson, et al. (Feb. 2010). “The Great Observatories Origins Deep Survey. VLT/ISAAC near-infrared imaging of the GOODS-South field”. In: A&A 511, A50, A50. arXiv: 0912.1306 (cit. on p. 31).

Robotham, A. S. G., S. P. Driver, L. J. M. Davies, et al. (Nov. 2014). “Galaxy And Mass Assembly (GAMA): galaxy close pairs, mergers and the future fate of stellar mass”. In: MNRAS 444, pp. 3986–4008. arXiv: 1408.1476 (cit. on pp. 18, 65).

Rodighiero, G., E. Daddi, I. Baronchelli, et al. (2011). “The Lesser Role of Starbursts in Star Formation at z = 2”. In: ApJ 739.2, L40, p. L40. arXiv: 1108.0933 [astro-ph.CO] (cit. on pp. 5, 6, 28).

Rodighiero, G., A. Enia, I. Delvecchio, et al. (June 2019). “Active Galactic Nuclei in Dusty Starbursts at z = 2: Feedback Still to Kick in”. In: ApJ 877.2, L38, p. L38. arXiv: 1905.06955 [astro-ph.GA] (cit. on pp. 23, 99).

Rodighiero, G., M. Vaccari, A. Franceschini, et al. (June 2010). “Mid- and far-infrared luminosity functions and galaxy evolution from multiwavelength Spitzer observations up to z ∼2.5”. In: A&A 515, A8, A8. arXiv: 0910.5649 [astro-ph.CO] (cit. on p. 10).

Röllig, M., V. Ossenkopf, S. Jeyakumar, J. Stutzki, and A. Sternberg (June 2006). “[CII] 158 μm emission and metallicity in photon dominated regions”. In: A&A 451.3, pp. 917–924. arXiv: astro-ph/0601682 [astro-ph] (cit. on p. 62).

Roman-Duval, J., J. M. Jackson, M. Heyer, J. Rathborne, and R. Simon (Nov. 2010). “Physical Properties and Galactic Distribution of Molecular Clouds Identified in the Galactic Ring Survey”. In: ApJ 723, pp. 492–507. arXiv: 1010.2798 (cit. on p. 75).

Rosdahl, J. and J. Blaizot (June 2012). “Extended Lyα emission from cold accretion streams”. In: MNRAS 423.1, pp. 344–366. arXiv: 1112.4408 [astro-ph.CO] (cit. on p. 52).

Rosenberg, J. L., Yanling Wu, Emeric Le Floc’h, et al. (Feb. 2008). “Dust Properties and Star Formation Rates in Star-Forming Dwarf Galaxies”. In: ApJ 674.2, pp. 814–830. arXiv: 0710.5514 [astro-ph] (cit. on p. 83).

Rosolowsky, Erik, Adam K. Leroy, Antonio Usero, et al. (Jan. 2015). “CO Line Ratios in Nearby Galaxies”. In: American Astronomical Society Meeting Abstracts #225. Vol. 225. American Astronomical Society Meeting Abstracts, p. 141.25 (cit. on p. 61).

Rowlands, K., L. Dunne, S. Maddox, et al. (Jan. 2012). “Herschel-ATLAS/GAMA: dusty early-type galaxies and passive spirals”. In: MNRAS 419.3, pp. 2545–2578. arXiv: 1109.6274 [astro-ph.CO] (cit. on p. 3).

Rujopakarn, W., E. Daddi, G. H. Rieke, et al. (2019). “ALMA 200 pc Resolution Imaging of Smooth Cold Dusty Disks in Typical z 3 Star-forming Galaxies”. In: ApJ 882.2, 107, p. 107. arXiv: 1904.04507 [astro-ph.GA] (cit. on p. 28).

Rujopakarn, W., J. S. Dunlop, G. H. Rieke, et al. (Dec. 2016). “VLA and ALMA Imaging of Intense Galaxy-wide Star Formation in z
2 Galaxies”. In: ApJ 833, 12, p. 12. arXiv: 1607.07710 (cit. on pp. 11, 28).

Saintonge, Amélie, Barbara Catinella, Linda J. Tacconi, et al. (Dec. 2017). “xCOLD GASS: The Complete IRAM 30 m Legacy Survey of Molecular Gas for Galaxy Evolution Studies”. In: ApJS 233.2, 22, p. 22. arXiv: 1710.02157 [astro-ph.GA] (cit. on p. 60).

Saintonge, Amélie, Guinevere Kauffmann, Jing Wang, et al. (July 2011). “COLD GASS, an IRAM legacy survey of molecular gas in massive galaxies - II. The non-universality of the molecular gas depletion time-scale”. In: MNRAS 415.1, pp. 61–76. arXiv: 1104.0019 [astro-ph.CO] (cit. on pp. 61, 62).

Salim, Samir, R. Michael Rich, Stéphane Charlot, et al. (Dec. 2007). “UV Star Formation Rates in the Local Universe”. In: ApJS 173.2, pp. 267–292. arXiv: 0704.3611 [astro-ph] (cit. on p. 92).

Salpeter, E. E. (Jan. 1955). “The Luminosity Function and Stellar Evolution.” In: ApJ 121, p. 161 (cit. on p. 29).

Sánchez, S. F. (Feb. 2015). “IFUs surveys, a panoramic view of galaxy evolution”. In: Galaxies in 3D across the Universe. Ed. by B. L. Ziegler, F. Combes, H. Dannerbauer, and M. Verdugo. Vol. 309. IAU Symposium, pp. 85–92. arXiv: 1410.0295 (cit. on p. 66).

Sánchez, S. F., R. C. Kennicutt, A. Gil de Paz, et al. (Feb. 2012). “CALIFA, the Calar Alto Legacy Integral Field Area survey. I. Survey presentation”. In: A&A 538, A8, A8. arXiv: 1111.0962 (cit. on p. 66).

Sargent, M. T., M. Béthermin, E. Daddi, and D. Elbaz (Mar. 2012). “The Contribution of Starbursts and Normal Galaxies to Infrared Luminosity Functions at z < 2”. In: ApJ 747.2, L31, p. L31. arXiv: 1202.0290 [astro-ph.CO] (cit. on pp. 5, 6).

Scalo, J. and B. G. Elmegreen (Sept. 2004). “Interstellar Turbulence II: Implications and Effects”. In: ARA&A 42, pp. 275–316. eprint: astro-ph/0404452 (cit. on p. 66).

Schawinski, Kevin, C. Megan Urry, Brooke D. Simmons, et al. (May 2014). “The green valley is a red herring: Galaxy Zoo reveals two evolutionary pathways towards quenching of star formation in early- and late-type galaxies”. In: MNRAS 440.1, pp. 889–907. arXiv: 1402.4814 [astro-ph.GA] (cit. on p. 6).

Schreiber, C., D. Elbaz, M. Pannella, et al. (May 2016). “Observational evidence of a slow downfall of star formation efficiency in massive galaxies during the past 10 Gyr”. In: A&A 589, A35, A35. arXiv: 1601.04226 [astro-ph.GA] (cit. on p. 7).

Schreiber, C., D. Elbaz, M. Pannella, et al. (Jan. 2018a). “Dust temperature and mid-to-total infrared color distributions for star-forming galaxies at 0 z 4”. In: A&A 609, A30, A30. arXiv: 1710.10276 (cit. on pp. 7, 22, 33, 35, 37, 40, 43).

Schreiber, C., I. Labbé, K. Glazebrook, et al. (Mar. 2018b). “Jekyll Hyde: quiescence and extreme obscuration in a pair of massive galaxies 1.5 Gyr after the Big Bang”. In: A&A 611, A22, A22. arXiv: 1709.03505 (cit. on pp. 33, 55).

Schreiber, C., M. Pannella, D. Elbaz, et al. (Mar. 2015). “The Herschel view of the dominant mode of galaxy growth from z = 4 to the present day”. In: A&A 575, A74, A74. arXiv: 1409.5433 (cit. on pp. 1, 5–7, 18, 28, 45).

Schruba, Andreas, Adam K. Leroy, Fabian Walter, et al. (June 2012). “Low CO Luminosities in Dwarf Galaxies”. In: AJ 143.6, 138, p. 138. arXiv: 1203.4231 [astro-ph.CO] (cit. on pp. 57, 60–62).

Scoville, N., H. Aussel, K. Sheth, et al. (Mar. 2014). “The Evolution of Interstellar Medium Mass Probed by Dust Emission: ALMA Observations at z = 0.3-2”. In: ApJ 783.2, 84, p. 84. arXiv: 1401.2987 [astro-ph.GA] (cit. on p. 15).

Scoville, N., N. Lee, P. Vanden Bout, et al. (Mar. 2017). “Evolution of Interstellar Medium, Star Formation, and Accretion at High Redshift”. In: ApJ 837.2, 150, p. 150. arXiv: 1702.04729 [astro-ph.GA] (cit. on p. 15).

Scoville, N., K. Sheth, H. Aussel, et al. (Apr. 2016). “ISM Masses and the Star formation Law at Z = 1 to 6: ALMA Observations of Dust Continuum in 145 Galaxies in the COSMOS Survey Field”. In: ApJ 820.2, 83, p. 83. arXiv: 1511.05149 [astro-ph.GA] (cit. on p. 15).

Sharp, R., J. T. Allen, L. M. R. Fogarty, et al. (Jan. 2015). “The SAMI Galaxy Survey: cubism and covariance, putting round pegs into square holes”. In: MNRAS 446, pp. 1551–1566. arXiv: 1407.5237 [astro-ph.IM] (cit. on pp. 66, 67).

Sharp, R., W. Saunders, G. Smith, et al. (June 2006). “Performance of AAOmega: the AAT multi-purpose fiber-fed spectrograph”. In: Society of Photo-Optical Instrumentation Engineers (SPIE) Conference Series. Vol. 6269. Proc. SPIE, 62690G. eprint: astro-ph/0606137 (cit. on p. 67).

Shi, Yong, Lee Armus, George Helou, et al. (Oct. 2014a). “Inefficient star formation in extremely metal poor galaxies”. In: Nature 514.7522, pp. 335–338. arXiv: 1410.5504 [astro-ph.GA] (cit. on p. 62).

– (Oct. 2014b). “Inefficient star formation in extremely metal poor galaxies”. In: Nature 514.7522, pp. 335–338. arXiv: 1410.5504 [astro-ph.GA] (cit. on pp. 83, 86, 94, 95, 98).

Shi, Yong, George Helou, Lin Yan, et al. (June 2011). “Extended Schmidt Law: Role of Existing Stars in Current Star Formation”. In: ApJ 733.2, 87, p. 87. arXiv: 1103.3711 [astro-ph.CO] (cit. on pp. 92, 94).

Shi, Yong, Junzhi Wang, Zhi-Yu Zhang, et al. (May 2015a). “The Weak Carbon Monoxide Emission in an Extremely Metal-poor Galaxy, Sextans A”. In: ApJ 804.1, L11, p. L11. arXiv: 1504.01453 [astro-ph.GA] (cit. on pp. 57, 60–62).

– (May 2015b). “The Weak Carbon Monoxide Emission in an Extremely Metal-poor Galaxy, Sextans A”. In: ApJ 804.1, L11, p. L11. arXiv: 1504.01453 [astro-ph.GA] (cit. on pp. 83, 94).

Shi, Yong, Junzhi Wang, Zhi-Yu Zhang, et al. (Dec. 2016). “Carbon monoxide in an extremely metal-poor galaxy”. In: Nature Communications 7, 13789, p. 13789. arXiv: 1612.03980 [astro-ph.GA] (cit. on pp. 57, 58, 60–62).

Shi, Yong, Junzhi Wang, Zhi-Yu Zhang, et al. (Apr. 2020). “Oversized Gas Clumps in an Extremely Metal-poor Molecular Cloud Revealed by ALMA’s Parsec-scale Maps”. In: ApJ 892.2, 147, p. 147. arXiv: 2002.10209 [astro-ph.GA] (cit. on pp. 58, 59).

Simpson, J. M., Ian Smail, A. M. Swinbank, et al. (July 2015). “The SCUBA-2 Cosmology Legacy Survey: ALMA Resolves the Bright-end of the Sub-millimeter Number Counts”. In: ApJ 807.2, 128, p. 128. arXiv: 1505.05152 [astro-ph.GA] (cit. on p. 14).

Simpson, J. M., A. M. Swinbank, Ian Smail, et al. (June 2014). “An ALMA Survey of Submillimeter Galaxies in the Extended Chandra Deep Field South: The Redshift Distribution and Evolution of Submillimeter Galaxies”. In: ApJ 788.2, 125, p. 125. arXiv: 1310.6363 [astro-ph.CO] (cit. on p. 11).

Smith, D. J. B., L. Dunne, E. da Cunha, et al. (Nov. 2012). “Herschel-ATLAS: multi-wavelength SEDs and physical properties of 250 μm selected galaxies at z < 0.5”. In: MNRAS 427.1, pp. 703–727. arXiv: 1208.3079 [astro-ph.CO] (cit. on p. 3).

Solomon, P. M. and P. A. Vanden Bout (Sept. 2005). “Molecular Gas at High Redshift”. In: ARA&A 43.1, pp. 677–725. arXiv: astro-ph/0508481 [astro-ph] (cit. on p. 59).

Springel, V., S. D. M. White, A. Jenkins, et al. (June 2005). “Simulations of the formation, evolution and clustering of galaxies and quasars”. In: Nature 435, pp. 629–636. eprint: astro-ph/0504097 (cit. on pp. 28, 45, 49).

Stach, Stuart M., Ian Smail, A. M. Swinbank, et al. (June 2018). “An ALMA Survey of the SCUBA-2 Cosmology Legacy Survey UKIDSS/UDS Field: Number Counts of Submillimeter Galaxies”. In: ApJ 860.2, 161, p. 161. arXiv: 1805.05362 [astro-ph.GA] (cit. on pp. 11, 14).

Stark, Daniel P., Richard S. Ellis, Andrew Bunker, et al. (June 2009). “The Evolutionary History of Lyman Break Galaxies Between Redshift 4 and 6: Observing Successive Generations of Massive Galaxies in Formation”. In: ApJ 697.2, pp. 1493–1511. arXiv: 0902.2907 [astro-ph.CO] (cit. on p. 5).

Stark, Daniel P., Matthew A. Schenker, Richard Ellis, et al. (Feb. 2013). “Keck Spectroscopy of 3 < z < 7 Faint Lyman Break Galaxies: The Importance of Nebular Emission in Understanding the Specific Star Formation Rate and Stellar Mass Density”. In: ApJ 763.2, 129, p. 129. arXiv: 1208.3529 [astro-ph.CO] (cit. on p. 5).

Steidel, Charles C., Mauro Giavalisco, Max Pettini, Mark Dickinson, and Kurt L. Adelberger (May 1996). “Spectroscopic Confirmation of a Population of Normal Star-forming Galaxies at Redshifts Z > 3”. In: ApJ 462, p. L17. arXiv: astro-ph/9602024 [astro-ph] (cit. on p. 4).

Steinhardt, Charles L., Josh S. Speagle, Peter Capak, et al. (Aug. 2014). “Star Formation at 4 < z < 6 from the Spitzer Large Area Survey with Hyper-Suprime-Cam (SPLASH)”. In: ApJ 791.2, L25, p. L25. arXiv: 1407.7030 [astro-ph.GA] (cit. on p. 5).

Stilp, A. M., J. J. Dalcanton, E. Skillman, et al. (Aug. 2013). “Drivers of H I Turbulence in Dwarf Galaxies”. In: ApJ 773, 88, p. 88. arXiv: 1306.2321 (cit. on p. 79).

Straatman, C. M. S., L. R. Spitler, R. F. Quadri, et al. (Oct. 2016). “The FourStar Galaxy Evolution Survey (ZFOURGE): Ultraviolet to Far-infrared Catalogs, Medium-bandwidth Photometric Redshifts with Improved Accuracy, Stellar Masses, and Confirmation of Quiescent Galaxies to z
3.5”. In: ApJ 830, 51, p. 51. arXiv: 1608.07579 (cit. on pp. 31, 32, 41, 42, 44, 49).

Strateva, Iskra, Željko Ivezić, Gillian R. Knapp, et al. (Oct. 2001). “Color Separation of Galaxy Types in the Sloan Digital Sky Survey Imaging Data”. In: AJ 122.4, pp. 1861–1874. arXiv: astro-ph/0107201 [astro-ph] (cit. on pp. 3, 4).

Swinbank, A. M., J. M. Simpson, Ian Smail, et al. (2014). “An ALMA survey of sub-millimetre Galaxies in the Extended Chandra Deep Field South: the far-infrared properties of SMGs”. In: MNRAS 438.2, pp. 1267–1287. arXiv: 1310.6362 [astro-ph.CO] (cit. on p. 28).

Symeonidis, M., A. Georgakakis, M. J. Page, et al. (Oct. 2014). “Linking the X-ray and infrared properties of star-forming galaxies at z < 1.5”. In: MNRAS 443.4, pp. 3728–3740. arXiv: 1407.4511 [astro-ph.GA] (cit. on p. 23).

Tacconi, L. J., R. Genzel, R. Neri, et al. (Feb. 2010). “High molecular gas fractions in normal massive star-forming galaxies in the young Universe”. In: Nature 463, pp. 781–784. arXiv: 1002.2149 (cit. on pp. 18, 65).

Tacconi, L. J., R. Genzel, A. Saintonge, et al. (Feb. 2018). “PHIBSS: Unified Scaling Relations of Gas Depletion Time and Molecular Gas Fractions”. In: ApJ 853.2, 179, p. 179. arXiv: 1702.01140 [astro-ph.GA] (cit. on pp. 7, 17).

Tacconi, L. J., R. Neri, R. Genzel, et al. (May 2013). “Phibss: Molecular Gas Content and Scaling Relations in z ~1-3 Massive, Main-sequence Star-forming Galaxies”. In: ApJ 768.1, 74, p. 74. arXiv: 1211.5743 [astro-ph.CO] (cit. on pp. 7, 16, 17).

Tacconi, Linda J., Reinhard Genzel, and Amiel Sternberg (Mar. 2020). “The Evolution of the Star-forming Interstellar Medium across Cosmic Time”. In: arXiv e-prints, arXiv:2003.06245, arXiv:2003.06245. arXiv: 2003.06245 [astro-ph.GA] (cit. on pp. 16, 18).

Tamburro, D., H.-W. Rix, A. K. Leroy, et al. (May 2009). “What is Driving the H I Velocity Dispersion?” In: AJ 137, pp. 4424–4435. arXiv: 0903.0183 [astro-ph.GA] (cit. on p. 66).

Tasker, E. J. and J. C. Tan (July 2009). “Star Formation in Disk Galaxies. I. Formation and Evolution of Giant Molecular Clouds via Gravitational Instability and Cloud Collisions”. In: ApJ 700, pp. 358–375. arXiv: 0811.0207 (cit. on p. 66).

Taylor, E. N., A. M. Hopkins, I. K. Baldry, et al. (Dec. 2011). “Galaxy And Mass Assembly (GAMA): stellar mass estimates”. In: MNRAS 418, pp. 1587–1620. arXiv: 1108.0635 [astro-ph.CO] (cit. on p. 69).

Thomas, D., C. Maraston, R. Bender, and C. Mendes de Oliveira (Mar. 2005). “The Epochs of Early-Type Galaxy Formation as a Function of Environment”. In: ApJ 621, pp. 673–694. eprint: astro-ph/0410209 (cit. on p. 29).

Toft, S., V. Smolčić, B. Magnelli, et al. (Feb. 2014). “Submillimeter Galaxies as Progenitors of Compact Quiescent Galaxies”. In: ApJ 782.2, 68, p. 68. arXiv: 1401.1510 [astro-ph.GA] (cit. on p. 11).

Toomre, A. (May 1964). “On the gravitational stability of a disk of stars”. In: ApJ 139, pp. 1217–1238 (cit. on p. 18).

Toshikawa, Jun, Matthew A. Malkan, Nobunari Kashikawa, et al. (Jan. 2020). “Discovery of Protoclusters at z $\sim$ 3.7 and 4.9: Embedded in Primordial Superclusters”. In: ApJ 888.2, 89, p. 89. arXiv: 1912.01625 [astro-ph.GA] (cit. on p. 52).

Valentino, Francesco, Georgios E. Magdis, Emanuele Daddi, et al. (Dec. 2018). “A Survey of Atomic Carbon [C I] in High-redshift Main-sequence Galaxies”. In: ApJ 869.1, 27, p. 27. arXiv: 1810.11029 [astro-ph.GA] (cit. on p. 35).

Valentino, Francesco, Georgios E. Magdis, Emanuele Daddi, et al. (2020a). “The properties of the interstellar medium of galaxies across time as traced by the neutral atomic carbon [CI]”. In: arXiv e-prints, arXiv:2001.01734, arXiv:2001.01734. arXiv: 2001.01734 [astro-ph.GA] (cit. on pp. 35, 37).

Valentino, Francesco, Masayuki Tanaka, Iary Davidzon, et al. (Feb. 2020b). “Quiescent Galaxies 1.5 Billion Years after the Big Bang and Their Progenitors”. In: ApJ 889.2, 93, p. 93. arXiv: 1909.10540 [astro-ph.GA] (cit. on p. 11).

van de Sande, J., J. Bland-Hawthorn, L. M. R. Fogarty, et al. (Jan. 2017). “The SAMI Galaxy Survey: Revisiting Galaxy Classification through High-order Stellar Kinematics”. In: ApJ 835, 104, p. 104. arXiv: 1611.07039 (cit. on p. 69).

van den Bergh, S. (June 1976). “A new classification system for galaxies.” In: ApJ 206, pp. 883–887 (cit. on p. 3).

Varidel, M., M. Pracy, S. Croom, M. S. Owers, and E. Sadler (Mar. 2016). “Resolved Gas Kinematics in a Sample of Low-Redshift High Star-Formation Rate Galaxies”. In: PASA 33, e006, e006. arXiv: 1602.00737 (cit. on pp. 19, 72).

Varidel, Mathew R., Scott M. Croom, Geraint F. Lewis, et al. (May 2019). “The SAMI Galaxy Survey: Bayesian inference for gas disc kinematics using a hierarchical Gaussian mixture model”. In: MNRAS 485.3, pp. 4024–4044. arXiv: 1903.03121 [astro-ph.GA] (cit. on p. 20).

Varidel, Mathew R., Scott M. Croom, Geraint F. Lewis, et al. (May 2020). “The SAMI galaxy survey: gas velocity dispersions in low-z star-forming galaxies and the drivers of turbulence”. In: MNRAS 495.2, pp. 2265–2284. arXiv: 2005.04874 [astro-ph.GA] (cit. on p. 19).

Veilleux, S. and D. E. Osterbrock (Feb. 1987). “Spectral classification of emission-line galaxies”. In: ApJS 63, pp. 295–310 (cit. on p. 69).

Walter, F., R. Decarli, C. Carilli, et al. (June 2012a). “Evidence for Low Extinction in Actively Star-forming Galaxies at z > 6.5”. In: ApJ 752.2, 93, p. 93. arXiv: 1204.3426 [astro-ph.CO] (cit. on p. 57).

Walter, Fabian, Roberto Decarli, Manuel Aravena, et al. (Dec. 2016). “ALMA Spectroscopic Survey in the Hubble Ultra Deep Field: Survey Description”. In: ApJ 833.1, 67, p. 67. arXiv: 1607.06768 [astro-ph.GA] (cit. on pp. 12, 13).

Walter, Fabian, Roberto Decarli, Chris Carilli, et al. (2012b). “The intense starburst HDF 850.1 in a galaxy overdensity at z$\approx$5.2 in the Hubble Deep Field”. In: Nature 486.7402, pp. 233–236. arXiv: 1206.2641 [astro-ph.CO] (cit. on pp. 13, 28, 55).

Wang, T., D. Elbaz, E. Daddi, et al. (Sept. 2016a). “Discovery of a Galaxy Cluster with a Violently Starbursting Core at z = 2.506”. In: ApJ 828, 56, p. 56. arXiv: 1604.07404 (cit. on pp. 29, 53, 54).

Wang, T., D. Elbaz, C. Schreiber, et al. (Jan. 2016b). “Infrared Color Selection of Massive Galaxies at z 3”. In: ApJ 816, 84, p. 84. arXiv: 1512.02656 (cit. on pp. 4, 99).

Wang, T., C. Schreiber, D. Elbaz, et al. (2019). “A dominant population of optically invisible massive galaxies in the early Universe”. In: Nature 572.7768, pp. 211–214. arXiv: 1908.02372 [astro-ph.GA] (cit. on pp. 14, 28, 37, 41, 55).

Warren, Steven R., Edward Molter, John M. Cannon, et al. (Nov. 2015). “CARMA CO Observations of Three Extremely Metal-poor, Star-forming Galaxies”. In: ApJ 814.1, 30, p. 30. arXiv: 1510.03518 [astro-ph.GA] (cit. on p. 57).

Webb, T., A. Noble, A. DeGroot, et al. (Aug. 2015). “An Extreme Starburst in the Core of a Rich Galaxy Cluster at z = 1.7”. In: ApJ 809, 173, p. 173. arXiv: 1508.04982 (cit. on p. 29).

Weingartner, Joseph C. and B. T. Draine (May 1999). “Interstellar Depletion onto Very Small Dust Grains”. In: ApJ 517.1, pp. 292–298. arXiv: astro-ph/9812469 [astro-ph] (cit. on p. 95).

Whitaker, Katherine E., Marijn Franx, Joel Leja, et al. (Nov. 2014). “Constraining the Low-mass Slope of the Star Formation Sequence at 0.5 < z < 2.5”. In: ApJ 795.2, 104, p. 104. arXiv: 1407.1843 [astro-ph.GA] (cit. on p. 12).

Whitaker, Katherine E., Pieter G. van Dokkum, Gabriel Brammer, and Marijn Franx (Aug. 2012). “The Star Formation Mass Sequence Out to z = 2.5”. In: ApJ 754.2, L29, p. L29. arXiv: 1205.0547 [astro-ph.CO] (cit. on pp. 5, 11).

White, S. D. M. and M. J. Rees (May 1978). “Core condensation in heavy halos: a two-stage theory for galaxy formation and clustering.” In: MNRAS 183, pp. 341–358 (cit. on p. 1).

Williams, Rik J., Ryan F. Quadri, Marijn Franx, Pieter van Dokkum, and Ivo Labbé (Feb. 2009). “Detection of Quiescent Galaxies in a Bicolor Sequence from Z = 0-2”. In: ApJ 691.2, pp. 1879–1895. arXiv: 0806.0625 [astro-ph] (cit. on pp. 4, 5).

Willis, J. P., R. E. A. Canning, E. S. Noordeh, et al. (Jan. 2020). “Spectroscopic confirmation of a mature galaxy cluster at a redshift of 2”. In: Nature 577.7788, pp. 39–41. arXiv: 2001.00549 [astro-ph.GA] (cit. on p. 29).

Wilson, C. D., B. E. Warren, J. Irwin, et al. (Jan. 2011). “The JCMT Nearby Galaxies Legacy Survey - IV. Velocity dispersions in the molecular interstellar medium in spiral galaxies”. In: MNRAS 410, pp. 1409–1422. arXiv: 1009.3279 (cit. on p. 80).

Wisnioski, E., N. M. Förster Schreiber, S. Wuyts, et al. (Feb. 2015). “The KMOS^{3D} Survey: Design, First Results, and the Evolution of Galaxy Kinematics from 0.7 = z = 2.7”. In: ApJ 799, 209, p. 209. arXiv: 1409.6791 (cit. on pp. 19, 65).

Wolfire, Mark G., David Hollenbach, and Christopher F. McKee (June 2010). “The Dark Molecular Gas”. In: ApJ 716.2, pp. 1191–1207. arXiv: 1004.5401 [astro-ph.GA] (cit. on p. 57).

Wu, Yanling, V. Charmandaris, Lei Hao, et al. (Mar. 2006). “Mid-Infrared Properties of Low-Metallicity Blue Compact Dwarf Galaxies from the Spitzer Infrared Spectrograph”. In: ApJ 639.1, pp. 157–172. arXiv: astro-ph/0510856 [astro-ph] (cit. on p. 83).

Yang, C., A. Omont, A. Beelen, et al. (2016). “Submillimeter H_2O and H_2O^+emission in lensed ultra- and hyper-luminous infrared galaxies at z 2-4”. In: A&A 595, A80, A80. arXiv: 1607.06220 [astro-ph.GA] (cit. on p. 35).

Yu, Xiaoling, Yong Shi, Yanmei Chen, et al. (July 2019). “What drives the velocity dispersion of ionized gas in star-forming galaxies?” In: MNRAS 486.4, pp. 4463–4472. arXiv: 1904.11431 [astro-ph.GA] (cit. on p. 19).

Zhou, L., D. Elbaz, M. Franco, et al. (Aug. 2020). “GOODS-ALMA: Optically dark ALMA galaxies shed light on a cluster in formation at z = 3.5”. In: arXiv e-prints, arXiv:2008.08518, arXiv:2008.08518. arXiv: 2008.08518 [astro-ph.GA] (cit. on pp. 21, 25, 99).

Zhou, Luwenjia, Christoph Federrath, Tiantian Yuan, et al. (Oct. 2017). “The SAMI Galaxy Survey: energy sources of the turbulent velocity dispersion in spatially resolved local star-forming galaxies”. In: MNRAS 470.4, pp. 4573–4582. arXiv: 1706.04754 [astro-ph.GA] (cit. on p. 25).

Zhou, Luwenjia, Yong Shi, Taino Diaz-Santos, et al. (May 2016). “Spatially resolved dust emission of extremely metal-poor galaxies*”. In: MNRAS 458.1, pp. 772–780. arXiv: 1602.05362 [astro-ph.GA] (cit. on p. 24).

Zhu, Ming, Padeli P. Papadopoulos, Emmanuel M. Xilouris, Nario Kuno, and Ute Lisenfeld (Dec. 2009). “Tracing Molecular Gas Mass in Extreme Extragalactic Environments: An Observational Study”. In: ApJ 706.2, pp. 941–959. arXiv: 0908.1600 [astro-ph.CO] (cit. on p. 90).

List of Figures

1.1 **a**: Spectral energy distributions (SEDs) for typical galaxies - an old elliptical galaxy (red), two types of spiral galaxies (Sb in green and Sd in blue), an AGN (Markarian 231, solid black), a QSO (dotted black), and a merging and star-bursting galaxy Arp 220. Template spectra are taken from Polletta et al. (2007). Courtesy: CANDELS blog. **b** The spectral energy distributions (SEDs) of a typical star-forming galaxy (H-ATLAS J090713.1-000322). The total SED is in grey, with the stellar component in red and the corresponding dust emission in blue. The green curve denotes the unattenuated stellar light. Figure from Smith et al. (2012). **c**: Example of SED fitting - an old, dust free galaxy (blue) and a young, dusty galaxy (red) both fit the observed data points (green) in the UV to mid-infrared (MIR) regime. Courtesy: CANDELS blog. 3

1.2 The SED of a typical Lyman break galaxy at $z \sim 3$, and the images of this galaxy taken with photometric filters at $U_{\rm n}$, G, $R_{\rm s}$ bands. Courtesy: CANDELS blog. 4

1.3 **Left**: The galaxy absolute magnitude-color diagram in SDSS filter colors, where absolute magnitude has been converted to stellar mass. Figure adapted from Schawinski et al. (2014) by S. Majewski. **Right**: Schematic representation of the main sequence and other galaxies with different star formation modes. Courtesy: CANDELS blog. 6

1.4 **Left**: The evolution of star formation main sequence with redshift. The average SFR of star-forming galaxies as a function of redshift and stellar mass are parameterized as in Eq. 1.1, see also Schreiber et al. (2015). **Right**: Double Gaussian decomposition of the distribution of starburstiness ($\mathrm{R_{SB}} = \mathrm{SFR/SFR_{MS}}$). Figures from Schreiber et al. (2015). . . 6

1.5 Cosmic star formation rate density (SFRD). **a**: Cosmic SFRD before dust attenuation correction. **b**: Mean dust extinction in magnitude as a function of redshift. **c**: Cosmic SFRD derived from the UV data after dust attenuation correction and from IR, respectively. **d**: Cosmic SFRD derived from the combination of the UV data after dust attenuation correction and IR data. Figures from Madau and Dickinson (2014). 8

1.6 Illustration of K-correction: The observed flux densities for a typical $10^{12.5}\,\mathrm{L_\odot}$ infrared-luminous galaxy as a function of redshift. The curves are color coded with the observed wavelength. Figure from Casey et al. (2014). 10

1.7 Illustration of the SED the Cosmic Microwave Background (CMB), the Cosmic Infrared Background (CIB) and the Cosmic Optical Background (COB). Their approximate brightness in $\mathrm{nW\,m^{-2}\,sr^{-1}}$ is marked in the boxes. Figure from Dole et al. (2006). 11

1.8 **Left:** SFR as a function of stellar mass of the SMGs at $1.7 < z < 2.6$ studied by Lang et al. (2019). The solid and dotted lines indicate the main sequence and the 0.3 dex scatter from Whitaker et al. (2014). **Right:** Histograms of the effective radii for the ALMA 870μm continuum emission, stellar mass profiles, and H-band emission from the same work. Figures from Lang et al. (2019). 12

1.9 GOODS-ALMA 1.1mm image tapered at 0″60, reaching an rms of 0.18 mJy beam^{-1} (Franco et al., 2020b). The white and blue circles with a diameter of 4″ indicate the blind detections with S/N above the 4.8σ and detections with priors at 3.5 $\sim$ 4.8σ, respectively. Black contours show the different slices (labeled A to F) used to construct the homogeneous 1.1 mm coverage. Blue lines indicate the HST/ACS field and the green lines indicate the HST-WFC3 deep field. The cyan contours represent the limit of the Dunlop et al. (2017) survey covering all of the Hubble Ultra Deep Field region, the yellow contours show the ASAGAO survey (Hatsukade et al., 2018), the gray contours show the ASPECS Pilot survey (Walter et al., 2016), the pink contours show the ASPECS Large Program (Decarli et al., 2019). 13

1.10 **Left:** Contribution of optically dark galaxies to the cosmic SFRD. Figure from Wang et al. (2019). **Right:** Upper panel: SFR density for all galaxies (black), protoclusters (blue), and cores (red). Lower panel: Fractional contributions to the total cosmic SFRD. Figure from Chiang et al. (2017). 14

1.11 Illustration of "CO dark" gas in molecular clouds. Figure from Madden et al. (2020). 16

1.12 **Left:** Spatially resolved atomic (**a**), molecular (**b**) and total (**d**) gas – star formation law and gas column density distribution (**c**). Figures from Bigiel et al. (2008). **Right:** Disk averaged total gas – star formation law (**d**). Figure from Kennicutt and Evans (2012). . . . 17

1.13 Molecular gas fraction as a function of redshift. Figure from Tacconi et al. (2020). 18

1.14 Illustration of a datacube. 20

3.1 ***Left:*** Part of the spectrum obtained from the ALMA band 4 observation of AGS4. The yellow shade highlights the detected emission line. The emission line map is shown in the bottom-left corner. The contours denote 1 to 5σ, with the step of 1σ. ***Right:*** Same as on the left, but for AGS17. The contours in the map denote 1 to 6σ, with the step of 1σ. . . . 34

3.2 Upper limit of the [CI](2-1)/CO(7-6) flux ratio of AGS4 (blue arrows), compared with existing observations of local and high-redshift MS galaxies, starburst galaxies and AGNs (data compiled in Valentino et al. (2018); Valentino et al. (2020)). If the detected emission line is indeed CO(7-6), then the flux ratio would fall at the lower end of the trend shown by the existing observations. 35

3.3 ***Top-left:*** The SED of AGS4. Top: Photometric redshift probability distribution function derived by EAzY (Brammer et al., 2008). Bottom: The SED fittings. The green curve shows the best-fit of AGS4 at z_{phot} = 4.02 using EAzY, and we shift the SED to the spectroscopic redshift (z_{spec} = 3.556) of AGS4 in light blue for comparison. The grey curve shows the SED of the optically-bright neighbor, ID$_{\rm ZFOURGE}$ = 12333. ***Top-right:*** The SED of AGS15. The blue curve shows the best-fit at z_{phot} = 3.96 derived by EAzY and we shift the SED to the redshift peak of the over-density, at z = 3.472, in light blue for comparison. The grey curve shows the SED of the optically-bright neighbor, ID$_{\rm CANDELS}$ = 3818. ***Bottom-left:*** The SED of AGS24. Same as AGS15. ***Bottom-right:*** The SED of AGS25 at z_{phot} = 4.70, fitted by EAzY with the photometry retrieved from the ZFOURGE catalog. 36

3.4 Images of AGS4 from the observed B (435 nm, rest-frame UV) to near-infrared observed K_s (2.2 μm, rest-frame B) bands. The red contours denote the ALMA detection at 1.1mm at the resolution of 029. The green dashed contours denote the ALMA detection at 2mm at the resolution of 088. The astrometric corrections between ALMA and HST images are applied throughout this work. The cyan "x" denotes the optical bright neighbor, $\mathrm{ID_{CANDELS}} = 8923$ ($z_{phot} = 0.24$). The magenta "x" denotes the detection by ZFOURGE based on the K_s-band image, $\mathrm{ID_{ZFOURGE}} = 12333$ ($z_{phot} = 3.76$). If not stated otherwise, the images in this paper are all oriented with the North up and East to the left. 39

3.5 Images of AGS25 in the H-band (1.6 μm), K_s-band (2.2 μm) and IRAC1-band (3.6 μm). The contribution of a 3″ distant bright neighbor of AGS25 was subtracted to produce the IRAC image as in F20a. The red contours denote the ALMA detection at 1.1mm at the resolution of 060. The magenta "x" is the ZFOURGE counterpart $\mathrm{ID_{ZFOURGE}} = 11353$. . . 41

3.6 Redshift distribution of the 11674 galaxies with a redshift (either photometric or spectroscopic) located within the 6.9′×10′ GOODS-ALMA field (grey). The sub-sample of 395 galaxies located within 50″ of the most massive galaxy in the field at $z > 3$, AGS24, are shown in blue. The insert shows the distribution of the spectroscopic redshifts of the 121 galaxies at $3 \leq z_{spec} \leq 4$ over the GOODS-ALMA field. Ten galaxies fall in the redshift bin $3.470 \leq z_{spec} \leq 3.480$. The mean redshift of the ten galaxies is $z_{spec} = 3.472$. The redshifts are from the ZFOURGE (Straatman et al., 2016) and VANDELS DR3 (McLure et al., 2018; Pentericci et al., 2018) catalogs. 42

3.7 Images of AGS24 in the *B*, *V*, *H* and K_s band, IRAC 3.6 and 4.5μm, JVLA 6 GHz (3.7σ) and 3 GHz (5.7σ). The contours are the same as in Fig. 3.4 but for AGS24. The three neighbor galaxies are labeled with $\mathrm{ID_{ZFOURGE}}$ or $\mathrm{ID_{CDFS}}$ and their redshift separately. . . 44

3.8 ***Top:*** Images of AGS11 in the *J* band, *H* band, K_s band and IRAC 3.6 μm . The magenta "x" denotes the detection in K_s-band by ZFOURGE, $\mathrm{ID_{ZFOURGE}} = 7589$ ($z_{phot} = 4.82$). ***Bottom:*** Same as above, but for AGS17. The cyan "x"s denote the optical bright neighbors, $\mathrm{ID_{CANDELS}} = 4414$ ($z_{phot} = 0.03$, below) and $\mathrm{ID_{CANDELS}} = 4436$ ($z_{phot} = 0.95$, above). The magenta "x" denotes the detection in K_s-band by ZFOURGE, $\mathrm{ID_{ZFOURGE}} = 6964$ ($z_{phot} = 1.85$). 47

3.9 Same as in Fig. 3.4, but for AGS15. The cyan "x" denotes the optical bright neighbor, $\mathrm{ID_{CANDELS}} = 3818$ ($z_{phot} = 4.27$). The magenta "x" denotes the detection in K_s-band by ZFOURGE, $\mathrm{ID_{ZFOURGE}} = 6755$ ($z_{phot} = 3.47$). 47

3.10 Local over-density (δ) of individual galaxies in the GOODS-ALMA field at $3.42 < z < 3.57$. The black dots show the sliding medians of δ at different stellar masses. The filled circles indicate all the ALMA detections. The purple circles are the HST dark galaxies and the red circle indicates AGS24. 50

3.11 Projected density of 364 galaxies (40 with z_{spec}) at $3.42 \leq z \leq 3.57$. The contours show 1,2,3,4σ level of the over-density. ***Left*** panel covers the field observed in GOODS-*South* ALMA. ***Right*** panel shows the zoom-in of the extended structure in the bottom right corner of GOODS-ALMA field, which encompasses 126(18) galaxies over 15 arcmin^2. The red star indicates the position of AGS24. The red circle indicates a 50″ radius region (2 arcmin^2) including 26(3) galaxies. The yellow stars refer to the HST-galaxies AGS 11, 15 and 17 located also in this larger structure. The green circles represent the AGS 1 and 5 which are also in this redshift range but not optically-dark. The white circles show the 40 galaxies with spectroscopic redshifts. We note that the two white circles falling on the red star of AGS24 are two galaxies dissociated from AGS24. The magenta square denotes the center of the proto-cluster CCPC-z34-002 identified by Franck and McGaugh (2016). The cyan square denotes Candels5001, which used to be the most massive galaxy at $3 < z < 4$ in this field (Ginolfi et al., 2017). The 50″ scale in the figure is equivalent to a proper distance of 0.37 Mpc at $z = 3.5$. 51

3.12 Comparison of the auto-correlation function (ACF) of the 364 galaxies at $3.42 \leq z \leq 3.57$ in the ZFOURGE catalog (red dots), the cross-correlation function (CCF) between these galaxies and the ALMA detections (black triangles), and the cross-correlation function between these galaxies and the galaxies which are equivalently massive as the ALMA detections (green triangles), i.e., $M_\star > 10^{10.5}$ M$_\odot$. 52

3.13 Projected numbers of galaxies in the over-density as a function of their distance to AGS24 (black circles) and the black dashed line is the linear fitting to the profile. The red line shows the best-fit projected NFW profile (Navarro et al., 1996) of a galaxy cluster at $z = 2.506$, CL J1001+0220 (Wang et al., 2016a). 54

4.1 **Left:** CO J=2-1 emission and 1.3 mm continuum superimposed on HST V-band image. The red contours denote the CO J=2-1 detection at the resolution of 1″71 × 1″48, starting from 2 σ, in increments of 1 σ (3.3 mJy/beam) significance. The yellow contours denote the continuum detection at 1.3 mm at the resolution of 2″21 × 2″06, starting from 1 σ, in increments of 1 σ significance (0.024 mJy/beam). Dashed contours are in negative. **Right:**The CO J=2-1 spectra with a velocity resolution of 3 km s^{-1} from the merged, obs-17 and obs18 data cubes, extracted from the area defined by the 3-σ contour as shown in Figure 4.1-Left. The 1 σ uncertainty is 0.72, 0.72, 1.39 mJy, respectively. The grey dash line denotes the marginal detection at ∼46 km s^{-1}. 59

4.2 SED of IZw18, with CIGALE best fit adopting a delayed star formation history, a Draine et al. (2007) dust model, and a radio component. A modified blackbody fit is shown with a grey dotted line. The 1.3 mm continuum 3σ upper limit is shown as in the black box. . . . 60

4.3 The infrared luminosity and SFR (*Top-left*) versus $L'_{\rm CO(1-0)}$ (*Bottom-left*) as well as the SFR/$L'_{\rm CO(1-0)}$ as a function of metallicity. The upper limit of IZw18 is show as a black circle with an arrow, in comparison with the galaxies described in Section 5.4. In the two panels on the left, the blue dashed lines show the linear correlation by Gao and Solomon (2004) and the red dashed lines show the linear fit of the metal poor galaxies (Shi et al., 2015a; Shi et al., 2016; Hunt et al., 2015a; Cormier et al., 2014, DGS). In the right panel, the blue solid line denote the best fit of the metal poor galaxies in Hunt et al. (2015a) where galaxies in Schruba et al. (2012) are also included. The black solid line shows a power law fitting all the galaxies in the plot. 61

4.4 $L_{\rm CII}/L_{\rm CO(1-0)}$ ratio as a function of metallicity (*Left*) and specific SFR (*Right*). The Pearson correlation coefficients of the regression fits are shown in the bottom left corners in each panel. 63

5.1 Images of different components of each galaxy. Top: SFR surface density (extinction corrected) in $M_\odot$ yr^{-1} kpc^{-2}. Middle: ionised gas velocity in km s^{-1}. Bottom: ionised gas velocity dispersion in km s^{-1}. In all images, we only display spaxels with S/N > 34 (see Section 5.2.2.2 for the choice of S/N). The red crosses are the centres of the galaxies. The white solid lines are the major axes (see Section 5.2.2.1). 68

5.2 Dependence of gas velocity dispersion ($\sigma_{\rm gas}$) on velocity gradient ($v_{\rm grad}$, Equation 5.1). Points in each individual galaxy are labeled by colour. The solid line refers to $\sigma_{\rm gas}$ = 2 $v_{\rm grad}$ and the dashed line refers to $\sigma_{\rm gas}$ = $v_{\rm grad}$. The dotted line denotes the velocity gradient at 20 km s^{-1}. These three different lines represent the three different criteria that we tested to account for beam smearing (Section 5.2.2.3). 71

5.3 Spatially resolved dependence of $\sigma_{\rm gas}$ on $\Sigma_{\rm SFR}$. We remove pixels with $v_{\rm grad}$ > 0.5 $\sigma_{\rm gas}$ to account for beam smearing effects (see Figure 5.2 and Section 5.2.2). Our eight SAMI galaxies are compared to Lehnert et al. (2009, Figure 12 therein). Each filled circle refers to one spaxel in each galaxy and is colour-coded with the magnitude of velocity gradient ($v_{\rm grad}$, Equation 5.1). The crosses and asterisks in different colours refer to the 11 actively star-forming galaxies at $z \sim 2$ in Lehnert et al. (2009). The solid black curves show $\sigma \propto (\epsilon \dot{E})^{1/2}$, where $\dot{E}$ is the energy injection due to star formation, and ϵ is the coupling efficiency of the energy injected into the ISM. The dashed curves show $\sigma \propto (\epsilon \dot{E})^{1/3}$ assuming that velocity dispersions correspond to energy dissipation due to turbulent motions. The red solid curve shows the velocity dispersion of a 10^8 $M_\odot$ clump assuming a simple Jeans relation. A zoom-in of our SAMI galaxies with a logarithmic y-axis is also shown here. All of the models have included the typical thermal broadening of Hα of 12 km s^{-1}. The error bars in the zoom-in figure show the maximum range of the thermal broadening of 10 –15 km s^{-1}. The colourbar on the left shows the magnitude of the velocity gradient (v_g). 74

5.4 Global dependence of $\sigma_{\rm gas}$ on $\Sigma_{\rm SFR}$. Our eight SAMI galaxies compared to local high Hα luminosity galaxies from Green et al. (2014) and z > 1 star-forming galaxies and clumps (see Section 5.3.2.2 for further details). Each blue (red) filled diamond shows one entire galaxy in our sample including (excluding) the contribution from thermal broadening ($\sigma_{\rm thermal} \sim$ 12 km s^{-1}, Glazebrook, 2013). For the measurement of $\sigma_{\rm gas}$ and $\Sigma_{\rm SFR}$, see footnotes in Table 6.1. Green diamonds refer to the Hα luminous galaxies in Green et al. (2014). The black filled squares, dark green triangles, red open squares and blue open circles refer to the z > 1 star-forming galaxies and clumps. The grey contour denotes the distribution of local star-forming galaxies with gas velocity dispersion derived from HI (Dib et al., 2006), and we include the intrinsic thermal broadening of 12 km s^{-1} here. 77

5.5 Velocity dispersion as a function of velocity. Spaxels along the major axis are plotted with errorbars. Points in each individual galaxy are labeled by colour. 80

6.1 The Herschel images of our galaxies at 70, 160, 250 and 350 μm from left to right. The large ellipses indicate the extension of the whole star-forming disk and small circles are those individual dusty star-forming regions. 85

6.2 **Left**: The distribution of EMP star-forming regions, and integrated measurements of galaxies from DGS and KINGFISH in the $f_{70\mu m}/f_{160\mu m}$ vs. $f_{160\mu m}/f_{250\mu m}$ color-color diagram. The grid is a single modified black-body with a range of temperatures and emissivity indices. The solid line represents a constant emissivity index, β, with the temperature ranging from 10 to 100 K in a decrement of 5 K from the left-bottom to the upper-right. Dashed lines represent constant temperature with β ranging from 0.0 to 3.0 in a step of 0.5 from the left-bottom to the upper-right. The brown line is the trend of star forming galaxies predicted by the model of Dale et al. (2014). **Right**: Same as left but using $f_{160\mu m}/f_{250\mu m}$ vs. $f_{250\mu m}/f_{350\mu m}$. 89
6.3 The two modified black-body fitting to the SEDs. Reds dots are the flux density at different wavelength within each star-forming region. Black solid lines are the 2T MMB best fits with blue dotted lines the best fits of the warm dust components and blue dashed lines the best fits of the cold dust components. 90
6.4 The fraction of warm dust emission at 100 μm as a function of the Oxygen abundance based on the two modified black-body fitting. The red diamonds are the EMP star-forming regions, and blue circles are for the integrated dwarf galaxies from the DGS. 91
6.5 The IR colors as functions far-UV surface brightness, 24 μm surface brightness, SFR surface densities and stellar mass surface densities from left to right. 93
6.6 The dust-to-stellar mass ratio of our EMP star-forming regions and integrated galaxies of the DGS. The lines are the model predictions by Feldmann (2015). t_{ISM} is the dust growth time-scale which can be computed from basic collision theory (Weingartner and Draine, 1999) (solid or dashed lines). Q_{MS} denotes the (multiplicative) offset of a given galaxy from the main sequence (blue: 1/3, cyan: 1, green: 3). The data for IZw 18 and SBS 0335-052 are from Hunt et al. (2014). 95

List of Tables

3.1 Properties of the optically dark galaxies. . . . 43
3.2 Information of the neighbors of AGS24. . . . 44
3.3 Stellar masses of AGS24 assuming different SFHs and attenuation laws. . . . 46

5.1 Red and blue data cubes from LZIFU. . . . 67
5.2 Properties of the eight star-forming galaxies in our final sample of star-forming SAMI galaxies. . . . 69
5.3 Spearman correlation coefficient (r_s). . . . 77

6.1 Properties of our four EMP galaxies along with additional two galaxies from the literature . 85
6.2 Exposure time of *Herschel* data used in this paper. . . . 86
6.3 Photometry Of Individual Star-forming Regions In Metal Poor Galaxies . . . 87
6.4 Pixel sizes of *Herschel* data used in this paper. . . . 88
6.5 Results of Single MBB Fits to the SEDs at $\geq$ 100 μm . . . 91
6.6 Results of two MBB Fits to the Photometry . . . 92
6.7 Measurements of 2-D Densities of EMP Star-Forming Regions . . . 96

Colophon

This thesis was typeset with LaTeX 2$_\varepsilon$. It uses the *Clean Thesis* style developed by Ricardo Langner. The design of the *Clean Thesis* style is inspired by user guide documents from Apple Inc.

Download the *Clean Thesis* style at http://cleanthesis.der-ric.de/.

université PARIS-SACLAY

ÉCOLE DOCTORALE
Astronomie et Astrophysique d'île-de-France

Titre : Sonder les processus qui conduisent à la formation d'étoiles locales et distantes dans les galaxies à travers la poussière et les molécules

Mots clés : évolution des galaxies, formation d'étoiles, milieu interstellaire, ALMA, Herschel, NOEMA

Résumé : Les études sur l'évolution des galaxies ont été révolutionnées au cours des dernières décennies grâce aux nouveau télescopes et aux instruments de pointe. Les interféromètres Herschel, ALMA et NOEMA permettent d'observer l'émission des poussières tracant la formation des étoiles, invisible dans les bandes infrarouges proche observées par les télescopes optiques.
Dans cette thèse, je me concentre sur la formation des étoiles aux grandes échelles des galaxies ($\sim$kpc). En utilisant les données des téléscopes Herschel, ALMA, NOEMA, et SAMI IFU, ma thèse tente de mettre en lumière les questions suivantes : (1) Comment les premières galaxies ont-elles formé des étoiles à partir du gaz contenant peu de métaux ? (2) Comment les galaxies massives du début de l'Univers ont-elles rapidement constitué leur masse et finalement cessé de former des étoiles ? (3) Quel est le rôle joué par les environnements dans lesquels elles résident ? (4) Comment la rétroaction de la formation des étoiles affecte-t-elle la cinématique des galaxies ?
Premièrement, je présente l'étude de six galaxies optiquement sombres extraites de l'étude GOODS-ALMA (la plus grande étude cosmologique à 1,1m) dont le décalage vers le rouge est supérieur à $z = 3$.
Je présente des preuves que quatre d'entre elles appartiennent à la même surdensité de galaxies, situé à $z \sim 3.5$. L'une d'entre elles, AGS24, est la galaxie la plus massive, sans noyau galactique actif et situé à $z > 3$.
Cette dernière se situe également au centre du pic de densité de surface des galaxies, suggèrant que la surdensité environnante est un proto-amas en cours de virialisation et qu'AGS24 est un candidat progéniteur d'un futur amas de galaxie plus brillant.
Deuxièmement, en me basant sur une observation NOEMA, j'ai étudié la teneur en gaz moléculaire dans IZw18, l'une des galaxies les plus pauvres en métal de l'Univers local. J'ai obtenu une limite supérieure d'émission de CO(J=2-1) qui est dix fois plus faible que précédemment déterminée, ceci malgré la forte activité de formation d'étoiles. Sa faible teneur en CO (par rapport à sa luminosité infrarouge), son taux de formation d'étoiles, et sa luminosité [CII] indiquent un changement drastique dans la structure du MIS (environ quelques pourcents de la métallicité solaire). En particulier, la luminosité élevée [CII] par rapport au CO implique un réservoir moléculaire plus important que l'émetteur de CO dans l'IZw18.
Troisièmement, mes travaux sur les sources d'énergie des mouvements turbulents montrent qu'à des échelles inférieures au kpc, les galaxies locales formant des étoiles du relevé SAMI présentent une distribution plate de la dispersion de vitesse du gaz ionisé en fonction de la densité de surface du taux de formation d'étoiles. Cependant, le plancher de dispersion de vitesse est plus élevé que ce que prédisent les modèles "feedback-driven". Cela suggère que des sources supplémentaires à la rétroaction de formation d'étoiles entraînent des mouvements aléatoires du MIS dans les galaxies formant des étoiles.
Enfin, je présente mes travaux sur l'émission de poussières spatiallement résolue des galaxies extrêmement pauvres en métaux observées par HerschelCes galaxies présentent des températures de poussière plus élevées et des indices d'émissivité plus faibles que ceux des galaxies spirales. Environ la moitié de l'émission à 100um provient de la poussière chaude (50K), par opposition à la composante froide ($\sim$20K) de la poussière. Les couleurs de l'infrarouge lointain sont toutes liées aux densités de surface des jeunes étoiles, mais pas aux densités de surface des masses stellaires. Cela suggère que leur poussière (70$\sim$350μm) est principalement chauffée par le rayonnement des jeunes étoiles.

Université Paris-Saclay
Espace Technologique / Immeuble Discovery
Route de l'Orme aux Merisiers RD 128 / 91190 Saint-Aubin, France

université PARIS-SACLAY

ÉCOLE DOCTORALE
Astronomie et Astrophysique d'île-de-France

Title : Probing the processes driving distant and local star-formation in galaxies through dust and molecules

Keywords : galaxy evolution, star formation, interstellar medium, ALMA, Herschel, NOEMA

Abstract : Studies on galaxy evolution have been revolutionized during the last decade thanks to the state-of-the-art telescopes and instruments. *Herschel* Space Telescope, ALMA and NOEMA interferometers can observe the dust emission that traces star formation missed by optical to near-infrared telescopes. Their high sensitivity pushes further their detections to the most distant galaxies or the faintest local galaxies, of which the formation and evolution challenge current theories and models. And the integral field unit technique combines the spatial information with the properties extracted from spectra which allows a thorough study of galaxy kinematics.

In this thesis, I focus on the large-scale ($\sim$ kpc) star formation of galaxies. Taking advantage of the data from *Herschel*, ALMA, NOEMA, and the SAMI IFU survey, my thesis tries to put more constraints on the following questions: (1) How did the first galaxies form stars out of gas with little metal? (2) How did the massive galaxies in the early Universe rapidly build up their masses and finally stop forming stars? and (3) what is the role played by the environments they reside in? (4) How does star formation feedback affect the galaxy kinematics?

A large portion of the work done in this thesis is based on the GOODS-ALMA survey, the largest cosmological survey with the large ALMA interferometer at 1.1 mm. I studied the six optically dark galaxies with redshifts greater than $z = 3$ uncovered by this survey. We present evidence that four out of the six optically dark galaxies belong to the same overdensity of galaxies at $z \sim 3.5$. One of them, AGS24, is the most massive galaxy without an active galactic nucleus at $z > 3$ in the GOODS-ALMA field. It also falls in the very center of the galaxy surface density peak, suggesting that the surrounding overdensity is a proto-cluster in the process of virialization and that AGS24 is the candidate progenitor of the future brightest cluster galaxy. I also studied the molecular gas content in IZw18, one of the most metal poor galaxies in the local Universe based on the observation of NOEMA. I obtain an upper limit of CO J=2-1 emission, which is used as a tracer of molecular gas, to be ten times lower than previous studies despite its vigorous star formation activities. Such low CO content relative to its infrared luminosity, star formation rate and [C II] luminosity, indicates a drastic change in the structure of the ISM at around a few percentages of Solar metallicity. Especially, the high [C II] luminosity relative to CO implies a larger molecular reservoir than the CO emitter in IZw18.

My work on the energy sources of the turbulent motions shows that on sub-kpc scales, local star-forming galaxies from the SAMI survey display a flat distribution of ionized gas velocity dispersion as a function of star formation rate surface density. However, the velocity dispersion floor is higher than predicted by feedback-driven models. This suggests that additional sources to star formation feedback drive random motions of the interstellar medium in star-forming galaxies.

Finally I present my work on the spatially resolved dust emission of extremely metal-poor galaxies observed by *Herschel*. These galaxies show higher dust temperatures and lower emissivity indices compared to those of spiral galaxies. And about half of the emission at 100 μm comes from warm (50 K) dust, in contrast to the cold ($\sim$20 K) dust component. The far-infrared colours are all related to the surface densities of young stars, but not to the stellar mass surface densities. This suggests that their dust emission (70 $\sim$ 350 μm) is primarily heated by radiation from young stars.

Université Paris-Saclay
Espace Technologique / Immeuble Discovery
Route de l'Orme aux Merisiers RD 128 / 91190 Saint-Aubin, France